AlMo Nanocomposite Characterization, Device Fabrication and Biosensors

by

Remko Vincent van den Hurk

A thesis submitted in partial fulfillment of the requirements for the degree of

Doctor of Philosophy

in

Microsystems and Nanodevices

Department of Electrical and Computer Engineering
University of Alberta

Abstract

Nanocomposite materials are multiphase materials where at least one of the dimensions of one of the materials is less than 100 nm in size. The primary goal of nanocomposite materials development is to create material properties that are not available in traditional materials. AlMo nanocomposites can be fabricated by co-sputtering Al and Mo. A particular ratio with interesting properties is 68 atomic % Al and 32 atomic % Mo. Due to very low surface roughness and small grain size, it can be used to form ultrathin, ultrasmooth devices. Furthermore, the nanocomposite has good conductivity (in the metallic range). Such membranes have potential applications in micro- and nano-electromechanical systems which require thin, strong and conductive materials.

The objectives of this work were to further the characterization of the AlMo nanocomposite material for potential applications, fabricate devices for such potential applications and implement one or more of the devices in a proof of concept of the potential of the AlMo nanocomposite material. A number of properties of the nanocomposite were assessed. The values determined for density, hardness, Young's Modulus, Poisson's ratio and resistivity were generally in good agreement with previously published calculations and/or results.

Ultrathin very high-aspect ratio AlMo nanomembranes as thin as 10 nm were fabricated, and bulge and burst pressure measurements were performed. The fracture strength of the nanocomposite was found to be 1.89±0.45 GPa, which compares favorably to the measured fracture strength of fabricated silicon nitride membranes which was 3.28±0.28 GPa. Since the tensile strength is comparable to that of silicon nitride, it is reasonable to use the AlMo nanocomposite as a hybrid conductive/structural layer in devices.

The effect of temperature annealing and deposition pressure on the intrinsic stress was measured, as was the effect of deposition pressure on resistivity. Both annealing and alteration of the deposition stress were shown to be effective methods for adjusting the intrinsic stress of the AlMo nanocomposite, and thus the resonance frequency of the membranes. This can be valuable for energy harvesting and biosensor applications to increase efficiency or sensitivity, respectively.

Following characterization of the AlMo nanocomposite and AlMo nanomembranes, additional device fabrication was performed. Ni proof masses were electrodeposited onto AlMo membranes. Proof masses can be used to adjust the resonance frequency of devices, as was observed when the resonance frequency of these membranes was measured.

The second set of devices was freestanding Archimedes spirals. They were fabricated via a lift-off procedure and two-step release methods consisting of a deep reactive ion etch and a XeF_2 gas etch. The design of the spirals was similar to that used in an energy harvester for pacemakers, but at a much smaller scale.

The third set of devices consisted of two-armed nano-cantilevers with potential applications as sensors. The paddles were fabricated through electron beam lithography, a lift-off process and a XeF_2 gas etch release step. Such cantilevers, as they are conductive, could be used for potentiometric measurements of cantilever deflection where molecules bind to the cantilever surface.

The third element of the thesis concerns the implementation of the ultrathin AlMo membranes for resonance-based biosensors. A number of processes were used to successfully link detection molecules to the surface of the membranes. Several detection molecules were employed, including two monoclonal antibodies (Abs), and GP10, a bacteriophage tail spike

protein. The monoclonal Ab 3D9S was utilized to capture bovine herpesvirus-1, the monoclonal Ab 11B6 was used to capture the hexon protein of hemorrhagic enteritis virus, and bacteriophage GP10 protein was used to capture *Mycobacteria smegmatis* and *Mycobacteria avium (M. Avium)*. The change in resonance frequency of the membranes upon capture of protein, virus or bacteria was recorded. Calculations of the added mass were performed. Images of the membranes were taken, which showed that the change in resonance frequency and calculated added mass largely matched the quantity of material visible on the membrane surface. These results demonstrated the successful detection of bovine herpesvirus-1 and *M. Avium* through resonance measurements using the AlMo membranes. Furthermore, the *M. Avium* results indicate that the change in resonance frequency is related to the total mass that is captured on the surface.

Preface

Section 2.2 of chapter 2 was published as a review article *A Review of Membrane-Based Biosensors for Pathogen Detection* by Remko van den Hurk and Stephane Evoy, in Sensors, 2015; 15(6):14045-14078 with a few alterations. The review was written by myself with editing assistance from Dr. Evoy. Chapter 3 was published previously as *Fabrication and characterization of aluminum-molybdenum nanocomposite membranes* by Remko van den Hurk, Nathan Nelson-Fitzpatrick and Stephane Evoy, in the Journal of Vacuum Science & Technology B, 2014; 32(5): 052002. Dr. Nelson-Fitzpatrick provided the initial fabrication process for the AlMo membranes. The low-stress silicon nitride was deposited by University of Alberta Nanofab staff. Dr. Evoy provided editing assistance. The remainder of the work was performed by me. Sections of Chapter 5, particularly regarding functionalization with FBDP and detection of BHV-1 have been submitted to Sensors and Actuators A: Physical under the title *Al-Mo Nanocomposite Functionalization for Membrane-based Resonance Detection of Bovine Herpesvirus-1*. The e-beam lithography for the fabrication of the cantilevers described in section 4.3 was performed by Dr. Wei Zhang. The XPS measurements in section 5.1 were performed by University of Alberta Nanofab staff. The bacteria and GP10 protein used in chapter 5 were provided by Dr. Gabriel Rojas Ponce and Dr. Upasana Singh. The Ansys calculations in section 5.1 were largely performed by Dr. Masoud Baghelani. The bovine herpesvirus 1 and 3D9S antibody used in Chapter 5 were provided by Dr. Sylvia van den Hurk. The hemorrhagic enteritis virus, hexon protein and 11B6 antibody used in chapter 5 were provided by Dr. Jan van den Hurk.

Acknowledgements

I would like to thank my supervisor Dr. Stephane Evoy for his patience, support and guidance and my parents Drs. Jan and Sylvia van den Hurk for their aid and understanding. I would like to thank my co-supervisors Dr. Mojgan Daneshmand and Dr. Jie Chen for helping and supporting me after Dr. Evoy had to depart on long term medical leave. I would also like to thank Dr. Xihua Wang for agreeing to sit on my supervisory committee on short notice. I am grateful to the Nanofab staff in general, and Les Schowalter, Scott Munro, Stephanie Bozic, Peng Li, Dr. Shihong Xu and Shiau-Yin Wu in particular for teaching me about cleanroom fabrication and device characterization. I would also like to thank Dr. Gabriel Rojas Ponce and Dr. Upasana Singh for providing me with purified tail spike protein and bacteria. I appreciate the help Dr. Masoud Baghelani provided with the ANSYS calculations. I am appreciative of Dr. Wei Zhang for her help with e-beam lithography. I also want to thank Dr. Jeremy Sit and Dr. Jonathan Veinot for their suggestions regarding the silanization process.

Table of Contents

List of Tables

List of Figures

List of Abbreviations

(3-Aminopropyl)triethoxysilane (APTES)

1,2-Dipalmitoyl-sn-glycero-3-phosphocholine (DPPC)

11-Mercapto-1-undecanoicacid (MUA), 11-Mercapto-1-undecanol (MUO) and Dodecane-thiol (DOT)

1-Ethyl-3-(3-dimethylaminopropyl)carbodiimide (EDC)

4-formylbenzene diazonium hexafluorophosphate (FBDP)

3-Glycidoxypropyldimethylethoxysilane (GPDMES)

(3-Glycidyloxypropyl)trimethoxysilane (GPTMS)

alternating current (AC)

aluminum-molybdenum (AlMo)

atomic percent (at. %)

bis-peptide nucleic acid (PNA)

bovine herpes virus-1 (BHV-1)

bovine serum albumin (BSA)

capacitive micro-machined ultrasonic transducers (CMUTs)

carbon nanotube (CNT)

cell culture infective dose (CCID)

cellulose acetate (CA)

colony forming units (CFU)

deep reactive ion etching (DRIE)

differential pulse voltammetry (DPV)

direct current (DC)

direct epifluorescence technique (DEFT)

divinyl sulfone (DVS)

double-stranded DNA (dsDNA)

electrochemical impedance spectroscopy (EIS)

electron beam (E-beam)

enzyme-linked immunosorbent assay (ELISA)

Escherichia coli (*E. coli*)

ethylene di-amine pyro-catechol (EDP)

finite element analysis (FEA)

helium ion microscope (HIM)

horseradish peroxidase (HRP)

HRP-conjugated polyclonal Ab (HRP-pAb)

interferon gamma (IFN-γ)

hydroxypropyl cellulose (HPC)

isopropyl alcohol (IPA)

lead zirconate titanate (PZT)

low pressure chemical vapour deposition (LPCVD)

methylisobutylketone (MIBK)

methyltrimethoxysilane (MTMOS)

microelectromechanical-system (MEMS)

monoclonal antibody (mAb)

monosialoganglioside (GM1)

multi-walled carbon nanotube (MWCNT)

Mycobacteria avium (M. avium)

Mycobacteria Smegmatis (*M. Smegmatis*)

nanocrystal (NC)

nano electromechanical system (NEMS)

N-hydroxysulfosuccinimide (NHS)

Oleic acid (OLEA)

phosphate buffered saline (PBS)

photocrosslinkable poly(vinyl alcohol) bearing styrylpyridinium groups (PVA-SbQ)

physical vapour deposition (PVD)

plaque forming units (PFU)

plasma enhanced chemical vapour deposition (PECVD)

p-nitrophenol (*p*NP)

p-nitrophenyl phosphate (*p*NPP)

polycarbonate track-etched (PCTE)

polydimethylsiloxane (PDMS)
polyethylene glycol (PEG)
polylactic acid (PLA)
polymerase chain reaction (PCR)
polyvinylidene fluoride (PVDF)
protein phosphatase (PP)
quartz crystal microbalance (QCM)
reactive ion etching (RIE)
scanning electron microscope (SEM)
screen-printed carbon electrodes (SPEs)
silicon nitride (SiN)
single stranded DNA (ssDNA)
single-wall carbon nanotube (SWNT)
standard deviation (σ)
surface plasmon resonance (SPR)
tail spike protein (TSP)
tetramethoxysilane (TMOS)
tetramethylammonium hydroxide (TMAH)
tricosadiynoic acid (TRCDA)

1. Introduction

Nanocomposite materials are multiphase materials where at least one of the dimensions of one of the materials is less than 100 nm in size. The primary goal of nanocomposite materials development is to create material properties that are not available in traditional materials. A variety of different materials and techniques have been used to fabricate these nanocomposites. These include purely metal nanocomposites such as AlMo. AlMo is composed purely of elemental Al and Mo, and has been fabricated by co-sputtering Al and Mo. A particular ratio with interesting properties contains 32 atomic percent (at. %) Mo. In particular, this ratio leads to minimum surface roughness and grain size, which according to Hall-Petch strengthening corresponds to the strongest possible material. For this reason, this composition of the AlMo nanocomposite can be used to form ultrathin devices.[1-3] Furthermore, the nanocomposite has resistivity in the metallic range, is corrosion resistant and chemically reactive. These properties make the AlMo nanocomposite an attractive material for sensor and energy harvesting applications.

1.1. Motivation

When the component materials of nanocomposites are combined together, there is frequently a balancing of the material properties partway between the individual component materials. The composite density may, for example, be based on the percent atomic contribution of the individual materials and their bulk densities. Conversely however, the formation of a nanocomposite material may also lead to the introduction of desirable characteristics that are not simply a result of the blending of two or more materials. These can be properties not exhibited by either of the base materials on their own, such as increased strength or decreased surface roughness. It can also lead to the introduction of new properties to a base material, such as the introduction of piezoelectric or light emitting properties into polymeric membranes through the addition of piezoelectric or light emitting particles.

Several articles have been published concerning AlMo cosputtered nanocomposites.[1-3] It was discovered that in the region of 30-35 at. % Mo, it forms an amorphous Al structure with

islands of Mo.[3] The main features of such amorphous metals are near-atomic smoothness, isotropic chemical and mechanical properties, and increased strength.[3] Furthermore, this AlMo nanocomposite has conductivity in the metallic range and is corrosion resistant.[1] To maximize the properties of high smoothness and strength, fabrication was targeted in the center of this range with 32 at. % Mo. The 32 at. % Mo AlMo nanocomposite was subsequently used to fabricate structures as thin as 5 nm in thickness.[1]

The AlMo nanocomposite material appears promising for potential applications that benefit from ultrathin conductive structures. Initial applications for very thin membrane energy harvesters or sensors have been assessed (data not shown). In such applications the membranes could be used as both a structural layer and a conductive electrode simultaneously, potentially decreasing the overall thickness of the device. This could potentially increase the sensitivity of the sensor or the efficiency of the energy harvester.

A number of properties of the Al and Mo nanocomposites have been published previously. Transmission electron microscopy, atomic force microscopy, x-ray diffraction, and thermodynamic modeling were used to examine the changes in the thin film as the at. % of Al and Mo in the films was varied.[1,3] This was used to create a structure zone map.[2] The hardness and Young's modulus were determined through nanoindentation and cantilever resonance frequency measurements, the root mean square surface roughness was determined through atomic force microscopy, and the resistivity was determined through four-point probe measurements.[1,2] Cantilevers, doubly-clamped paddles and doubly-clamped beams between 20 and 5 nm thick were fabricated.[1] Furthermore, the resonance properties of fabricated cantilevers were presented and their damping mechanisms were shown to be related to device microstructure.[1,3]

Aside from the Young's modulus measurement that was performed using the cantilevers, the measurements were largely performed using a 1.5-2.0 μm thick thin film.[1] As the thickness approaches the nanoscale however, properties can change substantially. The AlMo structures that were fabricated were 5-20 nm thick, however, so it is important to examine or re-examine the properties of the AlMo nanocomposite at this scale. Furthermore, while the strength of the material was alluded to previously, it was not measured. In order to accurately assess the potential of the AlMo nanocomposite, it is therefore important to directly assess this material property and compare it to other common materials used for devices at this scale.

1.2. Objectives

The overarching goal of the thesis was to verify and expand the characterization of the 68 at. % Al and 32 at. % Mo nanocomposite, fabricate devices from this nanocomposite for possible applications and implement the devices for promising applications. These objectives were separated into three sub objectives as presented below. The results from each objective are described in chapters 3-5.

1.2.1. Material characterization

Among the material properties that were not tested previously is the strength of the nanocomposite. This is of interest for many fabrication applications, particularly for very thin structures. To this end, membranes were fabricated to test the tensile strength of the 32 at % Mo AlMo nanocomposite. Since the Young's modulus values that were determined from the cantilever and indentation measurements were different, this property was re-examined. The Poisson's ratio was also considered, as it was not presented previously. In addition, the density of the nanocomposite was measured as this was previously only calculated theoretically.

An attractive feature of the nanocomposite is the relatively high conductivity of the material, compared to silicon nitride (SiN) for example. The conductivity was determined for different membrane thicknesses. Furthermore, intrinsic stress can be of critical importance in many microelectromechanical systems (MEMS) or nanoelectromechanical systems (NEMS) applications. For this reason, the change in intrinsic stress with different temperatures and deposition pressures was determined. These values were determined by performing bulge measurements and resonance measurements, and were verified by Comsol simulations.

1.2.2. Device fabrication

To assess the functionality of the AlMo nanocomposite for energy harvesting and biosensor applications several different devices were fabricated. The first were proof masses that were fabricated onto the AlMo membranes. Proof masses are used to adjust the resonance frequency of devices. The purpose was to design a process that can be used to adjust the

resonance frequency of an energy harvesting device. When the resonance frequency of an energy harvesting device is matched to that of the source frequency, it can maximize power output.[4]

The second set of devices consisted of freestanding Archimedes spirals. The designs were similar to those used in an energy harvester for pacemakers.[5] In these energy harvesters physical compression was used to power the pacemaker. The design was much smaller than that published previously, however, and the eventual goal was to assess the potential benefits of shrinking the device down to the micro/nano-scale.

The third set of devices that were fabricated were two-armed nano-cantilevers with potential applications as sensors. Such cantilevers, as they are conductive, could be used for potentiometric measurements of cantilever deflection. When molecules bind to the surface of the cantilevers, it can lead to a change in the resistance of the cantilever. If specific capture methods are used, sensors can be developed for specific detection of chemical and biological materials.

1.2.3. Device implementation

A variety of ultrathin low mass structures have been used for biosensors, including singly and doubly clamped cantilevers[6,7], membrane-like structures[8] and structures midway between membranes and doubly-clamped cantilevers[9]. Like these structures, the resonance frequency of thin membranes varies with the inverse square-root of the mass of the structure. This means that like these other structures, they have potential in such biosensor applications. The ultrathin AlMo membranes that were fabricated also have certain advantages over other structures and materials for mass-based resonance detection. Firstly, the resonance measurements that were performed rely on variation in light intensity. Therefore, for this application, the increased reflectivity of the AlMo over other structural materials like silicon nitride is an advantage. Secondly, at low concentrations the greater surface area of biosensors such as membranes can increase the capture rate of the material being detected. Thirdly, membranes can potentially be fabricated in greater numbers without the need of substantial expensive e-beam lithography. Additionally, as opposed to open structures such as cantilevers, membranes can be impermeable and therefore the two surfaces of a sensor can be isolated. This makes it possible to separate a transduction signal, such as an interferometric measurement, from the physical interaction of the other side of the membrane with the analytes. Finally, Al and Mo are more reactive than other materials, such as

silicon nitride. This is important, because the method of attachment of the detection molecule to the sensor surface can have a significant impact on the sensitivity and consistency of the sensor.

For these reasons the ultrathin AlMo nanocomposite membranes were examined for biosensor applications. Different linking processes were examined for the attachment of Abs (Abs) and viral tail spike proteins (TSPs) to the membrane surface. These were then used to capture pathogens on the AlMo surface. Upon verification of the pathogen detection via scanning electron microscope (SEM) imaging, these capture processes were implemented on the membranes. Resonance measurements were performed to detect the change in mass of the material on the membranes following pathogen capture.

1.3. Thesis Outline

The outline for this thesis is as follows. Background information concerning nanocomposite materials, fabrication techniques, membrane biosensors for pathogen detection and interferometric measurements are presented in Chapter 2. The fabrication of the membranes and assessment of AlMo material properties are described in Chapter 3. The fabrication of proof masses, Archimedes spirals and deflection cantilevers is presented in Chapter 4. Biosensor preparation and measurements are presented in Chapter 5. Finally a summary and recommendations for future work are presented in Chapter 6.

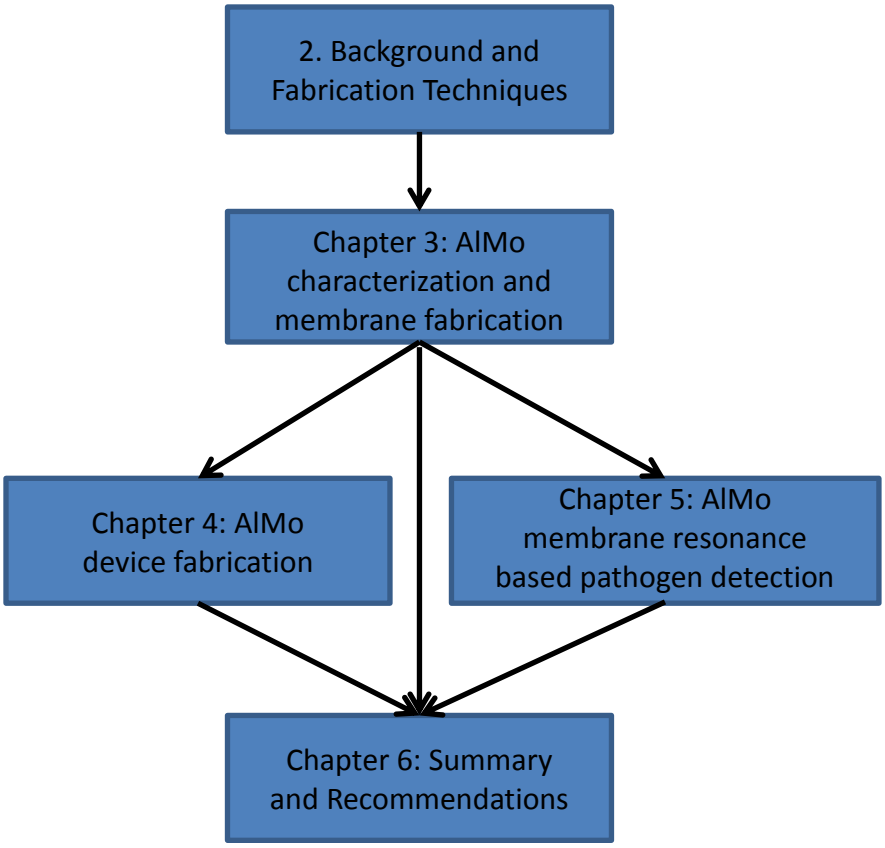

Figure 1.1: Schematic depiction of thesis outline.

2. Background and Fabrication Techniques

This chapter covers background information on four topics that are relevant to the work that is described in the subsequent chapters. In section 2.1, information about nanocomposite materials is presented. Subsequently, in section 2.2 fabrication processes, particularly from the perspective of membrane fabrication, are presented. The techniques used are equally applicable to fabrication of other structures and devices. This includes lithography, deposition, process adjustment, and structural release techniques. Section 2.3 contains a detailed examination of membrane use for pathogen detection. It includes information about the materials and techniques used to fabricate the membranes, the molecules used to detect the pathogens, how these molecules are linked to the surface of the membranes, the transduction methods used to give a readout signaling the presence of the pathogen, and the sensitivity of the technique used to detect the pathogen. Finally interferometry, and the process that was employed for the resonance measurements, is addressed in Section 2.4.

2.1. Nanocomposite Materials

Nanocomposite materials are multiphase materials where at least one of the dimensions of one of the materials is less than 100 nm in size. The primary goal of nanocomposite material development is to create material properties that are not available in traditional materials.[10] There are a number of more common nanocomposite materials. Polymer nanocomposites that are formed by the addition of carbon nanotubes (CNTs) to the polymer matrix are now routinely employed for several applications. The addition of the CNTs or other materials alters the tensile strength, Young's Modulus, conductivity and/or other material properties of the polymer material. Clay/polymer nanocomposite materials are also popular and used for a variety of vehicle components such as timing belt covers, rocker-box covers, body panels and bumpers. One current focus of research is to improve the fracture toughness of ceramic nanocomposites impregnated with CNTs.[11]

One type of popular commercial metal matrix composite consists of an aluminum and magnesium matrix impregnated with continuous carbon, silicon carbide or boron fibers.[12-14] The

benefits of these materials are low weight and good physical properties, which are beneficial in the automotive and aerospace industries. Metal nanocomposite research is still at a relatively early stage, however. As with the ceramic nanocomposites and polymer nanocomposites, metal/CNT nanocomposites are of particular interest and show improvements in material properties, particularly tensile strength and hardness.[11] Metal nanocomposites also have applications in microfabrication. They can, for example, be used to produce highly compliant cantilevers for sensor applications.[15]

Nanocomposites are increasingly being investigated and used for numerous different applications. Many books and articles have been written on the topic[16-20], including some aimed specifically at predicting their properties[21] or how to determine/verify said properties[22]. Among these applications are those in the field of micro- and nano-fabrication. A cursory examination yields applications for strength[23], strength and composition[24], mechanical compliancy[25], piezoelectricity[26,27], magnetism[28-30], light emission[31], low stress, increased photosensitivity and tensile strength[32], conductivity[33,34], and conductivity plus transparency[35]

Many different techniques have been used to create nanocomposites and devices. Membranes ~5 mm diameter and ~55 nm thick were generated through a sacrificial photoresist layer. The device layer was made of spin-coated polyelectrolytes impregnated with silica nanoparticles.[23] A piezoelectric material for sensing or actuating systems has been developed by integrating poly(vinylidene fluoride) and nanoparticles of barium titanate into poly(methyl methacrylate). [27] Ceramic/polymer composite and ceramic fibers have been made by extruding a UV-curable monomer and nanoparticle dispersion from a syringe and curing it. [24] An optically transparent piezoelectric material for MEMS-based piezoelectric sensors and energy-harvesting devices has been created by dispersing ZnO in SU-8.[26] A metal AuTa nanocomposite was created by cosputtering, and it was patterned through photolithography to create highly compliant cantilever beams and used to detect dodecanethiol through deflection of the cantilevers.[25] In another application, nanosilica was incorporated into SU-8 photoresist imparting increased photosensitivity, less stress and decreased cracking of the SU-8 structures.[32]

A purely metal-metal nanocomposite was formed using maghemite nanoparticles less than 50 nm in size. The particles were placed in suspension and deposited on a photoresist pattern. The liquid phase was allowed to evaporate and the undesirable particles were removed along with the photoresist. Iron cobalt alloy was then electroplated onto the areas between the

nanoparticle regions. Because both components of the composite were magnetic, it had better magnetic properties than similar polymer matrix nanocomposites.[28] One such polymer matrix nanocomposite was created through the integration of Oleic acid (OLEA)-capped iron oxide nanocrystals into an epoxy photoresist and was used to make AFM probes.[29] The same technique was also used to incorporate red-light-emitting CdSe/ZnS nanocrystals (NCs) into photoresist and create high-aspect-ratio 3D structures with light emitting properties for potential use in photonic, micro-optical, and bio diagnostic devices.[31] A third magnetic application was again implemented by incorporating magnetic nanoparticles into photoresist. The photoresist was transparent and was used to form several test structures; the authors envision applications in complex magnetically actuated MEMS and high transparency biological applications with magnetic control (perhaps in the eye).[30]

Several nanocomposites have been fabricated for electrical conductivity. Silicon nanowires were incorporated into PMMA resist and several structures were fabricated including doubly clamped beams.[33] A flexible electrically conductive nanocomposite was formed by ultrasonic agitation of multi-walled carbon nanotubes (MWCNT) in polydimethylsiloxane (PDMS) resist. This nanocomposite was used, through soft lithography micromolding, to fabricate hole and post structures.[34] Similar work was performed with single-wall carbon nanotubes (SWNTs) incorporated into SU-8 photoresist. Fabrication of posts and honeycomb shapes was demonstrated, as well as a contact-lens platform with a pressure sensing array incorporated into it.[35]

While not comprehensive, this selection of articles indicates the popularity of incorporating other materials into photoresist to create nanocomposites for development of micro- and nano- devices and other applications.[23,26,27,29,30,32-35] Purely metal nanocomposites are less common.[25,28] In this thesis the particular nanocomposite material that was investigated and utilized was the cosputtered Al and Mo nanocomposite.[1-3].

2.2. Processing techniques and methods

In this section the micro- and nano- fabrication techniques used to produce the AlMo membranes and other devices are briefly discussed with a focus on the membranes. These techniques were used for all the device fabrication described in this thesis. In general, the

techniques described are universal and applicable to micro- and nano- fabrication of MEMS, NEMS and other devices.

2.2.1. Lithography techniques

Lithography is a process whereby a desired pattern is transferred through etching or deposition onto a surface. It is derived from an old printing process that is still used today. The term photolithography, still the most common type of lithography used in micro- and nanofabrication, refers to lithography performed through the use of photographic images. In electron beam (E-beam) lithography a focused beam of electrons is applied to expose the resist rather than the UV light used in photolithography.

2.2.1.1. Photolithography

Photolithography is used in micro- and nano- fabrication to create patterns on substrate surfaces. A photomask is created using a soda lime or quartz glass plate with a thin layer of chromium deposited on the surface. Chromium is used because a thin layer is sufficient to block UV light from passing though.

Photoresist is a material that is generally composed of three components: a light-sensitive component like naphthoquinone diazide, a film-forming component like a cresol novolac resin and a solvent component like methoxy propyl acetate. For a positive photoresist, the light-sensitive component makes the film-forming component more soluble in the developer solution, whereas the opposite is true for a negative photoresist. The solvent component is important during the photoresist spinning process. During the spinning process the photoresist is dispensed onto the center of the substrate. The substrate is then rotated at low speed to spread the photoresist on the surface, and then at high speed to create an even thickness coating on the substrate surface. The thickness of the coating is dependent on the spin speed and the photoresist viscosity, which is where the solvent type and quantity is important. The solvent evaporates during the spin process.

Following the spinning process, the photoresist is baked to drive off any remaining moisture and harden the resist. The photoresist is then left to rehydrate before exposure to UV

light where the pattern is not protected by the photomask. There are different methods for exposure of the photoresist. Contact photolithography was used for the experiments described herein, but projection lithography may be used for industrial applications. There is less mask wear, and fewer issues with defects and it is easier to automate the process with projection lithography, but the process is more expensive.

The photomask is created by coating the chromium with photoresist, but the patterning is performed by a laser (or E-beam) which is rastered across the surface. The photoresist is then developed and the exposed chromium is etched away using a wet etch. Subsequently, solvents are used to wash away the remaining photoresist, and the photomask is ready for use.

2.2.1.2. E-beam lithography

E-beam lithography is performed in much the same way as photolithography. The major difference is that, as mentioned in section 2.1.1.1, an electron beam is rastered across the surface to increase the solubility of positive resist or decrease the solubility of negative resist. All lithography requires consideration of the physical limitations of pattern transfer. For photolithography this includes effects such as interference of the UV-light following reflection from the surface. Similarly, for e-beam lithography this involves effects such as electron scattering interactions. These effects may require the pattern of the photomask or the write pattern of the e-beam to be adjusted so that the desired pattern remains after development. This can be of particular importance for e-beam lithography as the devices are generally much smaller.

2.2.2. Deposition techniques

The majority of the deposition techniques and materials deposited during MEMS membrane fabrication are the same as those used for integrated circuit fabrication. Two of the most common materials used in membrane fabrication are silicon oxide and SiN.[36-40] A major reason for their preferred use is that they are inert to the etch processes that are commonly used to release membrane structures. Furthermore, they have good structural qualities and can serve as a passivation layer for electrodes. Wet or dry oxidation may be used to form the first layer of a

membrane structure. Both low pressure chemical vapour deposition (LPCVD) and plasma enhanced chemical vapour deposition (PECVD) techniques are commonly used to deposit SiN and silicon oxide. Alternatively, sputtering may also be used.

One of the main advantages of LPCVD and thermal deposition over PECVD is a better control of the layer thickness for crucial structures.[38] LPCVD SiN also has a better resistance to KOH etch solutions, which is an advantage during long etch processes.[41] The major advantage of PECVD is that the lower deposition temperature allows layers to be deposited over temperature-sensitive materials like aluminum. It should be noted, however, that as the deposition temperature decreases there are significant changes in the properties of the SiN film. The etch rate in KOH increases[42], probably due to a decrease in density[43]; furthermore, there may be more impurities due to vapour desorption from the chamber walls, and below 300°C the density of pinhole defects increases[44]. Therefore, there may be issues when low-deposition temperature PECVD nitride is used as a passivation layer for very long KOH etch processes.

For membrane fabrication metals are generally used as a conductive layer for electrical contact[37,39,40,45,46] or as a sacrificial layer[38] during etching. Physical vapour deposition (PVD) is generally used for the deposition of metals. Sputtering is the most common method of metal deposition, though evaporation is also used. Furthermore, metals like hafnium and titanium may be deposited by evaporation or sputtering and modified through oxidation to hafnium oxide[47] and titanium oxide[39].

Polymers are an attractive material for the fabrication of membranes due to their elasticity and low Young's modulus. There are a wide array of polymers that may be used including epoxies like SU-8[48], parylene and silicone[36], a combination of poly(allylamine hydrochloride) and poly(sodium 4-styrenesulfonate)[40], and many others. Spin coating is often used to deposit multiple thin film layers, although parylene is generally deposited by a dedicated system.

There are many other materials that may be deposited by other methods. This includes growth of GaN by molecular beam epitaxy[47], growth of GaInAs by epitaxial metalorganic chemical vapour deposition[49], sol-gel spin coating of lead zirconate titanate (PZT)[39], and others. This is not, of course, a comprehensive list of the deposition materials and methods that have been applied to fabricate membranes, but it serves to underline some of the more common techniques and materials that are available.

2.2.3. Process tuning and annealing for intrinsic stress adjustment

Intrinsic stress is a critical aspect of membrane fabrication. Where resonance behaviour is desired the intrinsic stress of the membranes may have a large impact on the resonance frequency and quality factor of the membranes. Furthermore, tensile intrinsic stress can substantially affect the mechanical strength of the membranes, whereas compressive stress can lead to membrane deformation and buckling. Stoichiometric LPCVD SiN is rarely used in membrane fabrication, because the very high intrinsic stress of the material causes it to fail more easily. Silicon-rich SiN is generally employed instead, because it has much lower intrinsic stress.

There are many different variables that play a role in the intrinsic stress of a thin film, some of which can be used to tune the stress to desired levels. In SiN thin films, for example, the intrinsic tensile stress increases as hydrogen desorbs from the SiN film. Therefore, high deposition temperature or annealing increases the intrinsic stress of the membranes. If lower stress is desired, ion bombardment may be used to increase compressive stress. Furthermore, the gasses used during deposition and their pressures also have a significant impact on the material stress. Another good method to control intrinsic stress during PECVD deposition is to introduce low-frequency power to the process.[50] Two examples of the effect of deposition parameters on PECVD intrinsic film stress are shown in Figure 2.1.

The same concerns about intrinsic stress apply to the PVD methods. Again, the intrinsic stress of the thin films depends on a number of different parameters including deposition pressure[51], power density[52], and gas ratio for reactive sputtering[53]. The effects sputter pressure and target power density may have on intrinsic stress are shown in Figure 2.2. Similar effects can be noted for evaporation systems. Furthermore, while the trends discussed should generally hold true, the precise effect of these process parameters on intrinsic stress for PVD, LPCVD and PECVD systems are all specific to a given deposition tool due to a number of variables unique to that particular tool. This means that precise stress tuning can be a challenging and time-consuming process.

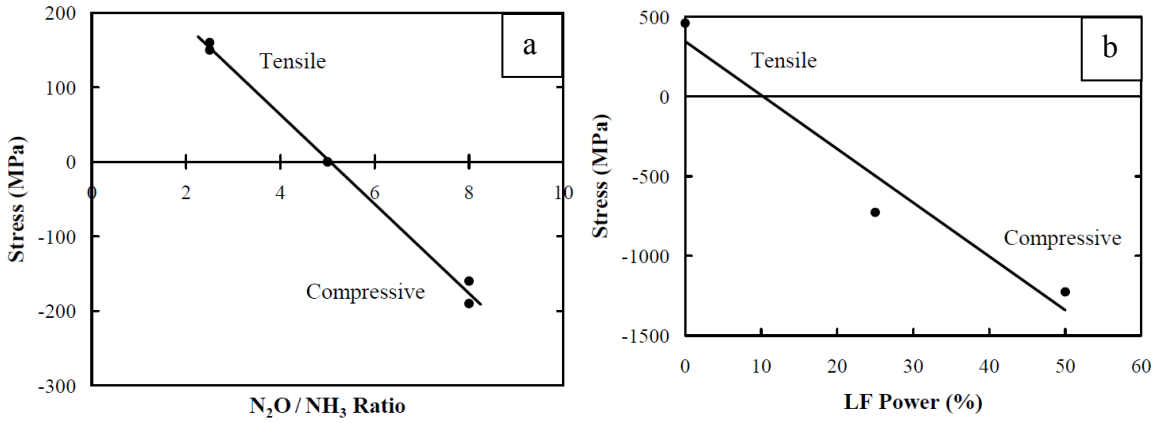

Figure 2.1: Examples of the effects of deposition parameters on the intrinsic stress of certain thin films. a) The effect of the gas ratio on the intrinsic stress of PECVD SiO_yN_x. b) The effect of low-frequency power on PECVD nitride intrinsic stress.[50] "Republished with permission of Electrochemical Society, Inc, from Stress Control of Si-Based PECVD Dielectrics, K. D. Mackenzie, D. J. Johnson, M. W. DeVre, R. J. Westerman, and B. H. Reelfs, PV2005-01, 2005; permission conveyed through Copyright Clearance Center, Inc."

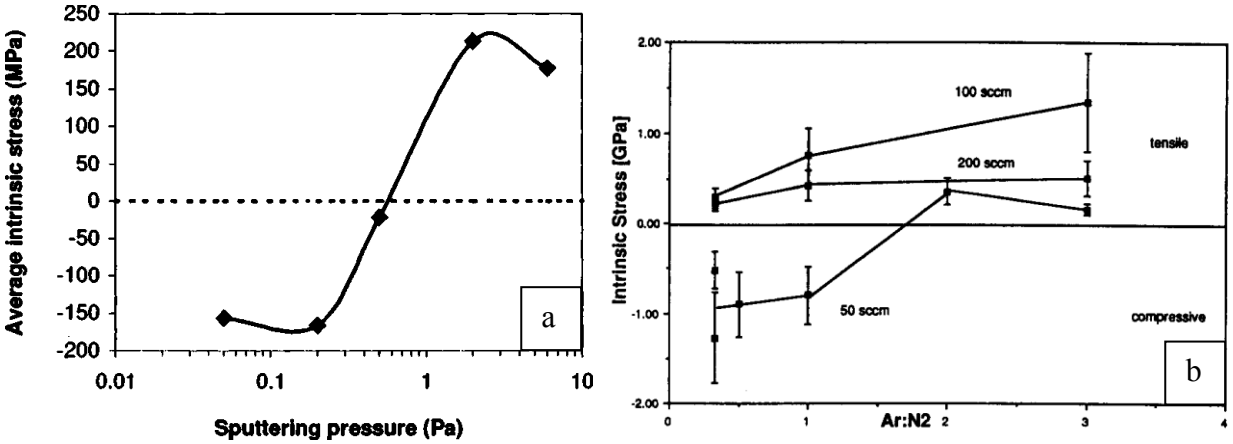

Figure 2.2: An illustration of the effect of sputtering pressure and gas ratio on the intrinsic stress of thin films. a) The effect of sputtering pressure on the intrinsic stress of Cu thin film. "Reprinted from Pletea, M., Brückner, W., Wendrock, H. & Kaltofen, R. Stress evolution during and after sputter deposition of Cu thin films onto Si (100) substrates under various sputtering pressures. JOURNAL OF APPLIED PHYSICS 87 (2005), with the permission of AIP Publishing."[51] b) The effect of gas ratio on the intrinsic stress of a sputtered AlN thin film. "Reprinted from Thin Solid Films, 228, Rille, E., Zarwasch, R. & Pulker, H. K., Properties of reactively d.c.-magnetron-sputtered AlN thin films, 215-217, Copyright (1993), with permission from Elsevier."[53]

2.2.4. Etching Processes

As with deposition, there are numerous different etch processes that may be employed during membrane fabrication. These methods can be separated into wet etching and dry etching techniques. Alkaline solutions such as KOH, tetramethylammonium hydroxide (TMAH) or ethylene di-amine pyro-catechol (EDP) are commonly employed to etch silicon.[39,45,54] Hydrofluoric acid (HF)-containing solutions are used to etch silicon dioxide[39], and other solutions are used to specifically etch metals and other materials. There are two main approaches for dry etching, through reactive gasses such as HF, XeF_2 or Cl_2 and through a reactive ion etch (RIE). A RIE may be used to pattern shallow layers, while deep reactive ion etching (DRIE) is applied to etch through thick layers of material.

2.2.5. Release Processes

A critical aspect of membrane fabrication is the release process. This may be performed at the beginning of the process or partway through the process, but is most commonly performed at the end of the process. When release is performed near the end of the process, etching selectivity becomes critical so that only the desired material is removed.

There are two main methods by which the release of the membrane structures is performed. The first is via a backside through-etch. This involves etching through the bulk of the silicon wafer holding the membrane and is usually accomplished with an alkaline solution of KOH, TMAH or EDP, or with a DRIE. The alkaline solutions perform an anisotropic etch based on the crystal orientation of the bulk silicon. The ratio of (100)/(111) silicon and (110)/(111) silicon are the greatest for KOH, followed by TMAH and EDP. The angle between the (100) and (111) plane is 54.74°, and the etch rate is strongly dependent on concentration and temperature.[55] While useful, this method of etching can significantly curtail the types of membrane structures that can be fabricated. Irregular or unaligned structures will be forced to align along the crystal directions as shown in Figure 2.3.[56] More complex shapes can be designed but it is evident that circular membranes cannot be produced in this manner. Release through a DRIE is commonly used to fabricate circular membranes.[39,47]

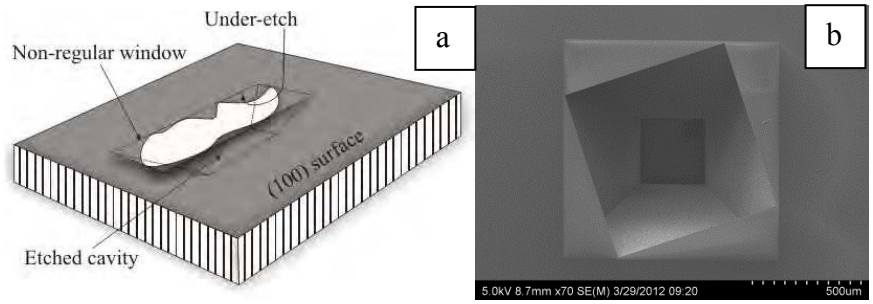

Figure 2.3: a) Schematic and b) SEM images of the undercut caused by non-regular or imperfectly aligned windows during membrane formation. The schematic image is ©2012 Salvador Mendoza-Acevedo, Mario Alfredo Reyes-Barranca, Edgar Norman Vázquez-Acosta, José Antonio Moreno-Cadenas and José Luis González-Vidal. Originally published in Micromachining Techniques for Fabrication of Micro and Nano Structures, Chapter 9 Release Optimization of Suspended Membranes in MEMS under Creative Commons Attribution 3.0 Unported License (https://creativecommons.org/licenses/by/3.0/legalcode). Available from: DOI: 10.5772/30909[56]

The other main method of membrane release is through the use of a front side etch in which a sacrificial layer is etched away, leaving a suspended structure. Various etch processes such as alkaline solutions, other wet etch solutions, or gaseous etch processes employing XeF_2, HF or Cl_2 may be used for this purpose. Directional etching such as RIE or DRIE may be used to create etch holes to accelerate the release process, but are not used for the release etch itself.[57] In general, the backside through etch process may be more convenient where large deflection is required of the membranes, such as for an energy-harvesting membrane[39], or if transparency is required, such as for microscopy windows[58]. The use of sacrificial layers is more convenient when the material does not need to be continuous, and the deflection required of the membranes is small.[38]

Often, the materials used to form a membrane device may not be resistant to alkaline or DRIE processes. Therefore, if a through etch is performed, an etch stop layer is necessary to prevent the through etch from damaging the membrane. SiN or silicon dioxide are often used for this purpose and may also serve as a sacrificial layer if they are not the desired structural layer. Contrary to when a frontside etch process is used, it is often convenient to remove this sacrificial layer via a RIE.

2.3. Membrane Biosensors for Pathogen Detection

MEMS membranes have been used for a variety of sensing applications. Specific applications of membrane sensors include the detection of thiolated molecules with gold-coated silicon membranes[59] and the detection of isopropyl alcohol (IPA) and toluene vapor with gold-coated Parylene membranes[60]. As described by Carlen *et al.*[59], surface stress induced by binding of thiolated molecules to the membrane surface resulted in deflection. This deflection was recorded by a phase scanning interferometric optical profilometer. Conversely, Satyanarayana *et al.*[60] leveraged the change in capacitance between the membrane and a secondary electrode to detect IPA and toluene vapors. Carlen *et al.*[59] suggested that capacitive measurements with sensitivity as low as 210 fm[61] may allow membranes to rival the sensitivity of resonance cantilever sensors, particularly in liquids. They also noted that the active surface of a membrane can be much more easily functionalized than that of a deflection cantilever, as the two surfaces can be readily isolated. Furthermore, there is interest in high quality factor membrane biosensors for increased detection sensitivity.[62-64]

Pathogens cause extensive illnesses and mortality around the globe. Contaminated water and food supplies are major sources of such infections. Appropriate and accurate detection and monitoring technologies are thus of importance in many settings. It is critical in a clinical setting to determine the cause of illness in humans in order to allow appropriate treatment. Detection technologies are also important in the agricultural industry both to ensure food safety and to maximize profitability by avoiding the spread of disease. They are also of importance for food and water processing and distribution to ensure safety of food products and water supplies. Finally, pathogen detection is important in warfare and population security given their potential use as biological weapons.

Conventional microbiological methods rely on culture-based assays that are time consuming, and cost-ineffective. Polymerase chain reaction (PCR) has been extensively used for amplification of small amounts of DNA obtained from a bacterium or virus, which is

subsequently detected by established methods.[65] Enzyme-linked immunosorbent assays (ELISAs) have also been investigated as Ab-based monitoring platforms.[66] This method offers the high specificity of monoclonal Abs and can be employed to detect bacterial toxins.[67,68] The combination of PCR and ELISA has also been used for detection of pathogens[69,70] and their toxins[71,72]. These methods may still require pre-enrichment to increase the bacterial concentration above the detection threshold.

A biosensor is an analytical system designed to detect and/or quantify the presence of a specific biological analyte. A biosensor typically integrates a bio-recognition element with a transduction system, as well as electronic systems such as signal amplifiers, processors, and display(s). Biosensors have been looked upon as alternative for monitoring of bacterial cells and their toxins.[73,74] Platforms such as quartz crystal microbalance (QCM)[75], micromechanical resonators[76-80], flow cytometry[73,81], amperometry[82,83], and surface plasmon resonance (SPR)[84-87] have been considered. The specificity of biosensors is imparted by a probe such as a nucleic acid, an Ab, an enzyme, a cell or an artificial receptor. Different biological probes such as DNA[88], RNA[89], monoclonal[90,91] and polyclonal Abs[92], bacteriophages[83,93-97] and their recombinant binding proteins[96,98] have been used for detection of bacteria.

Membranes are commonly used in a variety of biomedical applications. They are applied as filters for the concentration and isolation of cells, viruses and bacteria, detection of proteins, DNA and RNA in Western, Southern and Northern blots, respectively, and other tests such as direct epifluorescence technique (DEFT). Common materials for membranes include nitrocellulose and polycarbonate. Other materials such as lipid bilayer membranes are also of interest largely for their biomimetic properties. Such membranes are being incorporated into various sensors and biosensors in particular. These biosensors are being used to detect different compounds including proteins, DNA and RNA, bacterial cells and virus particles. Some of these sensors can be and have been used for the detection of pathogens.

The following sections contain a review of recent literature specific to the use of membranes for the detection of pathogens. The materials science and fabrication techniques employed for the realization of the membranes are discussed in the first section. The next two sections cover the different molecular probes and linker chemistries that have been employed in combination with such membranes. The various platforms that have been used for the readout of

these devices are discussed in the next section. The final sections contain a table of the detection limits of the techniques and a summary, respectively.

2.3.1. Membrane Materials and Fabrication

Membranes are commonly employed in biomedical applications. Often they are used either as a filter or as a support structure. Given these applications, there are two general areas of interest for membrane design, physical dimensions and chemical composition. The physical structure generally concerns parameters like surface area, surface roughness, pore size (if any) and distribution, and membrane thickness. The physical structure of the membrane is more critical for filtering applications, while the chemical composition is more critical for structural support applications. Given the prevalence of support structure applications, the composition of membranes has been divided into inorganic membranes, organic membranes and more complex hybrid or composite membranes.

2.3.1.1. Inorganic Membranes

While uncommon, inorganic membranes have been used in numerous biosensor applications. In general, the inorganic membranes serve purely as a support structure; however, they may also serve to increase the surface area of the sensor or to perform capillary action. In a number of cases inorganic and organic membranes were incorporated together for application in more complex sensing platforms. These will be covered in the hybrid membrane section.

Nanoporous alumina or aluminum anodized oxide membranes have been used in a number of applications.[99-106] In some cases the nanoporous aluminum was only nominally in the form of a membrane, as the surfaces were carved into alumina, which was deposited on an electrode[102], or sputtered onto the surface and then anodized[104]. Alumina membranes can also be obtained commercially, and one research group used commercially available Anodisc inorganic filter membranes from Whatman.[105] Alumina membranes have a number of desirable properties including non-conductivity, well-defined nanopores, small pore size, high pore density, and ease of functionlization.[103]

Aside from aluminum oxide membranes, gold[107,108], silver[105], titanium oxide[109] and glass[110-114] inorganic membranes have been used. A common application of glass fiber membranes is the transport of fluids by capillary action in more complex membrane-based sensors.[111-114] SiN has also been employed in hybrid membrane structures as a support for organic membranes.[115] In one case a number of different membranes were evaluated. Aluminum oxide, silver and gold-coated polycarbonate track-etched (PCTE) membrane filters were examined to determine the best material and pore size for surface-enhanced raman spectroscopy.[105] Since surface-enhanced raman spectroscopy was used as the transduction method, it is not surprising that the gold membranes performed the best.

2.3.1.2. Organic Membranes

Organic membranes are more commonly used for biosensor applications than inorganic membranes. The membranes are generally used as a support structure, but they may also be used for filtration or less frequently as an integral component of the sensing process. The first common membrane is nitrocellulose (also known as cellulose nitrate)[111-114,116-124], which is very suitable for many biomedical applications. Other membranes are made with polyethersulfone[118,125-132], PDMS[108], nylon[118,133-136], polypropylene[137], polylactic acid (PLA) nanofibers[138], cellulose[111-113], polycarbonate[139], polyacrylamide[140], cellulose acetate[141,142], polyvinyl chloride[143], polyamine/polyurethane[143] or polyvinylidene fluoride PVDF[132].

There are a plethora of commercial organic membranes available and a number have been used. Many of these membranes are sold in a pre-functionalized state. Simple incubation with the biomolecule of interest allows it to be immobilized on the surface of the membrane, either through adsorption or through covalent bonding. Examples include Biodyne B membranes, which consist of nylon functionalized with quaternary ammonium groups, Biodyne C membranes, which are also made of nylon but are functionalized with carboxyl groups that render them negatively charged, and Supor PES Membranes, which are made of polyether sulfone and are functionalized to be hydrophilic.[132]

One group evaluated nitrocellulose membranes as a visual response membrane sensor involving line formation. Membranes tested include AE 100, AE 98, Immunopore FP, Immunopore RP, HiFlow Plus HF135, HiFlow Plus HFB180, HiFlow Plus 090, and Unisart 140.

Interestingly, AE 98 was selected, because it provided the best line intensity and shape.[119] Another group compared the results from a number of different membranes including dialysis membranes, which were likely a type of cellulose (material not provided by Fisher Scientific); nitrocellulose, neutral nylon (Biodyne A), positively charged nylon (Biodyne B) from Gibco BRL, and preactivated membranes (ImmunodyneABC and UltraBind) from Pall Specialty Materials. For the detection of *E. coli* subspecies, the best results were obtained by direct protein binding to Immunodyne ABC membranes.[144]

A different group compared the performance of Ultrabind membranes to screen-printed carbon electrodes (SPEs) and Maxisorp microtiter wells. The greatest density of bound protein was found on the microtiter plates, while the membranes and electrodes had the highest stability during storage and highest stability during operation, respectively.[131]

Many materials and methods have been employed to manufacture membranes. One interesting example concerns membranes fabricated using polyacrylamide. Polyacrylamide was chosen because of its biocompatibility and hydrophilicity, which helps prevent nonspecific adhesion. The monomer concentration was altered to vary the pore size. Glass channels were functionalized with 3-(trimethoxysilyl) propyl acrylate to provide acrylate groups for attachment of the polyacrylamide membranes. The channels were filled with a acrylamide/bisacrylamide/ VA-086 photoinitiator solution and a laser was used to form the membrane. The unreacted polyacrylamide was washed through.[140]

Membranes are sometimes modified not for the linking process, but for the transduction process. In one case a microporous polycarbonate membrane was modified by polypyrrole modification to create conductive membranes to detect Salmonella-infecting phage.[143] In another case cellulose acetate (CA) membranes were grafted with hydroxypropyl cellulose (HPC). The hydroxypropyl cellulose was first crosslinked using divinyl sulfone (DVS) to form branching structures. The cellulose acetate was reacted with the DVS, and then the HPC was grafted onto the CA. The HPC expands into a hydrophilic state at temperatures below 43°C and collapses into a hydrophobic state above 43°C. The goal of the HPC (with a low critical solution temperature) is that theoretically, it can be used to decrease fouling of the membranes by using the temperature cycling to "shake off" contaminants.[142]

Another method of membrane fabrication is based on nanocomposites. For the purpose of nucleic acid detection, one group fabricated anion exchange nanomembranes that were made up

of quaternary ammonium containing divynylbenzene/polystyrene particles embedded in a polyethylene-polyamide/polyester matrix for mechanical stability.[145] In a different set of experiments, nitrocellulose particles were embedded in a cellulose acetate matrix. The nitrocellulose viscosity and concentration, as well as the cellulose acetate concentration, were varied to alter the capillary flow rate and maximize protein binding.[120]

Membranes were also formed using nonwoven fibers. In one case nonwoven polypropylene microfibers were obtained and polymerized with pyrrole and 3-thiopheneacetic acid using $FeCl_3$ and doped with 5-sulfosalicylic acid.[137] Another group used electrospinning to produce nanofiber nitrocellulose membranes. Parallel electrodes were used to create aligned mats of nanofibers to enhance capillary action.[123,124]

Many applications are based on the use of lipid bilayer membranes, often to better emulate or make use of physiological conditions. Some applications were based on membrane engineering[146-148] of live cells in order to use them for biosensor applications, while others relied on created biomimetic lipid bilayer membranes[115,149-153] to emulate the physiological conditions. One method for membrane engineering is electroinsertion of Abs to embed the desired Abs into the cell membrane.[147,148]

In another case, planar tethered bilayer lipid membranes were used for detection of bacteria. Lipid membranes were anchored to a gold surface with a gold-sulphur bond and the silane surface through the hydrogen bonds of a silane-hydroxyl bond. 2,3-di-O-phytanylglycerol-1-tetraethylene glycol-D,L-lipoic acid ester lipid, 2,3-di-Ophytanyl-sn-glycerol-1-tetra-ethylene glycol-(3-tryethoxysilane) ether lipid, and cholesterolpentaethyleneglycol were used for self-assembly of the first half of the membranes, while the second half was deposited by vesicles composed of 1,2-di-O-phytanoyl-sn-glycero-3 phosphocholine and cholesterol. Such assemblies allowed for the specific detection of toxins associated to pathogenic bacteria.[115]

In a different case, liposomes were used directly for the detection of cholera toxin and to transduce it into a visible output. The liposomes were formed by combining ganglioside GM1 and 5,7 docosadiynoic acid with a solvent, sonicating the solution, and causing polymerization to take place using UV radiation. Introduction of cholera toxin into the liposomes leads to a change in their light absorption.[152]

Another group created a biomimetic membrane from tryptophan-modified TRCDA (10, 12-Tricosadiynoic acid) and DMPC (1, 2-sn-glycero-Dimyristoyl-3-Phosphocholine) in agar and

liquid medium. The TRCDA generates polymers when exposed to UV light. It also creates a colourimetric change when TRCDAs polymers are exposed to mechanical stress, changes in pH, binding of biological agents or heat. TRCDAs have been used in vesicles for detection of nucleic acids, proteins and microorganisms.[153]

2.3.1.3. Hybrid Membranes

While many membranes are clearly composed purely of either organic or inorganic components, some hybrid membranes have inorganic and organic materials, which are effectively fused together. In one case a gold-coated PCTE membrane filter was used for surface enhanced Raman spectrometry-based detection of Giardia.[105] In another example a hybrid membrane was composed of a PDMS membrane coated with 20 nm of gold to allow linking of thiols to the surface.[108] A different group also used gold, but the membranes where formed on the inorganic surface in this case. Liposomes were formed using 1,2-Dipalmitoyl-sn-glycero-3-phosphocholine (DPPC), which is commonly found in cells and is therefore useful for a biomimetic application, to create a phospholipid membrane on the gold electrode surface. The liposomes were simply introduced in solution to the gold surface to form the membranes.[154] DPPC liposomes containing monosialoganglioside (GM1) have also been deposited on octanethiol attached to gold to form a GM1-containing phospholipid bilayer.[150] A similar method has been used for detection of bacteria. However, the gold electrode was prepared using thiol-containing molecules octanethiol, 1,2-dimyristoyl-sn-glycero-3-phosphothioethanol or spacerlipid A (created by the authors), after which the phospholipid was deposited through vesicle fusion. Such assemblies were employed to detect the presence of *Clavibacter* through the monitoring of related cytotoxins.[149]

Membrane formation can also be achieved through sol-gel methods. A sol-gel method was used to make nano-TiO_2 and nano-TiO_2–polyethylene glycol membranes. A solution of $Ti(OBu)_4$ (with polyethylene glycol for the second membrane) in acetic acid was added to a solution of condensed HCl, water, DMF and alcohol, and allowed to condense. The resulting gel was placed on the electrode by dip-coating.[109]

Another interesting method of membrane fabrication involved the formation of a bilayer lipid membrane through the activation of an egg phosphatidylcholine, hexadecylamine and cholesterol solution by KCl on top of an agar-coated Teflon surface.[151]

2.3.1.4. Composite Membranes

Composite membranes consist of multiple different membranes that are sandwiched together vertically or side to side to form a complete sensor. One group used a sample application pad consisting of a glass fibre membrane, a conjugate release pad made of a glass membrane, a signal generation pad made of a nitrocellulose membrane, and an absorption pad made of a cellulose membrane. Such devices were employed to monitor the presence of bacterial pathogens such as *E. coli* 0157 and *Yersinia pestis* (Figure 2.4).[111,113,114]

A similar design consisted of sample and absorption pads made of cellulose membranes, a fiberglass membrane for the conjugate pad and a nitrocellulose membrane for the capture pad.[112,155] Instead of the visual output, however, electrodes were also included beside the capture pad. Then polyaniline[155] (Figure 2.5) or iron oxide nanoparticle[112]-conjugated Abs were used to detect the antigen, and form an electrical circuit.

2.3.2. Molecular Probes

In order to specifically detect the pathogens of interest, it is generally necessary to use a sensing molecule or molecules that bind only the pathogen or component of the pathogen of interest. Like many biosensors, Abs[101,103,105,106,111-114,117,118,121,123,124,132,134,135,137,139-142,146-148,155] are the most common reagent for specific detection of biomolecules. Often two Abs are employed, one to specifically capture the pathogen and a second conjugated Ab to provide transduction into an observable output. In some cases, such as when piezoelectric sensing is used, the secondary Ab can also be used to amplify the signal output.[101] The use of specific DNA or RNA probes for oligonucleotide hybridization with extracted DNA or RNA from the pathogen of interest is nearly as popular.[99,100,102,104,107,109,110,119,122,125-130,137,145,151]

Some of the nucleic acid hybridization schemes were more complex than others, however. In one case a more complex DNA structure called a bis-peptide nucleic acid (PNA)

was used, which involved a looped complementary DNA structure. This structure undergoes hybridization with double-stranded DNA (dsDNA) from the pathogen; a single stranded DNA probe linked to a RecA protein was used to increase the biosensor sensitivity.[107] (Figure 2.6) Another interesting method to increase sensitivity was through the use of short sensing DNA probes to detect longer strands of pathogen DNA. The sensitivity was increased by using PCR to extend the probe DNA to the length of the pathogen DNA.[100]

There are also specific protein interactions that may be employed for pathogen detection. Cholera toxin, for example, binds to ganglioside GM1; thus this interaction can be used to determine the presence of cholera.[150,152] Another method of specific detection is through the use of viruses called bacteriophages to detect specific bacteria.[143]

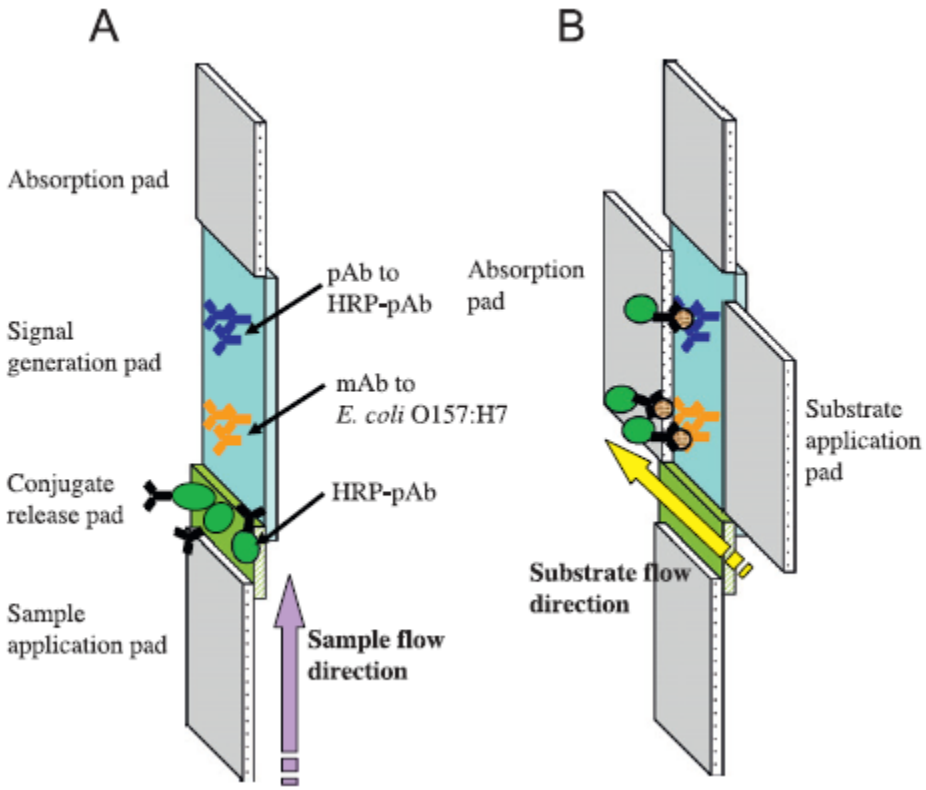

Figure 2.4: A composite membrane sensor. (A) The liquid sample containing E. coli is placed on the glass fiber membrane sample application pad. The solution flows towards the cellulose membrane absorption pad. Along its path horseradish peroxidase (HRP)-conjugated polyclonal Ab (HRP-pAb) enters the solution as it is released from the glass fiber conjugate release pad. Some of the HRP-pAb binds to the E. coli. The pathogen with attached HRP then binds to the monoclonal Ab (mAb) bound to the nitrocellulose membrane signal generation pad. Some

unbound HRP-pAb binds to the pAb as a control. (B) A reaction then takes place with a substrate solution which is catalyzed by the HRP to produce a visible output.[111] "Enzyme-linked immuno-strip biosensor to detect Escherichia coli O157 : H7" by Park, S., Kim, H., Paek, S.-H., Hong, J. W. & Kim, Y.-K., *Ultramicroscopy* 108(10), 2008, 1348-1351 (https://doi.org/10.1016/j.ultramic .2008.04.063) is licensed under CC BY 4.0 (https://creativecommons.org/licenses/ by/4.0/legalcode).

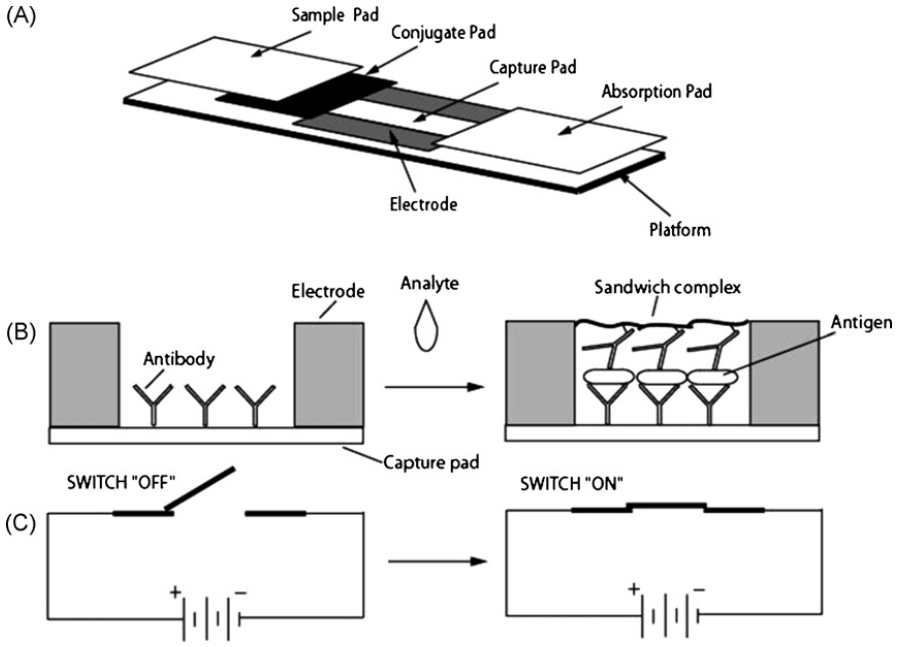

Figure 2.5: A composite membrane biosensor with a membrane composition similar to that in Figure 2.4. The pathogen was introduced in solution to the cellulose membrane sample pad. This solution flowed towards the absorption pad, also made of cellulose. Along the way the conductive material-conjugated Abs were released from the fiberglass conjugate pad and bound to the pathogen. These pathogens then bound to the Abs linked to the nitrocellulose capture pad and increased the conductivity of the circuit.[155] "Reprinted from Biosensors & Bioelectronics, 22, Pal, S., Alocilja, E. C. & Downes, F. P, Nanowire labeled direct-charge transfer biosensor for detecting Bacillus species, 2329-2336, Copyright (2007), with permission from Elsevier."

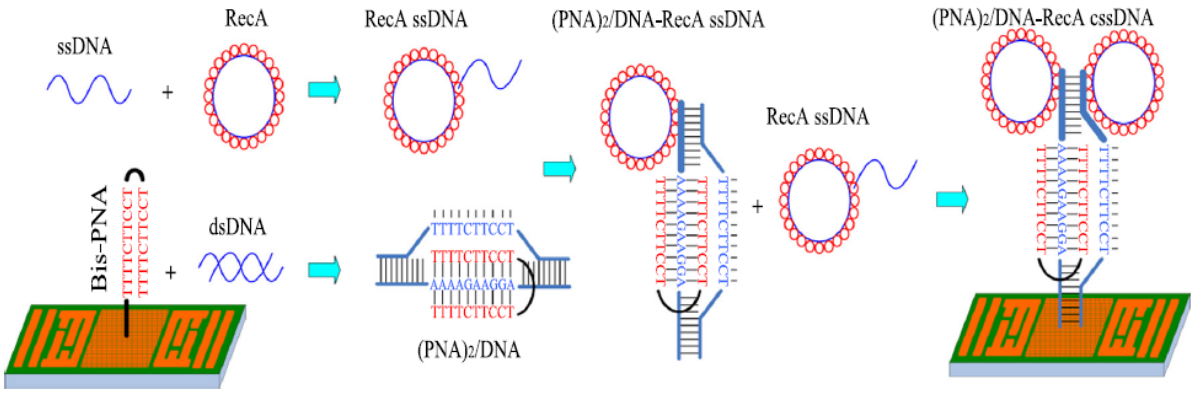

Figure 2.6: A complex DNA hybridization scheme. A bis-PNA DNA structure was used to specifically detect dsDNA from a pathogen. The mass change from this interaction is small however. In order to improve the detector sensitivity, single stranded DNA (ssDNA) linked to protein RecA was used to amplify the mass change while maintaining specificity as the ssDNA hybridizes only with the complex DNA structure already formed on the sensor surface.[107] "Reprinted from Biosens Bioelectron, 60, Liqun Zhang, Yunxia Wang, Ming Chen, Yang Luo, Kun Deng, Dong Chen, Weiling Fu, A new system for the amplification of biological signals: RecA and complimentary single strand DNA probes on a leaky surface acoustic wave biosensor, 259-264, Copyright (2014), with permission from Elsevier."

A number of other more unusual, and generally less specific, methods have also been employed for pathogen sensing applications. One group used a phospholipid membrane to detect spontaneously inserting protein channels from *Clavibacter michiganense ssp. Nebraskense*.[149] In two articles the use of arrays of lectins to identify pathogens are described. Lectins are proteins that bind to carbohydrates. In the first paper, ten different lectins were immobilized onto membranes. A solution containing one of four different *E. coli* strains was introduced to each different lectin-coated membrane, making 40 combinations in all. A solution containing ferricyanide, succinate, formate and menadione in growth medium lacking proteins and trace elements was added to each membrane. After incubation the ferrocyanide was detected by chronocoulometry. The change in charge for each of the 40 combinations along with statistical analysis was used to differentiate each of the four different *E. coli* strains. In fact, the authors found that only five lectins were necessary to distinguish between the four subspecies.[136] In a different paper, the same method was applied to distinguish between *E. coli, S. aureus, S.*

cerevisiae, B. cereus, P. vulgaris, and *E. aerogenes*. In addition to 10 lectins, binding to bovine serum albumin (BSA) and control membranes was also tested. As before, chronocoulometry was used in addition to statistical analysis to differentiate between the different bacterial species.[144]

There have been some reports of less specific and non-specific detection methods, which may nevertheless provide useful information. In one case, 11-Mercapto-1-undecanoicacid (MUA), 11-Mercapto-1-undecanol (MUO) and Dodecane-thiol (DOT) were investigated for *E. coli* detection. The authors were able to determine if the *E. coli* cells were alive or dead.[108] In another case, the authors were able to distinguish between catalase-positive and catalase-negative bacteria by the detection of hydrogen peroxide production.[133] Thirdly, the lectin Concanavalin A was used to detect dengue glycoproteins.[154] Lipids have also been employed for the detection of bacterial toxins through pore formation in the lipid bilayer.[115] Tryptophan-derivitized TRCDA was used for the detection of several species of bacterial cells.[153] One group made use of protein phosphatases to detect microcystins, which are produced by *Cyanobacteria*.[131]

2.3.3. Linking Procedure

The method that is used to link the molecular probe to the surface, in this case a membrane, is an important aspect of a biosensor. Linking is important because it can substantially affect the sensitivity and specificity of the biosensor. Glutaraldehyde is a simple short crosslinking molecule, and it is commonly used to link two amine groups together. Often one of these is a free amine group on an Ab. It was applied to link Abs to secondary amines in a polypyrrole-containing polymer membrane[137,144], a nitrocellulose membrane[123,124,155], Biodyne B membranes[135] and polycarbonate membranes that were aminated using nitric acid and sodium borohydride[139]. Glutaraldehyde was also used to attach aminated DNA probes to an aluminum oxide surface aminated by 3-aminopropyltrimethoxysilane.[100,102,104]

One group compared three linking procedures to attach protein phosphatase (PP) to SPEs. The first method was performed by using a sol gel formed by Tetramethoxysilane (TMOS), methyltrimethoxysilane (MTMOS), polyethylene glycol (PEG) and hydrocholic acid. This was mixed with the PP and deposited on the electrode. In the second method, glutaraldehyde was added to a solution of BSA and PP on the surface of the electrode. For the third method, photocrosslinkable poly(vinyl alcohol) bearing styrylpyridinium groups (PVA-SbQ) were mixed

with the PP and applied to the electrode. As the third method resulted in the highest density of the PP enzyme on the surface, this method was also used on two other surfaces, Maxisorp microtiter wells and Ultrabind polyethersulfone affinity membranes.[131]

Streptavidin and biotin is a pair of very tightly binding molecules that are commonly used in linking procedures.[156] Streptavidin is usually adsorbed directly to a surface, while the molecule of interest is linked to the biotin. This process is commonly used to link proteins such as Abs to surfaces. In the following cases strepavidin was used to link DNA or RNA to membrane surfaces. Subsequently, biotinylated DNA[125-129], RNA[130] or avidin-conjugated DNA[144], bound to the streptavidin adsorbed on the membrane surface. Avidin is an analogue of biotin which also binds tightly to streptavidin.

Silanes are another group of molecules that are very commonly used in linking processes for a variety of surfaces. Several of the previous linking processes included a silane as a component of the functionalization process. DNA[99] or Abs[101,103] have been linked to an alumina surface with (3-glycidoxypropyl)trimethoxysilane. Another group incorporated a silane group into their lipid (2,3-di-Ophytanyl-sn-glycerol-1-tetra-ethylene glycol-(3-tryethoxysilane)) to anchor a biomimetic membrane to a SiN surface.[115]

Other work with lipid bilayers involved living cells that were functionalized with Abs. This was performed using electroporation, which through the application of an electric potential to the cells causes pores to form in the cellular membrane. Abs can then attach in these pores.[146-148]

Another very popular crosslinking chemistry involves 1-Ethyl-3-(3-dimethylaminopropyl)carbodiimide (EDC) and N-hydroxysulfosuccinimide (NHS) or Sulfo-NHS. EDC binds free carboxyl group. Sulfo-NHS enhances the effectiveness of EDC and binds to EDC after it binds a carboxyl group and a free amino group. Hyaluronic acid was used to modify an alumina surface and create free carboxyl groups. Then EDC/sulfo-NHS chemistry was used to immobilize Abs.[106] Carboxyl groups were formed on the quaternary ammonium containing divynylbenzene/polystyrene particles embedded in a polyethylene-polyamide/polyester matrix by reaction with benzophenone tetracarboxylic acid and exposing it to UV light. EDC was then used to link the carboxyl groups to aminated oligonucleotide probes.[145] In another case, a nylon membrane was sequentially immersed in dimethyl sulfate and

6-aminocaproic acid solutions to create free carboxyl groups on the surface. EDC/sulfo-NHS chemistry was then used to link the Abs to the nylon surface.[134]

EDC can also be used without the addition of Sulfo-NHS, for example to link Abs to a hydroxypropyl cellulose membrane.[142] Linking can also be performed with other carbodiimides. One group linked Abs to Biodyne C membranes using Woodward's reagent (2-Ethyl-5-phenylisoxazolium-3′-sulfonate).[135] One of the simplest linking methods is based on sulfide groups, which naturally attach to gold surfaces. Sulfide groups were introduced to DNA strands[107], small organic molecules[108], and lipids[115] to link them to gold surfaces.

Hydrophobicity can play a major role in the linking process. Some proteins adhere to a phospholipid membrane simply through incubation.[154] Liposomes will naturally bind to a surface which is modified to be hydrophobic[150], and GM1 ganglioside will naturally be incorporated into liposomes during formation[152]. The addition of a hydrophobic dodecane tail to a DNA probe can be used to anchor it into a bilayer lipid membrane.[151]

In some cases, complex linking process are unnecessary and simple adsorption of antigen or Ab to a nitrocellose[111-114,117-119], glass fibre[111,112,114,155] or cellulose[111] membrane is sufficient. The same concept applies to adsorption of DNA to a sol-gel deposited membrane[109] and horseradish-peroxidase conjugated Abs to a nitrocellulose membrane[121]. This may even apply to certain components of more complex linking processes.

PCR is commonly used to amplify DNA or RNA from pathogens for detection, and was also employed in a number of the biosensors discussed here. In one case, it was used in an intriguing manner for specific detection of DNA. Microspheres coated with streptavidin were adsorbed onto glass membranes. Forward primers were labeled with biotin while reverse primers were labeled with fluorescein. If DNA is present, then after annealing, the ds-DNA would be labeled on one 5' end with biotin which binds to the microspheres on the surface, and the other 5' end with fluorescein to which gold nanoparticles coated which Abs specific to fluorescein can bind. These gold nanoparticles give a visual colour change which can be observed with the naked eye.[110] (Figure 2.7) Similar work was performed by replacing the fluorescein with digoxygenin that is bound by Ab to the surface and replacing the gold nanoparticles with carbon nanoparticles. The anti-digoxigenin and biotin-protein complex were adsorbed to the nitrocellulose membrane.[119] (Figure 2.8)

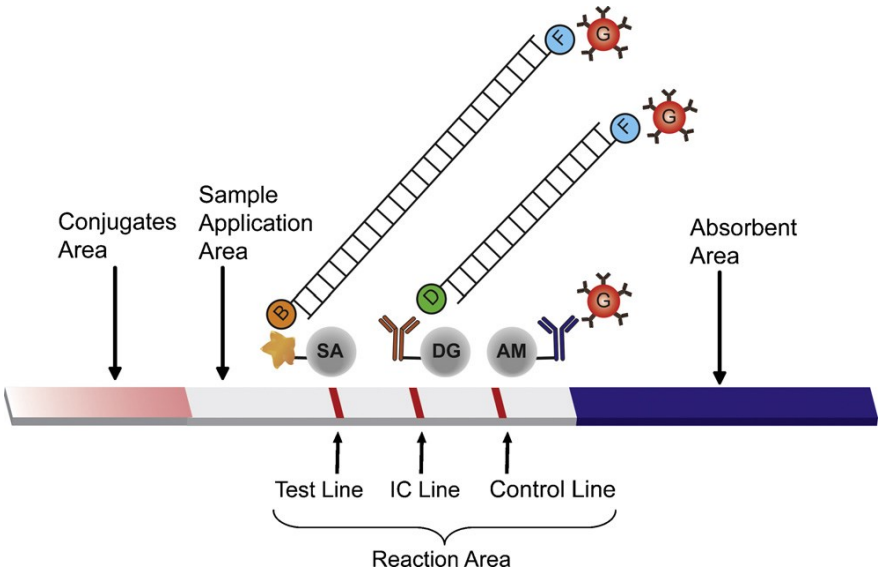

Figure 2.7: An example of a more complex linking process. Microspheres coated with streptavidin were adsorbed onto glass membranes. Forward primers were labeled with biotin while reverse primers were labeled with fluorescein. Upon pathogenic DNA binding and annealing, the ds-DNA labeled on one 5' end with biotin which binds to the microspheres on the surface, and the other 5' end with fluorescein to which gold nanoparticles coated which Abs specific to fluorescein can bind. These gold nanoparticles give a visual colour change which can be observed with the naked eye. The other two lines serve as controls to ensure proper conditions for PCR amplification (internal amplification control (IC)) and release of the Ab coated gold particles. The abbreviations are: streptavidin-coated microspheres (SA), biotin (B), fluorescein (F), antidigoxigenin Ab-coated microspheres (DG), digoxigenin (D), goat anti-mouse IgG Ab-coated microspheres (AM), and anti-fluorescein Ab-conjugated gold nanoparticles (G).[110] "Reprinted from Biosens Bioelectron, 26, Chua, A. L., Yean, C. Y., Ravichandran, M., Lim, B. & Lalitha, P, A rapid DNA biosensor for the molecular diagnosis of infectious disease, 3825-3831, Copyright (2011), with permission from Elsevier."

As mentioned in section 2.2.1, there are a number of prefunctionalized membranes that are available commercially. These include Immunodyne ABC and UltraBind membranes, which respectively feature nucleophile-selective and aldehyde-activated surfaces.[144] The Immunodyne ABC membranes, for example, were used to directly form covalent bonds with free amine groups on proteins introduced to the membranes, though the precise reaction was unspecified by the manufacturer.[136]

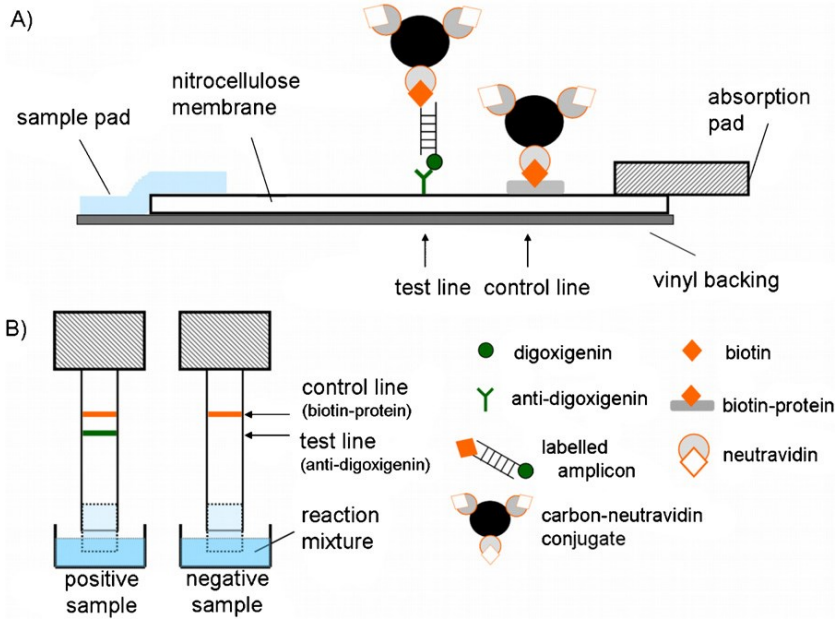

Figure 2.8: A similar membrane sensor to that shown in Figure 2.7. Labeled PCR amplicons are linked to the membrane surface through anti-digoxigenin Abs. Neutravidin coated carbon particles link to the other end of the labeled amplicons, which is visible to the naked eye. The anti-digoxigenin and biotin-protein complex were adsorbed to the nitrocellulose membrane.[119] "Reprinted from Biosens Bioelectron, 26, Blazkova, M., Javurkova, B., Fukal, L. & Rauch, P, Immunochromatographic strip test for detection of genus Cronobacter, 2828-2834, Copyright (2011), with permission from Elsevier."

Frequently membranes are not used purely as a support, but as a filter.[105,122,132,140,143] Simple adsorption or collection of viruses and bacteria may be sufficient for some biosensors. In this case linking to the surface is unnecessary. In one example, membranes were used for filtration in order to trap the cells while allowing unbound nanoparticles to pass through the pores in the membranes.[141] For some applications the membranes may even be used in reverse. One group, for instance, used a nylon membrane in a catalase activity sensor to prevent biofouling by bacterial buildup on the sensor.[133]

2.3.4. Transduction Systems

The transduction process is the method by which the biochemical interaction of the capture molecule and the target pathogen is converted into an observable output signal. Ideally this output can also be used to determine the concentration of the pathogen being detected. Numerous different detection methods have been employed. The most popular by far were those involving electrical or optical phenomena.

2.3.4.1. Electrical

Many transduction methods involve a change in the electrical conditions in the system. Frequently, the process of the capture molecule binding to the target pathogen or molecule can lead to a change in the electrical characteristics of the biosensor, including the potential, current, resistance, and/or impedance. Oligonucleotide hybridization on a positively charged nanomembrane[145] and binding of a glycoprotein to a membrane[154] were observed and quantified by electrodes and the resultant current vs. voltage (resistance) plot. Another group quantified binding of bacteria to a membrane by recording the change in membrane resistance.[137]

Impedance spectroscopy can likewise be used to record binding of a pathogen on an Ab coated membrane.[101] In another case impedance spectroscopy was used to characterize the spontaneous formation of anion channels inserted by bacteria into biomimetic membranes.[149]

A change in electrical current is often observed in transduction methods. Catalase-positive and negative bacteria were identified by hydrogen peroxide consumption. The hydrogen peroxide was detected amperometrically by a graphite–Teflon–peroxidase–ferrocene electrode.[133] In another study, a change in current of the modified patch-clamp pipette electrode was recorded, which allows changes in the concentration of nucleic acids to be determined.[151] Bacteria bound to membranes were detected electrochemically by cellular uptake of ferrocyanide through chronocoulometry.[144] Another group used Abs to bind *E. coli* cells to a membrane. Horseradise peroxidase-conjugated Abs were then used to detect the *E. coli* cells as in a sandwich ELISA. NaI, ortho-phenylenediamine and hydrogen peroxidase substrates caused a current to develop, which allowed for quantification of the *E. coli* cells.[135]

Like the other electrical characteristics, potentiometric-based transduction methods are also common. The attachment of viruses to Abs in a cellular membrane leads to a change in potential that can be recorded via electrodes.[147,148] One novel transduction method was based on the use of live cells which were engineered to detect specific pathogens. Virus particles bound to specific Abs which had been inserted into the cellular membrane. This resulted in a change in membrane potential that was detected using an electrode and a voltmeter.[146]

Similarly, several methods were tested for detection of bacterial toxins through lipid damaging or pore formation effects in lipid bilayers. These effects change the ion permeability of the membranes which can be detected by electrochemical impedance spectroscopy or plasmon resonance spectroscopy. *Staphylococcus aureus* (MSSA476), *Pseudomonas aeruginosa* (PAO1) and *E. coli* (DH5α) showed ion permeation through change in impedance.[115]

Another more unusual transduction method was based on the use of Abs conjugated to conductive materials to complete a circuit. Pathogens were immobilized on membranes and conductive polyaniline[155] or iron oxide nanoparticle[112] -conjugated Abs specific to the pathogens were used to detect the antigens, and complete an electrical circuit. The change in resistance and conductance, respectively, were used to quantify the pathogens. In different articles, the use of polyaniline and iron oxide nanoparticle-conjugated Abs for the concentration of bacteria and viruses by magnetic separation was presented. The Ab-covered bacteria and viruses were then bound to nitrocellulose nanofilament membranes through secondary Abs, and the change in resistivity was used to determine the concentration of bacteria or viruses.[123,124] This sensor's operation is shown in Figure 2.9.

Membranes may often serve as a physical support in the biosensor applications. Conversely, the properties of porous membranes may be harnessed directly by various electrical transduction methods. DNA hybridization in the membrane pores leads to blockages which can be detected with electrochemical impedance spectroscopy (EIS).[99] Sensitivity can be increased by linking gold nanoparticles to the pathogen DNA and by silver catalytic deposition. In a different experiment, DNA hybridization in alumina nanochannels was shown to restrict the binding of ferrocyanide to an electrode. This results in a decrease in peak current in cyclical voltammograms, which can be used to quantify the DNA.[102] In another similar experiment, DNA hybridization was again used to create ion blockages in alumina membranes. As before, the hybridization of the probe and target DNA took place in the pores of the membranes, and cyclic

voltammetry and EIS were used to quantify the DNA. In addition to the hybridization process, however, Taq DNA polymerase was used to elongate the 20 base pair probe sequences to the length of the full target DNA sequence. This led to a substantial enhancement of the ion blockage, thus increasing the sensitivity of the sensor.[100]

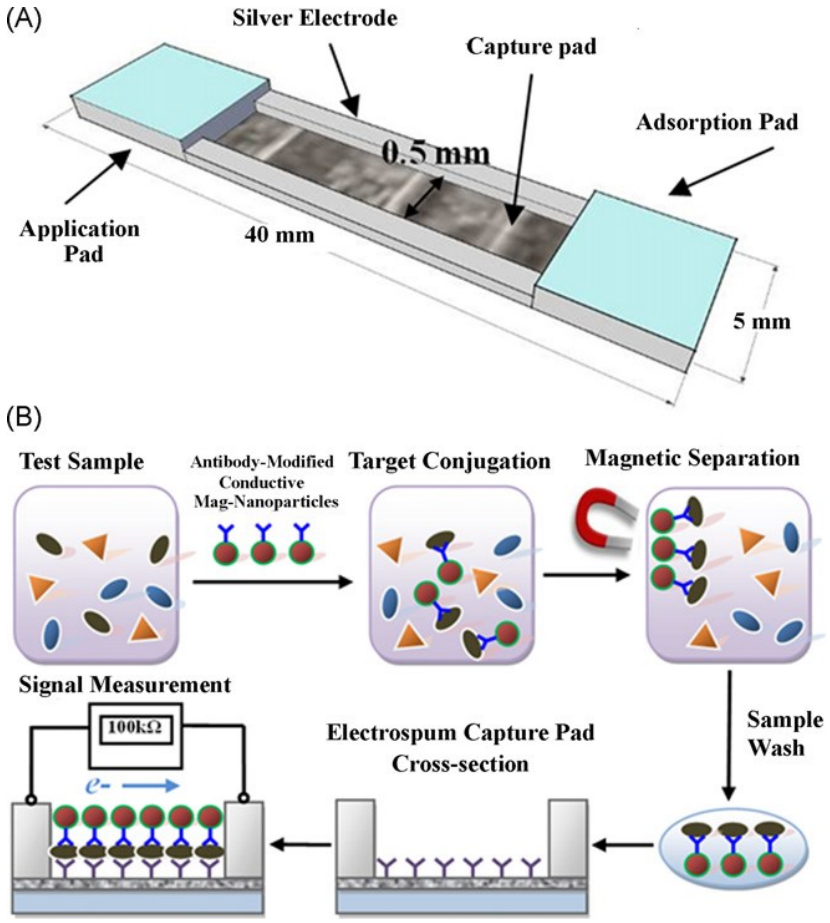

Figure 2.9: A lateral flow immunosensor. Schematic of the biosensor structure and membrane assembly consisting of cellulose application and absorption pads and electrospun cellulose nitrate capture pad. (B) Detection scheme of the lateral flow immunosensor based on the Ab-functionalized electrospun capture membrane.[123] "Reprinted from Biosens Bioelectron, 26, Yilun Luo, Steven Nartker, Hanna Miller, David Hochhalter, Michael Wiederoder, Sara Wiederoder, Emma Setterington, Lawrence T. Drzal, Evangelyn C. Alocilja, Surface functionalization of electrospun nanofibers for detecting E. coli O157:H7 and BVDV cells in a direct-charge transfer biosensor, 1612-1617, Copyright (2010), with permission from Elsevier."

Similar work was performed using viral RNA, porous alumina, differential pulse voltammetry (DPV) and ferrocyanide. The transduction process works such that the DPV oxidative peak current decreases as the viral RNA concentration increases.[104] In another study, Ab-pathogen binding in pores led to changes in impedance, which were analyzed by normalized impedance change.[106] Bacterial cells have been detected in a similar manner. The bacteria were captured by Abs attached to the membranes. This blocked the pores in the membrane, and thus the flow of the electrolyte, leading to an increase in the impedance of the sensor. The impedance was monitored by an impedance analyzer.[103] In a different, more direct, application of membranes, conductive membranes were used as a filter to capture *Salmonella* bacteria. Subsequently, the change in conductivity was recorded to quantify the *Salmonella* bacteria.[143]

2.3.4.2. Optical

Optical phenomena form the other common basis for many transduction methods. These types of transduction processes may be characterized by a colour change that is visible to the naked eye (and may be quantified by a reflectometer or microplate reader), photoluminescence (including fluorescence), chemiluminescence, absorbance, or radioactivity. They also include the use of external methods such as surface-enhanced raman spectroscopy and interferometry. Although these processes may also include some kind of electrical transduction method, such as a CMOS image sensor, they have been classified as optical as the primary output of the sensors is optical in nature.

2.3.4.2.1. Color Change

A visual colour change is one of the major optical transduction methods. In some cases it was used as a method of detection by the naked eye, while in others a reflectometer or absorbance measurement was performed for quantification. A number of experiments have been performed with liposome-conjugated DNA probes to detect pathogen DNA/RNA. Short single-stranded DNA or RNA probes were used to link single-stranded DNA or RNA from the pathogen to a membrane. Subsequently, DNA-linked liposomes containing a dye were applied to

label the other end of the pathogen's DNA/RNA. The dye was then released, and the colour change was quantified via a reflectometer.[125-130]

Another way to produce a visual colour change is through the attachment of gold[110] or carbon[119] nanoparticles to sensing molecules (Figures 2.7, 2.8). In a similar approach, commercially available carboxylated magnetic nanoparticles were coated with BSA using EDC/NHS chemistry. Gold nanoparticles were attached to the BSA on the magnetic nanoparticles through electrostatic attraction. Subsequently, Abs were attached to the composite nanoparticles through physical adsorption. These nanoparticles were used to bind to bacteria, and filtered through the membrane. The bacteria with bound particles were trapped while the unbound nanoparticles passed through the pores of the membranes. The detection of bacteria was then indicated by the visual colour change caused by the aggregated gold nanoparticles. The visibility of the colour change was enhanced by the addition of hydroxylamine and $HAuCl_4$.[141]

HRP is commonly used to catalyze colourimetric reactions. HRP-conjugated Abs bind to pathogens, and the addition of substrates such as tetramethylbenzidene[111,139] and SuperSignal West Femto[111] in addition to hydrogen peroxide allows a colourimetric reaction to take place. PP may also be used to catalyze colourimetric reactions, as seen in an experiment with Microcystins. Microcystins are toxic proteins produced by cyanobacteria such as *Microcystis*, *Anabaena*, *Oscillatoria* and *Nostoc* which inhibit the activity of PPs. In this experiment, PPs were immobilized on the membrane surface, and microcysteins were introduced in solution. Subsequently, colourless *p*-nitrophenyl phosphate (*p*NPP) was introduced in the PP. This converts the pNPP to yellow *p*-nitrophenol (*p*NP), which can be measured with a microplate reader. The enzymatic reaction demonstrates the presence of microcystins.[131]

In a different experiment, lectin proteins on a membrane were used to bind bacterial cells. Subsequently, the oxidants menadione and ferranocyanide, and the respiratory substrates, formate and succinate, were introduced to the cells. Oxidation of the ferranocyanide led to a change in colour, which was related to the quantity of bacteria.[136]

Two of the most unusual transduction methods involved colour changes based directly on interaction with the molecule of interest. In the first, polydiacetylene liposomes with embedded ganglioside GM1 were used to detect cholera toxin. The cholera toxin binds to GM1, and the binding interaction causes conformational changes in the polymer backbone of the liposomes. This results in a change of the liposome colour.[152] Similarly, tricosadiynoic acid (TRCDA)

vesicles change colour when exposed to lipolysaccharides from pathogens and other microorganisms.[153]

2.3.4.2.2. Light Emission

The emission of light is the other main transduction method used for membrane based pathogen detection. As with colour change, liposomes filled with fluorescent dye may be used for this transduction method. In this case fluorescent dye-filled liposomes attached to Abs were mixed with the antigen, and electrokinetically concentrated using a voltage applied across the membrane before being introduced to the capture bed. Detergent was used to release the fluorescent dye for quantification through video recording (Figure 2.10).[140]

Other particles may also be linked to Abs for light emission. CdSe/ZnS core/shell dendron nanocrystals were functionalized with Abs and bound to antigen on the membrane surface creating a "sandwich". The crystals are photoluminescent, which allows for quantification of the antigen.[134] In a similar case, the secondary Abs were conjugated to up-converting phosphor particles, a 980 nm laser was used to excite the phosphor particles and the resulting 541 nm wavelength luminescence was detected using a photomultiplier tube.[114]

In addition to catalyzing colourimetric reactions, HRP can also be used to catalyze light emitting reactions. In one case, HRP-conjugated Abs were used to detect virus particles and a luminol-based chemiluminescent reaction used to optically quantify the virus concentration.[118] In a different experiment superparamagnetic beads were linked to Abs and magnetically attached to a capture bed. Subsequently, bacterial cells were labeled with HRP-conjugated Abs and introduced to the Abs on the capture bed. Once again a catalyzed luminol and HRP-based reaction led to a chemiluminescent output, which was recorded using a luminometer.[132] In a similar process, also based on a sandwich configuration, the chemiluminescence produced by a HRP-conjugated Ab and luminol reaction was recorded using a lens-free CMOS image sensor.[113] (Figure 2.11)

Fluorescently-labeled Abs may also be used for emission-based transduction. In one case bacteria were introduced to Abs bound to a membrane, and Alexa fluor-conjugated (H+L) Ab fragments were used to detect the bacteria attached to the membrane. This output was observed with a fluorescence microscope.[142]

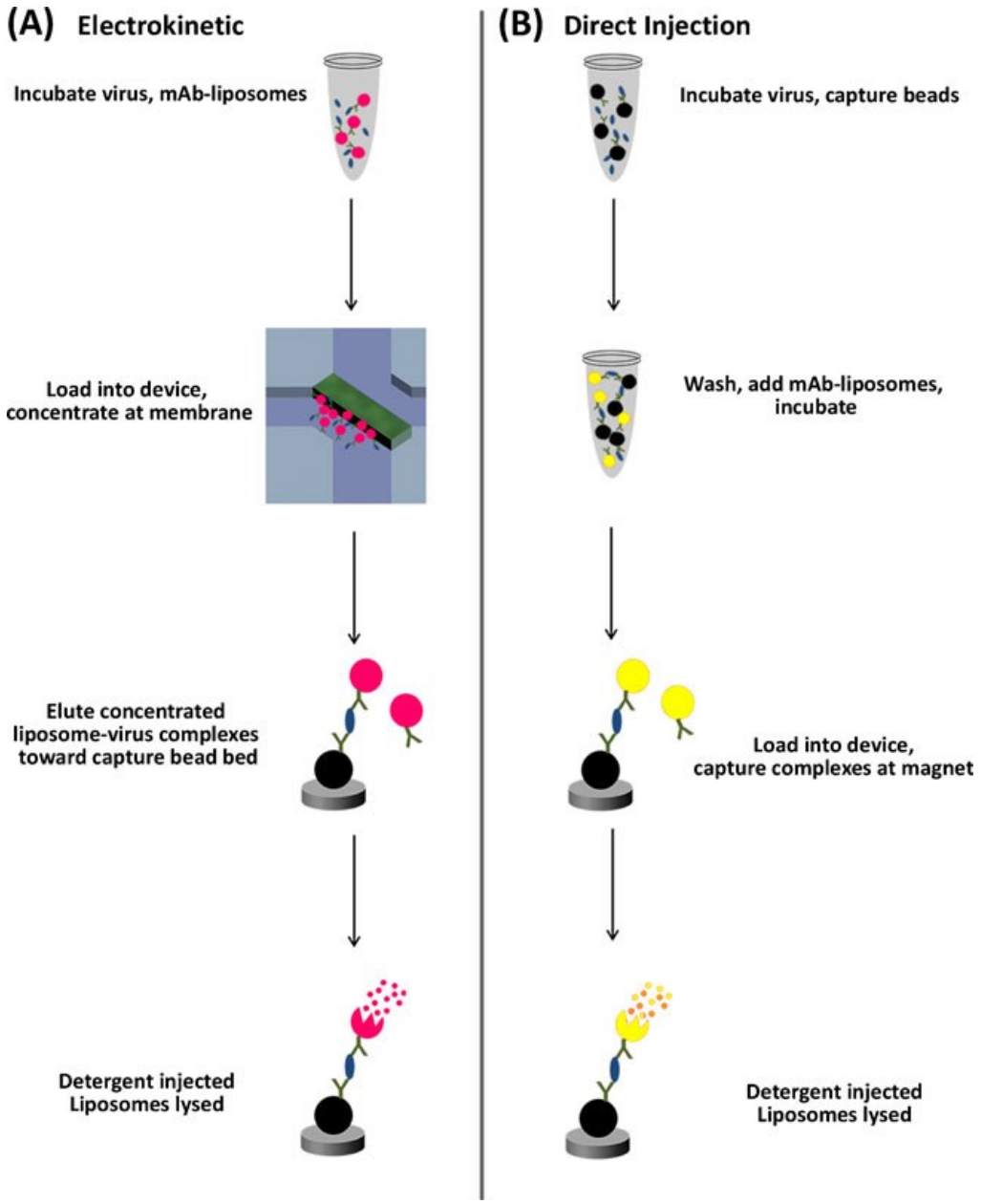

Figure 2.10: Detection of virus particles. A) with and B) without a concentration step using a membrane. The concentration step led to an order of magnitude better sensitivity.[140] Reprinted by permission from Springer Nature Customer Service Centre GmbH: Springer Nature Analytical and Bioanalytical Chemistry, Micro-total analysis system for virus detection: microfluidic pre-concentration coupled to liposome-based detection, John T. Connelly, Sowmya Kondapalli, Marc Skoupi, John S. L. Parker, Brian J. Kirby, Antje J. Baeumner, 2012.

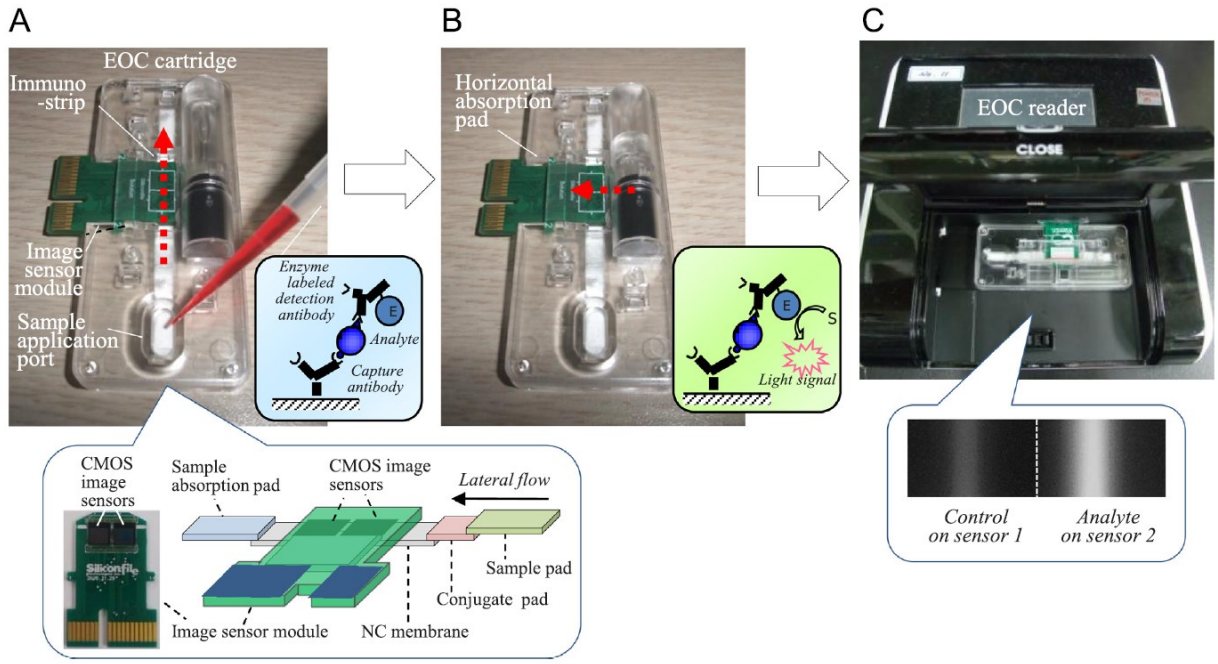

Figure 2.11: ELISA on a chip reaction with chemiluminescent output and lens free CMOS sensor. A) The substrate is added to the sample pad, the HRP-conjugated Ab is released from the conjugate pad and it subsequently binds to the antigen. The Ab-antigen complex then binds to the capture Ab on the nitrocellulose membrane. B) The luminol and hydrogen peroxide substrates are injected into the reaction chamber and the reaction is catalyzed by the HRP enzyme. C) The chemiluminescent output is recorded by the CMOS sensor and used to quantify the antigen concentration.[113] "Reprinted from Biosensors and Bioelectronics, 52, Jin-Woo Jeon, Jee-Hyun Kim, Jong-Mook Lee,Won-Ho Lee, Do-Young Lee, Se-Hwan Paek, Rapid immuno-analytical system physically integrated with lens-free CMOS image sensor for food-borne pathogens, 384-390, Copyright (2014), with permission from Elsevier."

A somewhat more antiquated transduction method (due to safety issues rather than accuracy and sensitivity) involves radiolabeling. Bacterial cells were captured by filtration through a nitrocellulose membrane, and the cells were chemically lysed. Radiolabeled DNA probes were added to bind to the DNA from the lysed cells. The autoradiography was recorded using autoradiography film.[122]

2.3.4.2.3. Spectroscopic/Interferometric

Other than the inherent characteristics of the system, external light sources may be used in transduction methods. In the first case, unusually, the mechanical deflection of the membrane was observed. A white light interferometer and a fiber optic interferometer where used to determine deflection of the membranes caused by the binding of the pathogen.[108] In the second case, membrane filters were used to capture bacteria and Ab-coated gold nanoparticles were used to label the bacteria. The nanoparticles were detected through surface enhanced raman spectroscopy.[105]

2.3.4.3. Other

Aside from electrical and optical transduction systems, several other transduction methods have also been employed. In one case a commercial leaky surface acoustic wave system was used to detect pathogen DNA.[107] Surface acoustic wave biosensors generally emit a wave through a material via the piezoelectric effect. Binding of biomolecules to the surface of the sensor increases the mass of the material, which leads to a change in the velocity of the wave. This change in velocity can be observed in a number of different ways. One such method is to record the change in time it takes the wave to progress through the material.

Piezoelectric quartz crystals are also popular for mass sensing. The binding of molecules to the surface changes the resonance frequencies of the quartz crystal. This change in frequency can be used to determine the quantity of bound antigen. In this case quartz crystals were used determine the quantity of bound bacterial DNA and cholera toxin.[109,150]

Magnetic beads coated with Abs were employed to simultaneously detect two virus strains. The number of beads was determined using a magnetic reader with two frequency magnetic excitation.[117] An oxygen meter was used to detect *E. coli* cells. In another case HRP-conjugated Abs specific to *E. coli* were immobilized onto nitrocellulose membranes. These membranes were fixed outside the Teflon membrane of the oxygen meter. Hydrogen peroxide was used to produce the oxygen, which was then recorded by the oxygen meter. The production of oxygen was amplified with 2,2'-Azino-bis(3-ethylbenzothiazoline-6-sulfonic acid)

diammonium salt. When the *E. coli* cells were added to the solution, they reduced access of the HRP to hydrogen peroxide, decreasing the production of oxygen.[121]

2.3.5. Pathogen Detection Limit

Numerous different pathogens have been detected, largely through interactions with DNA or RNA, or whole bacteria or virus particles. It can be difficult to directly compare the different detection limits because the units are different. Whole bacteria and virus particles have a much greater mass than their DNA or RNA, which means that the DNA and RNA concentrations in a sample will naturally be much smaller in mass/volume, unless they have been amplified (usually through PCR). This is important, because in direct mass/volume comparisons, the DNA/RNA methods will almost inevitably appear to be more sensitive for this reason, even though the mass of the virus, and especially the bacteria, in a sample will be much greater than that of the DNA/RNA produced from those viruses or bacteria in a DNA/RNA sensor.

Table 2.1: A summary of the pathogens detected, form of detection and detection limit or range where provided. Unit abbreviations are colony forming units (CFU), cell culture infective dose (CCID) and plaque forming units (PFU).

Pathogen	**Detection Type**	**Membrane Sensor**	**Transduction Method**	**Detection limit or range**
Bacillus anthracis	RNA	Polyethersulfone membrane with linked ssDNA probe	Reflectometer-based detection of dye-filled liposome linked to reporter DNA probe	1 nM[157]
	RNA	Polyethersulfone membrane with linked ssDNA probe	Reflectometer-based detection of dye-filled lyposome linked to reporter probe	1.5 fmol[158]
Baccilus cereus	whole bacteria	Immunodyne ABC membranes with various linked lectins	Chemometric data analysis of pathogen binding chronocoulometry results were used to distinguish between different pathogens	not given[144]
Baccilus cereus	whole bacteria	Composite sensor composed of glass fiber, cellulose and nitrocellulose membranes with linked capture antibodies	Detection of antigen with conductive polyaniline nanowire-conjugated antibodies and quantification via change in conductance	10 CFU/ml[155]

Pathogen	Detection Type	Membrane Sensor	Transduction Method	Detection limit or range
Bovine viral diarrhea virus	virus particle	Nanofiber nitrocellulose membranes with linked antibodies	Pathogens coated by conductive nanoparticle-conjugated antibodies were immobilized on the membrane and quantified via the change in resistance	10^3 CCID/ml[123]
Brucella	RNA	Nanomembrane composed of polystyrene-divinylbenzene particles with quaternary ammonium groups and polyamide/ polyestertextile fiber embedded in polyethylene with linked oligonucleotide probe	Change in ion current with oligonucleotide hybridization	1 pM[145]
Cherry leaf roll virus	virus particle	Cellular membrane of live bacterial cells with inserted antibodies	Change in membrane potential due to binding	1 pg/ml[146]
Clavibacter	anion channel formation	Lipid membrane composed of octanethiol, 1,2-Dimyristoyl-sn-glycero-3-phosphocholine, spacerlipid A on a gold electrode which are then coated with phospholipid	Toxic inserted channel proteins were detection by impedance spectroscopy	not given[149]
Cronobacter spp.	RNA	Composite sensor composed of glass fiber, cellulose and nitrocellulose membranes with linked oligonucleotide sandwich	Visual colour change due to carbon nanoparticles bound to ssDNA	8 ng or 3 ug/ml[119]
Cucumber mosaic virus	virus particle	Cellular membrane of live fibroblast cells with electroinserted antibodies	Antibody-antigen binding was quantified by the observed change in electric potential	1 ng/ml[148]
	virus particle	Cellular membrane of live mammalian cells with electroinserted antibodies	Antibody-antigen binding was quantified by the observed change in electric potential	1 ng/ml[147]
Cyanobacteria	microcystin MC-LR protein	Ultrabind polyethersulfone membranes with linked protein phosphatase	Microcystin inhibits PP activity, reducing production of yellow pNP from colorless pNPP substrate	0.30 ug/ml[131]
	microcystin MC-RR protein	Ultrabind polyethersulfone membranes with linked protein phosphatase	Microcystin inhibits PP activity, reducing production of yellow pNP from colorless pNPP	0.52 ug/ml[131]
Dengue virus	virus particle	Polyethersulfone membrane with linked DNA capture probe	Reflectometer-based detection of dye-filled liposomes linked to reported probes	serotype 2 - 50 molecules[129]

Pathogen	Detection Type	Membrane Sensor	Transduction Method	Detection limit or range
	RNA	Nanoporous alumina membrane with linked ssDNA probe	Change in ionic conductivity due to oligonucleotide hybridization in pores was recorded by cyclic voltammetry and DPV	$9.55x10^{-12}$ M[104]
	glycoproteins	Lipid membrane modified by Concanavalin A on and gold electrode	Binding of dengue virus particles was observed using cyclic voltammetry and electrochemical impedance techniques	not given[154]
	RNA	Polyethersulfone membrane with linked DNA capture probe	Reflectometer-based detection of dye-filled liposomes linked to ssDNA reported probes	roughly10 PFU/ml[127]
	RNA	Nanomembrane composed of polystyrene-divinylbenzene particles with quaternary ammonium groups and polyamide/polyestertextile fiber embedded in polyethylene with linked oligonucleotide probe	Change in ion current with oligonucleotide hybridization	1 pM[145]
DNA sensing for pathogen detection	DNA	Nanoporous alumina membrane with linked ssDNA probe	EIS-based detection of DNA hybridization in the pores	50 pM[99]
Enterobacter aerogenes	whole bacteria	Immunodyne ABC membranes with various linked lectins	Chemometric data analysis of pathogen binding chronocoulometry results were used to distinguish between different pathogens	Not given[144]
Escherichia coli	whole bacteria	ImmunodyneABC Nylon membranes coated with 10 different lectins	Detection of pathogen through chronocoulometric results and factor analysis for identification of 4 E. *coli* subspecies	$1.8x10^{7}$ CFU/ml[136]
	whole bacteria	Nylon membrane used to prevent fouling of graphite–Teflon–peroxidase–ferrocene composite electrode	Change in current, due to presence or absence of catalase- based decomposition of hydrogen peroxide, was recorded by the electrode	2×10^{6} CFU/ml[133]
	RNA	Nanomembrane composed of polystyrene-divinylbenzene particles with quaternary ammonium groups and polyamide/polyestertextile fiber embedded in polyethylene with linked oligonucleotide probe	Change in ion current with oligonucleotide hybridization	1 pM[145]

Pathogen	Detection Type	Membrane Sensor	Transduction Method	Detection limit or range
	whole bacteria	Nanoporous alumina membrane with linked antibodies	Antibody-antigen binding was quantified by impedance amplitude changes	~1000 CFU/ml[103]
	RNA	Polyethersulfone membrane with linked ssDNA capture probe	Reflectometer-based detection of dye-filled liposomes linked to ssDNA reported probes	5 fmol[130]
	virulence factors	Membranes were composed of either 2,3-di-O-phytanylglycerol-1-tetraethylene glycol-D,L-lipoic acid ester lipid, 2,3-di-Ophytanyl-sn-glycerol-1-tetra-ethylene glycol-(3-tryethoxysilane) ether lipid, or cholesterolpentaethyleneglycol and 1,2-di-O-phytanoyl-sn-glycero-3 phosphocholine or cholesterol	Bacterial toxins were detected through change in impedance caused by pore formation in the lipid bilayer	not given[115]
	whole bacteria	Gold coated PDMS membrane with linked thiols	Stress-based membrane deflection detected by white light and fiber optic interferometers	Distinguish between living and dead cells[108]
	whole bacteria	Immunodyne ABC membranes with various linked lectins	Chemometric data analysis of pathogen binding chronocoulometry results were used to distinguish between pathogens	not given[144]
	whole bacteria	Vesicles formed from TRCDA and DMPC	TRCDA vesicles change colour when exposed to lipopolysaccharides from pathogens	~10^8 CFU[153]
Escherichia coli DH1	DNA	Nitrocellulose membranes coated with the contents of lysed E. coli cells	PCR was performed and radiolabeled DNA probes were added to bind to the DNA from the lysed cells. The autoradiography was recorded using autoradiography film	not given[159]
Escherichia coli O157:H7	whole bacteria	Nanoporous alumina membrane with linked antibodies	Change in impedance due to antibody-antigen binding via electrochemical analyzer	10^2 CFU/ml[101]
	whole bacteria	Nitrocellulose membrane with linked anti-E. coli O157:H7 antibody conjugated to HRP placed over oxygen probe membrane	On pathogen binding, the decrease in HRP activity is recorded by a Clark-type oxygen electrode probe	50 cells/ml[121]

Pathogen	Detection Type	Membrane Sensor	Transduction Method	Detection limit or range
	whole bacteria	Polypropylene microfiber membrane coated with conductive polypyrrole and linked with antibodies	Change in resistance due to antibody-antigen binding	log 0 - 9 CFU/ml[137]
	whole bacteria	Nanoporous nylon membrane with linked antibodies	Pathogen detected by photoluminescent CdSe/ZnS core/shell dendron nanocrystal-conjugated antibodies	2.3 CFU/ml[134]
	whole bacteria	Nylon membrane with linked capture antibody	Sandwich ELISA with NaI, ortho-phenylenediamine and hydrogen peroxide substrates which were measured amperometrically	100 cells/ml[135]
	whole bacteria	Nitrocellulose membrane with linked capture antibody	Sandwich ELISA with luminol-based chemiluminescent output	10^5–10^6 CFU/ml[118]
	whole bacteria	Nanofiber nitrocellulose membranes with linked antibodies	Pathogens coated by conductive nanoparticle-conjugated antibodies were immobilized on the membrane and quantified via the change in resistance	61 CFU/ml[123]
	DNA	Aluminum anodized oxide membrane with linked	Change in ionic conductivity due to DNA hybridization in pores measured by cyclic voltammetry and impedance spectroscopy	0.5 nM[100]
	whole bacteria	Composite sensor composed of glass fiber, cellulose and nitrocellulose membranes with linked capture antibodies	Visual output from sandwich ELISA using 3,3',5,5'-tetramethyl-benzidene and SuperSignal West Femto substrates	$1.8x10^3$ to $1.8x10^8$ CFU/ml[111]
	whole bacteria	Composite sensor composed of cellulose and nitrocellulose membranes with linked antibodies	Detection of antigen with conductive nanoparticle-conjugated antibodies and quantification via change in conductance	67 CFU/ml[124]
Escherichia coli O157:H7	whole bacteria	Nanoporous alumina membrane with linked antibodies	Change in ionic impedance of electrolytes in nanopores due to antibody-antigen binding	83.7 CFU/ml[106]
Feline calicivirus	virus particle	Nanoporous polyacrylamide membrane used for pathogen concentration	Antibodies conjugated to fluorescent dye filled liposomes were used to quantify the pathogen	1.6×10^5 PFU/ml[140]
Giardia lamblia	*Giardia lamblia* cysts	Gold-coated PCTE membrane filter	Immunogold labeled antigen quantified via Raman spectroscopy	200 cysts/ml[105]

Pathogen	Detection Type	Membrane Sensor	Transduction Method	Detection limit or range
Hepatitis B virus	surface antigen	Nanoporous nylon membrane with linked antibodies	Pathogen detected by photoluminescent CdSe/ZnS core/shell dendron nanocrystal-conjugated antibodies	5 ng/ml[134]
Human Papilloma virus	DNA	Gold membrane with linked bis-peptide nucleic acid probe	Surface acoustic wave based detection of DNA hybridization	1.21 pg/L[107]
Influenza A virus	virus particle	Nitrocellulose membrane coated with antigen	Detection of antigen with magnetic bead-conjugated antibodies which were quantified with a magnetic reader	1 to 250 ng/ml[117]
Legionella pneumophilla	DNA	Nanoporous alumina membrane with linked ssDNA probe	Change in ionic conductivity due to oligonucleotide hybridization in pores was recorded by cyclic voltammetry and DPV	3.1×10^{-13} M[102]
Mycobacterium avium subspecies paratuberculosis	RNA	Polyethersulfone with linked oligonucleotide sandwich	Reflectometer-based detection of dye-filled liposomes linked to reported probes	10 CFU[125]
	whole bacteria	Composite sensor composed of glass fiber, cellulose and nitrocellulose membranes	A primary antibody and secondary conductive nanoparticle-conjugated antibody bind to the antigen, and the change in conductivity is recorded	serum dilution of 1:80[112]
Mycobacterium parafortuitum	whole bacteria	HPC modified cellulose acetate ultrafiltration membrane with linked antibody	Fluorescently labeled secondary antibodies were used to detect the immobilized pathogen	not given[142]
Potato virus Y	virus particle	Cellular membrane of live mammalian cells with electroinserted antibodies	Antibody-antigen binding was quantified by the observed change in electric potential	minimum detection of 1 ng/ml[147]
Proteus vulgaris	whole bacteria	Immunodyne ABC membranes with various linked lectins	Chemometric data analysis of pathogen binding chronocoulometry results were used to distinguish between different pathogens	not given[144]
Pseudomonas aeruginosa	DNA	TiO_2 and TiO_2-polyethylene glycol membranes on piezoelectric quartz with linked ssDNA probe	DNA hybridization detected by shift in resonant frequency	10^{-4} g/L[160]

Pathogen	Detection Type	Membrane Sensor	Transduction Method	Detection limit or range
	virulence factors	Membranes were composed of either 2,3-di-O-phytanylglycerol-1-tetraethylene glycol-D,L-lipoic acid ester lipid, 2,3-di-Ophytanyl-sn-glycerol-1-tetra-ethylene glycol-(3-tryethoxysilane) ether lipid, or cholesterolpentaethyleneglycol and 1,2-di-O-phytanoyl-sn-glycero-3 phosphocholine or cholesterol	Bacterial toxins were detected through change in impedance caused by pore formation in the lipid bilayer	not given[115]
Saccharomyces cerevisiae	whole bacteria	Immunodyne ABC membranes with various linked lectins	Chemometric data analysis of pathogen binding chronocoulometry results were used to distinguish between different pathogens	not given[144]
Salmonella Newport	GIII bacteriophage	Polypyrrole modified microporous polycarbonate membrane	Pathogen cells drawn into membrane pores, GIII bacteriophage added to pathogen and change in impedance recorded	not given[143]
Salmonella spp.	whole bacteria	Nitrocellulose membrane with linked capture antibody	Sandwich ELISA with luminol-based chemiluminescent output	10^6–10^7 CFU/ml[118]
Salmonella Typhi	whole bacteria	Polycarbonate membranes with linked antibodies	Sandwich ELISA with colourimetric output from 3,3',5,5' tetramethyl benzidine-hydrogen peroxide substrates	$2x10^3$ cells/ml[139]
Salmonella typhimurium	whole bacteria	Vesicles formed from TRCDA and DMPC	TRCDA vesicles change colour when exposed to lipolysaccharides from pathogens	~10^8 CFU[153]
	whole bacteria	Nitrocellulose membrane coated with biotin	Urease, linked to bacteria on the surface, converts urea to ammonia and CO_2 which results in a pH change which is measured as a change in electric potential	119 CFU[116]
	whole bacteria	Composite sensor composed of glass fiber, cellulose and nitrocellulose membranes with linked capture antibodies	Visual output from sandwich ELISA using chemiluminescent substrate solution quantified by CMOS image sensor	$4.22x10^3$ CFU/ml and $1.1x10^2$ CFU/ml with pre-separation and concentration[113]

Pathogen	Detection Type	Membrane Sensor	Transduction Method	Detection limit or range
Shigella sonei	whole bacteria	Vesicles formed from TRCDA and DMPC	TRCDA vesicles change colour when exposed to lipolysaccharides from pathogens	~10^8 CFU[153]
Staphylococcus aureus	whole bacteria	Polyethersulfone membrane	Pathogen cells were labeled with HRP conjugated antibodies, collected by the membrane and quantified by a luminol-based luminescent reaction	$3.8x10^4$ CFU/ml[132]
	DNA (enterotoxins B gene)	Membranes composed of egg phosphatidylcholine, cholesterol and hexadecylamine with linked ssDNA probes	DNA hybridization detected by change in current through the membrane	20 ng/ml[151]
	whole bacteria	Immunodyne ABC membranes with various linked lectins	Chemometric data analysis of pathogen binding chronocoulometry results were used to distinguish between different pathogens	not given[144]
	virulence factors	Membranes were composed of either 2,3-di-O-phytanylglycerol-1-tetraethylene glycol-D,L-lipoic acid ester lipid, 2,3-di-Ophytanyl-sn-glycerol-1-tetra-ethylene glycol-(3-tryethoxysilane) ether lipid, or cholesterolpentaethyleneglycol and 1,2-di-O-phytanoyl-sn-glycero-3 phosphocholine or cholesterol	Bacterial toxins were detected through change in impedance caused by pore formation in the lipid bilayer	~240 pM[115]
	whole bacteria	Nanoporous alumina membrane with linked antibodies	Antibody-antigen binding was quantified by impedance amplitude changes	~1000 CFU/ml[103]
	whole bacteria	Cellulose acetate membrane filters	Pathogen-antibody/gold nanoparticle/magnetic nanoparticle complexes were filtered through the membrane and the colour change was quantified by the optical density.	$1.5x10^3$ CFU for pure bacteria and $1.5x10^5$ CFU in milk[141]
	whole bacteria	Nanoporous alumina membrane with linked antibodies	Change in impedance due to antibody-antigen binding was recorded by an electrochemical analyzer	10^2 CFU/ml[101]
Streptococcus pneumoniae	whole bacteria	Nylon membrane used to prevent fouling of graphite–Teflon–peroxidase–ferrocene composite electrode	Change in current, due to catalase- based decomposition of hydrogen peroxide	2×10^5 cfu/ml[133]

Pathogen	Detection Type	Membrane Sensor	Transduction Method	Detection limit or range
Tobacco mosaic virus	virus particle	Cellular membrane of live bacterial cells with electroinserted antibodies	Antibody-antigen binding was quantified by the observed change in electric potential	1 pg/ml[146]
Tobacco rattle virus	virus particle	Cellular membrane of live mammalian cells with electroinserted antibodies	Antibody-antigen binding was quantified by the observed change in electric potential	1 ng/ml[147]
Vibrio cholerae	DNA	Composite sensor composed of glass fiber and cellulose membranes with linked oligonucleotide sandwich	Visual colour change due to gold nanoparticles bound to ssDNA	5 ng or 250 ng/ml[110]
	cholera toxin protein complex	Lipid membrane composed of octanethiol on a gold electrode which was then coated with DPPC and GM1	Cholera toxin induced liposome agglutination on the piezoelectric sensor was detected by the resonant frequency shift	25 ng/ml[150]
	cholera toxin protein complex	Polydiacetylene liposomes with incorporated ganglioside, GM1	Cholera toxin induces a change in the liposome light absorption	not given[115]
Yersinia pestis	whole bacteria	Composite sensor composed of glass fiber, cellulose and nitrocellulose membranes with linked capture antibodies	Secondary antibodies conjugated to up-converting phosphor particles were excited, and the resultant luminescence was quantified by a photomultiplier tube	10^4 CFU/ml[114]

2.3.6. Summary

Membranes have been used in a number of biosensor designs for the detection of pathogens. In this review, the central components of these sensors were divided and examined individually: membrane composition, detection biomolecule, linking process, transduction process and sensitivity. For the majority of membrane biosensors, the membrane material is an important aspect for the sensing application, largely for functionalization purposes. In cases where the membrane is used for filtration or is an integral part of the detection or transduction process, other properties of the membranes become more important. A number of reports involved the use of aluminum oxide. It was selected for properties such as high resistivity, well defined small pore size, high pore density and the simplicity with which it can be functionalized. Other inorganic materials were mainly used in conjunction with organic materials, sometimes to facilitate linking processes such as sulfide-gold linkages, and sometimes to enhance transduction

such as surface-enhanced raman spectroscopy. Glass membranes were used for capillary action to combine organic molecules used in the sensor while SiN was used for mechanical support.

Several other reports, however, involved organic membranes rather than inorganic ones. Predictably, the most common membrane material is nitrocellulose. It is commonly used in biomedical applications. Other common membrane materials were polyethersulphone and nylon. Several researchers acquired readily available commercial membranes, many of which are prefunctionalized for adhesion or covalent bonding. Use of lipid-bilayer based membranes was also reported.

Abs and nucleic acid hybridization were by far the most common methods used for pathogen detection. Abs are often used in sandwich applications, with a capture Ab for initial detection and a conjugated Ab for transduction. Nucleic acid-based detection mostly consisted of simple hybridization of complementary probe and DNA or RNA strands from pathogens. Other approaches included bacteriophage-mediated detection and non-Ab based protein-protein interactions.

Linking procedures are frequently used to attach sensing/detection molecules to the membranes. Covalent bonding is often preferable as it strongly secures the detection molecules to the surface, preventing them from being washed off. The most common covalent crosslinker used was glutaraldehyde. EDC and Sulfo-NHS were also commonly used for covalent crosslinking. Silanes, which bind covalently to a variety of surfaces, were used to either directly link molecules to membrane surfaces or indirectly through a crosslinker like glutaraldehyde. Simple adsorption to the membrane surface without a linker was also employed, particularly for prefunctionalized membranes. Streptavidin-biotin binding may be used to augment this process by orienting the sensing molecule being linked to the surface. As an alternative, electroporation has also been employed to attach molecular probes.

Electrical and optical transduction methods were most commonly used to convert biological sensing into a readable output. In many cases, the hybridization of nucleic acids or protein binding sufficiently changed the electrical properties of the membranes (such as resistance, voltage, current and impedance) that they could be observed via simple electrodes. In some cases electrical current was generated through enzymatic or other chemical reactions. In other approaches, the change in electrical current in porous membranes due to nucleic acid or

protein binding in the pores was recorded. Some bacteria produce proteins which create pores in membranes.

In turn, optical transduction methods can be categorized based on type of output, including color changes, light emission, and spectroscopic/interferometric approaches. Colour change was achieved in a number of ways, including dye-containing liposomes linked to nucleic acid tags, Abs conjugated to gold and carbon nanoparticles, several HRP-catalyzed and other chemical reactions, and change of colour due to protein interaction with liposomes. Some similar methods were employed for transduction through photon emission.

Other transduction methods involved mass sensing through leaky surface acoustic waves, piezoelectric effects, magnetic readout of Abs conjugated to magnetic beads, as well as oxygen measurements of the cellular respiration of living bacterial cells.

The main goal of a pathogen biosensor is to specifically detect as few live bacteria or infectious virus particles in as large a volume as possible. Viruses and bacteria are mainly detected as whole units, through their structural proteins, through the proteins or other materials they produce, or through their DNA or RNA sequences. For certain proteins, such as those found inside the pathogen, and for DNA or RNA sequences, this may involve additional processing to break up the pathogen and release the DNA, RNA or protein for detected. Unfortunately, it can be very difficult to compare the effectiveness of nucleic acid sensors with protein sensors and whole virus or bacterial sensors. A whole virus or bacterium naturally has a much greater mass than a protein, and a protein generally has a greater mass than a small strand of DNA or RNA. Therefore, nucleic acid detection methods generally need to have a lower mass/volume detection limit than protein detection methods or whole pathogen detection methods.

2.4. Interferometric measurement technique

In physics, interference refers to the superposition of one or more waves. Interferometry is based on this wave superposition and can be used to measure various properties. Generally, electromagnetic waves are used to perform these measurements. Among many other applications, interferometry can be used for surface topographical measurements, length measurements, vibration measurements, rotation sensing, temperature measurements, surface structure analysis, velocity measurements, wavelength measurements, and more.[161]

A very common setup for optical interferometric measurements is the Michelson interferometer. Light from a coherent beam source passes through a beam splitter, such as a partially reflective mirror. The phase difference due to the different path length or refractive index then creates an interference pattern when the beams recombine, which is apparent when the combined beam arrives at the detector.

The Fabry-Perot interferometer is another common type of interferometer. It consists of two mirrors with very high reflectance or a transparent plate with two reflecting surfaces. Light enters one of the two highly reflecting surfaces. The majority of the light is then reflected back and forth between the two highly reflecting surfaces while some of the light is transmitted. The transmitted light creates a high-resolution circular interference pattern.

In the experiments presented in chapters 3-5, membrane resonators were attached to 1 cm x 1 cm silicon chips. The chip was then attached to a piezoelectric disc via carbon tape and placed in a vacuum chamber. A 650 nm laser diode was then aligned with the resonator surface through a beam splitter and 50 x magnification 0.45 NA lens. The beam travelling back from the membrane again passed through the splitter and travelled to the detector. The detector converts light intensity into an electrical signal output which is AC (alternating current)-coupled. This means that the DC (direct current) component of the signal was filtered out and only the AC component reached the signal analyzer. The chip was vibrated by the piezoelectric disc according to frequency output from the signal analyzer. The signal analyzer scans across a range of signals. If the scan does not include a resonance frequency of the membrane, the membrane does not deflect significantly and the reflected light intensity is constant. This means that there is no change in the amplitude of the detector output.

If the scan includes a resonance frequency, the membrane begins to deflect with much greater amplitude when the resonance frequency is approached. This may result in a combination of effects. The dimensions of the cavity formed by the membrane and the silicon chip it is attached to changes, the thickness of the membrane may be altered, and the shape of the membrane changes. The membrane chips were mounted on a reflective silicon surface, and therefore form a Fabry-Perot cavity with a width of 300 or 550 μm, depending on the width of the silicon wafer. Furthermore, when the membrane deforms, the changing angle of the surface may reflect light away from the path that reaches the detector. Therefore, the resultant interference pattern is likely a combination of the Michelson and Fabry-Perot interferometer

effects. Fundamentally however, what is important is the change in light intensity over time because this is what is being shown by the signal analyzer. A schematic of the experimental setup is shown in figure 2.12.

The resonance frequency of the membranes is dependent on the mass of the membrane. When molecules bind to a membrane resonator, the total mass of the membrane increases, thus decreasing the resonance frequency of the membrane resonator. Mass measurements can therefore be performed by measuring the resonance frequency before and after the application of mass to the membrane surface. With proper functionalization of the membrane surface, this process can be applied to biosensor applications. This process is described in detail in chapter 5. A schematic depiction of the process is shown in Figure 2.13. The resonance frequency of the membrane was measured first (Figure 2.13a). It was measured a second time following the addition of the material required to specifically detect the biological material (Figure 2.13b). Finally, it was measured for the third time following the capture of the biological material of interest (Figure 2.13c). In each case the decrease in the resonance frequency is related to the increase in mass on the membrane surface.

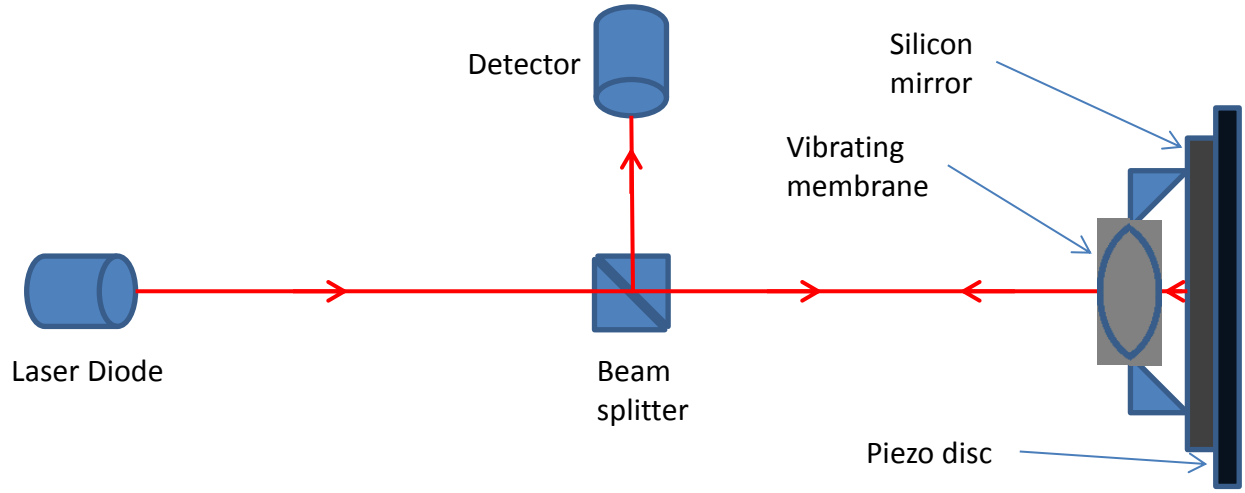

Figure 2.12: An illustration of the interferometry setup.

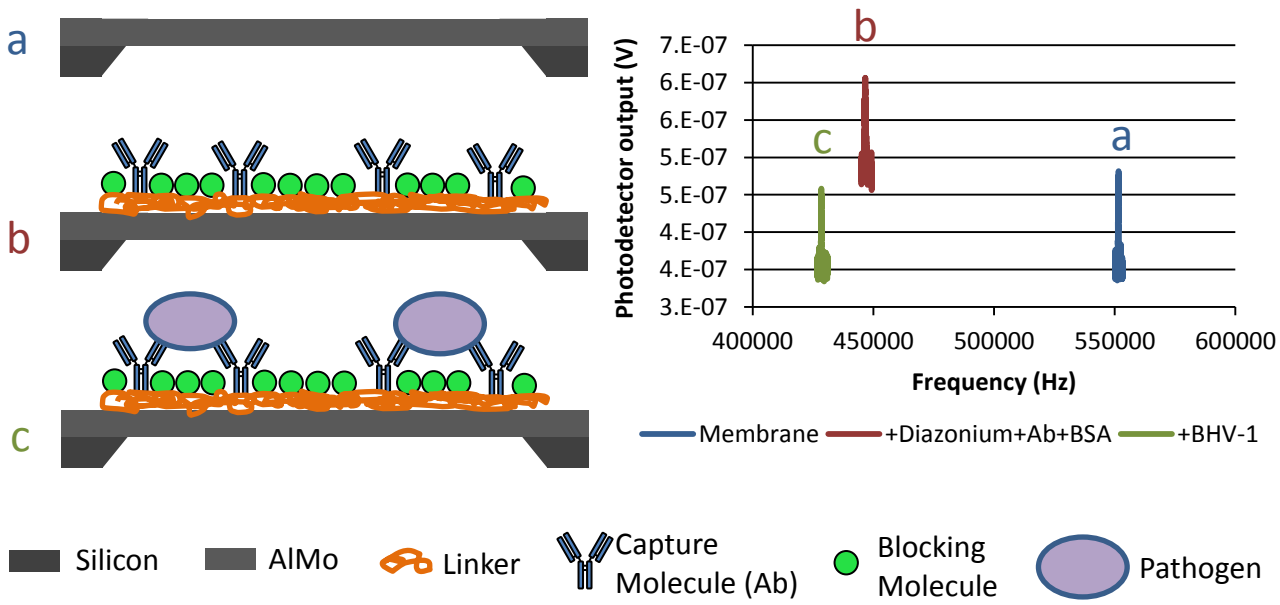

Figure 2.13: An illustration of resonance frequency changes with added mass. Side-view schematic depictions are shown on the left, while the associated measured resonance frequency shift is shown on the right. The resonance frequency peaks are data that were recorded for the functionalization shown in the schematic on the left. a) resonance frequency of the bare membrane, b) resonance frequency of the membrane with added linking chemistry, capture molecule (Ab) and blocking molecule (BSA), and c) the resonance frequency following the capture of the pathogen BHV-1 by the functionalized membranes.

3. Membrane Fabrication and Characterization

3.1. Introduction

Micro- and nanomechanical structures such as cantilevers, paddle oscillators, beams and membranes have received sustained attention for a wide range of applications including sensing, energy harvesting, telecommunications, and information processing. Membranes have specifically been employed in devices such as bio- and chemical[59,60,162], tactile[163,164] and pressure[165] sensors; actuators[166]; optical devices[167]; plasmonic structures[168], fuel cells[169]; sorting of biomolecules[170]; supercapacitors[171], lithium ion storage batteries[172], capacitive micro-machined ultrasonic transducers (CMUTs)[173], and acoustic energy harvesters[174]. Use of thinner membranes leads to appreciable performance gains in most of these applications. For instance, thinner membranes increase stress and pressure sensor sensitivity; the energy storage density of capacitors and batteries; and the efficiency of energy harvesters. To that end, nanoscopically thin membranes have recently been reported in materials such as SiN[64], graphene[175], and (Cr or Mo)-Si-O[176]. Some devices, such as CMUTs and energy harvesters, also require the integration of conductive materials in addition to structural layers. One approach to achieve thinner devices would be to replace the insulating structural and conductive metal layers with a single conductive membrane that serves both as structural layer and electrode.

There have been several reports of polymer-based conductive nanomembranes with embedded carbon nanotubes[40] and carbon nanotube sheets[171]. These membranes are highly flexible with low Young's Modulus and low tensile strength. Their electrical resistivity's were 19 μΩ-m for 66 nm thick membranes[171] and 95 μΩ-m for 26 nm thick membranes[40]. These materials are, however, somewhat incompatible with microfabrication processes, particularly

those requiring higher deposition temperatures. Furthermore, they have relatively low mechanical strength as compared to common structural materials like silicon or SiN.

Carbon nanosheets are promising alternatives as conductive structural layers. These nanomaterials require annealing at temperatures as high as 1200 K to achieve low resistivity.[177] Subsequent high temperature processing is thus unlikely to cause problems. The tensile strength of carbon nanosheets has been reported as 430~700 MPa, which is substantially greater than that of polymer-based nanomembranes.[178] They also have a minimum resistivity of roughly 100 μΩ-m[177], which is comparable to those of the polymer-based membranes discussed above. Furthermore, this resistivity can also be reduced by stacking multiple carbon nanosheets, yielding a resistivity of 20 μΩ-m.[179]

Alternatively, novel co-sputtered metal nanocomposites optimized for the fabrication of micromechanical devices have recently been reported.[1,2,25,180] These nanocomposites feature grain size as low as a few nanometers as well as residual stresses substantially lower than pure metals.[180] These materials also offer intrinsic tunability of their affinity to target chemisorbed species through control of their atomic composition.[25] More specifically, a metal nanocomposite composed of 68 at. % Al and 32 at. % Mo has previously been reported.[1,2] The high strength and low surface roughness of the material permits the fabrication of very thin structures including cantilevers as thin as 4.3 nm. The material has a resistivity of $\rho = 4.5$ μΩ-m[1], and Young's modulus values of 147 GPa[2] and 112 GPa[1] were determined via cantilever resonance while a Young's modulus values of 120 GPa[1] was determined via nanoindentation. The material thus has lower resistivity than those used in the fabrication of conductive nanomembranes[2,40,179] and potentially a higher tensile strength given that the small grain size usually leads to Hall-Petch strengthening.[181,182] Furthermore, membranes fabricated from such metal nanocomposites would be compatible with subsequent high temperature processes.

In this article is reported the first successful realization and characterization of ultra-thin membranes fabricated from such metal nanocomposites. The density, Young's modulus, hardness and resistivity of the nanocomposite material were further assessed. Furthermore, the tensile strength, resonance frequencies and intrinsic stress of the membranes were determined. These results indicate that these nanocomposite membranes offer resilience comparable to SiN membranes of similar thickness while retaining the high electrical conductivity of metals.

Finally, methods for tuning the intrinsic stress of the nanocomposite material are presented. Such features would allow the design of devices featuring ultra-thin and tunable conductive membranes in applications such as sensors, energy harvesters, and filtering. For mass sensors, ultrathin membranes may lead to reduced device mass, and therefore increased sensitivity. [1] Similarly, for energy harvesters, ultrathin devices may lead to increased deflection of the devices, thus potentially increasing energy generation. Furthermore, tuning the intrinsic stress of very thin devices can be used to tune the resonance frequency of those devices. This can be useful for matching the resonance frequency of an energy harvesting device to the source frequency which can maximize power output.[4] Additionally, resonance-based mass sensors may be limited by the instrumentation used to detect the resonance frequency. For example, the spectrum analyzer used for the resonance measurements discussed herein cannot resolve frequencies with a separation less than 1 kHz. As the intrinsic stress of stress-dominated devices such as ultrathin membranes is increased, however, the resonance frequency shift of a given mass increases. This thus means that a smaller change in mass can reach the detection limit of the spectrum analyzer (in this case 1 kHz), thus increasing the overall sensitivity of the sensor.

3.2. Materials and Methods

Double-sided polished <100> boron doped Si wafers were cleaned in a 3:1 v/v 86% sulfuric acid: 30% hydrogen peroxide piranha solution, washed in water and dried in a spin rinse drier. LPCVD was used to deposit roughly 200 nm of silicon-rich low-stress SiN on both sides of the wafers. A silanization oven (Yield Engineering Systems) was used to deposit hexamethyldisilazane onto the wafer to promote adhesion of the photoresist. HPR 504 photoresist (Fujifilm) was spun onto the wafer for 10 s at 500 rpm and 40 s at 4000 rpm using a photoresist spinner (Solitec). The photoresist then underwent a 90 s softbake at 115°C using vacuum hotplate (Solitec). The wafers were allowed to rehydrate for 15 min before being exposed to a dose of 180 mJ/cm^2. They were then placed in Microposit 354 developer for 20 s, washed in water and dried with a nitrogen gun.

Windows were etched into the SiN on the backside of the silicon wafers using a reactive ion etch (RIE) system (Phantom, Trion Technology). The etch pressure was 150 mTorr, the gas flow rates were 45 standard cubic centimeter per minute (sccm) CF_4 and 5 sccm O_2. The etch

power was 125 W and the etch time was 180 s. The wafers were washed sequentially in acetone, IPA and water to remove the remaining photoresist. Subsequently, the cleaned wafers were dried in a spin rinse drier. A through etch was performed using 25% v/v KOH in water at 85°C to create released SiN membranes, and the wafers were washed 5x in deionized water and dried with a nitrogen gun. A planar magnetron sputter system with 3" targets was used to co-sputter aluminum and molybdenum onto the SiN membranes with 32 at. % molybdenum and 68 at. % aluminum with a base pressure of 1 μTorr, aluminum sputtering power of 300 W, and argon sputtering pressure of 7.0 mTorr. A more precise RIE system from Surface Technology Systems was used to precisely etch away the SiN beneath the Aluminum-Molybdenum (AlMo) membranes. The process flow is shown in Figure 3.1.

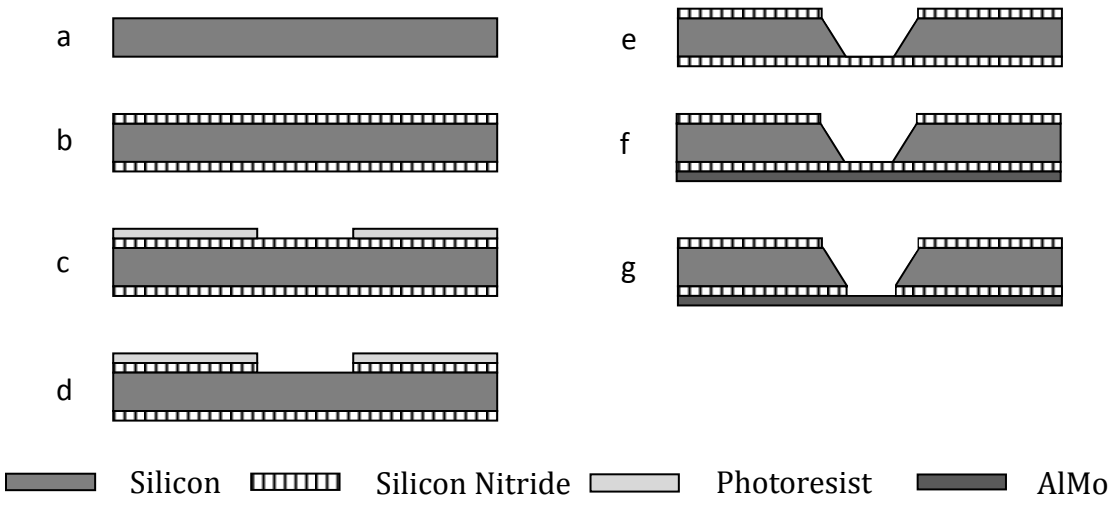

Figure 3.1: Process flow for AlMo membrane fabrication. a) Clean silicon, b) LPCVD SiN deposition, c) photoresist spin-on and optical lithography, d) RIE to open windows in the SiN, e) KOH silicon through etch, f) deposition of AlMo, g) RIE to remove the SiN from the membranes.

AlMo membranes with five different widths and six different thicknesses were tested in order to quantify the physical properties of the membranes. More specifically, five 180±10 nm thick AlMo membranes with widths of 1130±20, 600±10, 340±10, 180±10 and 130±10 nm and six 630±20 nm wide AlMo membranes with thicknesses of 371±3, 284±6, 183±4, 97±4, 48±3, and 28±3 nm were examined. The mechanical properties of these membranes were compared to

those of three 240±5 nm thick silicon-rich SiN membranes which were 1110±20, 590±10 and 330±10 nm wide, respectively. The electrical properties were compared with those of three conductive nanomembranes reported in the literature.[2,40,179]

To evaluate the density of the AlMo thin films, the mass of a wafer was recorded before and after AlMo was sputtered onto it. A milligram scale (Acculab VIC-303) was used to determine the mass of the wafer. The scale had a sensitivity of ±0.001 g. The thickness was determined using a stylus profilometer (Tencor Alphastep 250). The thickness of the AlMo layer was used to determine the added volume. This was then used in conjunction with the change in mass to determine the density of the thin film.

Bulge testing was also used to determine certain physical properties of a membrane material based on its dimensions and deflection at its center. For a rectangular membrane, the pressure P applied across it will result in its bulging as per the following relationship:

$$P = c_1(a,b)\frac{t}{a^2}\sigma_0 h + c_2(a,b,\nu)\frac{t}{a^4}\frac{E}{1-\nu}h^3 \quad (1)$$

where t is the thickness of the membrane, a is the half-width of the shorter side of the rectangular membrane, σ_0 is the intrinsic stress of the membrane, h is the deflection at the center of the membrane, and E is Young's Modulus and ν is Poisson's ratio.[183-187] For a square membrane with a given Poisson's ratio various values for c_1 and c_2 have been proposed. It has been reported[186,188] that coefficients of c_1 = 3.4 and c_2 = 1.37(1.075-0.292ν) fitted experimental data best for square membranes. By plotting P vs. h and fitting a third-order polynomial, one can extract the intrinsic stress from the first order term and Young's modulus from the third order term:

$$P = Ah + Bh^3 \quad (2)$$

where $A = 3.4\frac{t}{a^2}\sigma_0$ and $B = 1.37(1.075 - 0.292\nu)\frac{t}{a^4}\frac{E}{1-\nu}$.

A pressure chamber was custom-designed to perform such bulge/burst measurements. The 3x4x5 cm hollow aluminum chamber was constructed with three ports: one for a nitrogen intake line, one for a pressure gauge, and one to provide the differential pressure across the membrane. Three pressure sensors were used to cover the wide range of pressure values required for the burst pressure measurements. The 0-35 kPa range was covered by the Terranova Model 906A convection gauge controller and a Granville- Phillips 275 convectron gauge with resolution of 5 Torr. The 35-305 kPa range was covered by a 0-30 PSI pressure gauge from

Swagelok with an accuracy of ±1% of the span. The 305-500 kPa pressure range was covered by a 0-160 PSI pressure gauge from Topring with accuracy of ±2% of the span. The chamber was fixed to a thin aluminum base to hold it in place. The membranes were sealed between a nitrile 20 duro shore o-ring with an inner diameter of 1.5 mm set into the measurement chamber, and a 2x2x0.4 cm spring-loaded aluminum top plate. Kapton tape was placed around the edges of the chips to prevent damage to the devices. A pressure regulator was used to gradually raise the pressure difference across the membrane, and the deflection of the membranes was measured using a Zygo optical profilometer.

Nanoindentation of the AlMo thin film was performed with a Hysitron TI900 TriboIndenter using a Berkovich tip. The calibration procedure was followed as outlined in the instrument's user manual.[188] The indentations on the AlMo surface were performed next to the membranes which were ruptured during the burst testing. As recommended by Hysitron, the indents were performed to a depth of 1/3 the membrane thickness to avoid effects from the material below the membranes. The loading and unloading process was trapezoidal with a 5 s loading ramp from zero μN to the maximum load, 5 s at the maximum load and a 5 s unloading ramp from the maximum load to zero μN. The indents were performed in a square pattern of 16 indents with separation of 50 μm between the indents. The maximum load within each indent pattern was varied from 900 μN on the top left to 1100 μN on the bottom right. Triboscan version 8.1.1 software was used to determine the reduced modulus and hardness of the AlMo and SiN thin films. The thermal drift rate of the indenter was less than 0.05 nm/s.[188]

An optical interferometric technique was used to measure the resonance frequencies of the membranes.[6,189-191] The membrane chips were mounted on a piezoelectric disk and placed in a vacuum chamber, which was evacuated to 0.5 ± 0.3 mTorr. The output from a Hewlett Packard ESA-L1500A spectrum analyzer was used to drive the piezoelectric disk. The beam from a 650 nm wavelength laser diode was directed through a beam splitter and focused on the center of the membrane using a 0.45 NA microscope objective. The reflection from the resonating membrane generated an interference pattern which was detected by a New Focus 1601 AC-coupled photodetector. The output from the photodetector was then read by the spectrum analyzer.

It was not convenient to measure the resistivity of the membranes directly because contact would cause them to rupture. Alternatively, the sheet resistivity of the AlMo thin film located near the structures was measured using a Signatone four-point probe. The measurement

was performed on 4-5 locations for each film thickness. While the same probe force was employed in all measurements reported here, slight variations of the probe force did not noticeably affect the conductivity measured. The thickness of the thin films was determined by a Tencor Alphastep IQ profilometer.

To determine the effect of deposition pressure on the intrinsic stress and resistivity of the AlMo material, the deposition pressure was varied from 7 mTorr to 3 mTorr, while the thickness and the at. % ratio of the AlMo thin film was held constant. A Flexus wafer stress measurement system was used to determine the intrinsic stress of the thin films. The Flexus system was also used to determine the effect of thermal annealing on the intrinsic stress. This was performed by heating the 3 mTorr and 7 mTorr wafers inside the system while recording the intrinsic stress of the thin film at strategic intervals.

3.3. Results and Discussion

One of the advantages of the AlMo nanocomposite material is the small grain size of the molybdenum embedded in the aluminum-rich amorphous matrix. Such feature allows the realization of ultrathin released structures.[2,15] Scanning electron microscope (SEM) images of the membranes are shown in Figure 3.2, with an individual membrane shown in 2a and the nanostructure of the AlMo shown in 2b. The images were taken using a high resolution SEM (Hitachi S4800). The mass of a 4" silicon wafer was determined before and after the deposition of a 430 nm ±5% thick layer of AlMo. By dividing the volume by the change in mass, the density of the films was determined to be 5000±550 kg/m^3, in agreement with a rule of mixture previously employed for such assessment.[2] A value of $\nu = 0.33$, common for aluminum alloys[192], was employed for the purpose of fitting experimental data to Equation 2.

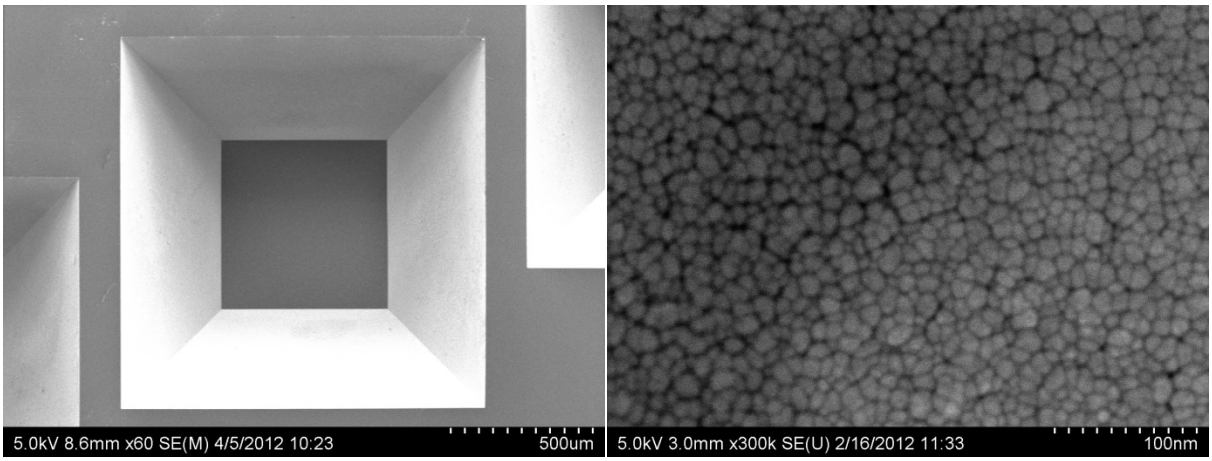

(a) (b)

Figure 3.2: SEM images AlMo membranes. a) an individual membrane and b) a high resolution SEM image of an AlMo thin film showing its nanoscale structure.

Previously reported values of Young's modulus were determined via cantilever resonance and nanoindentation. Values of 147 GPa[2] and 112 GPa[1] were determined via cantilever resonance while a value of 120 GPa[1] was determined via nanoindentation. In the current work, a reduced modulus of 157±17 GPa was determined by indenting, which relates to a Young's Modulus of 164±26 GPa, in rough agreement with the previous value of 147 GPa. In turn, an average Young's modulus value of E = 127±21 GPa was determined from the bulge testing data, which is in agreement within error with all the previous results. As such, this value was used in subsequent calculations. The Young's moduli as determined by the bulge test are listed in Table 1. The error for each calculated value was evaluated using differential error propagation. For comparative purpose, a similar bulge analysis was performed on 3 silicon-rich SiN membranes (bottom entries of Table 1). In this case, a Poisson's ratio of $\nu = 0.27$ was employed.[193] This resulted in a Young's Modulus of 287±54 GPa and agrees within error with the average of 232±28 GPa published previously[194]. The variability in the Young's moduli obtained for the different AlMo membranes (Table 1) is likely related to small variations in the ratios of Al and Mo obtained from deposition run to deposition run, which in turn may lead to large variations in the Young's modulus of the composite. Finally, the hardness of both the AlMo and SiN thin films was also determined from the indentation data. The hardness of the SiN was 23.6±2.0 GPa and the hardness of the AlMo was 6.57±0.37 GPa, which agrees within error with the 6.3 GPa hardness determined previously.[1]

The resonance frequency (in rad/s) of a rectangular membrane is given by:

$$\omega_{mn} = \sqrt{\frac{\sigma_0}{\rho}\left[\left(\frac{n\pi}{l}\right)^2 + \left(\frac{m\pi}{w}\right)^2\right]} \quad (3)$$

where σ_0 is the intrinsic stress, ρ is the density, n and m are natural numbers, l is its length and w is its width.[195,196] For a square membrane $l = w$, and for the fundamental resonance frequency (f_r) in Hz, $n = m = 1$, the intrinsic stress (σ_0) is thus be given by:

$$\sigma_0 = 2{f_r}^2 w^2 \rho \quad (4)$$

Equations (3, 4) are valid when the effects of Young's modulus and Poisson ratio on the resonance frequency are negligible compared to that of the intrinsic stress. Finite element analysis was again employed to verify such assumption. These finite element simulations employed the Poisson's ratio and average Young's modulus reported above in order to extract the tensile stress (σ_0) from the resonance frequencies observed experimentally.

The FEA model used was relatively straightforward. A single rectangular cuboid with fixed boundary conditions on four sides was used to model the membranes. Due to the high width to thickness aspect ratio, a rectangular cuboid swept mesh was used to ensure a sufficient number of elements along the membrane thickness to obtain reasonable accuracy. The resonance frequency solver was used to determine the resonance frequency of the membranes. To find the intrinsic stress of the membranes, the intrinsic stress of the model was varied until the model resonance frequencies matched the experimentally observed resonance frequencies.

The experimental resonance frequencies are shown in Table 1. As expected from equation (4), the frequency decreased with width and was essentially unaffected by membrane thickness. The intrinsic stress of each membrane, as calculated from equation (1), equation (4), and FEA, is also shown in Table 1. The stress derived from the FEA and the analytical values calculated from equation (4) are nearly identical and agree within error, while all but two of the bulge test results agree with the other calculations within error. This strongly suggests that the membrane behavior is stress dominated. No trend was observed linking intrinsic stress to membrane geometry.

Table 3.1: The resonance frequency, intrinsic stress, Young's modulus (as determined by the bulge test) and the sputtering deposition time for each membrane. The first 5 AlMo membranes are listed by width and have a thickness of 180±10 nm, while the next 6 are listed by thickness (T) and have a width of 640±10nm.The SiN membranes are listed by width (W) and have a thickness of 240±5 nm.

Membrane Material	**Membrane Width (μm) /Membrane Thickness (nm)**	**Experimental Resonance Frequency (kHz)**	**Intrinsic Stress (MPa)**			**Young's Modulus (GPa)**	**Deposition Time**
			Equation (1)	**Equation (4)**	**Comsol FEA**		
AlMo	1130 ± 20 W	217.5 ± 0.5	600 ± 100	600 ± 90	590	120 ± 30	6 m 51 s
AlMo	600 ± 10 W	388 ± 2	530 ± 70	540 ± 80	527	115 ± 7	6 m 51 s
AlMo	340 ± 10 W	620 ± 10	430 ± 80	440 ± 90	427	128 ± 5	6 m 51 s
AlMo	180 ± 10 W	1125 ± 6	400 ± 100	400 ± 90	395	108 ± 5	6 m 51 s
AlMo	130 ± 10 W	1680 ± 30	500 ± 200	500 ± 100	492	100 ± 10	6 m 51 s
AlMo	371 ± 3 T	339 ± 5	460 ± 40	460 ± 80	444	120 ± 20	14 m 32 s
AlMo	284 ± 6 T	302 ± 3	360 ± 40	360 ± 60	352	100 ± 20	10 m 40 s
AlMo	183 ± 4 T	320 ± 4	470 ± 60	410 ± 70	399	120 ± 30	7 m 7 s
AlMo	97 ± 4 T	320 ± 3	560 ± 70	410 ± 60	392	150 ± 30	3 m 50 s
AlMo	48 ± 3 T	332 ± 2	550 ± 80	450 ± 70	435	200 ± 40	1 m 55 s
AlMo	28 ± 3 T	370 ± 20	600 ± 100	600 ± 100	555	150 ± 40	53 s
SiN	1110 ± 20 W	180.5 ± 0.8	380 ± 50	250 ± 40	234	300 ± 50	-
SiN	590 ± 10 W	340 ± 2	290 ± 40	250 ± 40	236	290 ± 50	-
SiN	330 ± 10 W	605 ± 4	280 ± 50	250 ± 40	232	280 ± 60	-

The pressure chamber employed to perform the bulge measurements was also used to assess the maximal pressure differential the membranes could sustain without bursting. This is useful to determine the fracture stress of the membranes, an important figure of merit for most applications. The burst pressures of the membranes are shown in Figure 3.3. The burst pressure increased as the membrane width decreased, and increased as the membrane thickness increased.

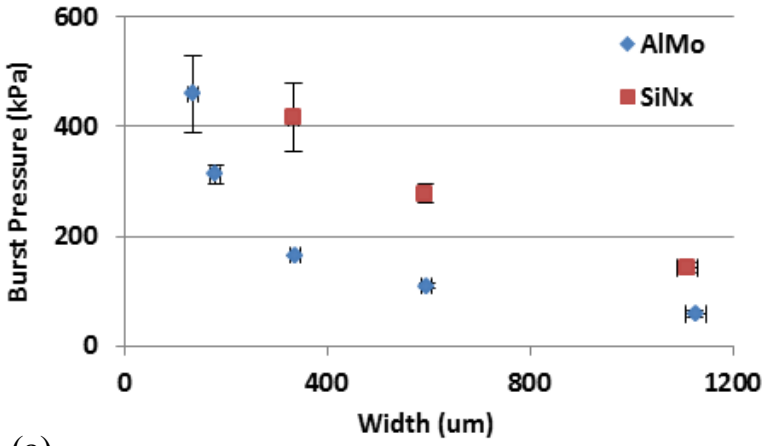

(a)

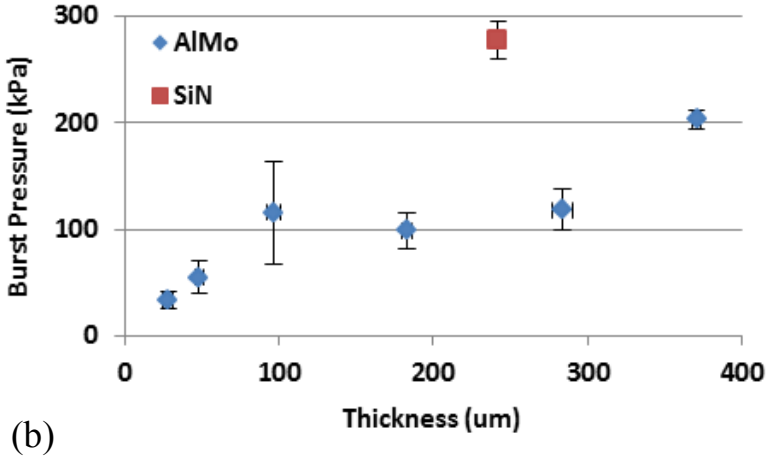

(b)

Figure 3.3: Burst pressure for membranes of different width and thickness. The AlMo and SiN membranes in (a) were 180 nm and 240 nm thick respectively while in (b) they are 630 nm and 590 nm wide respectively. The burst pressure represents the average of three measurements while the error bars represent one standard deviation.

FEA was used to determine the stress associated with these burst pressure values. In order to determine the fracture strength of the membranes, pressure was applied to one surface of the membrane, a parametric sweep of applied pressure was performed and the resultant maximum deflection was recorded. While the model was relatively accurate, there was an average error of 4-14% between the theoretical and experimental membrane deflection for the measured pressures. The fracture strength was determined from the FEA model by calculating the maximum stress in each membrane at the corresponding experimental burst pressure. For a square membrane this is located at the center of each side. The extracted fracture strengths for

each membrane are shown in Figure 3.4. The fracture strengths σ_f of the AlMo membranes varies from 1.5 to 2.5 GPa, while the fracture strengths σ_f of the SiN membranes varies from 3 to 3.5 GPa. These correspond to fracture strains of $\sigma_f/E \sim 1.3 - 1.5$ % for both AlMo and SiN. In comparison, micromechanical silicon have shown fracture strains in the $\sigma_f/E \sim 2.5 - 3$ % range, but the value is, however, as low as $\sigma_f/E \sim 0.4$ % for aluminum.[44] The AlMo membranes therefore show resilience comparable to SiN, with a fracture strain that is 3-4 times greater than pure aluminum. In comparison, conductive polymer membranes with mechanical strengths of $\sigma_f = 135 \pm 8$ MPa have been reported[171], corresponding to fracture strains of ~ 1 %, significantly lower than the AlMo membranes described here.

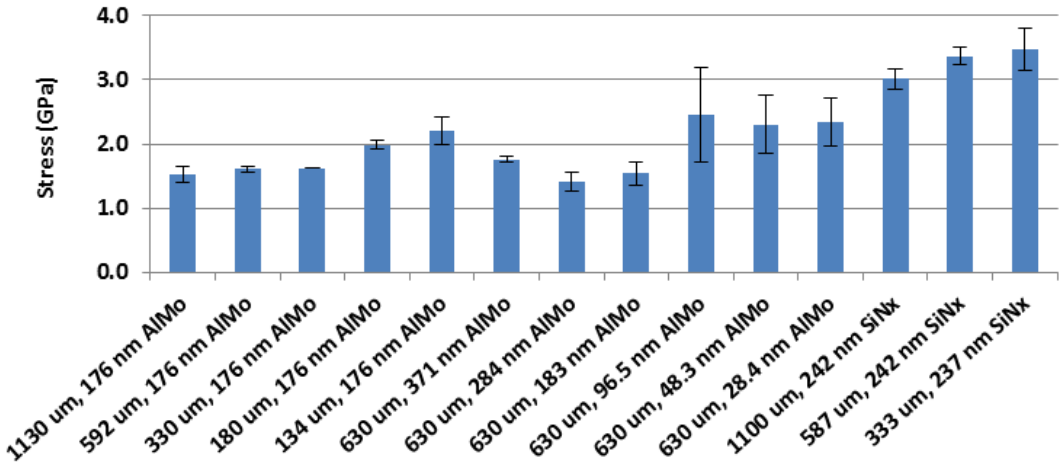

Figure 3.4: Fracture strength of the membranes at the center of a given side at the burst pressure. The error bars were determined by entering the error from Figure 3 into the Comsol model.

These results demonstrate that such metal nanocomposites have strong potential for the development of ultra-thin membranes in applications requiring both the resilience of SiN and the electrical conductivity associated with metals. In addition, these materials are compatible with high-temperature processes, a feature not offered by most polymeric materials.

Figure 3.5 shows the resistivity of the membranes as determined by four-point probe measurements. The sheet resistance and resistivity decreased as the membrane thickness increased, a trend that was also observed in other published results.[2,40,179] Liu and Ong also saw a similar effect on Co–Zn–O thin films.[197] The structure of these films is similar to the one of the AlMo films. Indeed, these materials feature Co-based nano-crystallites embedded in a (Zn,O)

amorphous matrix, as opposed to Mo nano-crystallites embedded in an Al-rich amorphous matrix. Liu and Ong suggest that such increase in resistivity with decreased film thickness may be caused by substrate-film interface effects.[197] Another possible origin is the effect of the native aluminum and molybdenum oxides becoming more important for very thin films. As the film thickness decreases, the oxides make up a greater percentage of the thin film, which may lead to an overall increase in the resistivity.

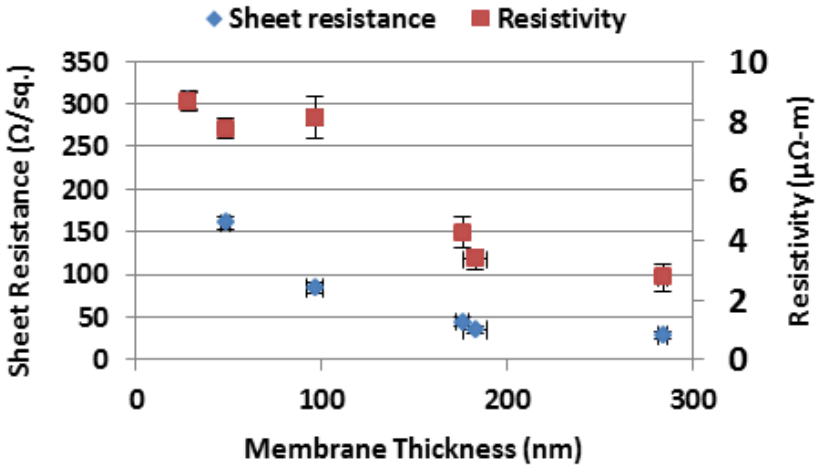

Figure 3.5: Change in sheet resistance and resistivity with membrane thickness.

As discussed, all previous AlMo membranes were fabricated with a 7 mTorr deposition pressure. In some applications lower tensile stress or even compressive stress membranes may be desirable. Therefore the tuning of the intrinsic stress of the AlMo thin films through changing the deposition pressure and thermal annealing was investigated. Figure 3.6 shows the tensile stress of films deposited under various conditions, as function of annealing temperature. The thin films in Figure 6a were 101±5 nm thick while the ones in Figure 3.6 were 300±20 nm thick. The intrinsic stress shifted from tensile to compressive as deposition pressure decreased. In turn, the resistivity of the films tended to decrease at lower depositions pressures. This trend could be explained by variations of numerous materials properties, such as density, local structure, and composition. Tensile stress is caused by increased scattering collisions at higher gas pressures, which lead to less energetic bombardment and looser packing of the thin film. The compressive stress at lower gas pressures is a result of fewer collisions which leads to reflected Ar molecules and neutralized target molecules peening the surface.[198] Gradually increasing the temperature of the films induced a temporary increase in the measured compressive stress or reduction in the

measured tensile stress, but on cooling the compressive stress transitioned to tensile stress or the tensile stress was increased. The change in intrinsic stress appears permanent as it did not change with a second annealing cycle.

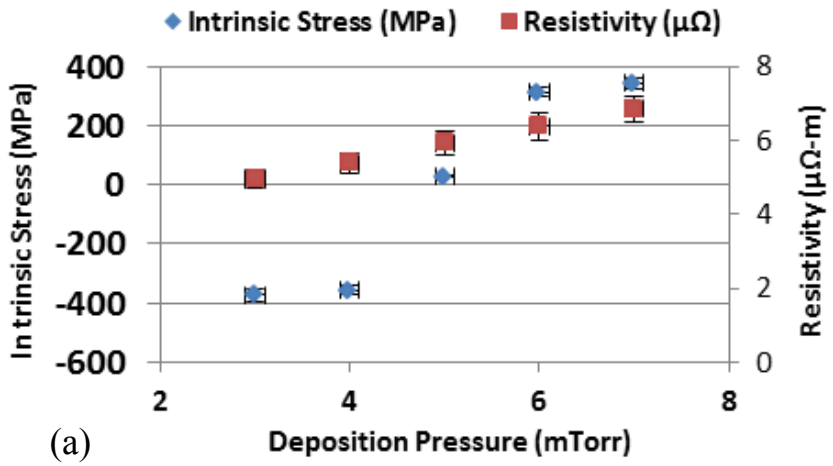

(a)

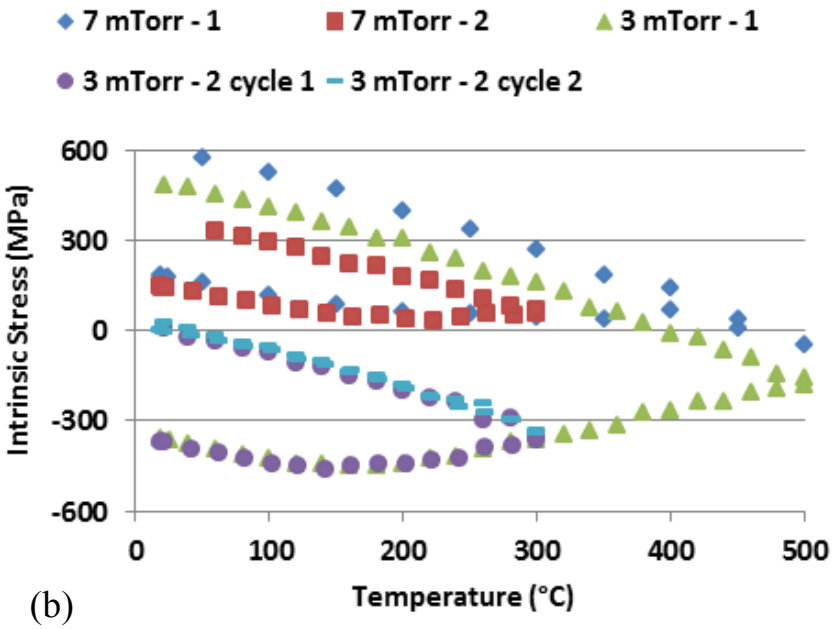

(b)

Figure 3.6: Stress tuning of AlMo thin films through changing deposition pressure.

3.4. Conclusions and Summary

AlMo membranes as thin as 28.4 nm were fabricated. The density of the membranes was determined to be 5000±550 kg/m^3. The Poisson's ratio and Young's Modulus were determined

to be 0.33±0.05 and 127±21 GPa respectively. The intrinsic stress of the membranes was determined by bulge testing, FEA and classical mechanics. The resonance frequencies of the membranes were determined through optical interferometry and were verified using FEA. The hardness of the AlMo was 6.57±0.37 GPa. The fracture strength of the AlMo and SiN membranes was determined as 1.89±0.45 GPa and 3.28±0.28 GPa, respectively, and the average resistivity of the AlMo membranes was 5.81±0.44 μΩ-m. The average fracture strength of the AlMo membranes is roughly 0.6 times that of the SiN membranes. Such features make this material attractive as a structural layer for membrane devices, inasmuch as offering resilience comparable to SiN and amenability to ultra-thin structures, while maintaining the conductivity of metals and compatibility with high-temperature processes. The combination of *all four* of these features is unavailable in SiN, silicon, pure metals, or conductive polymers. The metal nanocomposite membranes reported here could be useful in applications such as sensors or energy harvesters where the decreased thickness and increased conductivity of the material would increase overall performance.

4. Device Fabrication

Following the fabrication of membranes and characterization of the AlMo nanocomposite, several different structures were produced. Proof masses were fabricated on freestanding membranes. They can provide, among other applications, additional control of the resonance frequency of the membranes. Freestanding Archimedes spirals were fabricated for possible energy harvesting applications. While designed for energy harvesting, however, the spirals may also be suited to sensor applications similar to those that use deflection cantilevers. Nanometre scale cantilevers were fabricated for possible application as sensors. Finally, a technique for creating compressive stress membranes is presented.

4.1. Proof Masses on Membranes

From a micro- or nano-fabrication perspective, a proof mass is generally a large heavy structure attached to a membrane/plate/diaphragm, cantilever or other device. It may also be referred to as a mesa structure, because anisotropic etching often causes the mass to be shaped like a mesa. Proof masses are commonly used to adjust the properties of the device. For resonance measurements, they are frequently used to decrease the device resonance frequency. For physical sensors, proof masses can be employed as a means of attachment that does not damage a thin or fragile structure. Proof masses are of particular interest for pressure sensors.[199,200] In this context, a number of journal articles purely focused on modelling have been published.[201-203] They can also be used in other applications, such as a high-dose radiation sensor[204], force and deflection measurements[205], microvalves[206,207], accelerometers[208,209] and micropumps[210].

There are several convenient methods for the fabrication of devices with proof masses, but they each have disadvantages. As discussed previously, membranes are frequently fabricated via a through etch of the wafer. One simple method for fabricating a proof mass is to block a region in the center of the membrane from being etched by covering the region with SiN. A wet etch release process in a KOH or TMAH solution leads to the formation of a square or rectangular proof mass with the customary sloped sides of these techniques. One downside of

these types of proof masses is that the sharp vertices, especially from KOH etching, can create points of high stress, which may damage thin membranes. If a circular region in the center of the membrane region is protected by photoresist, it is possible to create proof masses with rounded edges through a DRIE. This is more difficult to achieve with thinner membranes, however, as there is little room for error if the membrane layer material is not a perfect chemical etch stop.

Common microfabrication deposition methods such as evaporation or sputtering are generally not ideal for large-scale deposition on the order of tens or hundreds of micrometers. Alternatively, a thick photoresist such as SU-8 may be utilized, but for applications that require resonance SU-8 may not be ideal. Comsol simulations were performed (results not shown) which showed that vibration of a structure with a relatively long SU-8 proof mass may lead to resonance within the proof mass itself.

The process presented here for the fabrication of proof masses on freestanding membranes employs Ni electrodeposition. It allows for the formation of relatively thick proof masses with rounded edges on thin membranes. The density of Ni is greater than that of Si or SU-8, which means that smaller structures are required to achieve an equivalent mass, decreasing the likelihood of undesirable resonance effects. It is also simpler to adjust the deposition thickness, and thus the mass of the proof mass, than when a silicon proof mass is used.

4.1.1. Materials and Methods

A mask was designed with circular openings that were 60% of the membrane width in diameter and located in the centers of the membranes. Since photoresists and Al are rapidly etched by the TMAH or KOH, it is not possible to simply fabricate the AlMo membranes and proof masses on the silicon wafer and then release the membranes. Several different methods were therefore examined for the fabrication of proof masses on the membranes.

The addition of greater than 1.4 wt. % Si to a TMAH solution has been shown to prevent etching of Al.[211] When this approach was implemented to release AlMo membranes it was not successful, however. The TMAH etched through the AlMo thin film in many locations. Some visible impurities from the Si powder were still present after 15 hr in the TMAH solution, however. This may have been a result of the fact that 99% pure silicon powder was used, which was not as pure as the silicon pieces described in the published article.[211] It is possible that the

impurities were deposited on the wafer surface during the etch process and that this caused etching to commence. Lower purity silicon powder was employed due to the prohibitive cost of silicon wafer pieces given the volume of the KOH bath and the extensive time that would have been required for them to dissolve in the TMAH solution.

Other alternatives that were investigated were coating the AlMo surface and proof masses with a protective layer during the release process and etching away the protective layer afterwards, or depositing the photoresist and proof mass on top of the released membranes. The protective coating process was implemented using PECVD nitride. LPCVD nitride was not used, because the very high deposition temperature required is incompatible with the melting point of Al which is 660°C. Instead, PECVD silicon nitride was deposited on a thin film of AlMo on a silicon wafer. Unfortunately, the PECVD was etched much more quickly than expected in the KOH solution, even given the expected increase in etch rate discussed previously. Because of this, all the AlMo was etched away. This may have been caused by an increase in pinhole defects and/or because the PECVD SiN deposited at the University of Alberta Nanofab contains carbon.

The fabrication of proof masses on released membranes was the last method to be implemented. Released AlMo membranes 300 nm thick were fabricated (section 3.2), but the SiN was not etched away from the backside. The equipment used during the proof mass fabrication process was identical to that described in section 3.2, aside from the electrodeposition setup. The membrane wafer was attached to a carrier wafer via Kapton tape during photolithography to decrease the probability of damage to the membranes. The photoresist used was AZ4620. The photoresist was applied to the wafer with a 10 s 500 rpm spread step and 25 s 2000 rpm spin step. A softbake at 100°C was performed for 90 s with the wafer floating on nitrogen and 60 s with the vacuum on. Due to the thickness of the photoresist, the wafer was left to rehydrate for 2 hr. Wafer alignment was performed, and the exposure dose was 730 mJ/cm^2. The wafer was developed in diluted AZ400K developer.

In order to ensure adhesion of the Ni to the membrane surface, a 10 nm thick Cr adhesion layer and a 100 nm thick Ni seed layer was sputtered onto the surface. Submersion in an acetone bath removed the photoresist and excess Ni and was followed by washes in IPA and water. The wafer was dried in a stream of nitrogen gas. A new layer of AZ4620 photoresist was deposited and patterned using the same procedure.

The Ni electrodeposition parameters were set to minimize the intrinsic stress of the deposited Ni. The bath volume was 7.55 L. The solution consisted of 44% v/v Ni sulfamate concentrate, 4% v/v nickel bromide concentrate, 30g/L boric acid, 1% v/v HN-5 wetting agent, and 2.5% JB-100 stress reducer. The remaining solution composition was DI water. The chemicals were obtained from Technic Inc. Water, Ni sulfamate and Ni Bromide were combined first, heated to 50°C and thoroughly mixed. The boric acid was added and the solution was again mixed thoroughly. The wetting agents and additives were then stirred into the solution. The temperature was set to 38^{o}C and the pH was set to 4.0 to minimize the intrinsic stress. An electrode was attached to the top and bottom of the membrane wafer, and an electric current of -0.25 A with initial voltage of -2.2 V was applied. Electrodeposition was allowed to proceed for 1 hr. The photoresist was then stripped away by washing in acetone, IPA and water, and the wafer was dried in a N_2 gas stream. The nitride was removed from the backsides of the membranes as described in section 3.2.

4.1.2. Results and Discussion

The electrodeposition process was successful. Proof masses were created on the surfaces of the membranes and the majority of the membranes were intact following the RIE of the backside SiN. Resonance measurements of eight square membranes with side length 276±4 μm were performed. SEM images of the proof masses are shown in Figure 4.1 and images from a Zygo optical profilometer are shown in Figure 4.2.

The masses of the Ni proof masses were calculated and a plot of resonance frequency vs. the mass of the proof mass is presented (Figure 4.3). As mentioned previously, proof masses can be used to adjust the resonance frequency of the resonating membranes. This can be useful for matching the resonance frequency of an energy harvesting device to the source frequency, which can considerably increase the deflection of the energy harvester, and therefore increase energy output. As such, a plot such as Figure 4.3 can be used to select the correct proof mass to match the desired frequency.

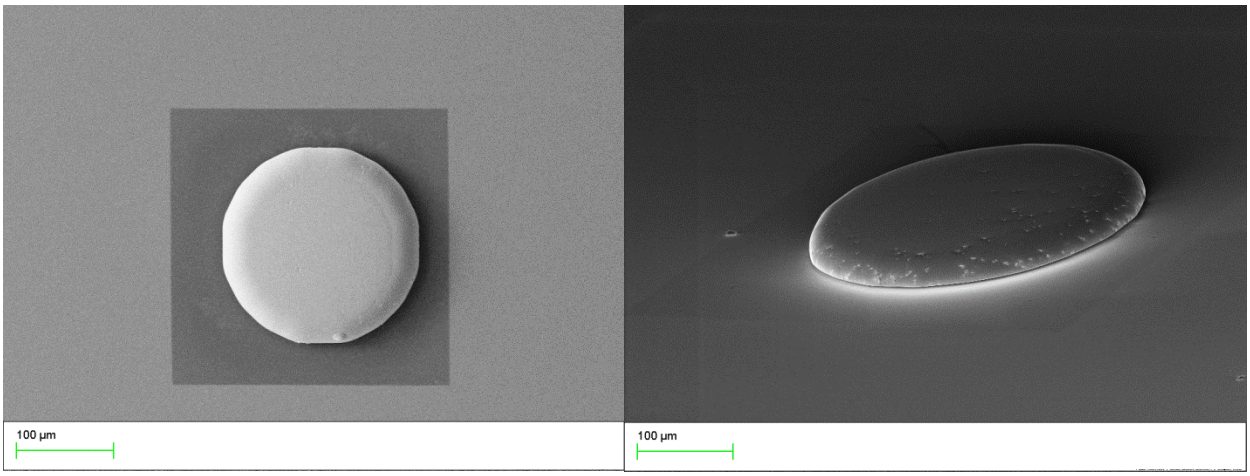

Figure 4.1: SEM images of two proof masses. The image on the right was recorded by tilting the SEM stage. In it the proof mass is observed to cause the membrane to deflect downwards as the stem of the mushroom shape of the proof mass is no longer visible.

The Ni electrodeposition of the proof masses was performed on intact Si wafers that cannot fit into the interferometry setup. For this reason, resonance measurements could not be performed beforehand, and therefore the intrinsic stress of the original membranes is unknown. The intrinsic stress observed for AlMo membranes was between 300 MPa and 700 MPa (Table 3.1), which for membranes with side length 276±4 µm would lead to an initial resonance frequency of between 619 kHz and 969 kHz. These frequencies are much greater than the less than 100 kHz resonance frequencies observed following the addition of the proof masses to the membranes (Figure 4.3), and are indicative of the substantial change in resonance frequency that can be implemented using proof masses.

An important observation concerning the electrodeposition process is that the mass of Ni that was deposited decreased as the distance from the electrodes increased. This was clear from both the decreasing diameter and height of the proof masses. For a full wafer with one electrode, the difference in height was roughly one order of magnitude (3-30 µm). Two electrodes were used in the presented results in order to reduce this effect, but the difference in deposition thickness was still significant. This effect was likely a result of the relatively large resistance of the AlMo thin film to current flow. A potential solution to this issue would be to perform electrodeposition on smaller substrates, thus reducing the distance between the electrode and the deposition location.

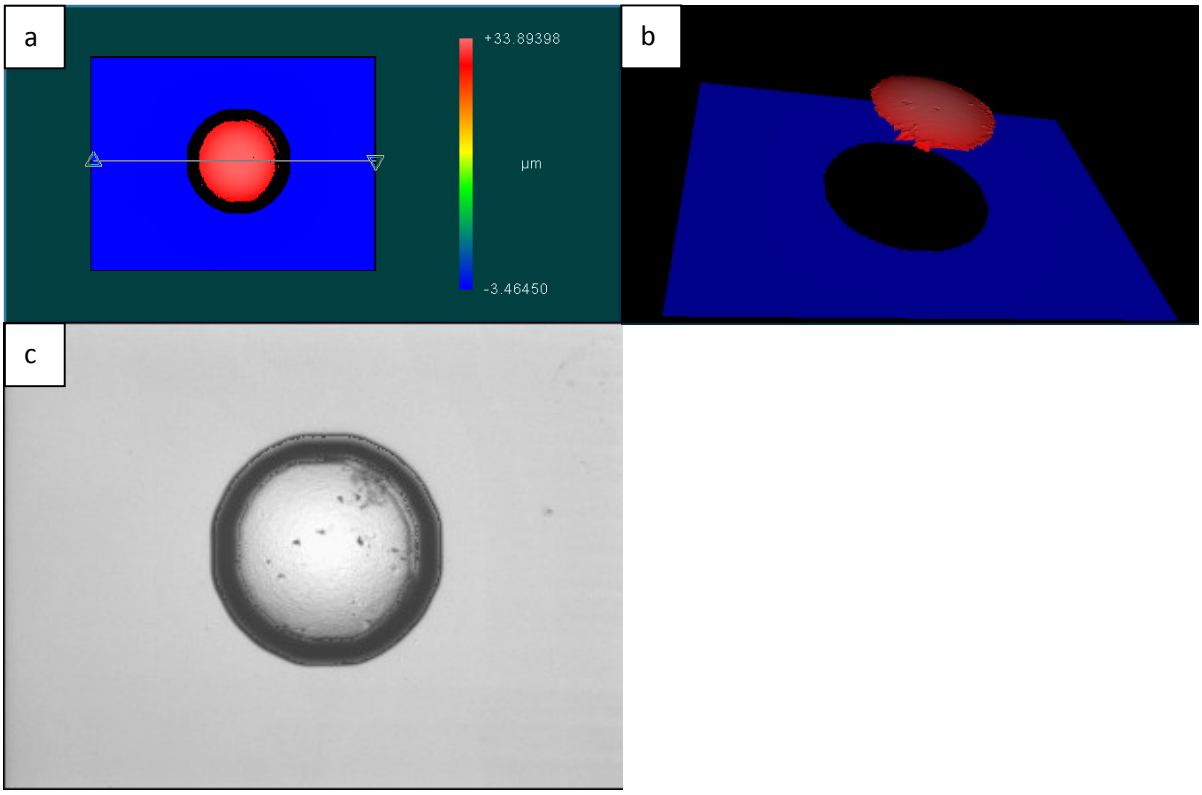

Figure 4.2: Optical profilometer images of a proof mass on a membrane. a) An image which shows the height of the proof mass. b) A partial three 3-D image of the same device in a). This was the extent to which the proof mass could be measured by the profilometer. c) An optical microscope image of the same proof mass.

A further result, which is evident from the profilometer images, is that the proof masses extended beyond the height of the photoresist. This caused mushroom shaped structures rather than cylindrical structures to be formed. Finally, it was observed that the proof masses were sufficiently massive that they caused substantial deflection of the membranes. For this reason the "stalk" region of the mushroom shape is not visible in the images in Figure 4.1.

Overall, the process was successful in reducing the resonance frequency of the membranes. Furthermore, the majority of devices fabricated remained intact following the removal of the SiN layer. This is in contrast to similar devices, which were fabricated using square silicon proof masses, the majority of which were damaged or broken by the proof masses.

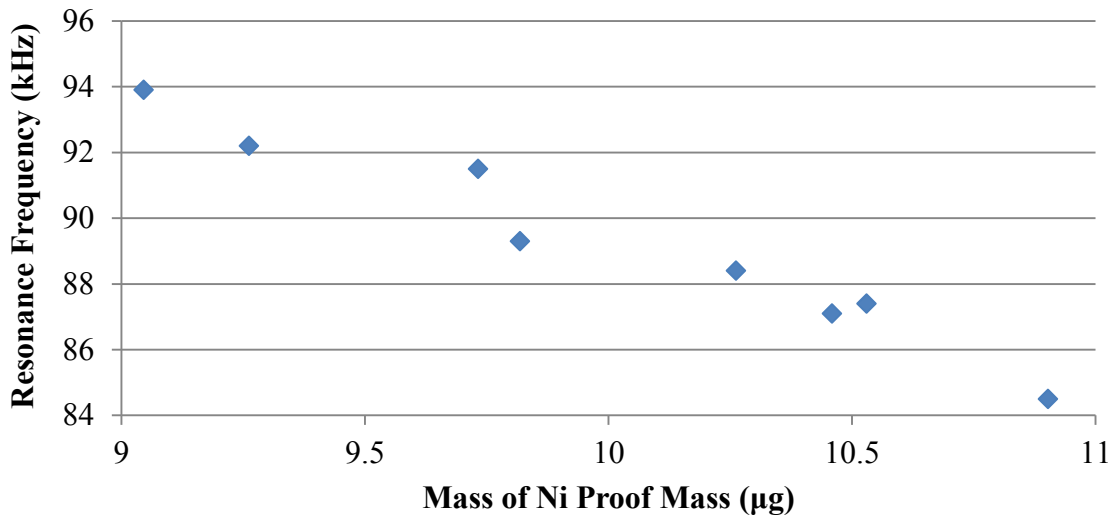

Figure 4.3: Experimental change in the resonance frequency of the membranes with added mass.

4.2. Archimedes Spirals

Spiral structures can be used for a variety of purposes. Examples of applications include antennas[212], energy harvesting[5], actuators[213], and motion and acceleration sensors[214]. Thin, strong and conductive materials such as AlMo present certain potential advantages for energy harvesting devices. Piezoelectric materials are generally very stiff, so consideration may be made to increase compliance of energy harvesters.[215] One example of this is the addition of proof masses such as those described in section 4.1.[215] Such proof masses are often implemented to reduce the resonance frequency of energy harvesters. Furthermore, energy harvesting devices are commonly composed of multiple layers. These may include an elastic layer, electrode layers and a piezoelectric layer.[216] The material properties of the AlMo nanocomposite make it possible to use it as both the elastic and electrode layers, which may make it possible to reduce the total thickness of the energy harvester. This would increase the compliance of the device, potentially increasing power generation. The primary goal of the devices that were fabricated was to replicate the electrode design of an intercardiac pacemaker[5] on the nanoscale in order to evaluate whether this improves performance. If successful, the energy harvesting could then potentially be amplified by arranging spirals into horizontal or vertical arrays.

4.2.1. Materials and Methods

The patterns for the Archimedes spirals were designed in autoCAD and imported into the Nanofab CAD mask design software. Three types of spirals were created: 2-arm Archimedes spirals, 3-arm Archimedes spirals and 10-arm Archimedes spirals. Different sizes of each type of spiral were included in the mask design in order to evaluate which dimensions would be the most effective.

Several methods were investigated for the fabrication of the Archimedes spirals. Two main pattern transfer approaches were employed: AlMo deposition followed by etching of the device layer and photoresist patterning and AlMo deposition followed by a lift-off process. Dry etching would be ideal for etching the device layer, but the common RIE gasses SF_6 and CF_4 etch Al very slowly, and O_2 plasma hardly etches either metal. Ion milling is a dry process that etches both Al and Mo. AlMo membranes 300 nm thick were fabricated as described in section 3.2, but the SiN was not immediately etched away. The 300 nm thickness membranes were selected because they were a standard thickness used for many of the membranes. The thickness could readily be altered for other applications. The wafer was attached to a carrier wafer as in section 4.1, and the photolithography process from section 3.2 was performed to transfer the spiral pattern to the membranes. Ion milling was then performed, which resulted in all the membranes to be broken, likely due to heating effects.

In the second approach, the previous process was repeated, but as an alternative to ion milling, wet etching was performed. Like dry etching, many chemical compositions are not suitable for etching both Al and Mo. KOH or H_2SO_4 rapidly etches Al but not Mo. A Mo etch solution such as 180 parts H_3PO_4:11 parts CH_3COOH:11 parts 70% HNO_3:150 parts H_2O_2 by volume etches Mo at a reasonable rate, but it etches Al 35 times more slowly and it etches photoresist substantially more quickly than the Al.[41] Dilute aqua regia (3 parts 37% HCl:1 part 70% HNO_3:2 parts H_2O) was found to etch both Al and Mo at a reasonable rate. The RIE from section 3.2 was performed to remove the SiN on the backside. The spirals sustained substantial damage during the release step (Figure 4.4), however, potentially due to the inversion of the spirals following the RIE of the SiN on the backside.

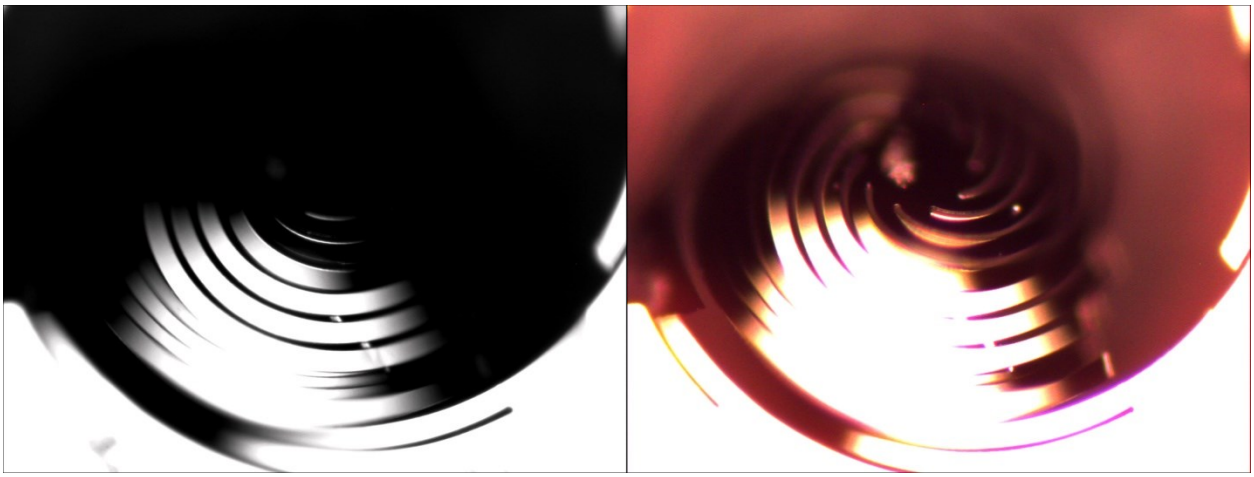

Figure 4.4: Optical microscope images of larger spirals following aqua regia etch and RIE of the backside SiN. The lack of focus is due to spirals bending down below the wafer surface.

The third method that was implemented was a photoresist lift-off process with AZ 5214 photoresist. The photoresist was deposited with a 10 s 500 rpm spread step and 40 s 4000 rpm spin step to form a 1.7 μm thick photoresist layer. The photoresist was soft-baked for 50 s at 90°C and exposed (18 mJ/cm^2). It was then baked for 2 min at 130°C and a flood exposure was performed (486 mJ/cm^2). The wafer was developed in MF CD 319 developer solution. Subsequently, a 300 nm thick layer of AlMo was sputtered onto the surface, and lift-off through sonication in acetone was performed. A Bosch DRIE was performed with an Oxford Estrales DRIE machine to etch deeply into the surface (Figure 4.5). The etch depth varied with opening width as is common for a DRIE. The membranes were released using XeF_2 gas. The chamber pressure was set to 150 mTorr with a 60 s expansion period to fill the chamber with gas and a 60 s etch period per cycle. In total 45 cycles were performed. Images of two of the released structures are shown in Figures 4.6 and 4.7.

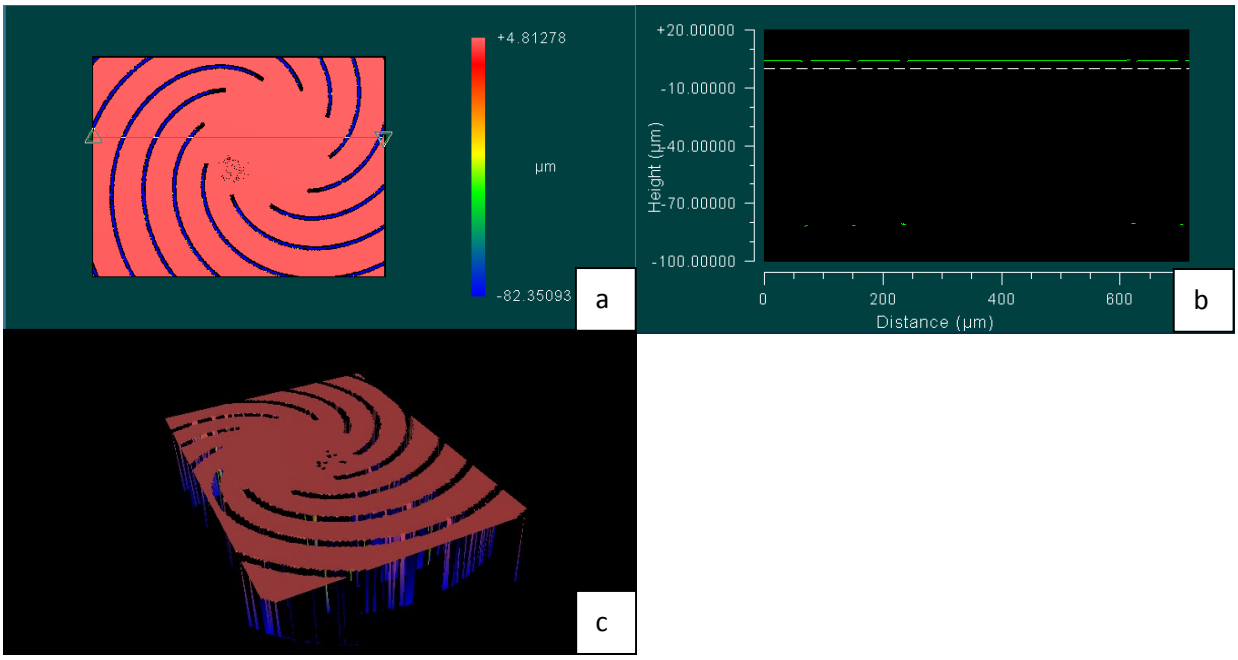

Figure 4.5: Optical profilometer images of a 10-arm Archimedes spiral following the DRIE. a) A depth profile of the DRIE. b) A graph of the depth profile indicated by the line between the triangles in a). c) A 3-D image of the Archimedes spiral.

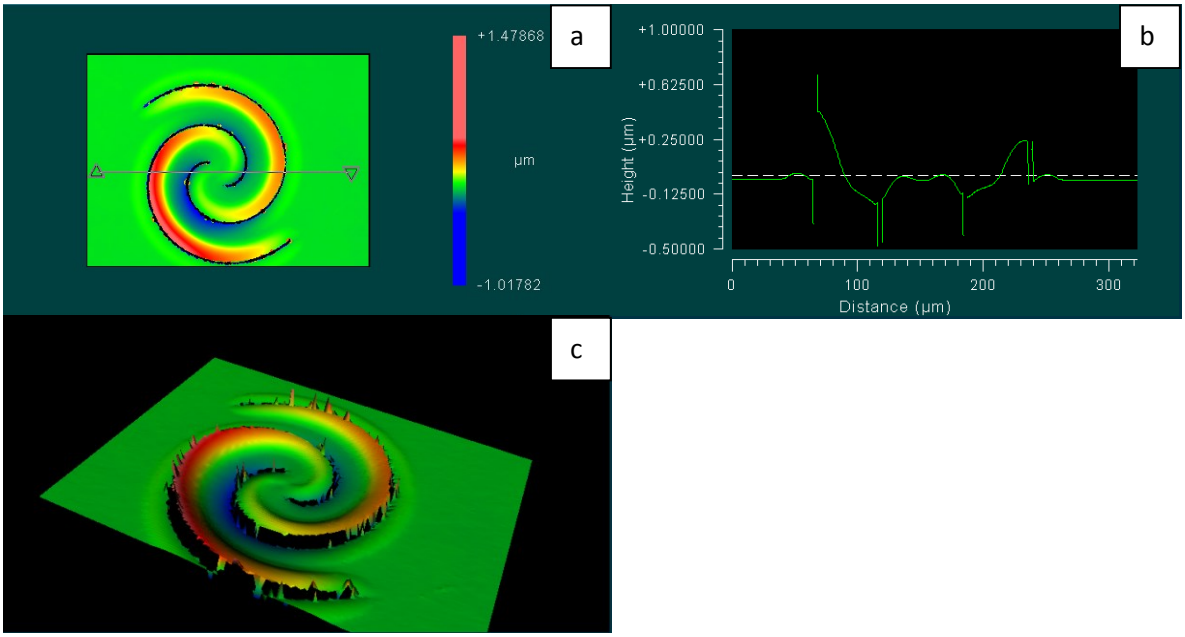

Figure 4.6: Optical profilometer images of a released 2-arm Archimedes spiral following the lift-off process. a) A depth profile of the released spiral. b) The cross-section of the line between the triangles in a). c) A 3-D images of the Archimedes spiral.

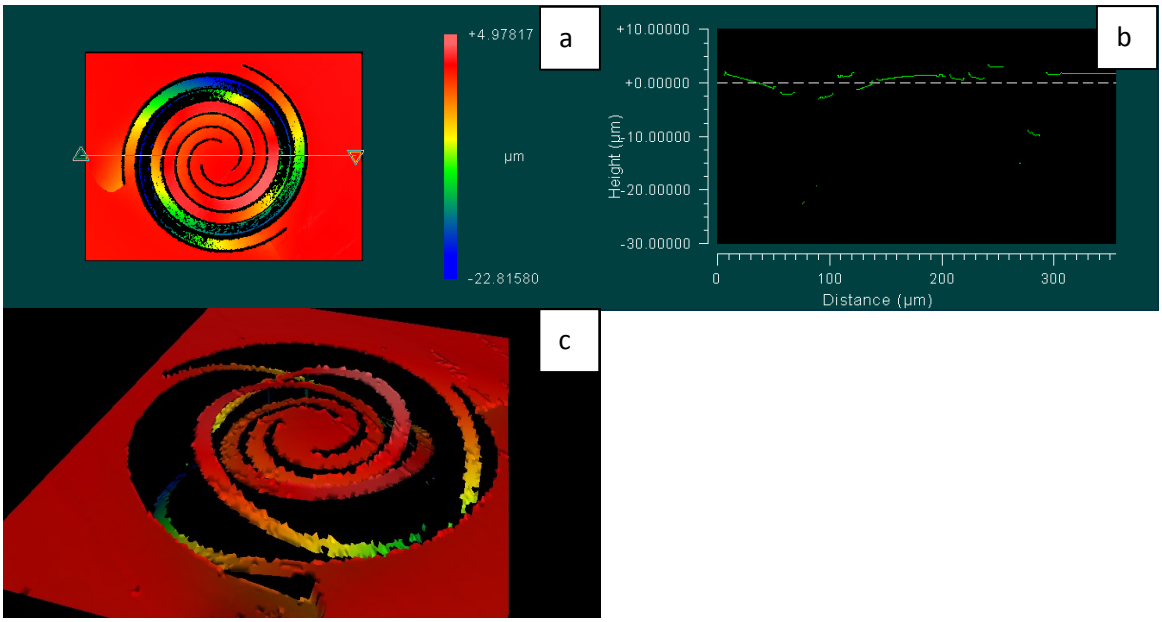

Figure 4.7: Optical profilometer images of a released 3-arm Archimedes spiral following the lift-off process. a) A depth profile of the released spiral. b) The cross-section of the line between the triangles in a). c) A 3-D images of the Archimedes spiral.

4.2.2. Results and Discussion

The optical profilometer images taken of the 3-arm and 2-arm Archimedes spirals show intact freestanding structures, indicating that the fabrication process was successful. There are a number of aspects of the different approaches that should be discussed, however. Firstly, the ion milling process was likely unsuccessful due to heating issues and/or impact of the ions on the membrane surface causing damage to the membranes. Ion milling generates considerable heat due to the impact of the ions on the surface. Furthermore, as discussed in section 5.3, the AlMo membranes, due to the large width to thickness aspect ratio, transfer heat relatively slowly, particularly when in a vacuum.

There were some issues with the lift-off process. Generally, lift-off processes work well when the photoresist is roughly three times thicker than the device layer. A 300 nm thick film is thicker than usual for a lift-off process, however, and substantial material was left from the side walls as seen in Figure 4.6. This may partially be a property of the AlMo material, however.

Similar sidewall remnants are present in previously reported 5 to 20 nm thick devices that were fabricated via lift-off processes.[1]

Another aspect of interest is the shape of the Archimedes spirals following the release process. The relatively minor deflection of the 2-arm spiral was likely caused by the intrinsic stress in the thin film. The substantial deflection of the 3-arm spiral, however, can be of greater importance. Spirals with high flexibility could be useful if incorporated into sensors or energy harvesting devices. The high flexibility causes difficulties during the fabrication process, however. Unlike the cantilevers (section 4.3), where the XeF_2 etch was performed with the devices facing upward, the chips for the diluted aqua regia process had to be placed upside down during the RIE process. Following this process, the chip was flipped upright. This does not significantly affect the membranes, which due to the high intrinsic stress are relatively static. There was substantial damage to the Archimedes spirals following the RIE release step, which may have been caused by the action of rotating them upright. Future work would involve depositing a piezoelectric layer and top electrode on the AlMo spirals and measuring the properties of the energy harvesters. The addition of the piezoelectric layer would also likely reduce deflection from the intrinsic stress of AlMo layers.

4.3. Cantilevers

Cantilevers can be used for a variety of purposes such as switching[217], energy harvesting[218], relays[219], and many more. Structures for potential sensor applications have been designed and fabricated. They consist of pairs of cantilever beams connected by a larger rectangular region. One potential application would be for deflection cantilever sensors. Reflection of a laser from the tip of a cantilever beam can be used to measure deflection of the cantilever.[220] The large pads would allow for the reflection of the laser, while the two thin arms would increase the sensitivity of the sensor and prevent the rectangular region from rotating.

4.3.1. Materials and Methods

A small silicon chip (roughly 1 cm^2) from a <100> wafer was cleaned in a piranha and hydrofluoric acid (1 HF: 10 NH_4F) solution. This chip was then dehydrated for 5 min on a

hotplate set to 200°C and permitted to cool for 2 min. PMMA 495k resist was dispensed on the chip and spun with a spread speed of 500 rpm for 10 s and 4000 rpm for 45 s. The chip was then baked at 180°C for 10 min and permitted to cool for 2 min. This process was repeated with PMMA 950k resist forming a 120 nm thick resist layer. The lithography was performed using a Raith150 Electron Beam Lithography system and developed in methylisobutylketone (MIBK) based developer (1 MIBK: 3 IPA). Subsequently, 50 nm of AlMo was sputtered onto the surface of the silicon chip, and lift-off was performed through sonication in an acetone bath. A XeF_2 etch was performed to release the AlMo cantilevers from the silicon surface as in section 4.2, though in this case only two cycles were performed.

4.3.2. Results and Discussion

The double cantilever design was implemented with a number of different dimensions. The two arms had dimensions of 50, 100, 150, 200 and 500 nm in width and 1, 1.5, 2, 2.5 μm in length. The release process was sufficiently long for the smaller 0.5 μm x 0.5 μm. 0.75 μm x 0.5 μm and 1 μm x 0.5 μm paddles but not the 1 μm x 1 μm paddles. In roughly half of the designs (48%), the photoresist could not be removed (Figure 4.8a) from between the cantilever arms even after sonication for 1 hr in the acetone bath. Furthermore, while this technique was used previously for roughly 50 nm thick Al and gold layers, substantial quantities of the AlMo sidewalls remained, as is evident in the images in Figure 4.8. As discussed in section 4.2, this may be due to the properties of the AlMo material rather than the thickness of the device. Some cantilevers were not fully released (Figure 4.8b). Of the fully released cantilevers the majority deflected downwards, likely due to differences in intrinsic stress within the cantilever. One exception was a cantilever with 1 μm long, 150 nm wide arms and a 500 x 500 μm paddle (Figure 4.8d) which did not deflect.

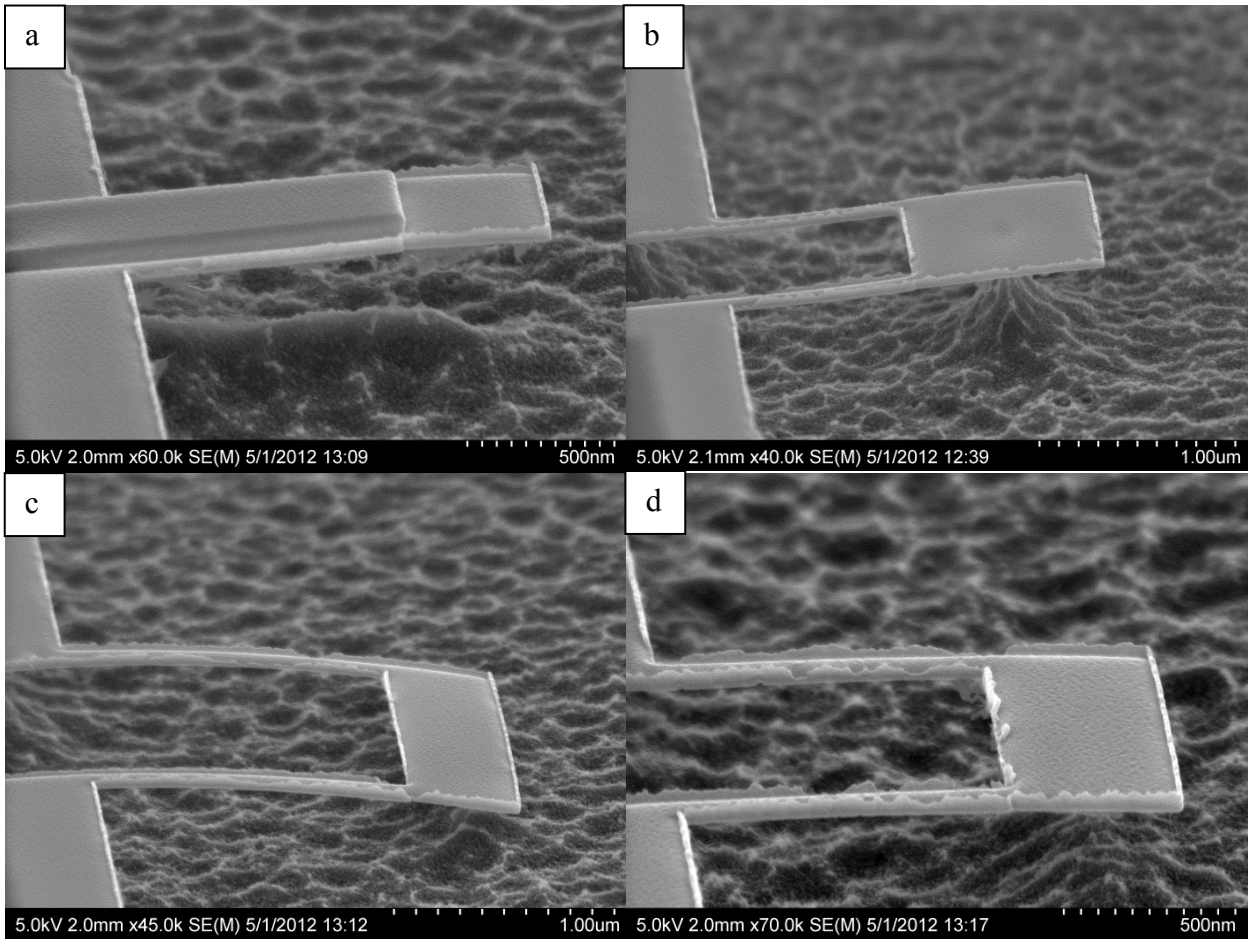

Figure 4.8: Images of the two-arm cantilevers after fabrication. a) A cantilever with incomplete lift-off. b) A Cantilever with incomplete release. c) A cantilever deflecting under the mass of the paddle. d) A straight released cantilever.

4.4. Compressive stress membranes

While the strength of the membranes produced in section 3.2 can be valuable, many membranes are permeable, which can be employed for several applications such as filtering/purification or to increase the surface area for sensor applications. One method for fabrication of such permeable membranes is through dealloying, where one component of the alloy is selectively etched away. From a material perspective, the fact that Al and Mo are largely etched via different chemistries should be an asset in this case. A number of efforts were made to dealloy the AlMo material and produce intact membranes, but they were not successful. This

may be because the Mo islands in the Al matrix are not connected, and the etchant therefore could not penetrate further than the surface of the membrane.

One particular experiment produced an interesting and potentially useful result. Stress can be difficult to control in suspended structures. Often high tensile stress was measured in the membranes. The following method led to the formation of intact compressive stress membranes. A 300 nm thick membrane was fabricated as described in section 3.2. It was then dipped in TMAH, washed in water and dried in a nitrogen stream. An optical microscope image of the membrane is shown in Figure 4.9. The deformation of the membrane is indicative that the membrane is not under tensile stress. This may have been caused by the removal of Mo on the surface of the membrane. Such a structure may have potential applications as an air fluctuation sensor[32], for example.

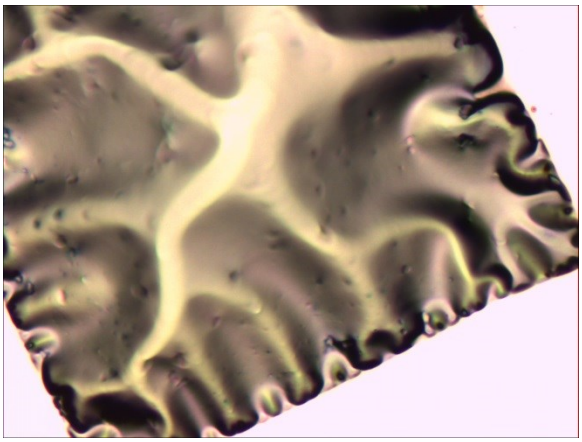

Figure 4.9: An optical microscope image of an intact compressive stress membrane.

4.5. Conclusions and recommendations

Several structures were fabricated using the AlMo nanocomposite including membranes with proof masses, freestanding Archimedes spirals and nanocantilevers. One advantage of the AlMo nanocomposite is that the low Young's modulus and the ability to make very thin structures means that very low stiffness devices can be created. This can be advantageous for applications like sensors and energy harvesting, but requires consideration when designing certain structures, such as the Archimedes spirals and nanocantilevers. The low stiffness was responsible for considerable deflection of the devices. In the future it would be advantageous to

adjust the fabrication device parameters to minimize the issue of deflection due to the intrinsic stresses. Furthermore, while they are effective, the liftoff processes leave behind substantial sidewall material. It would be useful to reduce this effect, potentially by applying the aqua regia etch process and carefully rotating the devices following the RIE release process to prevent breakage.

5. Biosensors for the Detection of Bacteria, Viruses and Proteins

Membranes have been used as biosensors for pathogen detection in a variety of ways (section 2.3). There are a number of aspects that should be considered in the construction of a biosensor. These include the membrane material and fabrication process, molecular probes used for specific detection, the process for linking the molecular probes to the membrane surface, and the transduction method used to convert the biochemical interaction of the capture molecule and the target pathogen into an observable output signal. In this chapter, the AlMo membranes and resonance measurement technique described in chapter 3 were implemented as a base for a biosensor. Proteins, namely monoclonal Abs and bacteriophage tail spike proteins (TSPs) were used as the molecular probes for specific pathogen detection. The Abs were used for the capture of bovine herpesvirus 1 (BHV-1) and the hexon protein of hemorrhagic enteritis virus (HEV). A hexon protein is a major capsid protein of adenoviruses like HEV. Furthermore, a bacteriophage tail spike protein (TSP) was used to capture *Mycobacteria smegmatis* (*M. smegmatis*) and *Mycobacteria avium (M. avium)*.

The transduction method of interest in this chapter is mass detection through resonance shift measured by laser interferometry. While this technique is more commonly employed in singly or doubly clamped cantilever beam experiments, membranes are not inherently less sensitive than such devices. Like cantilevers, the resonance frequency of membranes is proportional to $m^{-0.5}$ where m is the mass of the device. Generally, it is simpler to make much smaller and lighter cantilevers than membrane devices, which leads to more sensitive sensors.

Sensitivity is not the only important factor to consider regarding the quality of a sensor, however. When quantifying bacteria, for example, it is not necessary for the detection limit to far exceed the mass of a single bacterium. Another important consideration is surface area. Biosensors generally require submersion in a solution to detect the carbohydrates, lipids, proteins, DNA, RNA, bacteria, viruses, cells, or other biological material of interest. This means that surface area and concentration become important. If the concentration of the target is very low, and the sensor is very small, the sensor may not be able to detect the bacteria, because the bacteria may not land on the sensor due to its small size. This is where membranes biosensors

may play a role. They have a larger surface area than many tiny cantilevers or beams, yet reasonable dimension membranes are still sensitive enough to detect a single *E. coli* bacterium.

Several linking processes were employed to link the molecular probe proteins to the AlMo membranes surfaces. The first was 4-formylbenzene diazonium hexafluorophosphate (FBDP), a bifunctional diazonium molecule. The second was HDMS, a silane used to increase the hydrophobicity of a surface. The third pair of linkers were the epoxysilanes (3-glycidyloxypropyl)trimethoxysilane (GPTMS) and 3-glycidoxypropyldimethylethoxysilane (GPDMES), which are also bifunctional. The last linking process requires two chemicals: (3-aminopropyl)triethoxysilane (APTES) and glutaraldehyde. The following sections have been divided according to the linking process that was employed.

5.1. Diazonium linker chemistry

A diazonium compound or salt is an organic compound with a positively charged triple bond nitrogen-nitrogen functional group as shown in Figure 5.1. This functional group is reactive and has been shown to bind to a variety of materials including carbon powder, polymers such as polypropylene, polyethylterephthalate, and polyethyletherketone, inorganic compounds including TiN, SiC, SiO_2 and SiOC, vinylics, metals such as Al, Ca, Cr, Cu, Fe, Ga, In, Mg, Li, Na, Zn, and more.[221] It is nevertheless less commonly used than some other linkers such as silanes. Diazonium compounds are common intermediates in chemical reactions and diazonium itself is a leaving group that reacts with nucleophiles. The N_2^+ group is thermodynamically stable and it is therefore an energetically favoured reaction. The FBDP that was used in the following experiments was originally devised as a chemical crosslinker for protein-protein crosslinking.[19] The functional group of the FBDP is a free aldehyde which reacts with free amines, thus making it capable of linking proteins to a surface.

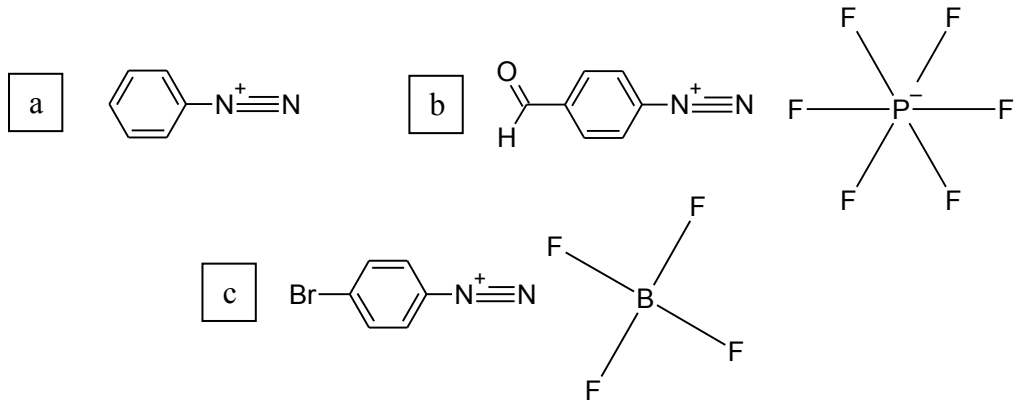

Figure 5.1: Examples of diazonium functional groups. a) Benzenediazonium (shown without a corresponding salt), b) FBDP, c) 4-Bromobenzenediazonium tetrafluoroborate.

5.1.1. X-ray Photoelectron Spectroscopy (XPS) Measurements and Analysis

While diazonium functional groups have been shown to bind to Al[221], the AlMo surface is not identical to a plain aluminum surface. Therefore, it was necessary to determine whether diazonium molecules bind to the AlMo nanocomposite before moving on to further linking experiments. Organic materials are mostly composed of carbon, oxygen, hydrogen and nitrogen. This can make it difficult to use usual analysis techniques to verify the attachment of the diazonium to the surface. In particular, it can be challenging to distinguish between organic contamination and the attachment of diazonium to the surface. For this reason the presence of diazonium on the AlMo nanocomposite surface was verified using the 4-bromobenzenediazonium tetrafluoroborate depicted in Figure 5.1c. Br can be readily identified using XPS.

5.1.1.1. Materials and Methods

Silicon chips coated with a 300 nm thick layer of AlMo (section 3.2) were placed in acetone and sonicated for 20 min, washed in IPA, and dried in a stream of nitrogen gas. Two common diazonium salt solvents were used: acetonitrile and water. Four chips were prepared. One chip was submerged in 10 mM 4-bromobenzenediazonium tetrafluoroborate dissolved in

water for 1 hr and one chip was submerged in 10 mM 4-bromobenzenediazonium tetrafluoroborate dissolved in acetonitrile for 1 hr. The two control chips were submerged in water or acetonitrile respectively, again for 1 hr. The acetonitrile chips were then washed in acetonitrile, and all the chips were washed 3x in DI water and dried in a stream of nitrogen gas. The XPS measurements were then performed. The process was then repeated, with similar results. Following the successful 4-bromobenzenediazonium tetrafluoroborate reaction, the water portion of the experiment was repeated with the linking chemical FBDP.

5.1.1.2. Results and Discussion

The XPS results for 4-bromobenzenediazonium tetrafluoroborate include the full energy spectrum for each chip (Figure 5.2), and a finer measurement around the Br binding energy (Figure 5.3). The Br peaks were clearly present for the chip functionalized with diazonium dissolved in water and not for either of the control chips. There was a very slight increase in the diazonium in acetonitrile signal near the first Br binding energy peak. This means that the functionalization with diazonium dissolved in water was successful, while the functionalization with diazonium dissolved in acetonitrile was not successful.

It is not evident why the acetonitrile process was not successful. One possibility is that the reaction takes place more rapidly in water, and that the acetonitrile solution would require a longer reaction time. This is supported by the presence of the very small peak near the first Br binding energy peak in Figure 5.3. Regardless, all subsequent diazonium experiments were performed with water as the solvent, as it allowed for rapid functionalization of the AlMo surface.

From the XPS spectrum in Figure 5.2 it was observed that there was a greater quantity of C on the chip functionalized with 4-bromobenzenediazonium tetrafluoroborate dissolved in water as compared to the control chip. This increase in C on the surface was similarly observed during the functionalization of a chip with FBDP (Figure 5.4). Analysis of the XPS spectrum (Figure 5.4) was used to determine that there was 36 at. % C on the control chip compared to 74 at. % C on the FBDP coated chip. While not specific, this supports the conclusion that the FBDP was successfully deposited on the surface. As mentioned previously, the C on the control chip surfaces was likely contamination.

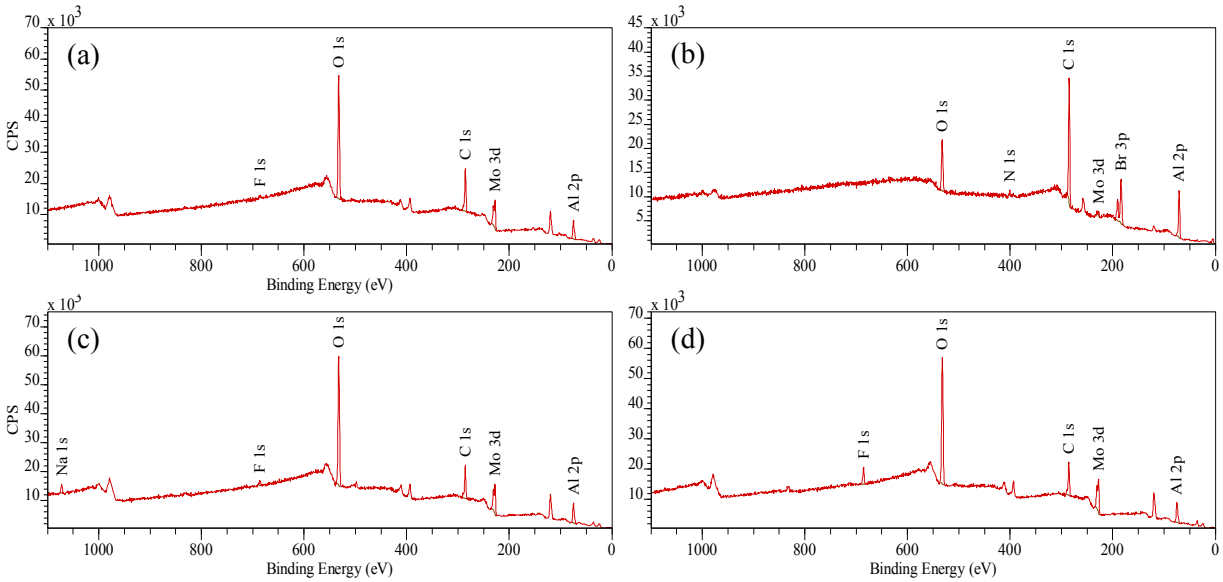

Figure 5.2: XPS spectrums for 4-bromobenzenediazonium tetrafluoroborate reaction on AlMo. a) water solvent control, b) diazonium in water, c) acetonitrile solvent control, d) diazonium in acetonitrile.

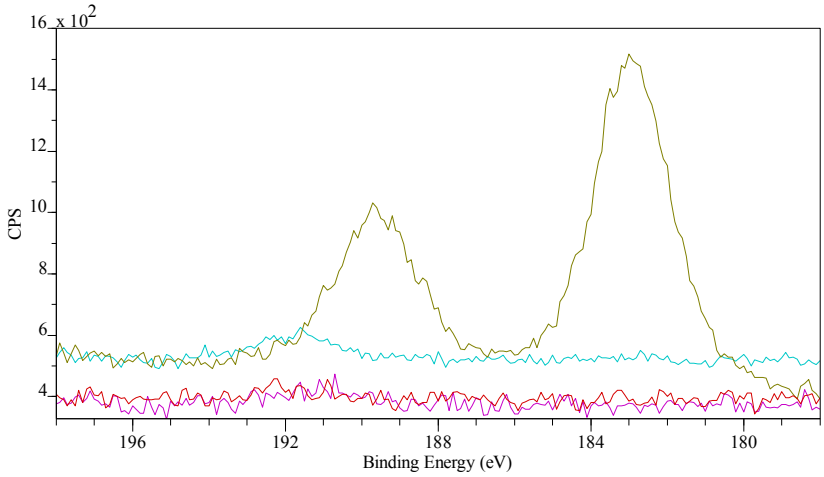

Figure 5.3: XPS spectrum for Br 3p peak for 4-bromobenzenediazonium tetrafluoroborate reaction on AlMo surface. The bottom two flat spectra are the control signals, the flat upper spectrum with the very slight peak is for the diazonium in acetonitrile, and the spectrum with two peaks is for the diazonium in water.

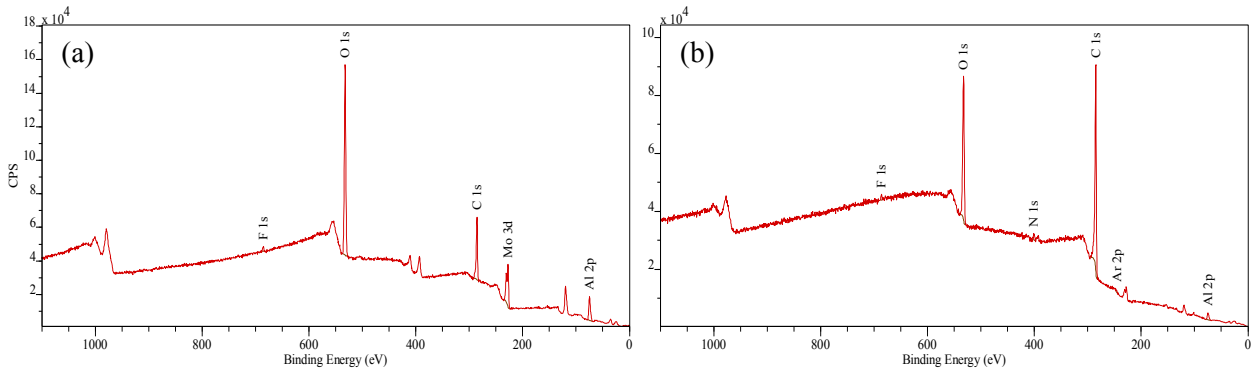

Figure 5.4: XPS spectrum of FBDP on an AlMo coated chip. The spectrum shown in a) is for the control chip coated with water. The spectrum shown in b) is for the active chip coated with FBDP in water.

5.1.2. BHV-1 capture on AlMo-coated chips and membranes

Following the XPS measurements, experiments were performed with FBDP for the specific capture of BHV-1 on AlMo-coated chips and AlMo membranes. The AlMo chips were used to investigate the process of linking Abs specific to BHV-1 to the AlMo surface for the capture of BHV-1. Following positive results on the AlMo chips, the process was implemented on AlMo membranes and resonance measurements were performed.

5.1.2.1. Materials and Methods

A monoclonal Ab (clone 3D9S) in ascites fluid was obtained from Dr. Sylvia van den Hurk. The monoclonal Ab was purified by a Protein G High Performance Spintrap from Sigma Aldrich by following the manufacturer's instructions with minor adjustments. A buffer exchange was performed using a Slide-A-Lyze Cassette from Fisher Scientific from the Tris buffer described in the instructions for the Protein G High Performance Spintrap to phosphate buffered saline (PBS). The concentration of the Ab was determined by measuring the absorption of 280 nm light using a spectrophotometer. The control monoclonal Ab used was a mouse anti-human interferon gamma Ab (IFN-γ Ab) from R&D Systems.

AlMo was sputtered onto a Si wafer as described in section 3.2 to form a thin film with a thickness of 300 nm. The wafer was diced into 5 mm x 7 mm chips. Four chips were washed

with acetone, IPA and DI water, and were dried in a nitrogen gas stream. The chips were then placed in a UV-ozone cleaner for 5 min. They were each functionalized with a 50 μL droplet of 5 mM FBDP in DI water solution for 1 hr. A 50 μL droplet of PBS was then placed on one of the bare diazonium chips for 1 hr. A 50 μL droplet of 100 μg/ml 3D9S Ab was placed on two of the other chips for 1 hr, and a 50 μL droplet of 100 μg/ml INF-γ Ab was placed on the final chip for 1 hr. Subsequently, all the chips were washed in DI water and dried in a nitrogen gas stream. A 50 μL droplet of 90 μg/ml BHV-1 in PBS was placed on the INF-γ Ab chip and one of the chips with 3D9S Ab. After 1 hr the chips were again washed in DI water and dried in a nitrogen gas stream. All the chips were coated with 20 nm of sputtered gold, and SEM imaging was performed.

Square AlMo membranes 400 μm x 400 μm x 10 nm were fabricated as discussed previously in section 3.2. They were washed in acetone, IPA and water, and dried in a stream of nitrogen gas. The chip was then cleaned in a UV-ozone cleaner for 5 min on each side. Subsequently, the resonance frequency of the membranes was measured. The chip was then functionalized by submerging it in 2 mL of 5 mM diazonium solution in DI water for 1 hr. It was washed with DI water and submerged in 2 mL of 100 μg/ml 3D9S Ab in PBS for 1 hr. Again, the chip was washed with DI water and dried in a nitrogen gas stream, and the resonance frequency of the membranes was determined. Subsequently, the chip was placed in a solution of 90 μg/ml BHV-1 in PBS for 1 hr. The chips were again washed in DI water and dried in a nitrogen gas stream, and the resonance frequency of the membranes was determined.

A BSA blocking step was added to the process to reduce nonspecific BHV-1 binding. The previous process with the AlMo-coated chips was repeated, but with the inclusion of a chip covered with 1% weight/volume BSA in PBS for 1 hr instead of the Ab functionalization step. Subsequently, 20 nm of Au was sputtered onto the chips, and SEM images were taken.

Since the BSA blocking successfully reduced nonspecific binding, it was incorporated into the functionalization process. The original AlMo chip coating process was repeated, except that the Ab-coated chips were blocked with 1% w/w BSA in PBS following the Ab functionalization step. Subsequent to the blocking step, the chips were washed with DI water and dried in a nitrogen gas stream.

The previous resonance measurement procedures for 3D9S Ab and INF-γ Ab were repeated with the addition of the 1 hr submersion in 1% BSA in PBS following the Ab functionalization steps. This was followed by washes in PBS and DI water.

5.1.2.2. Results and Discussion

AlMo membranes are more expensive and fragile than AlMo-coated silicon chips. Furthermore, the AlMo chips have the same chemical properties as the AlMo membranes. For this reason, the functionalization processes were examined on the AlMo coated chips before being implemented on AlMo membranes for resonance measurements. SEM images of the AlMo chip surface following the initial functionalization process are shown in Figure 5.5. The BHV-1 was clearly present on the 3D9S Ab-coated active chip and absent on the INF-γ Ab-coated negative control chip. (Figure 5.5).

Resonance frequency measurements were performed for the membranes coated with the active 3D9S Ab which specifically binds BHV-1 and the membranes coated with the control INF-γ Ab which specifically binds human INF-γ. The resonance frequencies are given in Figures 5.6 and 5.7. The average resonance frequency shift due to binding of BHV-1 was 93 kHz with a standard deviation (σ) of 4 kHz for the active membranes and 62 kHz with $\sigma = 2$ kHz for the control membranes. This is a distinct separation between the active and control chips as they do not overlap within 5σ. This supports the hypothesis that these membranes can be used as biosensor platform, and that the functionalized membranes can be used to detect BHV-1 at these concentrations.

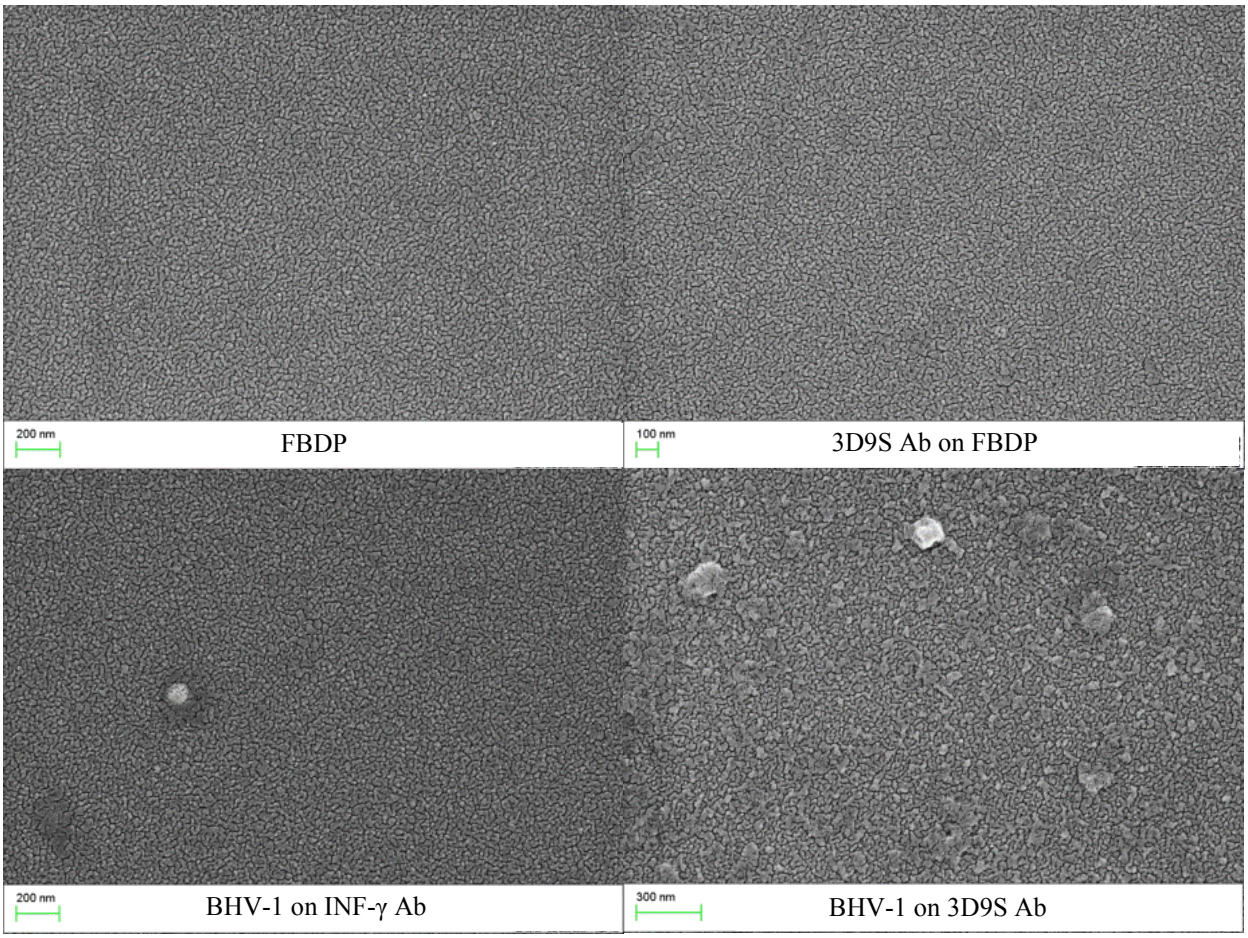

Figure 5.5: SEM images of the stages of AlMo chip functionalization and the capture of BHV-1. The images include a chip coated with FBDP, a chip coated with FBDP + 3D9S Ab, the negative control chip coated with FBDP + INF-γ Ab + BHV-1 (the white circle is an AlMo surface defect) and the active chip coated with FBDP + 3D9S Ab + BHV-1. The ~150 nm in diameter spherical objects in the final image are intact BHV-1 virus particles.

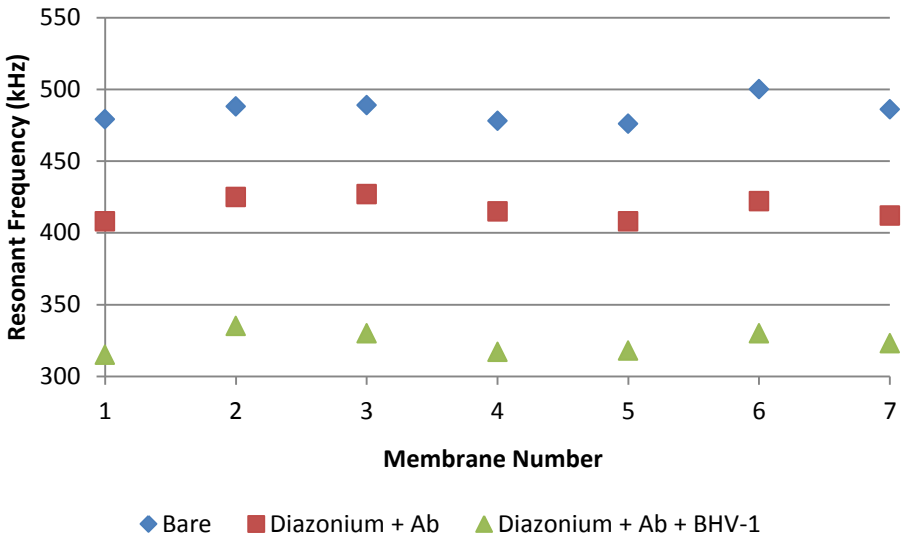

Figure 5.6: A plot of the resonance frequency of the bare membranes before functionalization (Bare), after functionalization with FBDP and 3D9S Ab, and after BHV-1 capture.

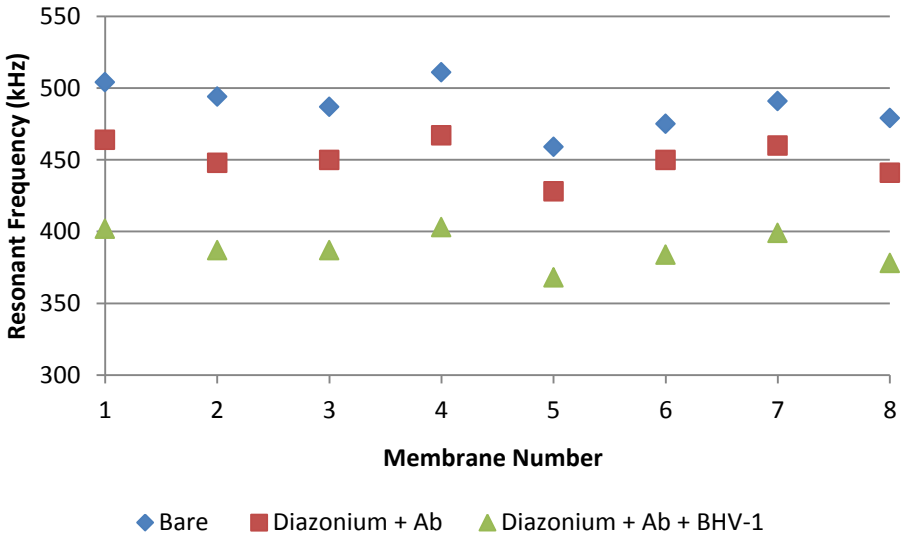

Figure 5.7: A plot of the resonance frequency of the bare membranes before functionalization, after functionalization with FBDP and mouse anti-human INF-γ Ab, and after BHV-1 capture.

One less desirable aspect of these results was the relatively large frequency shift from BHV-1 binding on the control membranes. This nonspecific binding was likely due to one of two causes: either the BHV-1 binds to the human INF-γ Ab, or the FBDP was not fully covered by the INF-γ Ab. The latter was more likely, because the Ab concentration used was not very high. This means that there may have been open regions on the surface for BHV-1 to attach to the

FBDP. BSA is a protein that is commonly used to block a surface to prevent nonspecific binding in assays like ELISAs. This BSA blocking was tested to determine whether it would reduce nonspecific BHV-1 binding. The SEM images shown in Figure 5.8 are an indication that BSA was effective. There was a clear decrease in BHV-1 binding from the 3D9S Ab-coated chip to the INF-γ Ab-coated chip and again from the INF-γ Ab-coated chip to the BSA-coated chip. This suggests that, while imperfect, BSA blocking decreased nonspecific binding of BHV-1 to the chip surface.

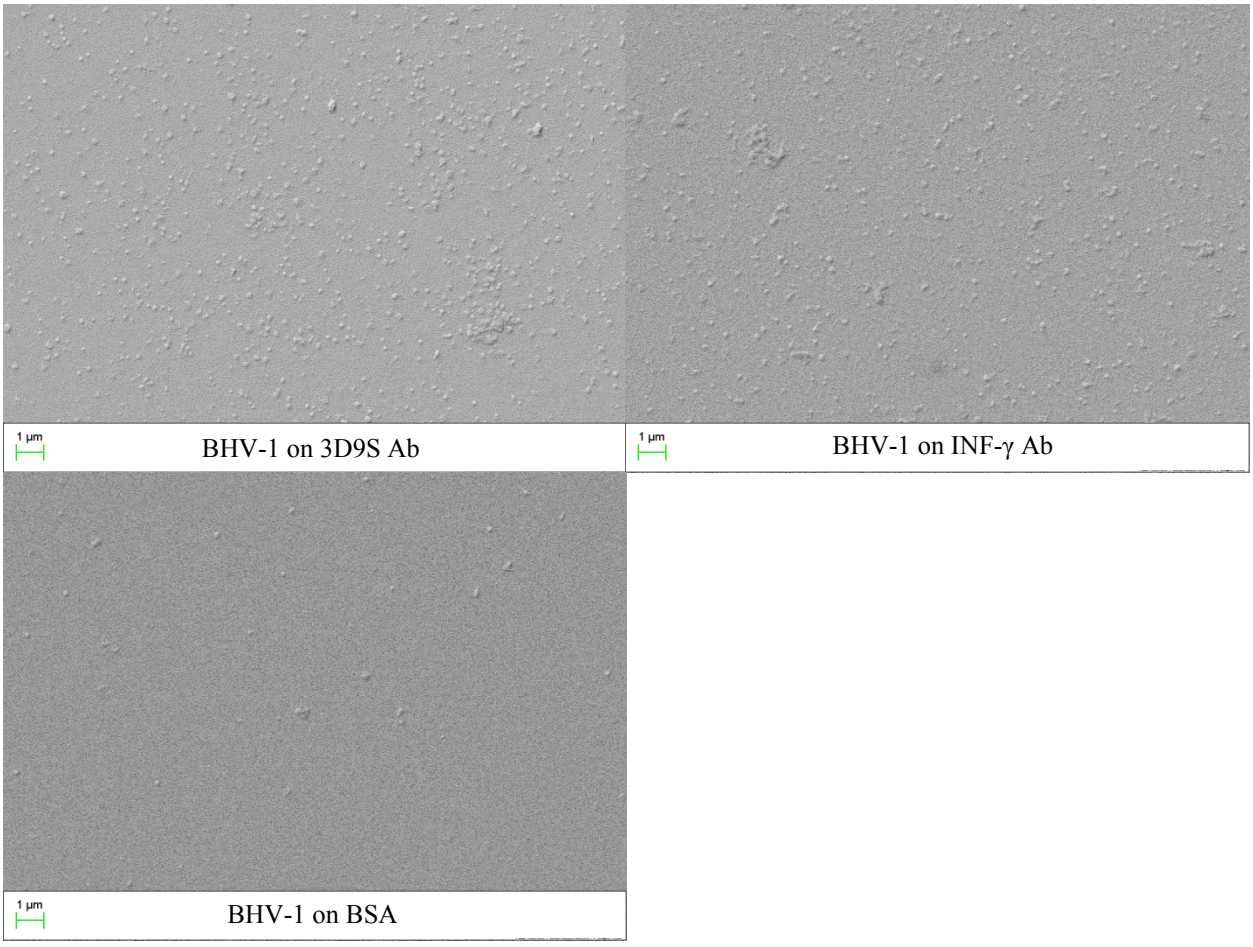

Figure 5.8: SEM images of BHV-1 binding to 3D9S Ab-, anti-human INF-γ Ab- and BSA-functionalized chips. They were coated with 20 nm of sputtered gold. There is an observable decrease in the quantity of BHV-1 on the surface between the active 3D9S-coated and the control INF-γ-coated chip and again between this control chip and the BSA-blocked chip.

BSA blocking was then incorporated into the functionalization process following the Ab binding step. SEM images of the chips are shown in Figure 5.9. The images show the same trend

as in Figure 5.8, except that there appears to be less BHV-1 on both the 3D9S Ab and INF-γ Ab chips, which suggests that nonspecific binding has been reduced on both the active and the control chips.

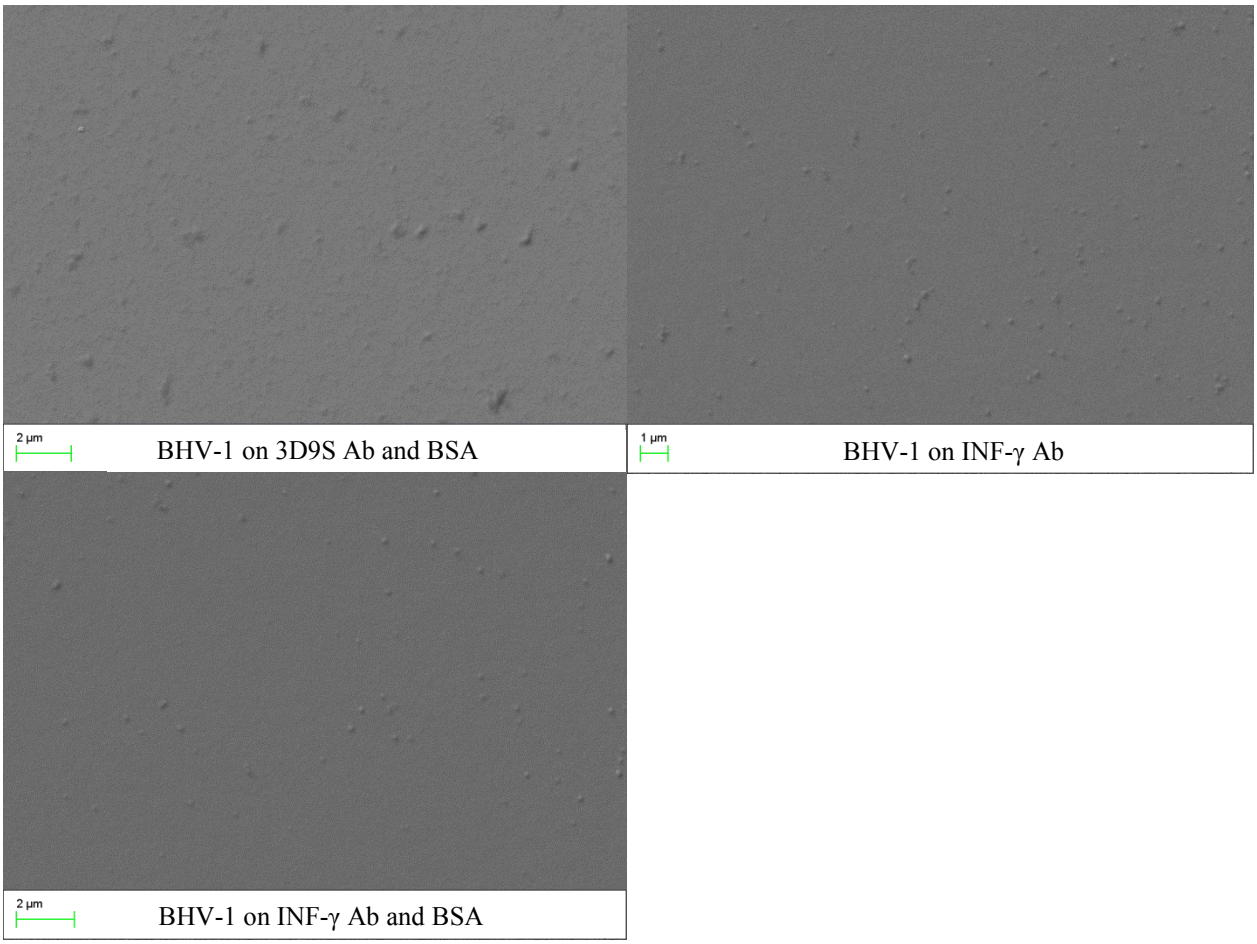

Figure 5.9: SEM images illustrating the effects BSA blocking on BHV-1 binding. The greatest quantity of bound BHV-1 was observed on the active AlMo chip coated with 3D9S Ab and blocked by BSA, less BHV-1 was observed on the control chip coated with INF-γ Ab and even less BHV-1 was observed on the control chip coated with INF-γ Ab and blocked with BSA.

Resonance frequency measurements were then performed with the inclusion of the BSA blocking step. The results are shown in Figures 5.10 and 5.11. Again, there was a clear difference between the active and control membrane measurements, with an average shift of 32 kHz with a σ of 4 kHz for the membranes coated with 3D9S Ab and an average of 21 kHz with a

σ of 2 kHz for the membranes coated with anti INF-γ Ab. This suggests that the BSA effectively reduced the nonspecific binding of both the active and control membranes.

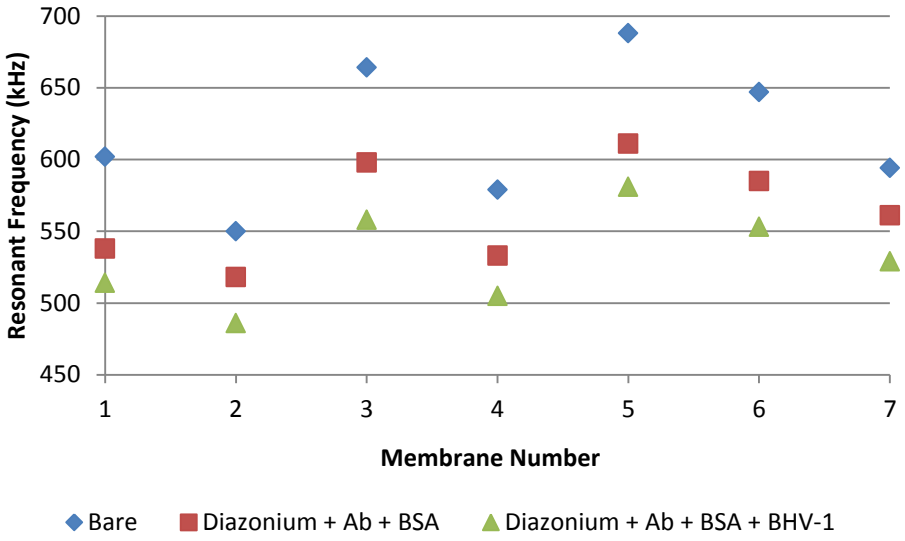

Figure 5.10: A plot of the resonance frequency of the bare membranes before functionalization, after functionalization with FBDP, 3D9S Ab and BSA, and after BHV-1 capture.

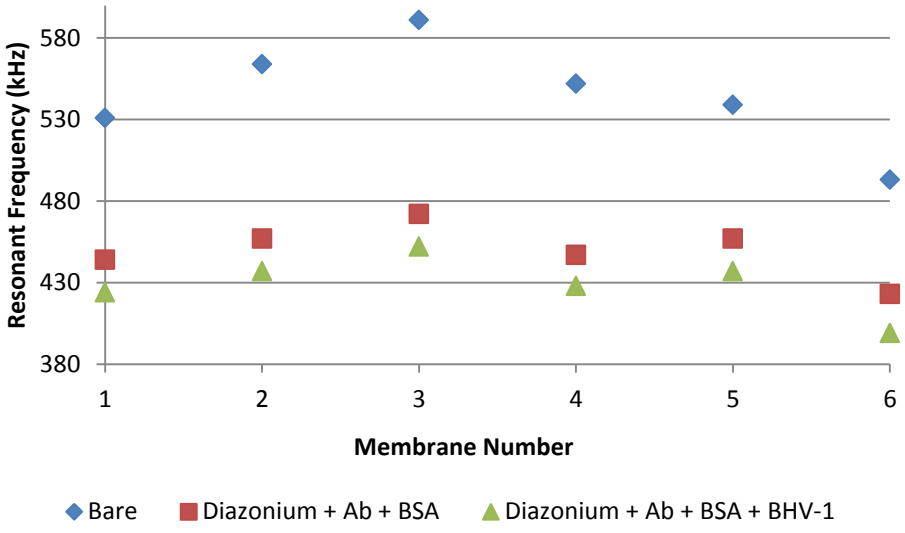

Figure 5.11: A plot of the resonance frequency of the bare membranes before functionalization, after functionalization with FBDP, anti-human INF-γ Ab and BSA, and after BHV-1 capture.

While the frequency shift results are a useful indicator of positive results, it is informative to consider the actual change in mass of the membranes with the addition of BHV-1. This can be

determined by calculating the intrinsic stress of the membranes and converting the density term in equation [4] to mass/volume. After rearranging the mass (m) is given as follows:

$$m = \frac{\sigma_0 t}{2{f_r}^2} \tag{5}$$

where σ_0 is the intrinsic stress of the membrane, t is the thickness of the membrane and f_r is the base resonance frequency of the membrane. For a change in resonant frequency (Δf_r), there is an associated change in mass (Δm). If the added mass is treated as an additional layer with uniform density and negligible stiffness, the thickness (t) is held constant, and the results can be presented as:

$$m + \Delta m = \frac{\sigma_0 t}{2(f_r - \Delta f_r)^2}$$

$$\Delta m = \frac{\sigma_0 t}{2(f_r - \Delta f_r)^2} - m \tag{6}$$

For verification, the same result can be determined from first principles. The effective mass contribution of or on a membrane varies based on the location of the mass. This is why a boss, similar to those fabricated in section 4.1.2, is fabricated in the center of a membrane or the tip of a cantilever. It is done to maximize the change in resonance frequency of the device. Therefore the resonance frequency of the membrane can be presented as:

$$f_r = \frac{1}{2\pi}\sqrt{\frac{k_{eff}}{m_{eff}}}$$

where k_{eff} is the effective stiffness of the membrane and m_{eff} is the effective mass of the membrane. As the linkers, Abs and virus particles bind to the membrane surface they contribute to m_{eff}, but as they are relatively pliable structures, in comparison to the large internal stress of the membrane, their contribution to effective stiffness is negligible.

Since the variation in the resonance frequency from BHV-1 binding was relatively small, and the distribution of virus particles on the AlMo surfaces appeared relatively uniform in SEM images, the distribution of the virus particles on the membrane surfaces was considered to be uniform. For this reason the added linkers, Abs and virus particles were modeled as an additional layer with a density and a very small Young's modulus.

The mechanical vibration equation for a thin membrane is:

$$z(x, y, t) = Z_{max} e^{-j\omega t} sin(k_{mx} x) sin(k_{ny} y)$$

where Z_{max} is the maximum deflection of the membrane in the z direction, t is time, k is a constant that depends on the dimensions of the membrane, and m and n are mode numbers in the x and y directions. Since only the base frequency was determined via measurement, only the base resonance frequency will be considered here, so $m = n = 1$. Furthermore, because the membrane is a square: $k_{1x} = k_{1y} = {}^{\pi}/_{a}$, where a is the length of one side of the square. The ultrathin nature of the membranes means that the dynamics within the thickness can be neglected. Subsequently, from Newton's first law and Hookes' law:

$$\iint_0^a \frac{1}{2}\omega^2\rho[z(x,y)]^2 dxdy = \int_0^{z_{max}} k_{eff} z(x,y) dz$$

Therefore, following some mathematical simplifications:

$$m_{eff} = \frac{m}{4}$$

As indicated previously, the contribution from the viruses can be modelled as a change in the effective mass Δm_{eff}. Consequently, the angular resonance frequency is:

$$\omega_r - \Delta\omega_r = \sqrt{\frac{k_{eff}}{m_{eff} + \Delta m_{eff}}}$$

Calculating through, the mass of viruses (Δm) on the membrane surface can be simply calculated as follows:

$$\Delta m = m\frac{(2\omega_r - \Delta\omega_r)\Delta\omega_r}{(\omega_r - \Delta\omega_r)^2} \quad (7)$$

Furthermore, if the intrinsic stress is calculated via equation [4], then [6] and [7] yield identical results. To further verify these equations, finite element analysis was performed with ANSYS.

A 400 µm x 400 µm x 10 nm membrane nearly identical to the ones used to produce the results in Figures 5.6 and 5.7 was modeled. An intrinsic stress of 260 MPa was applied to the edges of the membrane. The density (5000 kg/m^3), Poisson's ratio (0.33) and Young's modulus (127 GPa) from Chapter 3 were used in the model. A square mesh was used and the resonance frequency of the bare membrane was found to be 403 kHz, which is identical to the result from equation [4].

Given the dimensions of the virus particles compared to the membrane width, as well as the number of virus particles that were present, it was unfeasible to model the virus particles individually. Therefore, the virus layer was again modelled as a thin structure with the same side

length as the membrane, a variable density and very low Young's modulus. No intrinsic stress was applied to this layer. The density of the virus layer was then varied to represent different quantities of virus particles on the membrane and the associated changes in resonance frequency were determined. The results coincided very closely with those of equations [6] and [7]. The error was never greater than 7% and the average error was 1.4%.

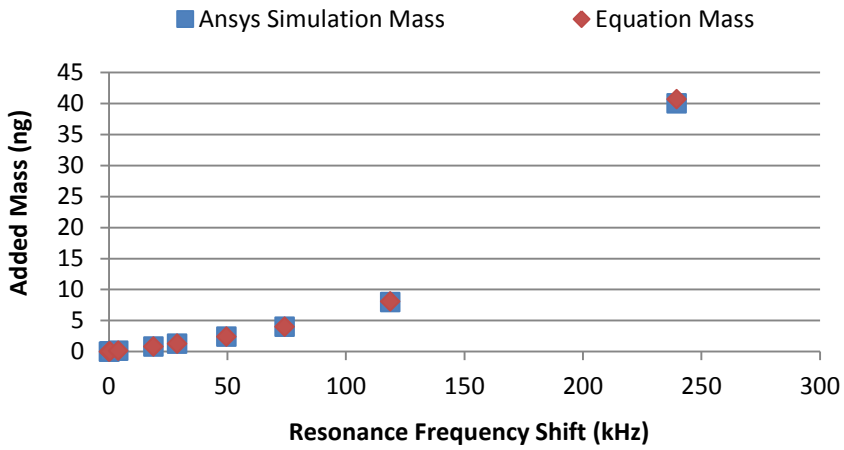

Figure 5.12: A plot illustrating the nearly identical results from equation [6]/[7] and the Ansys simulation. The added mass on the surface of the membrane is plotted against the resultant resonance frequency shift.

Equation [6]/[7] was used to determine the mass of BHV-1 on the surface of the membranes. In the first experiment without BSA, the 3D9S-coated membranes accumulated 7 ± 1 ng (where the error is the standard deviation), while the control INF-γ Ab coated membranes accumulated 3.1 ± 0.1 ng. The BSA- blocked 3D9S membranes accumulated 0.9 ± 0.1 ng while the control anti-human INF-γ membranes accumulated 1.0 ± 0.1 ng. While not conclusive, this is one reason why it is important to evaluate the mass, rather than to rely solely on the resonance frequency shift measurement. There were differences in both the side length and the intrinsic stress of the active and control membranes that contributed to the difference in conclusions between the frequency shift results and the identical (within error) calculated mass on the surface.

There are several possible reasons for the equivalent mass recorded on the active and control membranes in the second experiment. One possibility is that the 3D9S Ab and/or FBDP batch used in the second experiment should have been replaced, because the mass from the

functionalization process (FBDP + Ab + BSA) was much less than in the previous experiment. In the first experiment the average functionalization mass was 2.8 ± 0.3 ng for the active chips while in the second experiment it was 1.3 ± 0.4 ng. Conversely, the average mass from the functionalization process for the control chips was 1.3 ± 0.2 ng in the first experiment and 3.3± 0.6 ng. This indicates that the quantity of 3D9S Ab on the membranes was much less than in the first experiment, thus potentially decreasing the quantity of BHV-1 captured. This may have been caused by Ab aggregation over time which can reduce the quantity available for functionalization.

While the results from the FBDP experiments were promising, further experiments were not possible because the sale of FBDP was discontinued by Sigma-Aldrich. Furthermore, because it is such a new and specific chemical, no other supplier exists. Otherwise the second experiment would have been repeated with fresh reagents. Instead, it was necessary to continue the experiments with a different linking process.

5.2. Silane linker chemistry

Silane is a gas with the chemical formula SiH_4. However, silanes as a group can also refer to all chemical compounds that include one or more silicon atoms. Similarly to carbon compounds, silicon atoms are commonly tetrahedral centers for the attachment of other elements. Unlike carbon, however, silicon does not form stable double bonds.

Silanes are used in a variety of applications and industries. Hydride functional silanes are used as intermediates for other silanes and silicones, epitaxial silicon deposition, high purity silicon metal production, reducing agents and elastomer intermediates. Tetrachlorosilane is used in the production of fumed silica. Methyldichlorosilane is an important organohydrosilane, which is used for waterproofing, to increase fabric wear resistance and for electronics applications. It is also employed to produce phenyl, vinyl, and cyanoalkyl precursors for silicone fluid production. The combination of methyldichlorosilane and fluorocarbon alkenes is used in gum, rubber and silicone fluid production.[222]

The organosilanes that are commonly utilized as coupling agents are trialkoxysilanes, particularly trimethoxy- and triethoxy- silanes. They are used to make organic coupling compounds and are used as adhesion promoters in plastics.[222] For linking procedures, functional

groups are added to the silanes, which can react with organic molecules. Examples of such functional groups include carboxyl groups, amino groups, aldehydes and epoxies.

When organosilanes are used for linking processes the first step in the chemical process is hydrolyzation of the alkoxy group(s) into free hydroxyl groups. These hydroxyl groups may then interact with other hydroxyl groups on the surface to be silanized and/or other hydrolyzed silane molecules. The best surfaces for silanization are those with silicon dioxide. Metals with hydrolytically stable surface oxides like tin, titanium and aluminum, and heavy metals (with high density) also generally work well. The effectiveness is largely based on the number of hydroxyls available for the reaction. Metals like zinc, iron and copper cannot be functionalized effectively with a silane because they have water-soluble oxides.[223,224] Therefore, alkoxysilanes should adhere well to the AlMo nanocomposite surface, both to the aluminum due to the hydrolytically stable surface oxide and to the molybdenum, because it is a heavy metal with an oxide that is not water soluble.

5.2.1. Vapour deposition of hexamethyldisilazane (HDMS)

Sandwich ELISAs are commonly performed where Abs adhere to the surface of hydrophobic polystyrene 96-well plates. This indicates that hydrophobic surfaces can be used to capture Abs. HMDS is a silane that is composed of a secondary amine with two trimethylsilyl groups. On contact with a surface, a replacement reaction takes place where the amine reacts with the hydroxyl groups on the surface to form ammonia, and trimethylsiloxy groups are formed on the surface. This increases the hydrophobicity of the surface. This linking process is therefore different from the others that are presented in this thesis, because the process makes use of a hydrophobic interaction, like those seen in a sandwich ELISA, rather than covalent bonding interaction to link the Abs to the surface.

5.2.1.1. Materials and Methods

Four AlMo coated chips were washed in acetone, IPA and water, and dried in a N_2 gas stream. The chips were cleaned for 5 minutes on each side in the UV-ozone cleaner. Two chips were then coated with HDMS in a Yield Engineering Systems HDMS oven. This vacuum oven

was used to drive off the moisture from the surface in order to create a stable uniform layer of trimethylsiloxy groups. Droplets of 3D9S antibody (100 μg/ml) were placed on one HDMS-coated chip and one bare AlMo chip. Droplets of INF-γ Ab (100 μg/ml) were placed on the other HDMS-coated chip and the other bare AlMo coated chip. After 1 hr the chips were washed in PBS and DI water, and then blocked with 1% BSA in PBS for 1 hr. The chips were again washed in PBS and DI water, and droplets of BHV-1 (90 μg/ml) were placed on all the chips. After 1 hr the chips were washed with PBS and DI water, and dried in a N_2 gas stream. The chips were then coated with 10 nm of Au and SEM imaging was performed. Subsequently, the linking process with the 3D9S Ab was implemented on 10 nm thick AlMo membranes and resonance measurements were performed.

5.2.1.2. Results and Discussion

SEM images illustrating the successful functionalization process are shown in Figure 5.13. The functionalization process was performed both with HDMS and without HDMS to evaluate whether the HDMS could effectively capture Abs. The quantity of BHV-1 captured by the HDMS and 3D9S Ab-coated active chip was significantly greater than for the control chip coated with HDMS and INF-γ Ab. Furthermore, HDMS was shown to be more effective than bare AlMo surface for Ab attachment. Less BHV-1 was captured by the 3D9S Ab coated active chip without HDMS than with HDMS, while more was captured by the control chip coated with INF-γ Ab without HDMS. This means that the the HDMS linking process led to increased specific binding and decreased nonspecific binding.

Resonance measurements were performed to further evaluate the HDMS-3D9S functionalization process. The average frequency shift from BHV-1 binding was observed to be 13 ± 7 kHz, and the average BHV-1 mass on the surface of the membranes was calculated to be 500 ± 300 pg (where the error is the standard deviation). This suggests that the frequency shift and BHV-1 capture were considerably less than those obtained with the FBDP, while the variation between membranes was greater. This was verified by comparing SEM images of BHV-1 on a HDMS-coated chip with BHV-1 on a FBDP-coated chip. It was clear that there are substantially fewer BHV-1 virus particles on the HDMS-coated chip (Figure 5.14). Since the resonance shift and the mass captured during the resonance experiment were substantially less

than those obtained for the first FBDP measurement, additional silanization methods were investigated.

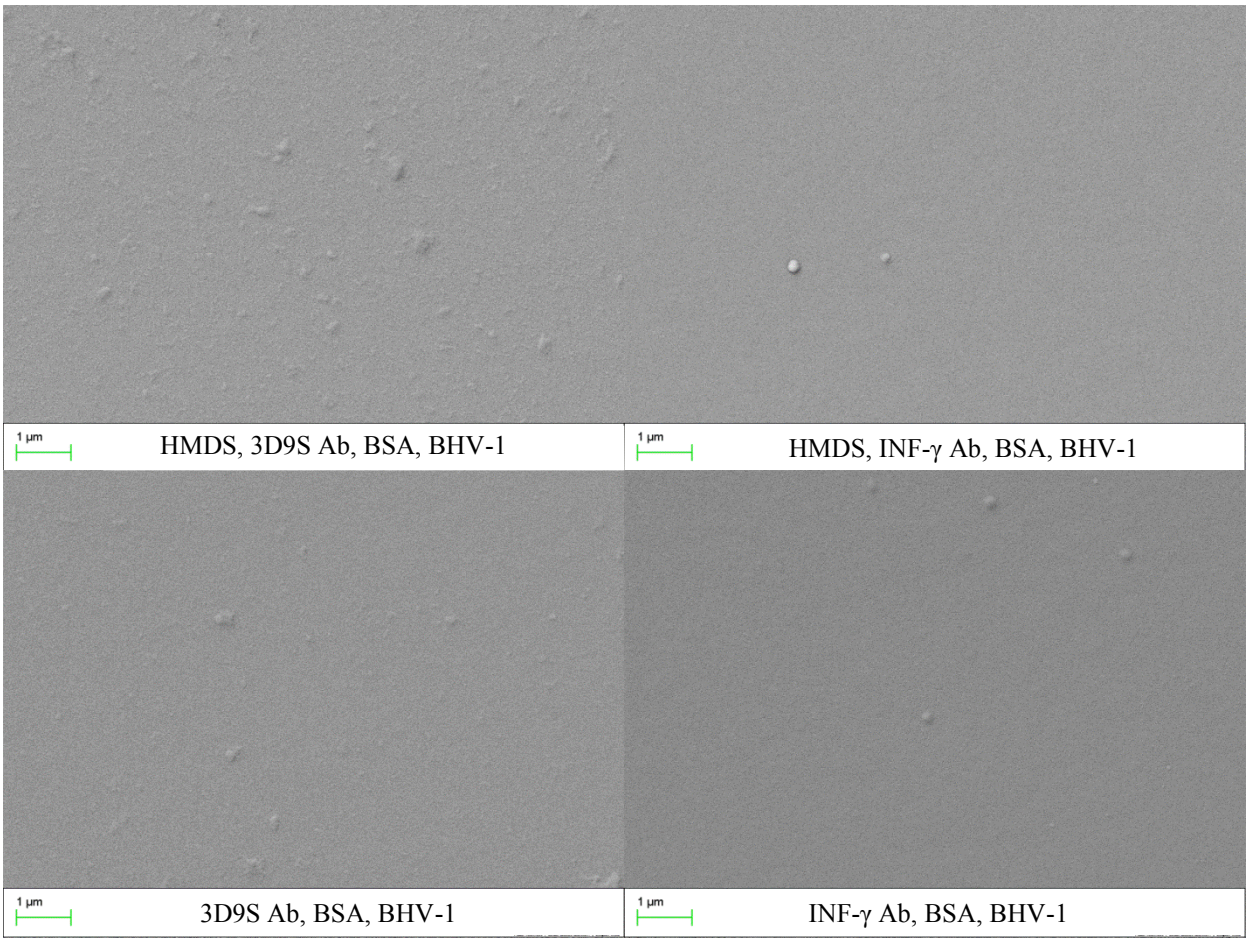

Figure 5.13: SEM images illustrating the effect of HMDS silanization. The functionalization materials are indicated below the images. There is a clear difference between the active chips and the control chips with HDMS linking, illustrating that the HDMS silanization leads to more BHV-1 capture than the bare AlMo chip, and that it is reasonably specific, as there is more BHV-1 on both 3D9S Ab chips than on the INF-γ control chips.

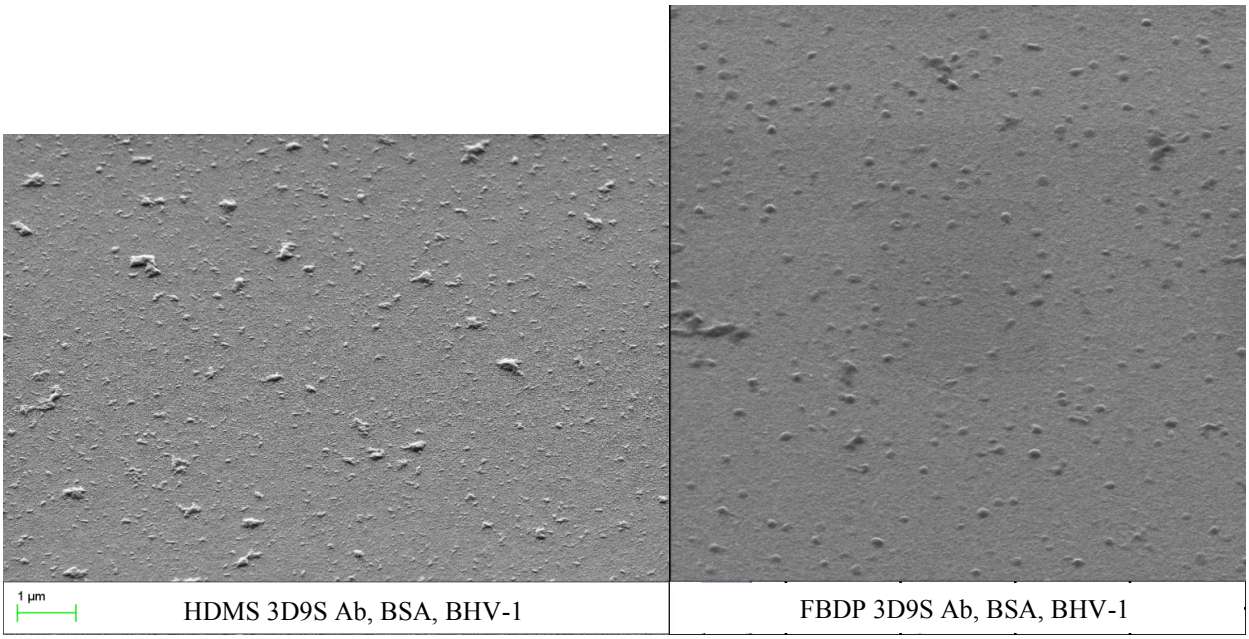

Figure 5.14: SEM image of the Au-coated HMDS-functionalized chip from Figure 5.13 and a helium ion microscope (HIM) image of the 3D9S Ab FBDP-functionalized membrane chip from Figure 5.6. The scale bar applies to both images. The BHV-1 virus particles are ~150-200 nm in diameter. There are fewer BHV-1 particles on the HMDS coated chip. There is some noticeable difference in contrast between the two images.

5.2.2. Epoxysilanization

The resonance frequency shift and captured BHV-1 mass observed for the HDMS silanization process were substantially less than for the FBDP experiments. For this reason, two epoxysilanes capable of covalent bonding were investigated. The two silanes that were used were GPTMS and GPDMES (Figure 5.15). Both compounds have epoxy functional groups, which can form covalent bonds with amines, acids, phenols, alcohols and thiols. They are identical except that one has three methoxy groups that can undergo hydrolysis, while the other only has one ethoxy group that can undergo hydrolysis. The advantage of three groups is that they may bind more securely to the surface, while the advantage of a single hydrolysable group is that there is no polymerization or multilayer formation. Methoxy and ethoxy groups function nearly identically except that the methoxy groups are slightly more reactive.[223]

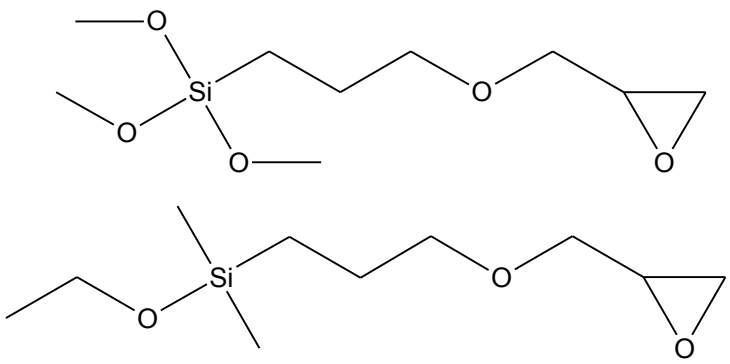

Figure 5.15: The structural formulas of the two epoxysilanes that were employed for membrane resonance-based mass detection. The GPTMS is shown on the top while GPDMES is shown on the bottom.

5.2.2.1. Materials and Methods

Contact angle measurements were performed to verify the attachment of silanes to the AlMo surface. The chips were washed in acetone, IPA and water, and they were dried in a stream of nitrogen gas. Subsequently, they were submerged for 0 min (no GPTMS), 1 min, 5 min or 60 min in 1% v/v GPTMS in either DI water or toluene. The 99% toluene was obtained from Sigma-Aldrich as were both epoxysilanes. The toluene solvent chips were washed in toluene and the water solvent chips were washed in water. All the chips were then washed with IPA and water, and were dried in a nitrogen gas stream. The contact angle was then determined for a droplet of water in contact with the silanized AlMo surface immediately after the silanization and again a week later.

The process was repeated with 1% GPTMS in toluene for 5, 30, 60, 120, 240 or 1140 min. Two chips were functionalized with 100 μg/ml 3D9S Ab in PBS for 1 hr following submersion for 240 or 1140 min in GPTMS. All the chips were washed in toluene, acetone, IPA and water, and dried in a nitrogen stream following silanization. Following functionalization with the Abs, the chips were washed in PBS and water, and dried in a stream of nitrogen gas. Three contact angle measurements were performed, separated by a period of 30 minutes.

Following the contact angle measurements, silanization in toluene was implemented for detection of hemorrhagic enteritis virus (HEV) and the HEV hexon protein. Hexon protein is a major adenovirus coat protein. The HEV, hexon protein and Abs specific to HEV and the hexon

were provided by Dr. Jan van den Hurk. An Ab specific to the hexon, termed 11B6, was purified using the same method as described for the 3D9S Ab in section 5.1.2.1. The AlMo-coated silicon chips were washed in acetone, IPA and water, and dried in a stream of nitrogen gas. Each side of the chip was exposed to the UV and ozone in the UV-ozone cleaner for 5 min. They were then submerged in 1% GPTMS in toluene for 1.5 hr, washed in toluene, IPA and DI water, and dried in a stream of nitrogen gas. Subsequently, 50 µl droplets of 300 µg/ml 11B6 Ab in PBS were placed on select chips for 1 hr. The chips were washed 2 x in PBS and 1 x in DI water, and dried with nitrogen gas. A droplet of 1:5 diluted HEV or hexon in PBS was each placed on a 11B6 Ab-functionalized chip for 1 hr. They were then washed 2 x in PBS and 1 x in DI water, and dried with nitrogen gas, and HIM images were taken. The process was repeated twice with GPDMES instead of the GPTMS, and imaging was again performed.

In addition to the HEV and hexon experiments, Ab linking with GPTMS in DI water for BHV-1 capture was examined. Chips were washed in acetone, IPA and DI water, and dried in a stream of nitrogen gas. Each side of the chip was cleaned in the UV-ozone cleaner for 5 min. The UV-ozone process serves the dual purpose of cleaning the chip surface and inducing the formation of hydroxyl groups on the surface. The chips were subsequently placed in 1% GPTMS in DI water for 0, 5, 10, 20, 40 and 60 min, respectively. They were washed in DI water and dried in a stream of nitrogen gas. All the chips were functionalized with 100 µg/ml 3D9S Ab for 1 hr, washed in DI water and dried in a stream of nitrogen gas. One chip that was silanized for 60 min was submerged in 100 µg/ml BHV-1 in PBS, while all the other chips were placed in contact with 100 µg/ml BHV-1 by placing 50 µl droplets on the surface. A HIM was used to take images on the surfaces.

A comparison of 3D9S- and INF-γ- coated chips that were both silanized with GPTMS in water was performed. Two chips were cleaned as in the previous experiment, coated with 1% silane in DI water for 1 min, and then washed in DI water and dried in a stream of nitrogen gas. One chip was submerged in 100 µg/ml 3D9S Ab for 1 hr, while the other was submerged in 100 µg/ml INF-γ Ab for 1 hr. They were then washed 2 x in PBS and 1 x in DI water, and dried in a stream of nitrogen gas. The chips were submerged in 100 µg/ml BHV-1 for 1 hr and then washed 2 x in PBS and 1 x in DI water and dried in a stream of nitrogen gas. A HIM was used to take images on the surfaces.

The previous experiment was repeated with a 1% BSA in PBS submersion step following the Ab incubation step. Again two washes in PBS and one in DI water were performed, followed by drying with nitrogen gas. Finally, AlMo membranes 20 nm thick were functionalized with GPTMS, 3D9S Ab and BSA, and used for BHV-1 capture as in the previous experiment. The resonance measurements were performed as in section 5.1.2.1.

5.2.2.2. Results and Discussion

The first silanization step was performed with varying submersion times in GPTMS. Two different solvents were evaluated: water and toluene. The results are shown in Table 5.1. It is evident that the GPTMS in water clearly reached a much larger contact angle much more quickly than the GPTMS in toluene. Interestingly, when the contact angle was determined for the same chips one week later, the contact angle for each sample had increased. It is possible that the silanization process was not yet complete due to incomplete dehydration of the surface.

Table 5.1: Contact angle of AlMo-coated chips following submersion in 1% GPTMS.

	Immediate measurement		One week later	
Time (±0.1 min)	Toluene (± 1°)	Water (± 1°)	Toluene (± 1°)	Water (± 1°)
0	27	27	28	28
1	26	59	53	61
5	40	61	50	66
60	39	64	50	80

The process was repeated for the 1% GPTMS in toluene and longer salinization times. Silanization via toluene is generally preferable, because silanization in water may lead to more polymerization, and therefore to the formation of a thicker layer of silane. This can decrease the sensitivity of the sensor, and in some experiments led to the destruction of 10 and 20 nm thick membranes. The results are shown in Table 5.2.

It is likely that the change in the silanization measurement over time was due to the presence of water on the surface. It is interesting to note the increase in hydrophobicity of the

Ab-coated chips between measurements. A possible cause may be that the rehydration of the Abs on the surface changes the configuration of the protein.

Subsequently, the same linking procedure was used to detect HEV and the HEV hexon protein with a specific Ab, 11B6. HIM images are shown in Figure 5.16. There was a clear difference between the 11B6 Ab chip and the 11B6+hexon chip, indicating successful capture of the hexon protein. Furthermore, while it is less obvious, closer examination of the 11B6 and 11B6-HEV chips revealed a clear difference, indicating capture of HEV. Since the hexon protein produced a more obvious visual change, it was used in further experiments. The same process was repeated twice with GPDMES instead of the GPTMS, and imaging was performed (Figure 5.17-18). Again, there was a clear difference, indicating hexon protein binding.

Table 5.2: Contact angle measurement for the AlMo chips following submersion in 1% GPTMS in toluene. The time indicates the period the chips were submerged in the silane solution. One 240 min and one 1140 min GPTMS-functionalized chip were coated with 100 μg/ml Ab solution before the contact angle measurement was performed. The measurements 1, 2, 3 were performed with a 30 minute separation.

	Silane measurement (± 1°)			Silane + Ab measurement (± 1°)		
Time (±0.1 min)	1	2	3	1	2	3
5	29	25	26	-	-	-
30	44	37	38	-	-	-
60	48	47	41	-	-	-
120	50	51	51	-	-	-
240	52	53	51	45	59	61
1140	53	51	51	58	62	-

Several experiments were performed with GPTMS in toluene to link 3D9S Ab to AlMo-coated chips for the capture of BHV-1, but with minimal success. Instead, silanization in DI water was examined. BHV-1 capture seemed to be considerably greater for all the silanized chips and unaffected by the silane submersion period when water was used instead of toluene (Figure 5.19). It is interesting to note, however, that submersion in the BHV-1 solution seemed to lead to substantially more BHV-1 capture than when the BHV-1 droplets were used.

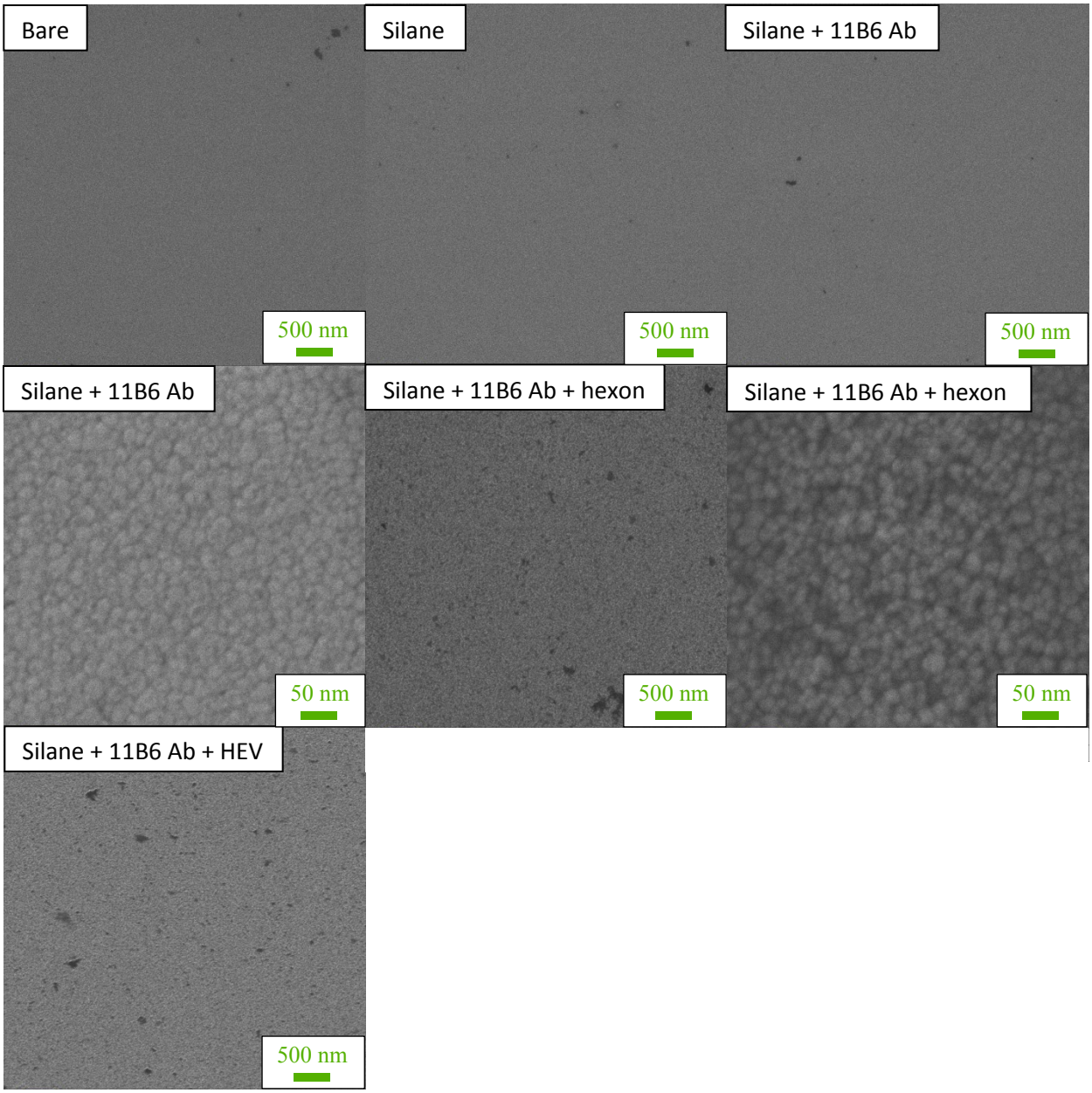

Figure 5.16: HIM images of AlMo-coated chips illustrating GPTMS silanization, functionalization with 11B6 Ab and capture of hexon protein and HEV.

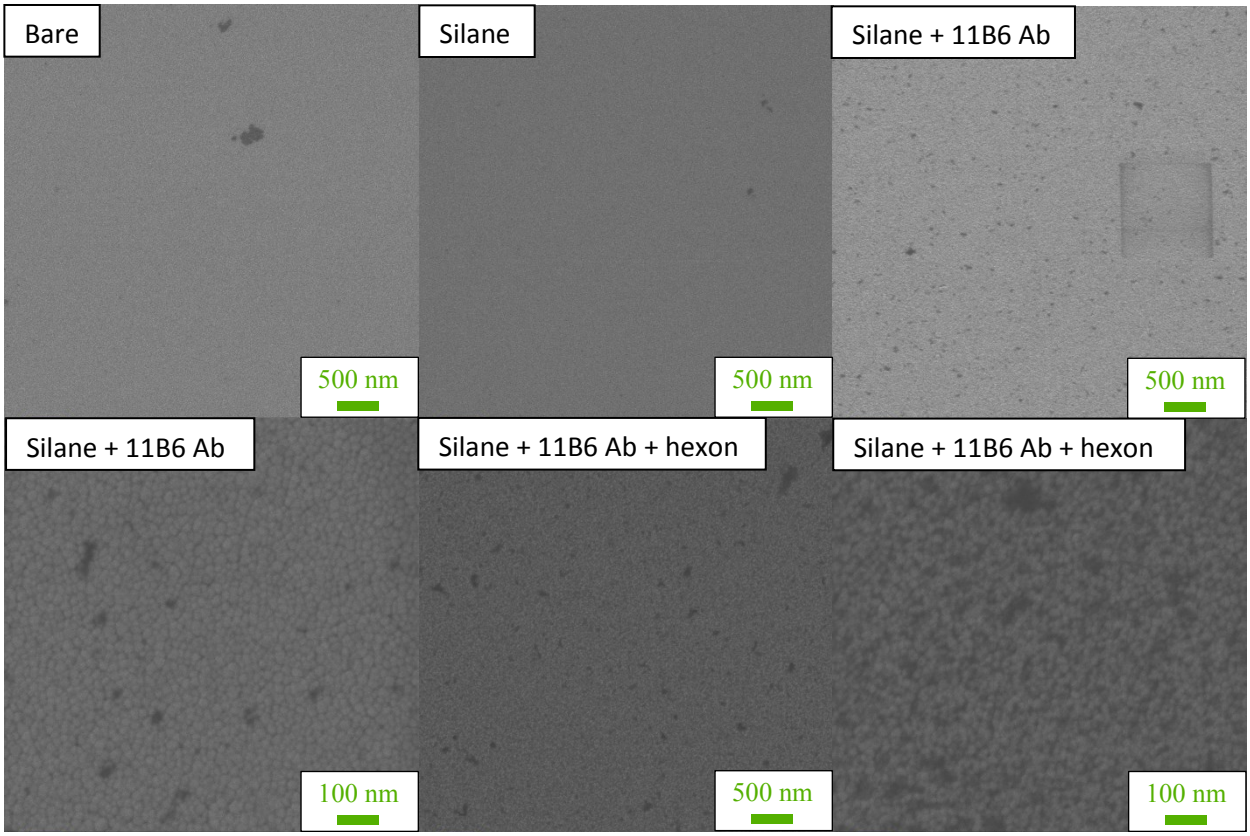

Figure 5.17: HIM images of AlMo-coated chips illustrating silanization (GPDMES), functionalization with 11B6 Ab and capture of hexon protein.

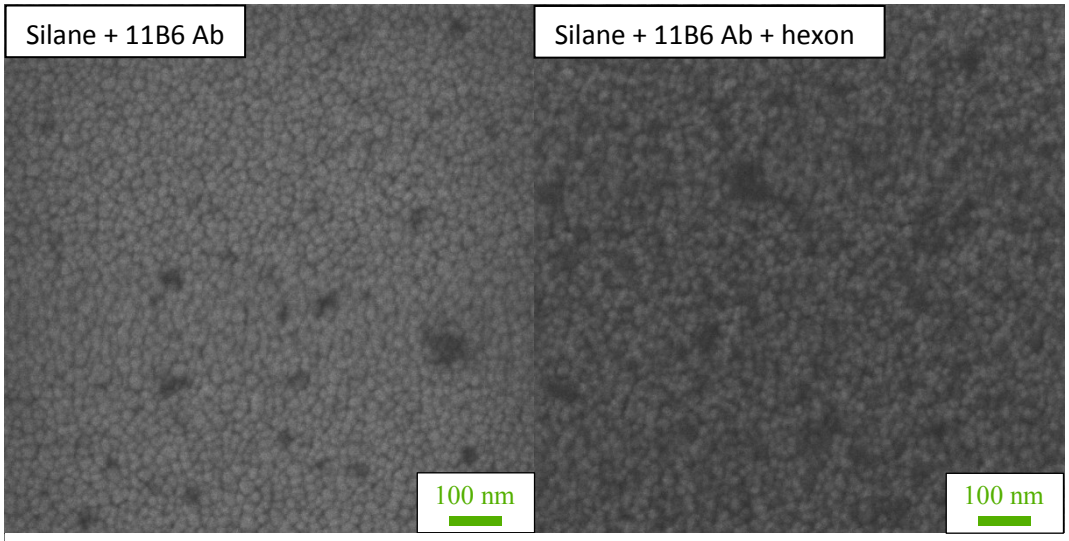

Figure 5.18: HIM images of AlMo-coated chips illustrating the difference between the 11B6 Ab functionalized chip and the captured hexon protein chip. The silane was GPDMES.

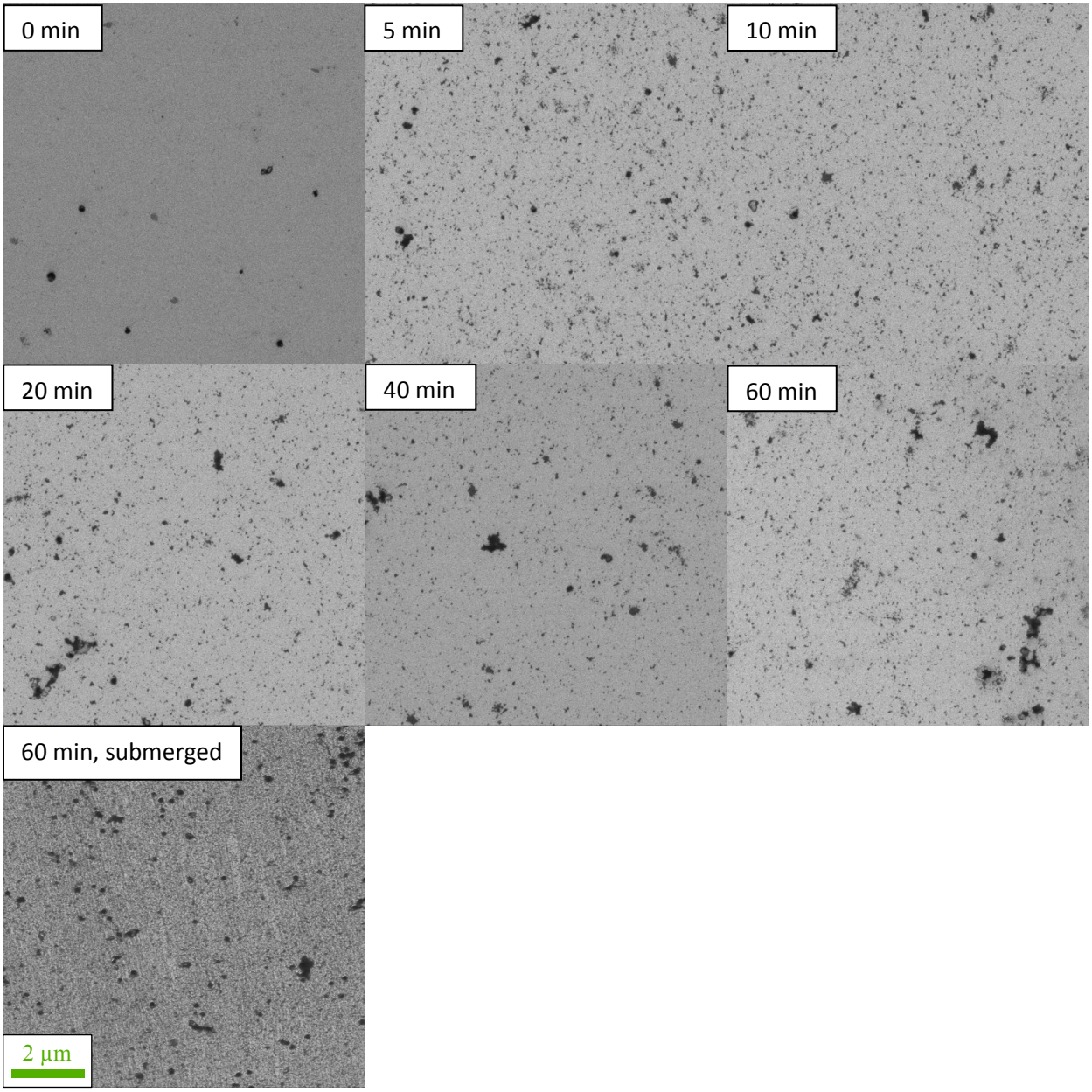

Figure 5.19: Helium ion microscope (HIM) images of BHV-1 captured by 3D9S Ab that was linked via GPTMS to the AlMo-coated chips. The chips were submerged in 1% GPTMS in water for different periods as indicated, functionalized with 3D9S Ab and used for BHV-1 capture. All the chips but one had a droplet of BHV-1 solution placed on them, while the last chip was fully submerged in the BHV-1 solution. The scale bar applies to all the images.

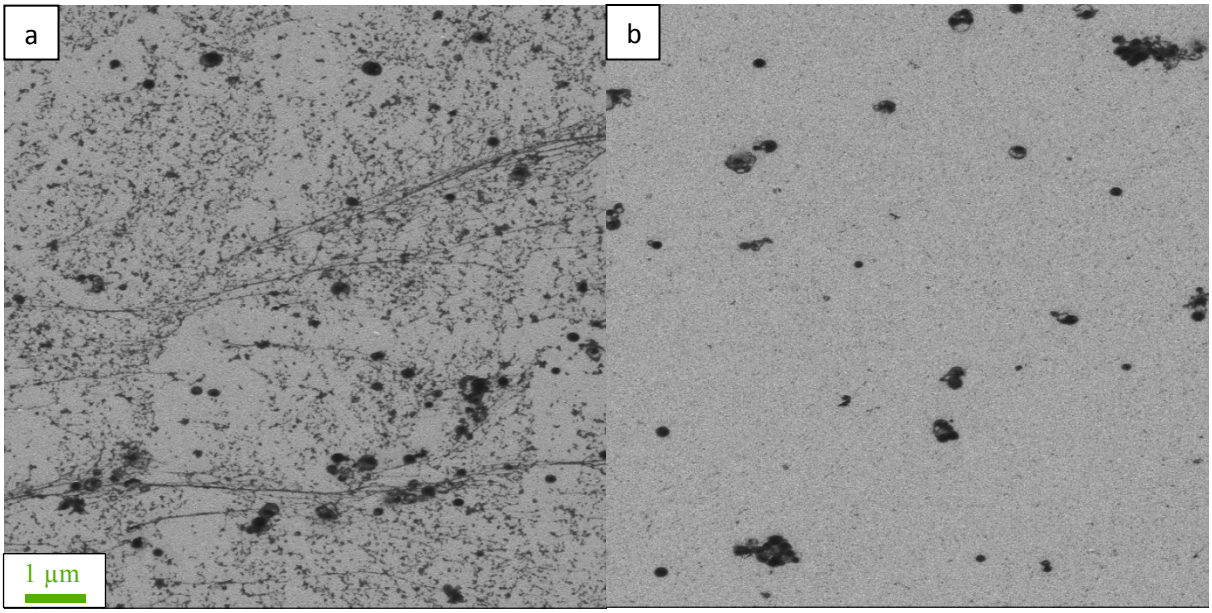

Figure 5.20: HIM images of BHV-1 binding on a) active 3D9S-functionalized chips and b) control anti-human INF-γ Ab-functionalized chips. Both chips were silanized with GPTMS. The larger round ~150 nm diameter particles are BHV-1. This was confirmed by the presence of the tegument and envelope surrounding the central raised capsid region. The smaller particles and streaking effects are only present on the 3D9S Ab active chip and not the control chip.

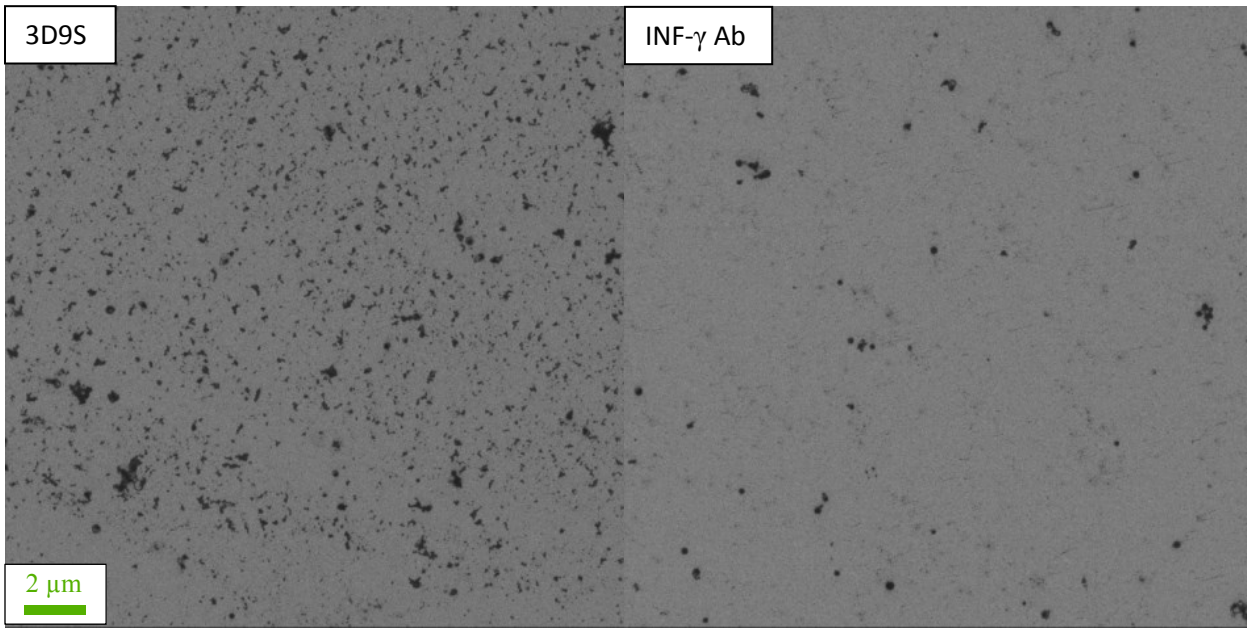

Figure 5.21: HIM images of BHV-1 capture by BSA-blocked 3D9S Ab and INF-γ Ab chips that were silanized by GPTMS in water.

Based on these results, further experiments were performed with silane in water. Images of the chips are shown in Figure 5.20. Whole virus particles were captured on the 3D9S Ab chip. Additionally, smaller particles were present on 3D9S Ab chip, as well as what appears to be streaks of material. Some whole virus particles were also present on the control chip surface. BSA was used as a blocking agent in subsequent experiments to examine whether the smaller particles, streaking effects and virus particles on the control chip were due to nonspecific binding.

The previous experiment was repeated with BSA blocking. Images of the chips are shown in Figure 5.21. Examination of the images suggests roughly four-fold less material on the control chip than on the 3D9S chip.

To measure the change in resonance frequency caused by BHV-1 capture, the previous process was implemented on AlMo membranes. AlMo membranes 20 nm thick were functionalized with GPTMS, 3D9S Ab and BSA, and used for BHV-1 capture as in the previous experiment. The resonance measurements were performed as in section 5.1.2.1. The average frequency shift from BHV-1 binding was 8 ± 1 kHz, and the average mass of BHV-1 on the membranes was 370 ± 50 pg, where the error is the standard deviation. Because this resonance frequency shift and the associated bound mass of BHV-1 were relatively small compared to the FBDP experiments, a different approach was warranted.

5.2.3. APTES and glutaraldehyde functionalization

The SEM images of BHV-1 capture where GPTMS was used as the linking chemical showed substantially more virus capture on the 3D9S Ab active chip surface than the INF-γ Ab control chip. Furthermore, the SEM images showed considerable capture of hexon protein. The resonance frequency shift and average bound mass of BHV-1 was substantially smaller than with the FBDP linking process, however. A concern with GPTMS, especially when in water, is that a large portion of the silane may be polymerizing in the solution and not reaching the surface, or it may be creating an uneven layer of silane on the surface. This polymerization may occur because the methoxy groups may bond with one another and/or the epoxy groups may bind to the methoxy groups after they are hydrolyzed.

An alternative linking process is the deposition of APTES on the surface, followed by glutaraldehyde. APTES is silane with three ethoxy reactive groups and an amine functional group. The ethoxy reactive groups are slightly less reactive than the methoxy groups in the GPTMS, which reduces the probability of polymerization. Furthermore, the amine group does not react with the ethoxy groups. Glutaraldehyde is a bifunctional molecule with two aldehydes. When it is introduced to the amines on the surface following the silanization process, one end can react with an amine on the surface leaving the other aldehyde free to react with amines on the surface of proteins in order to anchor them to the AlMo surface.

Another change that was made was that bacteria, specifically *M. smegmatis* and *M. avium*, were investigated in addition to the HEV hexon. This change was made because bacteria are substantially more massive than virus particles and should therefore result in a greater added mass and resonance frequency shift. Because they are larger, it can also make imaging more straightforward and less expensive. Furthermore, a bacteriophage tail spike protein (TSP)[225] was used to capture the bacteria. As before, the capture experiments were first performed on AlMo-coated chips, and were then implemented on membranes for resonance measurements.

5.2.3.1. Materials and Methods

Seven AlMo-coated chips were washed in acetone, IPA and DI water, and dried in a stream of nitrogen gas. Each side of the chips was exposed in the UV-ozone cleaner for 5 min. The chips were dipped in DI water and dried in a nitrogen gas stream. Six of the chips were immediately placed in 1% v/v APTES in toluene for 1 hr. They were then washed sequentially in toluene, IPA, and DI water. One chip was dried with nitrogen gas. The five remaining chips were placed in 2% v/v glutaraldehyde in PBS for 1 hr. They were then washed in PBS and DI water, and dried with nitrogen gas. Of the four remaining chips, one had a 1% (10 mg/ml) BSA in PBS droplet placed on it, while each of the other 3 had a 50 µl droplet of 500 µg/ml GP10 phage TSP placed on them. They were then washed in PBS and DI water, and dried with nitrogen gas. The BSA chip and one GP10 chip were covered with 50 µl droplets of *M. smegmatis*. One other GP10 chip was covered with a 50 µl droplet of 1 to 4 (*M. smegmatis* to PBS) diluted *M. smegmatis* for 1 hr. Subsequently, they were washed in PBS and DI water, and dried with the nitrogen gas. SEM imaging was performed. The TSP and 1 x 10^9 cell/ml *M. smegmatis* were

obtained from Dr. Upasana Singh. The APTES, glutaraldehyde and cysteamine were all obtained from Sigma-Aldrich. This process was repeated for *M. avium*, with an additional submersion in 4% formaldehyde in PBS for 1 hr to kill the bacteria. This process was then repeated on 20 nm thick membranes with *M. avium* and the resonance frequencies were determined as in section 5.1.2.

The effect of APTES + glutaraldehyde linking process on AlMo-coated chips was compared with a cysteamine + glutaraldehyde linking process on an Au-coated surface for the purpose of capturing hexon protein. The AlMo and 20 nm thick Au-sputtered chips were washed in acetone, IPA and DI water, and dried in a stream of nitrogen gas. Each side of the chips was exposed in the UV-ozone cleaner for 5 min. The Au chips were placed in 50 mM cysteamine-HCl in DI water for 1 hr. Two AlMo chips were placed in 1% APTES in toluene for 1 hr. The silanized chips were washed in toluene and IPA, and all the chips were washed in DI water and dried in a nitrogen gas stream. The chips were placed in 2% v/v glutaraldehyde in PBS for 1 hr. They were washed in PBS and DI water, and dried with nitrogen gas. One AlMo and one Au chip each had a 50 µl droplet of 600 µg/ml 11B6 Ab in PBS placed on them for 1 hr. They were washed in PBS and DI water, and dried with nitrogen gas. The chips were then blocked for 30 min with 1% BSA in PBS, and then washed in PBS and DI water, and dried with nitrogen gas. Droplets of hexon protein were placed on all the chips for 1 hr, and the chips were all washed in PBS and DI water, and dried with nitrogen gas. Imaging was performed with the HIM. The process was subsequently repeated on AlMo membranes. The square membranes were 430 um in width and 20 nm thick and resonance measurements were performed. Finally, the membrane experiment was repeated without the 11B6 Ab step, thus treating BSA as a control/blocking protein.

5.2.3.2. Results and Discussion

Linking with APTES and glutaraldehyde was performed for the capture of *M. smegmatis* on AlMo chips. The images are shown in Figure 5.22. The dark regions in Figure 5.22b were almost certainly APTES. In Figure 5.22c the glutaraldehyde appeared to increase the thickness of these regions. The GP10 did not seem to significantly alter the thickness of the dark regions, but the bacteria seemed to bind specifically to these areas. The lack of continuous APTES coverage

likely reduced the capture of the *M. smegmatis*. The density was 9 bacteria / 100 μm^2 and 3.4 bacteria / 100 μm^2 for undiluted and ¼ diluted *M. smegmatis*, respectively.

While it is generally important to avoid excessive polymerization, a discussion with Dr. Jonathan Veinot resulted in the conclusion that the silanization experiments in toluene were lacking in water, which is necessary for silanization to occur. This issue can be a particularly severe in the winter in Edmonton as humidity in the air decreases. For this reason, the chips in this experiment were dipped in water and briefly dried to increase the availability of water on the surface. This is an imprecise method to increase the quantity of available water during the silanization process, however, which may account for the difficulties that were experienced when the experiment was repeated. The process was also repeated with *M. avium* and after the binding of the *M. avium* to the surface, the bacteria were inactivated by being placed in 4% formaldehyde in PBS for 1 hr. It was evident following imaging that there was much less APTES and glutaraldehyde on the surface of the wafers (Figure 5.23b and 5.23c). Furthermore, from Figure 5.23 d, e and f it is evident that there was substantial variation in the distribution of the *M. avium* across the surface of the chip.

This process was repeated on membranes with GP10 to detect *M. avium*. The average frequency shift was 20 kHz with a σ of 27 kHz. The resonance frequency change for each membrane is shown in Table 5.3. The average mass and standard deviation of *M. avium* on the surface were determined to be 4 ± 6 ng as determined by equation [6]/[7]. Clearly, the *M. avium* was not evenly distributed across the membranes however, leading to a large standard deviation. This means that the distribution of bacteria was highly variable, and that equation [6]/[7] is likely no longer accurate. Therefore, while the calculated values of the mass of bacteria on the surface are given in Table 5.3, they should be taken as approximate figures only.

SEM images were taken of the membranes in order to ascertain the accuracy of the measurements. It was difficult to accurately assess the quantity of *M. avium* on the surface based on the SEM images. It is evident, however, that there were substantially more bacteria on the surface of membrane 5 (Figure 5.24) than on the other membranes shown, and that this corresponded to the greatest frequency shift and calculated mass of *M. avium*. This supports the hypothesis that the frequency shift results and mass calculations are related to the mass of material on the surface of the membranes.

As an alternative to the bacterial detection, APTES + glutaraldehyde linking on AlMo coated chips was compared with cysteamine + glutaraldehyde linking on an Au-coated surface for the purpose of capturing hexon protein. HIM images are shown in Figure 5.25. The bare chip without silane (Figure 5.25a) was clearly different from the silanized and aminated chips. This suggests that there was little nonspecific binding of the hexon protein to the bare AlMo surface. The Au chip results appeared to be quite different from the AlMo chip results. The hexon proteins appeared to be much more visible on the Au-coated surface than on the AlMo coated chips (Figure 5.25b-e). One possible reason for this is that the Au-sputtered layer is very thin (only 20 nm thick), which means that the grain structure is not visible. However, there appeared to be more material on the control chip (Figure 5.25e) than the active chip (Figure 5.25d) for the cysteamine functionalization. This indicates that the hexon protein may bind to BSA, suggesting that it is not an appropriate blocker for the hexon protein.

Resonance measurements were performed to measure hexon capture using the previous capture procedure with APTES and glutaraldehyde. The average mass of hexon on the active 11B6 coated membranes was 1.2 ± 0.2 ng, where the error is the standard deviation. The experiment was repeated without the 11B6 Ab step, thus treating BSA as a control/blocking protein. The average mass of hexon attached to the membranes was 4.5 ± 0.5 ng. Since the standard deviation was reasonably low, it is fair to assume a reasonably evenly distributed mass of hexon protein, which means that the mass calculation is likely accurate. This agrees with the HIM images shown in Figure 5.26, where it appears that there is more protein on the BSA control chip than the active 11B6-coated chip. This means that BSA is not a good control or blocking compound for the hexon protein. The binding of hexon protein to BSA is likely due to the hexon's structure. Hexon proteins have both exposed hydrophobic and hydrophilic regions. This means that it can be difficult to find an appropriate blocking agent, as it can bind to both hydrophobic and hydrophilic surfaces.

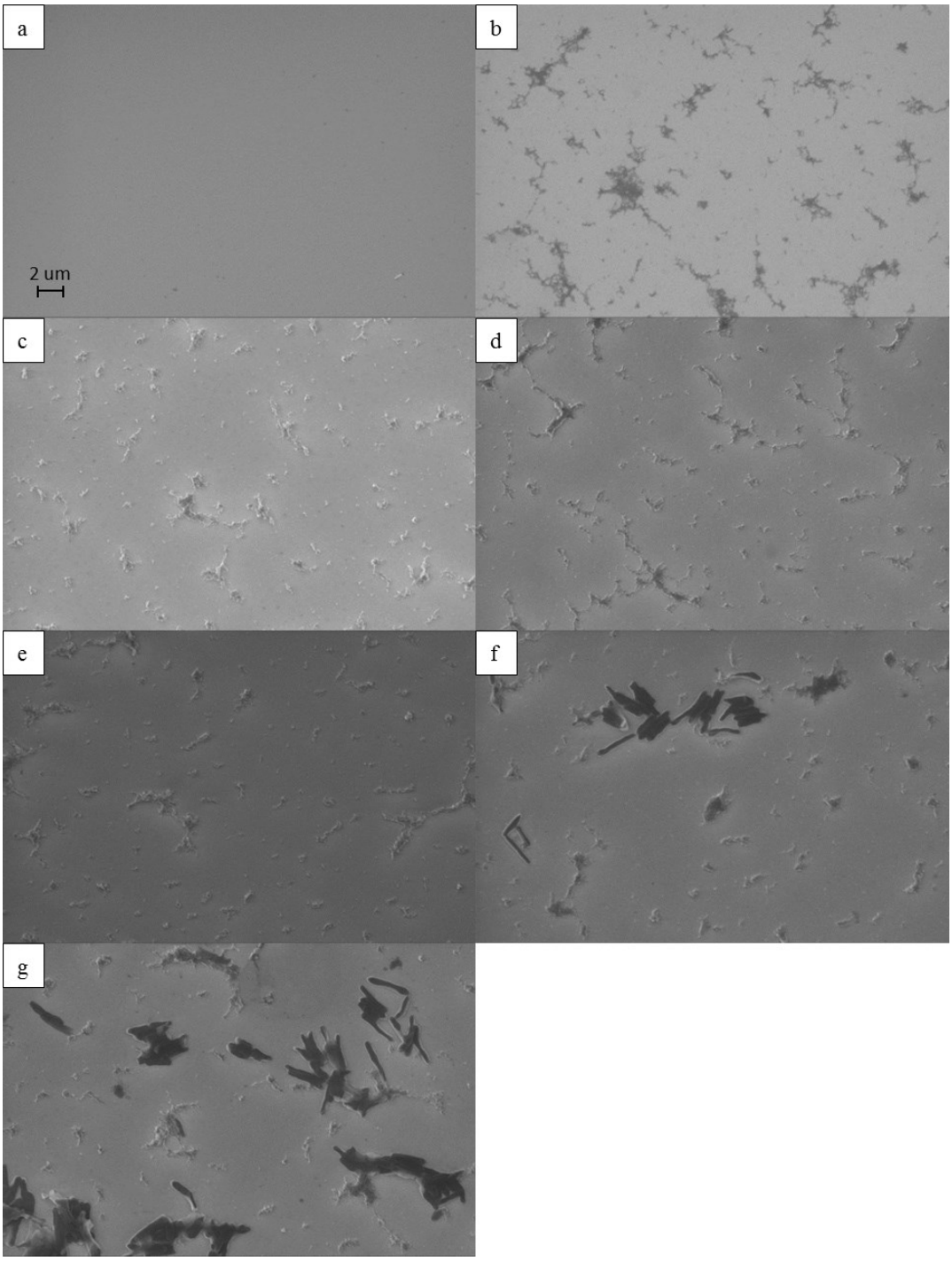

Figure 5.22: SEM images of the AlMo functionalization process and detection of *M. smegmatis*. The scale bar shown in a) is valid for all the images. a) bare AlMo, b) APTES, c) APTES + glutaraldehyde, d) APTES + glutaraldehyde + GP10, e) APTES + glutaraldehyde + BSA + *M. smegmatis*, f) APTES + glutaraldehyde + GP10 + ¼ *M. smegmatis*, g) APTES + gluteraldehyde + GP10 + *M. smegmatis.*

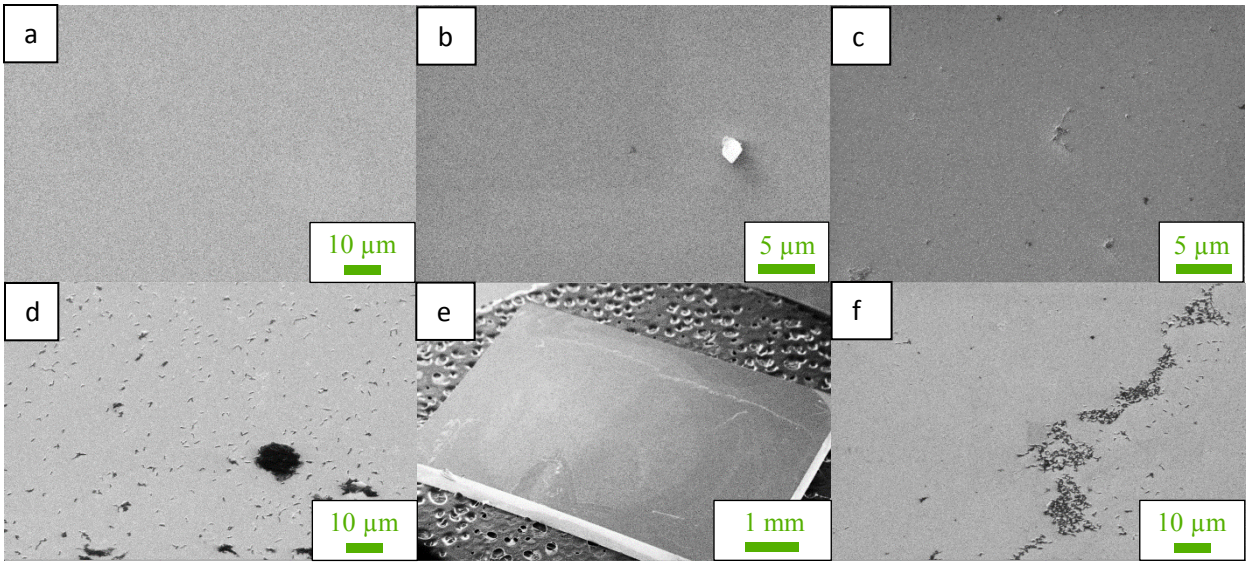

Figure 5.23: SEM images of the functionalization and *M. avium* detection on AlMo-coated chips. a) bare AlMo b) APTES c) APTES + glutaraldehyde + GP10. The last three images c), d), e) and f) are all from the same chip with APTES + glutaraldehyde + GP10 + BSA + *M. avium*. They show the variation in *M. avium* density on the chip surface.

Table 5.3: Frequency shift and associated mass of *M. avium* captured as calculated by equation [6]/[7]. The calculated mass of *M. avium* is only approximate. The membranes were functionalized with APTES, glutaraldehyde and GP10, and blocked with BSA before *M. avium* capture.

Membrane	Δf (± 2kHz)	*M. avium* (ng)
1	13	2.5
2	1	0.2
3	59	13.7
4	-1	-0.2
5	72	16.4
6	3	0.5
7	17	3.5
8	-1	-0.2
9	14	2.7

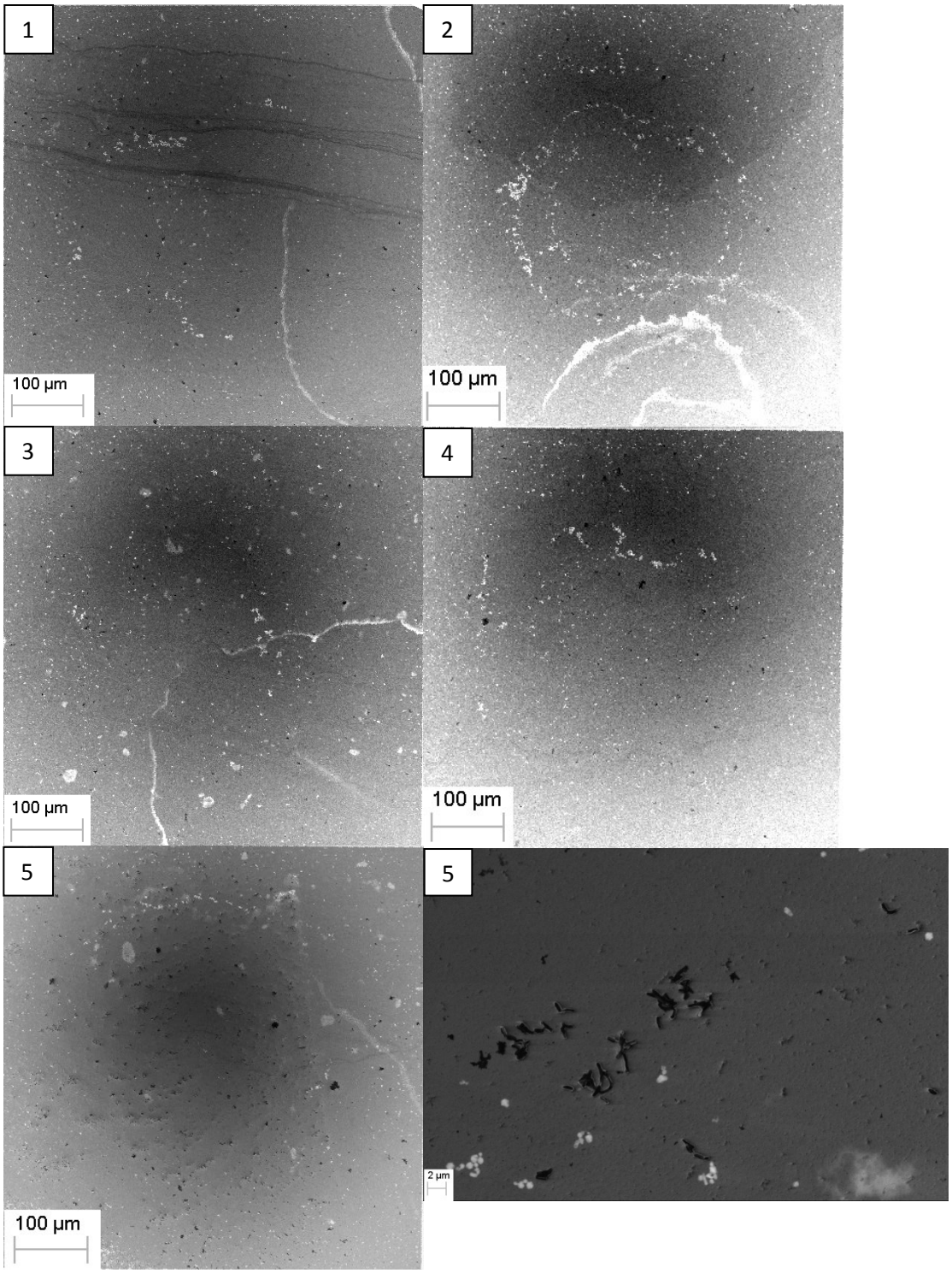

Figure 5.24: SEM images of membranes with the resonance frequency shifts shown in Table 5. The numbers match the numbers in Table 5. The membranes were functionalized with APTES, glutaraldehyde and GP10, and blocked with BSA before *M. avium* capture was performed. The black flecks in the lower magnification images are the *M. avium*.

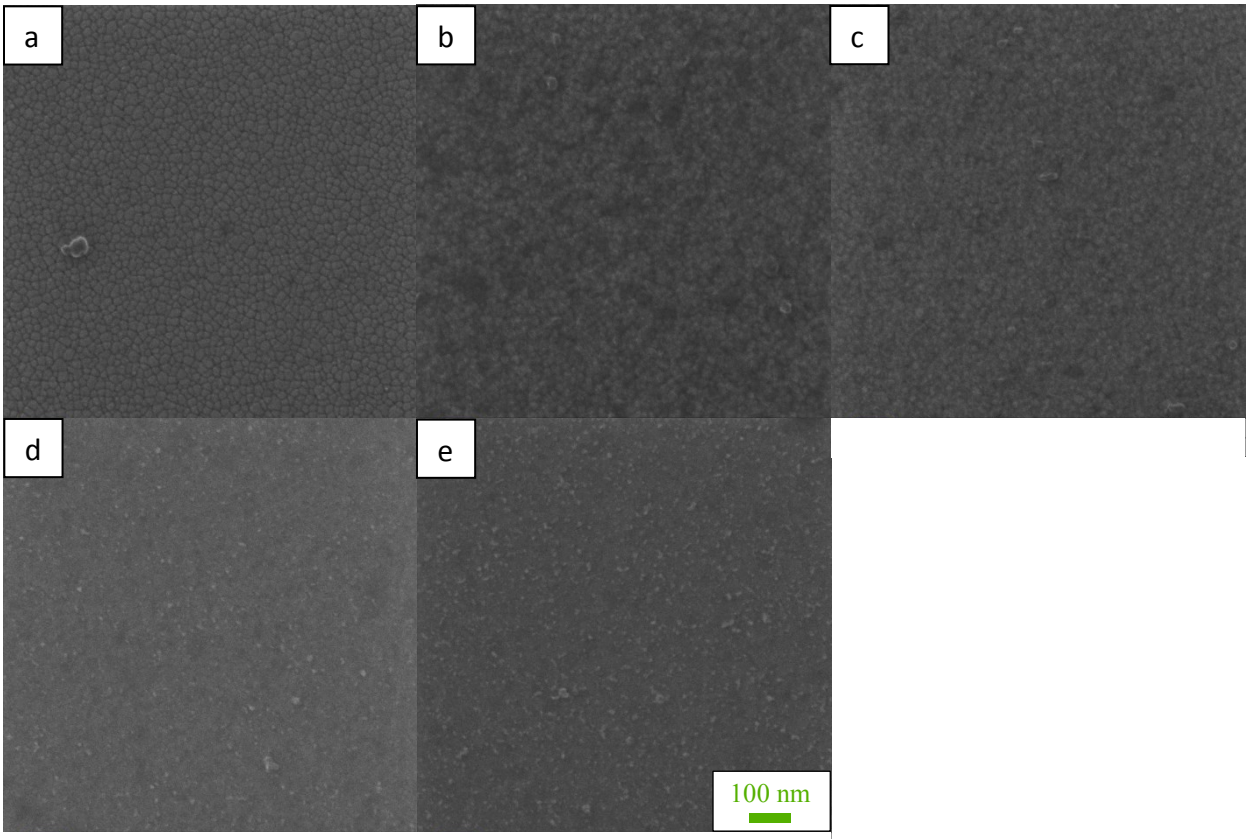

Figure 5.25: HIM images of chips used for hexon capture. The APTES and glutaraldehyde were applied to the AlMo coated chips and the cysteamine was applied to the Au coated chips. a) Glutaraldehyde, 11B6 Ab, BSA, hexon. b) APTES, glutaraldehyde, 11B6 Ab, BSA, hexon. c) APTES, glutaraldehyde, BSA, hexon. d) cysteamine, glutaraldehyde, 11B6 Ab, BSA, hexon. e) cysteamine, glutaraldehyde, BSA, hexon. The scale bar applies to all the images.

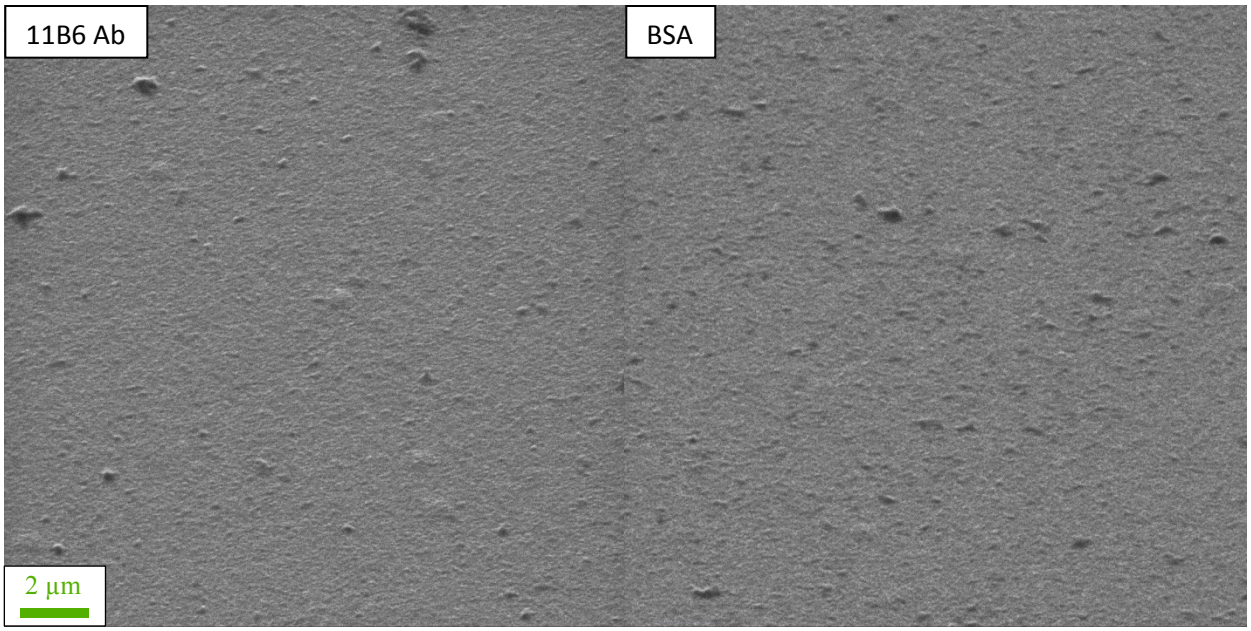

Figure 5.26: Representative HIM images of the membranes used for hexon detection. Both sets of membranes were silanized with APTES and glutaraldehyde was used to link 11B6 Ab or BSA to the membrane surface before they were used to detect hexon protein binding.

5.2.4. Vapor phase APTES deposition

A number of different silanes and methods of silanization in solvents were presented in the previous sections. Some protocols emphasize the importance of absolutely dry surfaces and solvents for successful silanization using liquid phase solvents. After substantial effort using different variations of the process it was determined that when toluene was used, it contained too little water for the reaction to proceed at a reasonable rate. This was illustrated when incompletely dry samples were placed in APTES solution and darker silanized regions formed where the glutaraldehyde and later the GP10 and bacteria would bind. Some large-scale commercial silanization processes involve dipping a substrate in water and then placing it directly into a silane solution. This is not ideal for a sensor, however, where a thin, uniform layer of silane is preferred. For this reason a dry silanization process was adopted for the final biosensor experiments.

5.2.4.1. Materials and Methods

In order to create a more uniform functionalized surface, a simple method of vapor phase deposition was used. Five AlMo-coated chips were cleaned via a RIE for 90 s with an O_2 flow rate of 50 sccm, a pressure of 150 mTorr and an RF power of 225 W. The chips were then placed upside down in a plastic petri dish lid with a hole cut in it. A glass petri dish with 500 µl of APTES was placed in the bottom of a desiccator. The plastic petri dish lid with the chips on it was place over top of the glass petri dish in the desiccator. The desiccator was then evacuated using the building vacuum line. The chips were left in the desiccator for 2 hr. Subsequently, the chips were rinsed in acetone, dried with nitrogen gas and baked at 110°C for 1 hr on a hotplate. The heater was then turned off and the chips were allowed to cool for 20 min. The chips were placed in 2% glutaraldehyde in PBS for 1 hr, rinsed in PBS and DI water, and dried in a nitrogen gas stream. Droplets of GP10 protein were placed on the chips for 1 hr. The chips were again rinsed in PBS and DI water, and dried with nitrogen gas. The chips were then placed in 1% BSA in PBS for 30 min, followed by washing in PBS and DI water, and drying with nitrogen gas. The chips were placed in $1.6x10^9$ cells/ml *E. coli* or $5 x 10^9$ cells/ml *M. avium* for 1 hr. They were rinsed in PBS and in DI water, and placed in 4% formaldehyde in PBS for 1 hr. Finally, they were again rinsed in DI water and dried.

Chips were removed at various stages of the process to observe the results. Chip 1 was cleaned with oxygen plasma as stated previously, and was then heated at 110°C for 1 hr to serve as a control to the other chips. Chip 2 was coated with APTES and heated at 110°C. Chip 3 was removed after the glutaraldehyde reaction. Chip 4 was allowed to react with *E. coli*, while Chip 5 was allowed to react with *M. avium*. All the chips were examined in the SEM. The previous process was repeated on AlMo membranes for *M. avium* detection, with *E. coli* as a negative control.

5.2.4.2. Results and Discussion

Vapour phase deposition of APTES and glutaraldehyde linking of GP10 was performed for the capture of *M. avium*. The resultant SEM images are shown in Figures 5.27 and 5.28. The brightness and contrast were identical for all the chips. It is clear that there was a substantial

change in the surface structure after the addition of the APTES. This is particularly evident when viewing the high magnification images on the right (Figure 5.27). There also appears to be a visual difference following the addition of glutaraldehyde, but this is more difficult to conclude definitively. Few *E. coli* were observed to be bound to the GP10, while many *M. avium* were observed on the GP10 surface. Unfortunately, many of the *M. avium* were clumped together. This is a property of *Mycobacteria* in general[226] and can be a difficult issue to solve. One option is to filter the solution, but this can decrease the concentration by three orders of magnitude. The current clumping situation makes it essentially impossible to treat the bacteria as a uniform distribution for the calculations, however.

The previous process was repeated on membranes for *M. avium* detection, with *E. coli* as a control. The average mass of the *M. avium* on the surface was 1 ± 1 ng. The standard deviation is again not representative of the accuracy of the measurement; the quantity of *M. avium* on the surface was highly location-specific. The resonance frequencies of the membranes are shown in Table 5.4, and images of the membranes are shown in Figures 5.29-5.31. Again, the masses as calculated by equation [6]/[7] are also given in Table 5.4, although they may not be accurate.

The images in Figures 5.29-31 show the quantity of *M. avium* on the surface of the membranes. In some places aggregation of the *M. avium* makes assessing the quantity of bacteria on the surface difficult. The mass differences listed in Table 5.4 appear to generally correlate with the quantity of bacteria visible on the membrane surfaces as shown in Figures 5.29-31. Based on a visual inspection, the quantities of *M. avium* on the membrane surfaces shown in Figure 5.29-31 generally match the quantities calculated in Table 5.4. It is clear that there are more bacteria on membranes 1 and 5 than on 2 and 9, 2 and 9 than on 6, 6 than 8, 8 than 7, 11 or 12 and 7, 11 or 12 than 15. This can be summarized by 1/5 > 2/9 > 6 > 8 > 7/11/12 > 15. What is not clear, due to the bacteria aggregation, is whether there is more *M. avium* on 5 than on 1 (5>1), that the quantity of *M. avium* on 2 and 9 is identical (2=9), that 12 has more *M. avium* than 7 and 7 has more *M. avium* than 11 (12>7>11), and how 16 compares. In general, however, the mass differences in Table 4 are evident in the images.

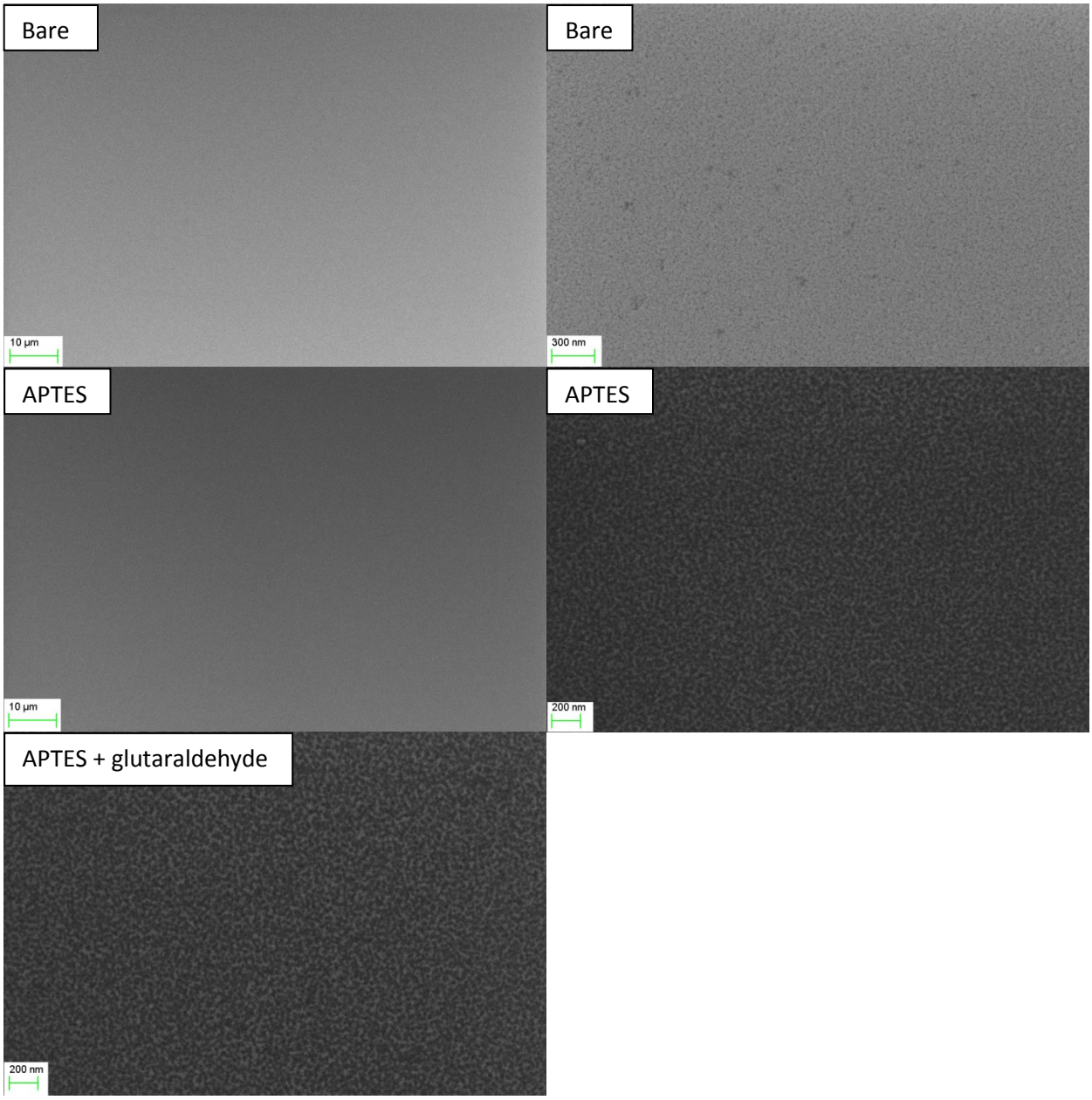

Figure 5.27: Low and high magnification SEM images of APTES and glutaraldehyde functionalized chips. The images were taken with identical brightness and contrast settings.

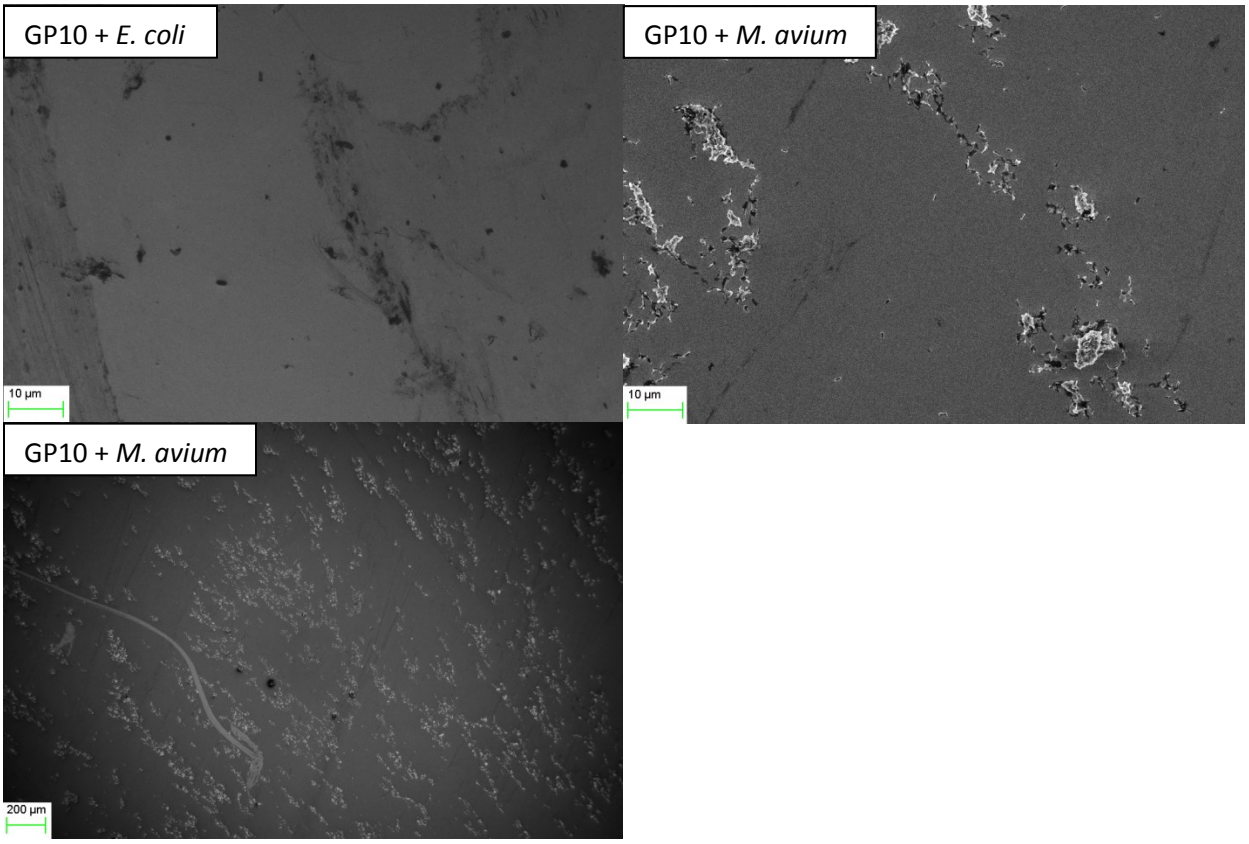

Figure 5.28: SEM images of *E. coli* and *M. avium* binding to the GP10-coated chips. The lower magnification image of the *M. avium* illustrates the variation in the distribution of the *M. avium* on the chip surface

Due to aggregation, it is difficult to determine the precise number of *M. avium* on the surface of the membranes. There are in fact two reasons for this. Firstly, as mentioned previously, the *M. avium* naturally aggregate and form clumps. Secondly, these clumps are large enough and therefore heavy enough to sink in the test tube. This means that the gradient seen roughly from the right to the left in Figure 5.29 is caused by the *M. avium* gradually settling to the base of the test tube. The left side was down and the right side was up in the test tube.

Table 5.4: The resonance frequency shifts and associated masses of *M. avium* on the individual membranes.

Membrane	Δf (±3 kHz)	M. avium (ng)
1	36	2.2
2	27	1.6
5	58	3.7
6	23	1.4
7	3	0.2
8	7	0.4
9	27	1.6
11	0	0.0
12	5	0.3
13	2	0.1
14	3	0.2
15	-1	-0.1
16	1	0.1

The process was repeated with the *E. coli* control chip membranes. The resonance shift from the *E. coli* cells was small (Table 5). The average mass of bound *E. coli* was 0.1 ± 0.1 ng, although again there was variation from membrane to membrane, though not nearly as much as the membranes shown in Figure 29-31. The difference in bound *E. coli* mass could be visually observed in the SEM images taken of the membranes. Adjusting for the difference in concentration between the *E. coli* and *M. avium*, and assuming a roughly equal mass for a single *E. coli* or *M. avium* bacterium would give 0.2 ± 0.3 ng. These results support the hypothesis that the binding of the *M. avium* to the GP10 TSP on the membranes was specific. Two representative membranes are shown in Figure 5.32. Membrane 16 has visible *E. coli* and a resonance shift of 3 kHz, whereas membrane 13 has very few *E. coli* on the surface and a resonance shift of -2 kHz.

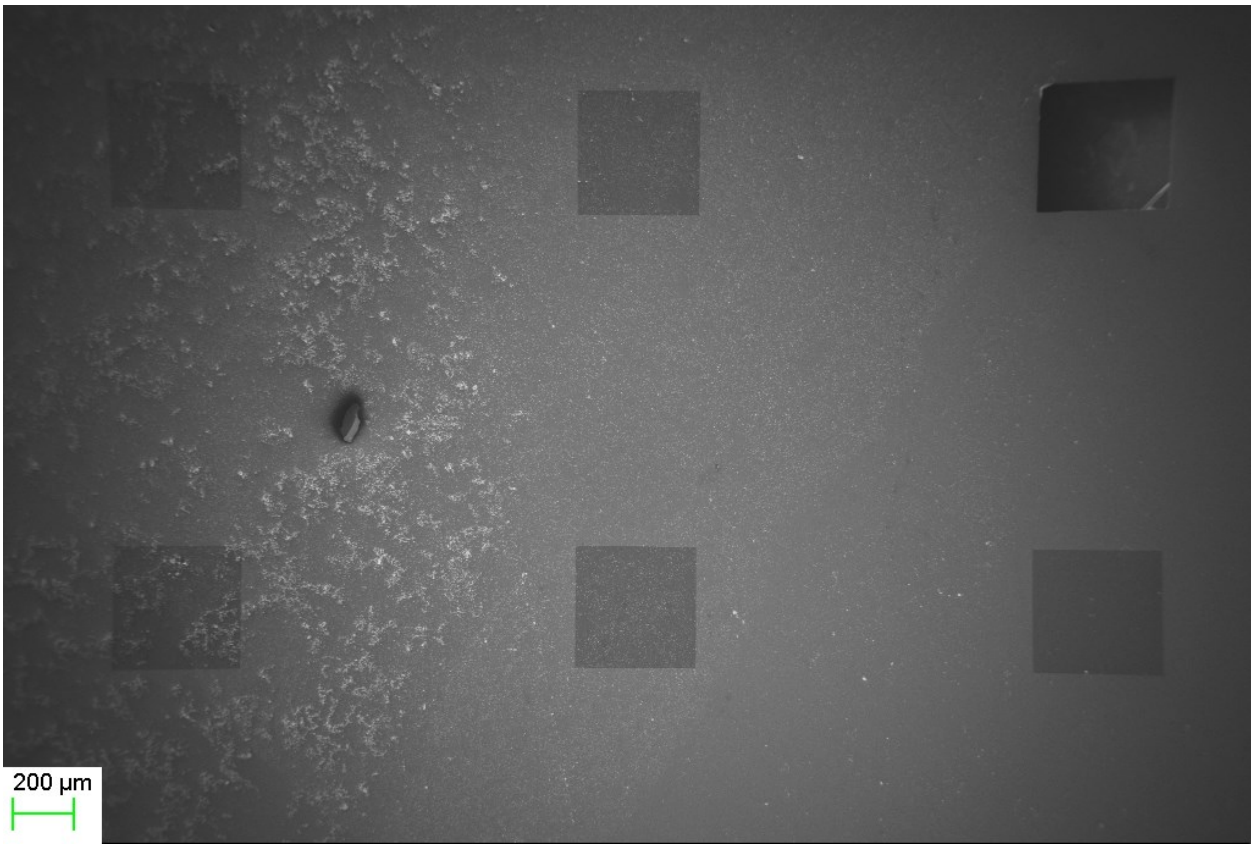

Figure 5.29: A SEM image of the membranes for which the resonance frequencies are given in Table 5.4. From the top left to the bottom right the membrane numbers are 1, 2, 3, 5, 6 and 7. Membrane 3 was broken while mounting the chip on the SEM stub. This image clearly illustrates the non-uniform nature of the *M. avium* distribution.

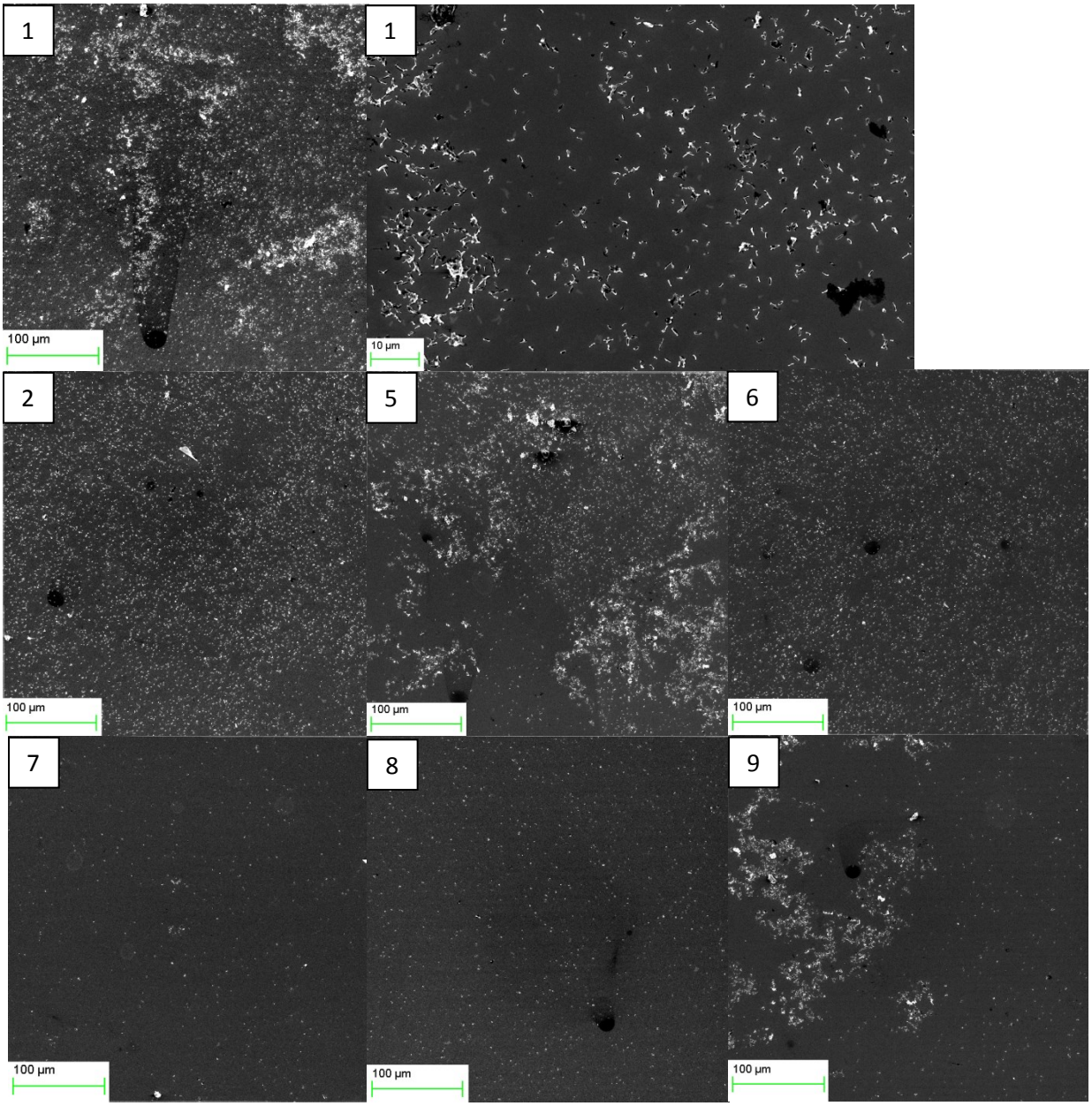

Figure 5.30: SEM images of the surfaces of the membranes for which the resonance frequency shifts are presented in Table 5.4. Membranes 1, 2 and 5-9 are shown in this figure while the remainder are shown in Figure 5.31. The white areas are bacteria, as can be seen in the higher resolution image of membrane 1. The circular black regions are a result of the laser heating the surface. There are two regions on the top center of membrane 5 and one on membrane 16 that cause charging effects (black spots) due to the thickness of the bacteria clumps. The large fragment on membrane 10 is debris.

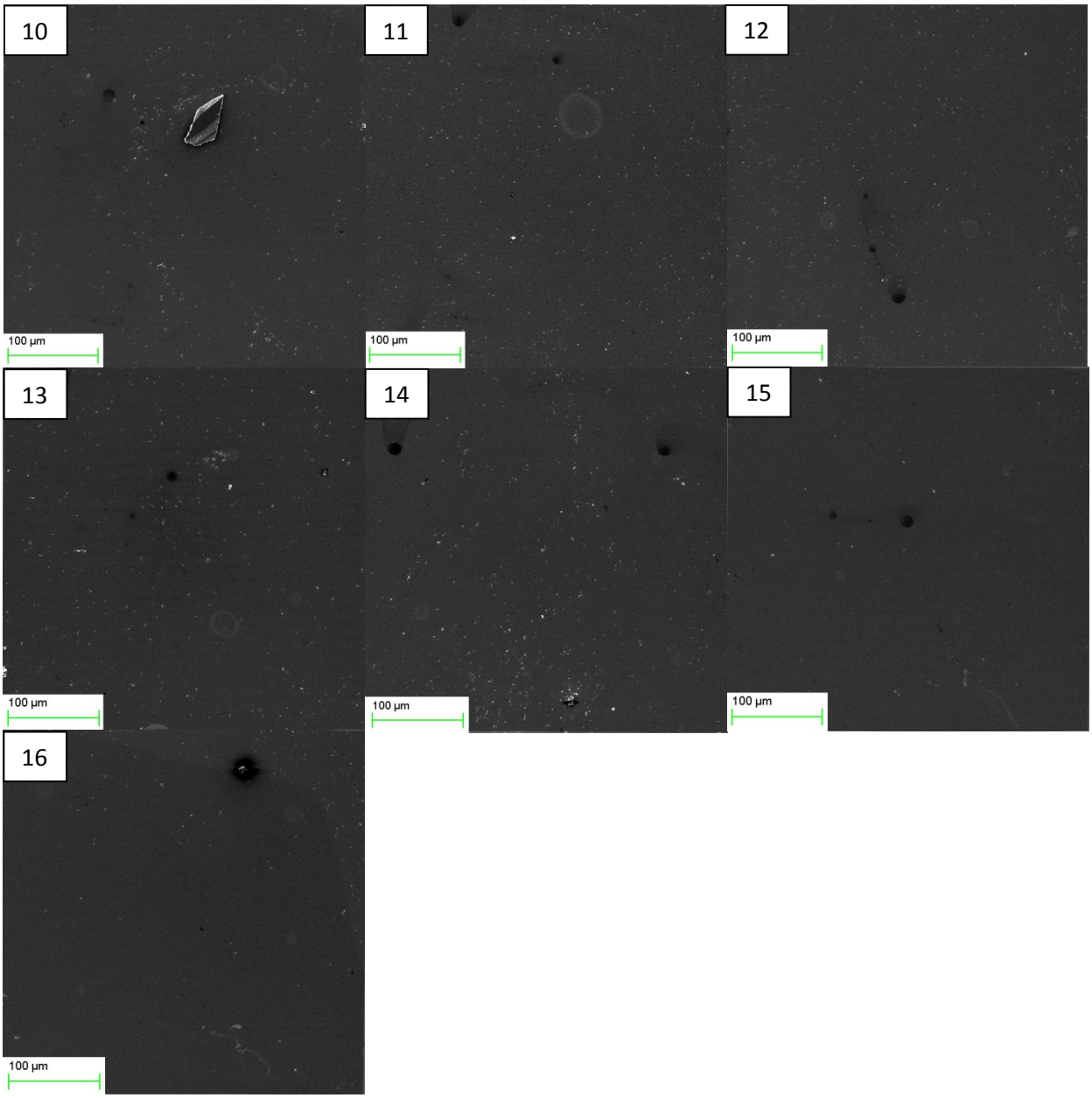

Figure 5.31: SEM images of the surfaces of the membranes for which the resonance frequency shifts are presented in Table 5.4. Membranes 10-16 are shown in this figure.

Table 5.5: Resonance frequency shift and associated mass of *E. coli* on the membranes.

Membrane	Δf (±3 kHz)	E. coli (ng)
3	1	0.1
4	4	0.2
5	-2	-0.1
6	0	0.0
7	1	0.1
8	2	0.1
9	1	0.1
10	0	0.0
11	-1	-0.1
13	-2	-0.1
14	2	0.1
15	2	0.1
16	3	0.2

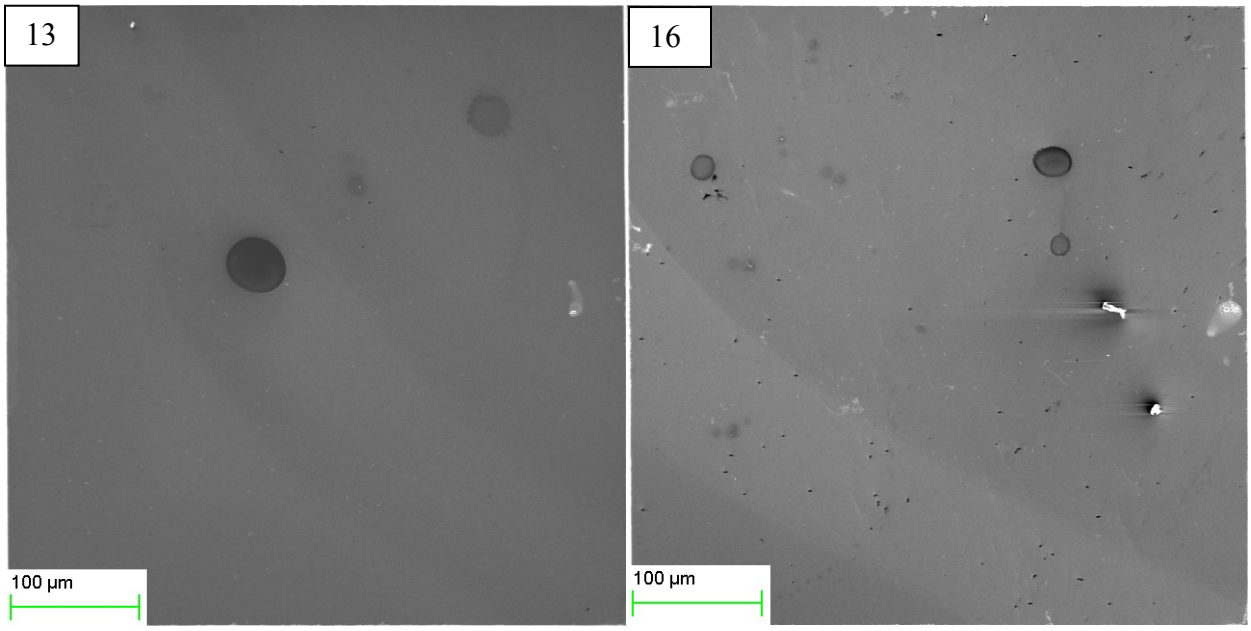

Figure 5.32: Two SEM images showing the difference in *E. coli* coverage. The calculated added mass was -0.1 ng and 0.2 ng for membranes number 13 and 16 respectively. The large circular black spots were caused by the laser.

5.3. The potential effects of the laser on the membranes

Accurate measurement of membrane resonance can be challenging for a variety of reasons. The laser used for the resonance measurement can cause substantial difficulty in performing the measurements. Heating effects in particular can have a significant impact on the measurement process. Because the measurement takes place in a vacuum (0.4 mTorr), there is little heat transfer due to convection. This means that heat is dissipated from the membrane devices to the body of the silicon chip. Previous measurements with the interferometric setup were performed using cantilever beam structures. While the devices are small and long, the figure of merit is the narrowness of the beams, and they are usually in the order of 200 nm x 200 nm x 10 μm. For some of the membranes discussed herein, the dimensions were 10 nm x 400 μm x 400 μm, which means that the heat must be conducted much farther through a much thinner structure. Therefore the laser power can have a significant effect on the resonance frequency of the membrane, and may even affect the physical structure of the membrane and/or attached organic materials.

5.3.1. The resonance frequency shift based on potential laser heating effects

In order to determine the resonance frequency on the spectrum analyzer, it is necessary to search a large range of frequencies for the resonance peak, particularly when the added mass is unknown. This means that it is often necessary to begin the search by sweeping across a greater range of frequencies. To find the peak under these conditions it is necessary to start the search at a higher laser power. This higher laser power changes the resonance peak, however. This may be due to the laser heating the membrane, thus reducing the tensile stress and stiffness in the membrane. This in turn would lead to a decrease in the resonance frequency. During measurements, once the peak had been located, the laser power was gradually reduced, which increased the resonance frequency. In Figure 5.33 the effects of laser power on the resonance frequency of three different membranes are plotted with linear trend lines. The membrane in Figure 5.33a had a width to thickness ratio of 40000 and frequency shift of approximately 14 kHz at 100 μW laser power. The membrane in Figure 5.33b had a width to thickness ratio of

28500 and frequency shift of approximately 3 kHz at 100 µW laser power. This suggests that as the width to thickness aspect ratio decreases, the effect of laser power on the resonance frequency decreases. Furthermore, the third membrane in Figure 5.33c had a proof mass on the surface of the membrane, and the laser power had no impact on the resonance frequency of the membrane. This was likely because the proof mass is sufficiently massive that the power transfer is negligible.

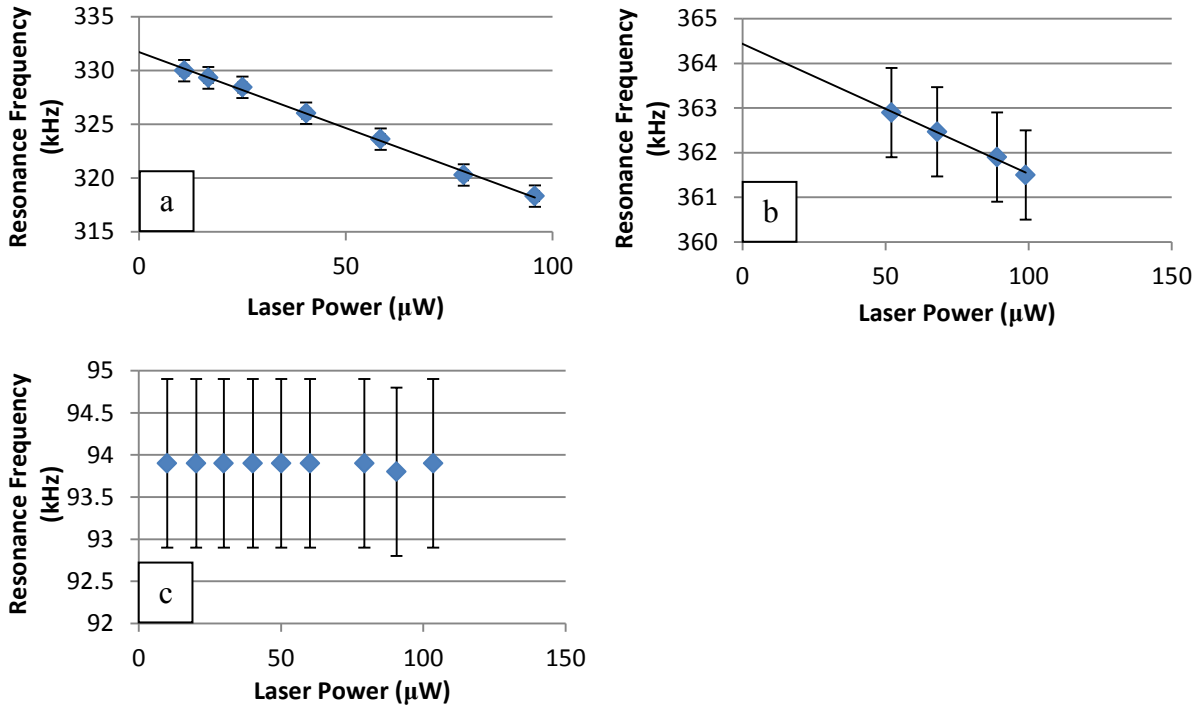

Figure 5.33: Plots illustrating the effect of laser power on the measured resonance frequency. a) A 10 nm thick and 400 µm wide membrane. b) A 20 nm thick and 570 µm wide membrane. c) A 300 nm thick and 275 µm wide membrane with a 9.1 µg proof mass.

5.3.2. Changes to the membrane surface due to the laser spot

In addition to the effects of laser power on resonance frequency, some membranes coated with organic materials appeared to be affected by the laser spot. This was especially evident when greater laser power and small thickness to width ratio membranes were used. When measurements are performed in the presence of organic materials, greater laser power may initially be required. This is because the addition of organic materials reduced the reflectivity of the membranes, increasing the challenge of finding the resonance peaks.

The images in Figure 5.34 were produced using an optical profilometer. They show the effect that laser power in the 1-3 mW range can have on a 300 nm thick and 600 µm wide membrane. On occasion, greater laser power has even caused the membranes to rupture entirely. In this case, extrusions up to 80 nm high and a hole nearly 60 nm deep were created. This is why the laser power was always kept a low as possible during frequency measurements and was never allowed to exceed 100 µW during the measurement process.

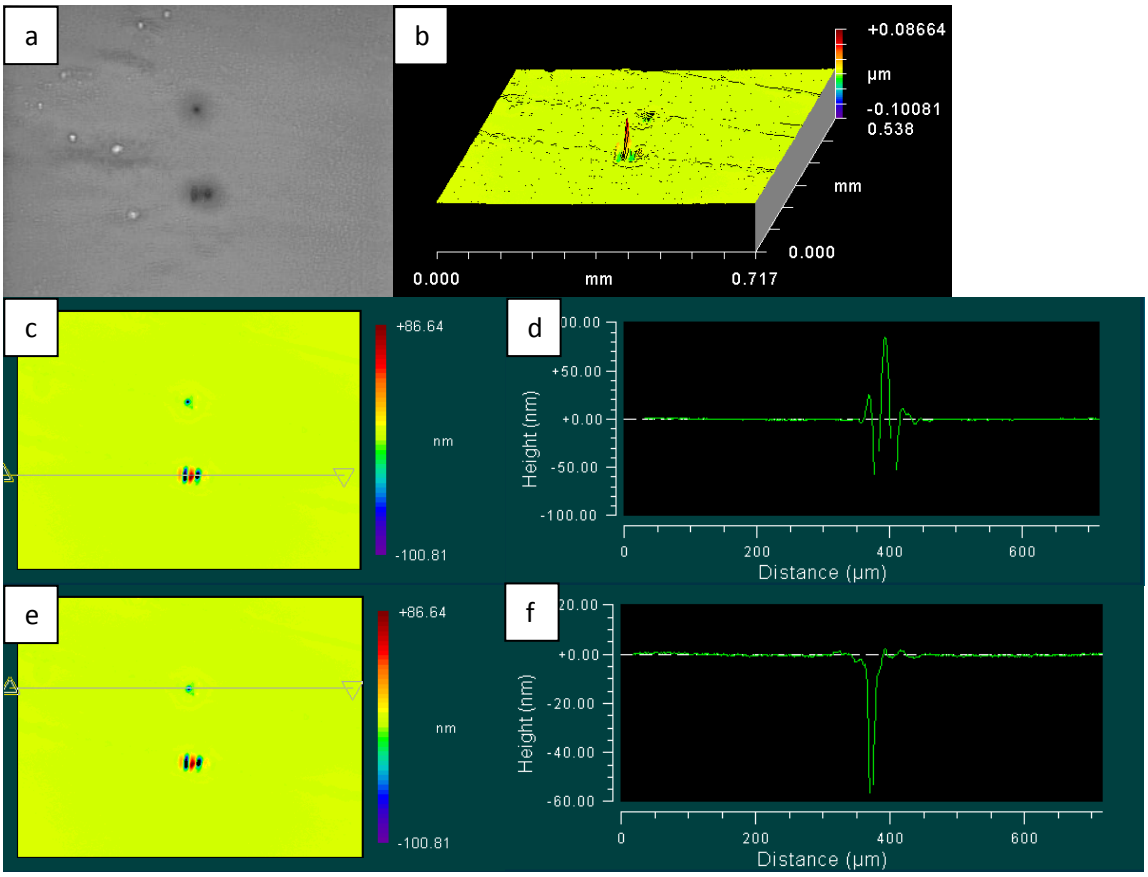

Figure 5.34: A membrane with laser damage. a) Optical microscope image. b) A 3-D Profile of the extrusion and cavity created by the laser. c) An image illustrating the height of the laser spot extrusion. d) Cross-sectional image of line in c). e) An image illustrating the depth of the hole created by the laser. f) Cross-sectional image of line in e).

The image in Figure 5.34 is an extreme case. Even lower laser power can have an effect on the organic material on the membranes, however. In Figure 5.35, a SEM image illustrates how the laser can alter the surface of the membranes. In this case there was no change to the C,

O or Si elemental distribution, however. This suggests that the alteration was largely cosmetic and that the majority of the organic material was unaffected. This was not always the case, however. In Figure 5.36, the organic material (APTES, glutaraldehyde, GP10, BSA and *M. avium*) on the membrane was likely more significantly affected. This is indicated by the change in C, O and Si distribution at the laser spot location. The Al and Mo EDX maps were not affected.

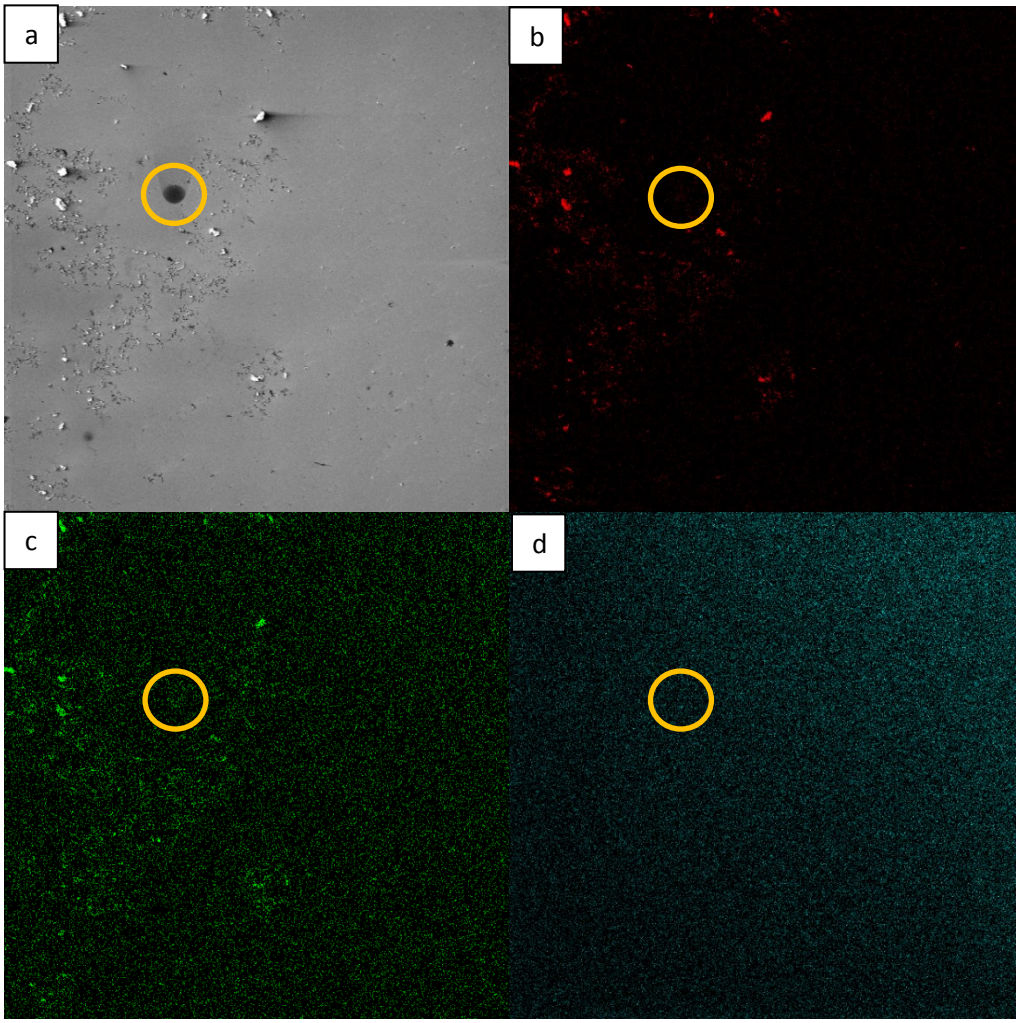

Figure 5.35: Images of a membrane with a visual change to the organic material that does not significantly affect the elemental distribution of the C, O or Si. a) A plain SEM image. b) EDX carbon map. c) EDX oxygen map. d) EDX silicon map.

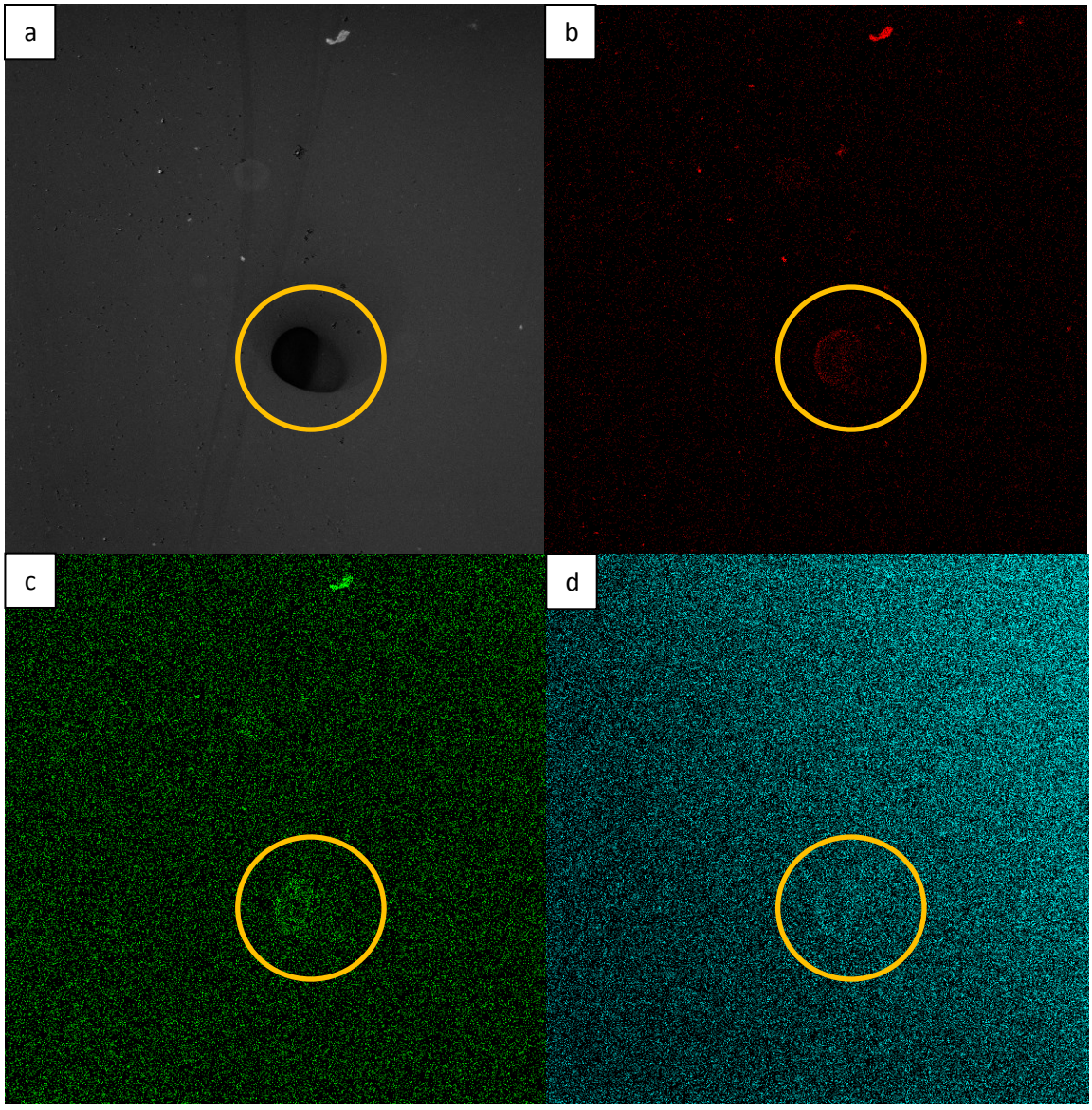

Figure 5.36: Images of a membrane where the laser had a significant impact on the elemental distribution. a) A plain SEM image. b) EDX carbon map. c) EDX oxygen map. d) EDX silicon map.

5.4. Summary and Conclusions

In this chapter, linking processes were examined for use on the AlMo nanocomposite surface. These processes were used to link Abs and GP10 to the surfaces of AlMo-coated chips and AlMo membranes for detection of BHV-1, HEV hexon protein, *M. smegmatis* and *M. avium*. The presence of diazonium on the AlMo surface was determined by XPS measurements. FBDP

was then used to attach 3D9S capture Ab and capture BHV-1. Images were taken with a SEM. While BHV-1 was observed on the chip with 3D9S Ab, no BHV-1 was observed on a control chip with mouse anti-human INF-γ Ab. Subsequently, resonance measurements were performed with functionalized membranes. The result was the capture of 7 ± 1 ng of BHV-1 on the 3D9S-functionalized membranes, and 3.1 ± 0.1 ng of BHV-1 on the control INF-γ Ab membranes. In an effort to reduce nonspecific binding, BSA blocking was performed on AlMo-coated chips. The results indicated reduced binding on both the active and control chips. BSA blocking was then applied on the AlMo membranes. The 3D9S membranes accumulated 0.9 ± 0.1 ng of BHV-1, while the control INF-γ Ab membranes accumulated 1.0 ± 0.1 ng of BHV-1. The relatively small quantity of BHV-1 captured by the active membranes was likely caused by a sharp reduction in 3D9S Ab linked to the membrane surface. Unfortunately, the experiments could not be continued because the FBDP was discontinued by Sigma-Aldrich and no other source exists.

Silanes were selected to replace the FBDP linker. HMDS was used to increase the hydrophobicity of the membranes, leading to 500 ± 300 pg of BHV-1 being captured, which is substantially less than with the FBDP linker. Epoxysilanes were selected for further experiments. Contact angle measurements were performed to verify adhesion to the AlMo surface. Further imaging of AlMo-coated chips was performed to examine the capture and distribution of BHV-1 on the 3D9S Ab-functionalized active chips and the anti-human INF-γ Ab-functionalized control chips. Considerably more BHV-1 was captured on the active chips. The resonance frequency shift and mass of BHV-1 captured were relatively small, however, 8 ± 1 kHz and 370 ± 50 pg respectively. The epoxysilane was also assessed for use in HEV hexon protein capture. AlMo-coated chips were functionalized with 11B6 capture Ab and SEM images were used to visually assess the capture of hexon proteins. The images clearly showed the capture of hexon protein, although additional work is required to confirm the specificity of capture.

Due to the small resonance frequency shift observed when the epoxysilanes were used, a different method of silanization was examined: APTES and glutaraldehyde. This method led to substantial *M. smegmatis* capture using GP10 TSP, although there was significant regional variation in the capture of the bacteria. This was also evident when the membrane measurements were performed. The average mass captured was 4 ± 6 ng; the standard deviation was large because the *M. avium* quantity on the surface varied significantly. The change in resonance

frequency varied from -1 to 72 kHz. This means that the mass on the surface cannot be assumed to be a uniform distribution and equation [6][7] may not be very accurate.

This functionalization method was also examined for the capture of hexon protein. The mass captured on the active membranes was 1.2 ± 0.2 ng, while the mass captured on the BSA control membranes was 4.5 ± 0.5 ng, indicating that BSA is not a useful control or blocking compound for hexon protein. Binding to BSA was likely due to the hexon protein having both hydrophobic and hydrophilic ends.

Gaseous deposition of APTES was used to improve the uniformity of the functionalization process. SEM images of functionalized AlMo-coated chips were taken, and substantial binding of *M. avium* was observed, while little binding of the control *E. coli* was observed. The process was implemented on membranes and an average mass of 1 ± 1 ng of *M. avium* was calculated. Again, the large standard deviation is a result of the variation in *M. avium* capture based on the location of the membrane on the chips and aggregation of the bacteria. This difference in density of the bacteria was observed in the SEM images and largely matched the mass calculated from the resonance shift. A control experiment was performed with *E. coli*; there was little nonspecific binding to the GP10-functionalized membrane surfaces, and the average mass of *M. avium* on the surface was 0.1 ± 0.1 ng. Again, there was some regional variation in the quantity of *E. coli*.

Finally, the effects of laser power on resonance frequency were presented. The effect of increasing laser power on high aspect ratio membranes was noted. Furthermore, the potential effects of the laser power on the organic material on the membrane surface were briefly discussed.

Overall, the FBDP, expoxysilane and APTES were successfully deposited on the AlMo surfaces in solvents, and APTES and HMDS were deposited in a vapour phase. BHV-1 virus particles, *M. avium*, *M. smegmatis* and hexon protein were successfully captured by using 3D9S Ab, GP10 TSP and 11B6 Ab on chips and membranes. On membranes, the resonance frequency shifts from the attachment of additional mass for the BHV-1 virus particles, *M. avium*, and the hexon protein were observed.

A major challenge for biosensors of this type can be the variation in mass capture based on location. Some membranes captured much larger quantities of BHV-1 and *M. avium* than others. This can make a direct comparison of active to control measurements difficult.

Furthermore, this cannot be attributed solely to variation in silane thickness observed from deposition in solution. The vapor deposition of APTES created a uniform linking layer, but there was still a large difference in the mass capture from one membrane to the next. While the difference in average mass captured by the active and control membranes was substantial (1 ng to 0.1 ng), they could not be said to be different within a standard deviation. This regional variation issue was exacerbated by the aggregation of the *M. avium* bacteria. The aggregation makes it very challenging to accurately assess the number of bacteria on the surface and compare them to the calculated mass of *M. avium* on the surface.

A strategy for further experiments would be to perform measurements with narrower (~5 μm wide) 10 nm thick membranes to increase sensitivity. To reduce regional variation during pathogen capture, the capture could be performed in a microfluidics system. Measurements in this form could also lead to real time measurement of pathogen capture if one side of the membrane is in contact with the pathogen solution and the resonance of the membrane is recorded on the other side of the membrane.

6. Summary and Recommendations

Nanocomposite materials are multiphase materials where at least one of the dimensions of one of the materials is less than 100 nm in size. AlMo nanocomposites can be fabricated by co-sputtering Al and Mo. The main topic of this thesis is 68 at. % Al and 32 at. % Mo cosputtered thin films. This nanocomposite can be used to form ultrathin, ultrasmooth devices.

The overarching goal of the thesis was to verify and expand the characterization of the 68 at. % Al and 32 at. % Mo nanocomposite, fabricate devices from this nanocomposite for possible applications and implement the devices for promising applications. Characterization of this AlMo material was performed with ultrathin films and very large aspect membranes with a minimum thickness of 10 nm for 450 μm wide membranes. The density of an AlMo thin film was determined experimentally to be 5000±550 kg/m^3. The resultant value agreed within error with the theoretically predicted value.[1] The Young's modulus of the material was determined via nanoindenting (164±26 GPa) and bulge measurements (127±21 GPa) with AlMo membranes. The second value was used in further calculations because it agreed within error with all three previously reported values. The resonance frequencies of the membranes were determined using an optical interferometry setup, and the results were verified with FEA. The hardness of the AlMo material was determined to be 6.57±0.37 GPa using nanoindentation of the thin film surface, which agreed with the previously reported value.[1] The nanoindentation results were verified by performing the nanoindentation on SiN thin films. The resultant Young's modulus for the SiN thin films also agreed within error with a value reported in the literature.[194]

The pressurization system that was built to perform the bulge measurements was also used to perform burst testing of the membranes. This test was used to determine the fracture pressure of the AlMo membranes (1.89±0.45 GPa) and low stress SiN membranes (3.28±0.28 GPa). The average resistivity of the AlMo thin film was measured to be 5.81±0.44 μΩ-m with a four point probe, which was comparable to previous measurements.

Tuning of the intrinsic stress of membranes and other structures can be important for device fabrication for purposes such as to change the resonance frequency or avoid stress fracture. As the deposition pressure was increased, the intrinsic stress changed from tensile to compressive. Conversely, thermal annealing resulted in a shift towards tensile stress.

The effect of the deposition pressure on the resistivity of the thin films was also examined. The resistivity decreased linearly with decreasing deposition pressure. This is likely the reason why the average resistance of the AlMo nanocomposite was greater than in previously reported measurements.[1] In the previously reported measurements the thickness of the thin film was greater, which according to the results presented here, leads to a lower resistivity.

A number of the properties that were analyzed make AlMo an attractive material as a structural layer for MEMS and NEMS devices. The resilience is comparable to SiN, it can be used to fabricate ultra-thin structures, it has the conductivity of a metal and it is compatible with high-temperature processes. To complete the second objective, several structures were fabricated that could lead to future research.

Firstly, Ni proof masses were electrodeposited onto freestanding ultrathin AlMo membranes. Proof masses are often used to adjust the resonance frequency of devices. The resonance frequency of these membranes was measured, and the resonance frequencies of the membranes were successfully altered through the addition of the proof masses.

The second series of new structures that were fabricated were freestanding Archimedes spirals. Different processes were employed to fabricate the structures, and the best results were obtained with a lift-off process for pattern transfer and a combination of DRIE and XeF_2 etch to release the structures. The edges of the pattern were quite rough, however. It would be useful to repeat the process with a carefully timed aqua regia etch, which may improve the smoothness of the pattern edges.

Potential future work with these techniques would be to create multi-arm Archimedes spirals with a piezoelectric layer sandwiched between two AlMo layers for energy harvesting applications. The piezoelectric layer would likely be sufficiently stiff to prevent the deflection issues experienced due to excessive flexibility and/or intrinsic stress. The proof mass electrodeposition process could then be implemented on the Archimedes spirals to tune the resonance frequency and/or increase the deflection of the spirals to increase energy harvesting. It could also serve as a point of strength where a lever could be attached for direct force application for energy generation.

The third class of new structures consisted of two-arm deflection cantilevers with paddles between them. E-beam lithography and lift-off in acetone were employed to pattern the AlMo thin film and the cantilevers were released with a XeF_2 etch. They have potential in deflection

cantilever sensor applications. The first step would be to increase the XeF_2 etch time to examine how far the cantilevers deflect in order to optimize the cantilever beam length and pad size. The paddles were large enough that laser-based measurement of cantilever deflection would be possible. Another alternative direction would be to fabricate the cantilevers with separate contact-pads for each cantilever beam. As the cantilever deflects from the adhesion of the gas or other material being detected, the dimensions of the cantilevers change subtly, and this may change the resistance of a current travelling through the cantilever structure.

In order to address the third objective, the AlMo ultrathin membranes were implemented as biosensors for pathogen detection. Specifically, BHV-1, HEV hexon protein, *M. smegmatis* and *M. avium* were captured on AlMo coated chips and detected via mass sensing using laser interferometry. Two monoclonal antibodies, 3D9S and 11B6, were used to capture the BHV-1 and HEV hexon protein respectively. GP10, a bacteriophage TSP, was used for the capture of *M. smegmatis* and *M. avium.* Several different approaches were used to chemically link the capture proteins to the AlMo surfaces.

The first linker implemented was FBDP, a bifunctional diazonium linker. The presence of FBDP on the AlMo surface was verified by using XPS. The 3D9S Ab was then attached to the AlMo surface via FBDP and used to capture BHV-1. BHV-1 was present on the 3D9S Ab-coated active chip and absent from the INF-γ Ab-coated control chip as seen in SEM images. Resonance measurements were performed and a clear separation was seen between the resonance frequency of the active 3D9S Ab-coated chip and the INF-γ Ab coated control chip. The average resonance frequency shift due to binding of BHV-1 was 93 ± 4 kHz for the active membranes and 62 ± 2 kHz for the control membranes, where the error is the standard deviation.

The nonspecific binding on the control chips was relatively large. Therefore, BSA was tested on AlMo-coated chips to reduce the nonspecific binding of BHV-1 to the control chips. There was less BHV-1 present on the SEM images, which indicated reduced nonspecific binding on both the active and control chips. The process was then applied to AlMo membranes and resonance measurements were performed. Again, there was a clear difference between the active and control membrane measurements, with an average frequency shift of 32 ± 4 kHz for the active membranes and an average frequency shift of 21 ± 2 kHz for the control membranes.

While the frequency shift results are a useful indicator of positive results, it is informative to consider the actual change in mass of the membranes with the addition of BHV-1. From the

relatively small standard deviation of the frequency shift, and the SEM images, the BHV-1 distribution was assumed to be uniform. For this condition, calculations were performed based on the equation for the resonance frequency of a thin plate, and verified via finite element analysis. For the first resonance measurements without the BSA, the average resonance frequency shifts were 7 ± 1 ng and 3.1 ± 0.1 ng for the active and control chips, respectively. For the BSA experiments, there did not appear to be a substantial difference between the resonance frequency shift of the active and control membranes. This may have been caused by aging reagents. The experiment would have been repeated with fresh reagents, but the FBDP was discontinued by Sigma-Aldrich. Possible alternative sources of FBDP were investigated, but none was found. For this reason it was necessary to choose a different linker. A possible future direction, given sufficient funds, would be to hire a chemist or a company to produce FBDP for additional experiments.

Several silanes were examined to replace the FBDP diazonium linker. Vapour-deposited HDMS was used to increase the hydrophobicity of AlMo membranes. Substantially more BHV-1 was present on the active 3D9S Ab-coated chip than the control INF-γ Ab-coated chip. Membranes were coated with 3D9S Ab and resonance measurements were performed. The calculated mass of BHV-1 captured was 500 ± 300 pg. As this was substantially less than the mass captured with the FBDP linker and because HDMS does not cause the 3D9S Ab to be covalently linked to the surface, different linkers similar to the FBDP were utilized instead.

Bifunctional silanes GPDMES and GPTMS were selected for further experiments. The GPTMS modification of the AlMo surface was verified through contact angle measurements. The GPTMS was then implemented for capture of BHV-1 with active 3D9S Ab-coated chips and control INF-γ Ab-coated chips. Substantially more BHV-1 was observed on the active chips than the control chips in SEM images. The epoxysilane was also assessed for capture of HEV hexon protein. AlMo-coated chips were functionalized with 11B6 capture Ab and SEM images were made to visually assess the capture of hexon proteins. SEM images clearly showed the capture of hexon protein, although additional work was required to confirm the specificity of capture. The GPTMS process was also implemented on the membranes. The resonance frequency shift (8 ± 1 kHz) and mass of BHV-1 captured (370 ± 50 pg).

APTES and glutaraldehyde linking was examined because the mass captured with the epoxysilanes was again substantially less than when the FBDP linking method was used.

Additionally, GP10 TSP was selected to capture *M. smegmatis* and *M. avium*, because bacteria are more massive than viruses and proteins, and should therefore result in a greater resonance frequency shift than BHV-1 or hexon protein. When this method was implemented on AlMo-coated chips it led to substantial *M. smegmatis* capture, although there was significant regional variation in the capture of the bacteria. Resonance measurements were performed and the average mass captured was 4 ± 6 ng; the standard deviation was large because the *M. avium* quantity on the surface varied significantly. The change in resonance frequency varied from -1 to 72 kHz. This means that the mass on the surface cannot be assumed to be uniformly distributed, and equation [6][7] may not be accurate.

This functionalization method was also examined for hexon capture. The mass captured on the active membranes was 1.2 ± 0.2 ng, while the mass captured on the BSA-functionalized control membranes was 4.5 ± 0.5 ng. The greater mass captured on the BSA-functionalised chips indicates that the hexon binds more strongly to the BSA on the control membranes than to the Ab on the active membranes. This means that future experiments would need to be performed to determine a more suitable blocking material than BSA.

Gaseous deposition of APTES was used to improve the uniformity of the functionalization process. Substantial binding of *M. avium* was observed in SEM images of functionalized AlMo-coated chips, while little binding of the control *E. coli* was observed. The process was implemented on membranes and an average mass of 1 ± 1 ng *M. avium* was calculated. The resonance frequency shift varied from -1 to 58 kHz ±3 kHz. Again, the large standard deviation is a result of the large variation in *M. avium* capture. The difference in bacteria density was observed in the SEM images, and largely matched the mass calculated from the resonance shift.

A control experiment was performed with *E. coli*; there was little nonspecific binding to the GP10-functionalized membrane surfaces, and the average mass of *E. coli* was 0.1 ± 0.1 ng. The resonance frequency shift varied from -2 to 4 kHz ±3 kHz. Again, there was some regional variation in the quantity of *E. coli* binding. Aggregation made it very difficult to assess the number of bacteria on the surface of the membranes. For this reason it was not reasonable to directly compare the calculated mass capture with the number of bacteria present on the membrane surface.

Finally, the effects of laser power on resonance frequency were presented. The effect of increasing laser power on high aspect ratio membranes was noted. Furthermore, the potential effects of the laser power on the organic material on the membrane surface were briefly discussed.

Overall, the FBDP, expoxysilane and APTES were successfully deposited on the AlMo surfaces in solvents and APTES and HMDS were deposited in a vapour phase. BHV-1 virus particles, *M. avium*, *M. smegmatis* and hexon protein were successfully captured by using 3D9S Ab, GP10 TSP and 11B6 Ab on chips and membranes. On membranes, the resonance frequency shifts from the attachment of additional mass for the BHV-1 virus particles, *M. avium*, and hexon protein were observed.

A major challenge for biosensors of this type can be the variation in mass capture based on location. Some membranes captured much larger quantities of BHV-1 and *M. avium* than others. This can make a direct comparison of active to control measurements difficult. Furthermore, this cannot be attributed solely to variation in silane thickness from deposition in solution. The vapor deposition of APTES created a uniform linking layer, but there was still a large difference in the mass capture from one membrane to the next. While the difference in average mass captured by the active and control membranes was substantial (1 ng to 0.1 ng), they could not be said to be different within a standard deviation. This regional variation issue was exacerbated by the aggregation of the *M. avium* bacteria. The aggregation made it very challenging to accurately assess the number of bacteria on the surface and compare them to the calculated mass of *M. avium* on the surface.

A strategy for further experiments would include measurements with narrower (~5 μm wide) 10 nm thick membranes to increase sensitivity. Furthermore, to reduce regional variation during pathogen capture, the capture could be performed in a microfluidics system. Measurements in this form could also lead to real-time measurement of pathogen capture if one side of the membrane is in contact with the pathogen solution and the resonance of the membrane is recorded on the other side of the membrane.

References

1 Lee, Z. *et al.* Metallic NEMS components fabricated from nanocomposite Al-Mo films. *Nanotechnology* **17**, 3063-3070, doi:10.1088/0957-4484/17/12/042 (2006).

2 Ophus, C. *et al.* Resonance properties and microstructure of ultracompliant metallic nanoelectromechanical systems resonators synthesized from Al-32 at. % Mo amorphous-nanocrystalline metallic composites. *Applied Physics Letters* **92**, doi:10.1063/1.2841849 (2008).

3 Ophus, C. *et al.* Nanocrystalline-amorphous transitions in Al-Mo thin films: Bulk and surface evolution. *Acta Materialia* **57**, 4296-4303, doi:10.1016/j.actamat.2009.05.029 (2009).

4 Li, H., Tian, C. & Deng, Z. D. Energy harvesting from low frequency applications using piezoelectric materials. *Applied Physics Reviews* **1**, 041301, doi:10.1063/1.4900845 (2014).

5 Deterre, M. *et al.* Micro Blood Pressure Energy Harvester for Intracardiac Pacemaker. *Journal of Microelectromechanical Systems* **23**, 651-660, doi:10.1109/JMEMS.2013.2282623 (2014).

6 Fischer, L. M. *et al.* Specific detection of proteins using nanomechanical resonators. *Sensor Actuat B-Chem* **134**, 613–617 (2008).

7 Yeri, A. & Gao, D. in *Biomedical Nanotechnology: Methods and Protocols* (ed Sarah J. Hurst) 119-139 (Humana Press, 2011).

8 Pepper, J. *et al.* Detection of proteins and intact microorganisms using microfabricated flexural plate silicon resonator arrays. *Sensors and Actuators B-Chemical* **96**, 565-575, doi:10.1016/s0925-4005(03)00641-5 (2003).

9 Lee, D. W., Lee, Y. L. & Kang, J. H. Fabrication and evaluation of a novel protein sensor based on Lorentz force. *Microelectronic Engineering* **84**, 1719-1723, doi:10.1016/j.mee.2007.01.193 (2007).

10 Ajayan, P. M., Schadler, L. S. & Braun, P. V. *Nanocomposite Science and Technology*. (John Wiley and Sons, 2003).

11 Bogue, R. Nanocomposites: a review of technology and applications. *Assembly Autom* **31**, 106–112 (2011).

12 Surappa, M. K. Aluminium matrix composites: Challenges and opportunities. *Sadhana* **28**, 319–334 (2003).

13 Rawal, S. Metal-Matrix Composites for Space Applications. *JOM* **53**, 14-17 (2001).

14 Carl Koch, Ovid'ko, I., Seal, S. & Veprek, S. *Structural Nanocrystalline Materials: Fundamentals and Applications*. (Cambridge University Press, 2007).

15 Nelson-Fitzpatrick, N. & Evoy, S. Highly compliant static microcantilevers fabricated in gold nanocomposite materials *J Micromech Microeng* **21**, 115022/115021-115028 (2011).

16 Trads, J. B., Tørring, T. & Gothelf, K. V. Site-Selective Conjugation of Native Proteins with DNA. *Accounts of Chemical Research* **50**, 1367-1374, doi:10.1021/acs.accounts.6b00618 (2017).

17 Jayasundara, D. R. *et al.* Carbohydrate Coatings via Aryldiazonium Chemistry for Surface Biomimicry. *Chemistry of Materials* **25**, 4122-4128, doi:10.1021/cm4027896 (2013).
18 Zhang, J., Men, Y., Lv, S., Yi, L. & Chen, J.-F. Protein tetrazinylation via diazonium coupling for covalent and catalyst-free bioconjugation. *Organic & Biomolecular Chemistry* **13**, 11422-11425, doi:10.1039/C5OB02053K (2015).
19 Gavrilyuk, J., Ban, H., Nagano, M., Hakamata, W. & Barbas, C. F. Formylbenzene Diazonium Hexafluorophosphate Reagent for Tyrosine-Selective Modification of Proteins and the Introduction of a Bioorthogonal Aldehyde. *Bioconjugate Chemistry* **23**, 2321-2328, doi:10.1021/bc300410p (2012).
20 Lee, Y. *et al.* Electrically Controllable Single-Point Covalent Functionalization of Spin-Cast Carbon-Nanotube Field-Effect Transistor Arrays. *ACS Nano* **12**, 9922-9930, doi:10.1021/acsnano.8b03073 (2018).
21 Moutsiopoulou, A. *et al.* Bioorthogonal Protein Conjugation: Application to the Development of a Highly Sensitive Bioluminescent Immunoassay for the Detection of Interferon-γ. *Bioconjugate Chemistry* **28**, 1749-1757, doi:10.1021/acs.bioconjchem.7b00220 (2017).
22 Lac, D. *et al.* Covalent Chemical Ligation Strategy for Mono- and Polyclonal Immunoglobulins at Their Nucleotide Binding Sites. *Bioconjugate Chemistry* **27**, 159-169, doi:10.1021/acs.bioconjchem.5b00574 (2016).
23 Zhang, S., Sun, D., Fu, Y. & Du, H. Recent advances of superhard nanocomposite coatings: a review. *Surface and Coatings Technology* **167**, 113–119 (2003).
24 de Hazan, Y., Wozniak, M., Heinecke, J., Muller, G. & Graule, T. New Microshaping Concepts for Ceramic/Polymer Nanocomposite and Nanoceramic Fibers. *J. Am. Ceram. Soc.* **93**, 2456-2459, doi:10.1111/j.1551-2916.2010.03802.x (2010).
25 Nelson-Fitzpatrick, N. & Evoy, S. Highly compliant static microcantilevers fabricated in gold nanocomposite materials. *Journal of Micromechanics and Microengineering* **21**, doi:10.1088/0960-1317/21/11/115022 (2011).
26 Prashanthi, K., Naresh, M., Seena, V., Thundat, T. & Rao, V. R. A Novel Photoplastic Piezoelectric Nanocomposite for MEMS Applications. *Journal of Microelectromechanical Systems* **21**, 259-261, doi:10.1109/jmems.2011.2178118 (2012).
27 Cork, J., Jones, R. M. & Sawyer, J. Low cost, disposable biosensors allow detection of antibodies with results equivalent to ELISA in 15min. *Journal of Immunological Methods* **387**, 140-146, doi:https://doi.org/10.1016/j.jim.2012.10.007 (2013).
28 Wen, X., Starr, J. D., Andrew, J. S. & Arnold, D. P. Electro-infiltration: A method to form nanocomposite soft magnetic cores for integrated magnetic devices. *Journal of Micromechanics and Microengineering* **24**, doi:10.1088/0960-1317/24/10/107001 (2014).
29 Maj, C. *et al.* in *2016 XII International Conference on Perspective Technologies and Methods in MEMS Design (MEMSTECH).* 12-15.
30 Guerrieri, S. *et al. Magnetically Active Polymeric Nanocomposites for Two-Photon Stereolithography*. (2014).
31 Ingrosso, C. *et al.* An epoxy photoresist modified by luminescent nanocrystals for the fabrication of 3D high-aspect-ratio microstructures. *Advanced Functional Materials* **17**, 2009-2017, doi:10.1002/adfm.200700098 (2007).

32 Yu-Hsiang, W., Lee, C.-Y. & Che-Ming, C. *A MEMS-based Air Flow Sensor with a Free-standing Micro-cantilever Structure*. Vol. 7 (2007).
33 Martinez, E. D., Lohr, J. H., Sirena, M., Sanchez, R. D. & Pastoriza, H. Silver nanowires in poly(methyl methacrylate) as a conductive nanocomposite for microfabrication. *Flexible and Printed Electronics* **1**, doi:10.1088/2058-8585/1/3/035003 (2016).
34 Khosla, A. & Gray, B. L. Preparation, characterization and micromolding of multi-walled carbon nanotube polydimethylsiloxane conducting nanocomposite polymer. *Mater. Lett.* **63**, 1203-1206, doi:10.1016/j.matlet.2009.02.043 (2009).
35 Cong, H. L., Hong, L. F., Harake, R. S. & Pan, T. R. CNT-based photopatternable nanocomposites with high electrical conductivity and optical transparency. *Journal of Micromechanics and Microengineering* **20**, doi:10.1088/0960-1317/20/2/025002 (2010).
36 Yang, X., Grosjean, C. & Tai, Y.-C. in *Solid-State Sensor and Actuator Workshop* (Hilton Head Island, SC, 1998).
37 Feng, C., Tang, Z., Yu, J. & Sun, C. A MEMS Device Capable of Measuring Near-Field Thermal Radiation between Membranes. *Sensors* **13**, 1998-2010 (2013).
38 Savoia, A. S., Caliano, G. & Pappalardo, M. A CMUT Probe for Medical Ultrasonography: From Microfabrication to System Integration. *IEEE Transactions on Ultrasonics, Ferroelectrics, and Frequency Control* **59**, 1127-1138 (2012).
39 Horowitz, S. B., Sheplak, M., Cattafesta, L. N. & Nishida, T. A MEMS acoustic energy harvester. *J. Micromech. Microeng.* **16**, S174-S181 (2006).
40 Kang, T. J. *et al.* Ultra-thin and Conductive Nanomembrane Arrays for Nanomechanical Transducers. *Adv. Mater.* **20**, 3131–3137 (2008).
41 Williams, K. R., Gupta, K. & Wasilik, M. Etch Rates for Micromachining Processing—Part II. *JOURNAL OF MICROELECTROMECHANICAL SYSTEMS* **12**, 761-778 (2003).
42 Smith, D. L., Alimonda, A. S., Chen, C.-C., Ready, S. E. & Wacker, B. Mechanism of SiNxHy deposition from NH3–SiH4 plasma. *J. Electrochem. Soc.* **137**, 614–623 (1990).
43 Claassen, W. A. P., Valkenburg, W. G. J. N., Willemsen, M. F. C. & v d Wijgert, W. M. Influence of deposition temperature, gas pressure, gas phase composition, and RF frequency on composition and mechanical stress of plasma silicon nitride layers. *J. Electrochem. Soc.: Solid-State Sci. Technol.* **132**, 893–898 (1985).
44 Allaert, K., Van Calster, A., Loos, H. & Lequesue, A. A comparison between silicon nitride films made by PCVD of N2–SiH4/Ar and N2–SiH4/He. *J. Electrochem. Soc.: Solid-State Sci. Technol.* **132**, 1763–1766 (1985).
45 Santini, J. T., Cima, M. J. & Langer, R. A controlled-release microchip. *Nature* **397**, 335-338 (1999).
46 Hamzah, A. A., Majlis, B. Y. & Ahmad, I. Fabrication of Platinum Membrane on Silicon for MEMS Microphone. *ICSE2004 Proc.,* 9-13 (2004).
47 Sameshima, H., Wakui, M., Hu, F.-R. & Hane, K. A Freestanding GaN/HfO2 Membrane Grown by Molecular Beam Epitaxy for GaN–Si Hybrid MEMS. *IEEE JOURNAL OF SELECTED TOPICS IN QUANTUM ELECTRONICS* **15**, 1332-1337 (2009).
48 Lukes, S. J. & Dickensheets, D. L. SU-8 2002 Surface Micromachined Deformable Membrane Mirrors. *JOURNAL OF MICROELECTROMECHANICAL SYSTEMS* **22**, 94-106 (2013).
49 Kusserow, T., Wulf, M., Zamor, R., Kanwar, K. & Hillmer, H. Processing of photonic crystals in InP membranes by focused ion beam milling and plasma etching. *Microelectronic Engineering* **102**, 25–28 (2013).

50 Mackenzie, K. D., Johnson, D. J., DeVre, M. W., Westerman, R. J. & Reelfs, B. H. in *Electrochemical Society Meeting*.
51 Pletea, M., Brückner, W., Wendrock, H. & Kaltofen, R. Stress evolution during and after sputter deposition of Cu thin films onto Si (100) substrates under various sputtering pressures. *JOURNAL OF APPLIED PHYSICS* **87**, 054908-054901-054907 (2005).
52 Zhang, S., Sun, D., Fu, Y., Du, H. & Zhang, Q. Effect of sputtering target power density on topography and residual stress during growth of nanocomposite nc-TiN/a-SiNx thin films. *Diamond & Related Materials* **13**, 1777–1784 (2004).
53 Rille, E., Zarwasch, R. & Pulker, H. K. Properties of reactively d.c.-magnetron-sputtered AlN thin films. *Thin Solid Films* **228**, 215-217 (1993).
54 Tsuchiya, M., Lai, B.-K. & Ramanathan, S. Scalable nanostructured membranes for solid-oxide fuel cells. *NATURE NANOTECHNOLOGY* **6**, 282-286 (2011).
55 Dutta, S. *et al.* Comparison of etch characteristics of KOH, TMAH and EDP for bulk micromachining of silicon (110). *Microsyst Technol* **17**, 1621–1628 (2011).
56 Mendoza-Acevedo, S., Reyes-Barranca, M. A., Vázquez-Acosta, E. N., Moreno-Cadenas, J. A. & González-Vidal, J. L. *Micromachining Techniques for Fabrication of Micro and Nano Structures*. 183-205 (InTech, 2012).
57 Robert, P. *et al.* M&NEMS : A new approach for ultra-low cost 3D inertial sensor. *CEA-LETI/MINATEC* (Grenoble, France, 2009).
58 Norcada. *Membrane Window Products*, <http://www.norcada.com/products.php> (2013).
59 Carlen, E. T., Weinberg, M. S., Dube, C. E., Zapata, A. M. & Borenstein, J. T. Micromachined silicon plates for sensing molecular interactions. *Appl. Phys Lett.* **89**, 173123-173121-173123 (2006).
60 Satyanarayana, S., McCormick, D. T. & Majumdar, A. Parylene micro membrane capacitive sensor array for chemical and biological sensing. *Sensor Actuat B-Chem* **115**, 494–502 (2006).
61 Doscher, J. ADXL105: A Lower Noise, Wider Bandwidth Accelerometer Rivals Performance of More Expensive Sensors. *Analog Dialogue* **33**, 27-29 (1999).
62 Lu, X., Guo, Q., Xu, Z., Ren, W. & Cheng, Z.-Y. Biosensor platform based on stress-improved piezoelectric membrane. *Sensor Actuat A-Phys* **179**, 32– 38 (2012).
63 Yu, P.-L., Purdy, T. P. & Regal, C. A. Control of Material Damping in High-Q Membrane Microresonators. *Physical review letters* **108**, 083603/083601–083605 (2012).
64 Adiga, V. P. *et al.* Approaching intrinsic performance in ultra-thin silicon nitride drum resonators. *J Appl Phys* **112**, 064323/064321-064326 (2012).
65 Steffan, R. J. & Atlas, R. M. DNA Amplification to Enhance Detection of Genetically Engineered Bacteria in Environmental-Samples. *Appl Environ Microb* **54**, 2185-2191 (1988).
66 Janyapoon, K. *et al.* Rapid detection of Salmonella enterica serovar Choleraesuis in blood cultures by a dot blot enzyme-linked immunosorbent assay. *Clinical and diagnostic laboratory immunology* **7**, 977-979 (2000).
67 Downes, F. P. *et al.* Development and evaluation of enzyme-linked immunosorbent assays for detection of shiga-like toxin I and shiga-like toxin II. *Journal of clinical microbiology* **27**, 1292-1297 (1989).
68 Basta, M., Karmali, M. & Lingwood, C. Sensitive receptor-specified enzyme-linked immunosorbent assay for Escherichia coli verocytotoxin. *Journal of clinical microbiology* **27**, 1617-1622 (1989).

69 Jones, M. E. *et al.* PCR-ELISA for the early diagnosis of invasive pulmonary aspergillus infection in neutropenic patients. *Journal of clinical pathology* **51**, 652-656 (1998).
70 Hong, Y. *et al.* Rapid detection of Campylobacter coli, C. jejuni, and Salmonella enterica on poultry carcasses by using PCR-enzyme-linked immunosorbent assay. *Applied and environmental microbiology* **69**, 3492-3499 (2003).
71 Gilligan, K., Shipley, M., Stiles, B., Hadfield, T. L. & Sofi Ibrahim, M. Identification of Staphylococcus aureus enterotoxins A and B genes by PCR-ELISA. *Molecular and cellular probes* **14**, 71-78, doi:10.1006/mcpr.2000.0286 (2000).
72 Baez, L. A., Juneja, V. K. & Sackitey, S. K. Chemiluminescent enzyme immunoassay for detection of PCR-amplified enterotoxin A from Clostridium perfringens. *International journal of food microbiology* **32**, 145-158 (1996).
73 Abdel-Hamid, I., Ivnitski, D., Atanasov, P. & Wilkins, E. Flow-through immunofiltration assay system for rapid detection of E. coli O157:H7. *Biosensors & bioelectronics* **14**, 309-316 (1999).
74 Lazcka, O., Del Campo, F. J. & Munoz, F. X. Pathogen detection: a perspective of traditional methods and biosensors. *Biosensors & bioelectronics* **22**, 1205-1217, doi:10.1016/j.bios.2006.06.036 (2007).
75 Fung, Y. S. & Wong, Y. Y. Self-assembled monolayers as the coating in a quartz piezoelectric crystal immunosensor to detect Salmonella in aqueous solution. *Analytical chemistry* **73**, 5302-5309 (2001).
76 Ilic, B. *et al.* Single cell detection with micromechanical oscillators. *J. Vac. Sci. Technol. B* **19**, 2825-2828 (2001).
77 Ilic, B., Yang, Y. & Craighead, H. G. Virus detection using nanoelectromechanical devices. *Appl. Phys. Lett.* **85**, 2604-2606 (2004).
78 Poshtiban, S., Singh, A., Fitzpatrick, G. & Evoy, S. Bacteriophage tail-spike protein derivitized microresonator arrays for specific detection of pathogenic bacteria. *Sensor Actuat B-Chem* **181**, 410-416 (2013).
79 Campbell, G. A., Medina, M. B. & Mutharasan, R. Detection of Staphylococcus enterotoxin B at picogram levels using piezoelectric-excited millimeter-sized cantilever sensors. *Sensor Actuat B-Chem* **126**, 354-360 (2007).
80 Fischer, L. M. *et al.* Specific detection of proteins using nanomechanical resonators. *Sens. Actuator B-Chem.* **134**, 613-617, doi:10.1016/j.snb.2008.06.003 (2008).
81 Abdel-Hamid, I., Ghindidlis, A. L., Atanasov, P. & Wilkins, E. *Sens. Act. B* **49**, 202-210 (1998).
82 Gau, J. J., Lan, E. H., Dunn, B., Ho, C. M. & Woo, J. C. A MEMS based amperometric detector for E. coli bacteria using self-assembled monolayers. *Biosensors & bioelectronics* **16**, 745-755 (2001).
83 Gervals, L. *et al.* Immobilization of biotinylated bacteriophages on biosensor surfaces. *Sensor Actuat B-Chem* **125**, 615-621, doi:DOI 10.1016/j.snb.2007.03.007 (2007).
84 Taylor, A. D., Yu, Q., Chen, S., Homola, J. & Jiang, S. Comparison of E. coli O157:H7 preparation methods used for detection with surface plasmon resonance sensor. *Sens. Act. B* **107**, 202-208 (2005).
85 Oh, B. K. *et al.* The fabrication of protein chip based on surface plasmon resonance for detection of pathogens. *Biosensors & bioelectronics* **20**, 1847-1850, doi:10.1016/j.bios.2004.05.010 (2005).

86 Arya, S. K. *et al.* Chemically immobilized T4-bacteriophage for specific Escherichia coli detection using surface plasmon resonance. *Analyst* **136**, 486-492, doi:Doi 10.1039/C0an00697a (2011).
87 Singh, A. *et al.* Bacteriophage tailspike proteins as molecular probes for sensitive and selective bacterial detection. *Biosens Bioelectron* **26**, 131-138, doi:DOI 10.1016/j.bios.2010.05.024 (2010).
88 Liao, W. C. & Ho, J. A. A. Attomole DNA Electrochemical Sensor for the Detection of Escherichia coli O157. *Anal Chem* **81**, 2470-2476 (2009).
89 Joung, H. A. *et al.* High sensitivity detection of 16s rRNA using peptide nucleic acid probes and a surface plasmon resonance biosensor. *Anal Chim Acta* **630**, 168-173 (2008).
90 Taylor, A. D., Yu, Q. M., Chen, S. F., Homola, J. & Jiang, S. Y. Comparison of E-coli O157 : H7 preparation methods used for detection with surface plasmon resonance sensor. *Sensor Actuat B-Chem* **107**, 202-208 (2005).
91 Oh, B. K. *et al.* The fabrication of protein chip based on surface plasmon resonance for detection of pathogens. *Biosens Bioelectron* **20**, 1847-1850 (2005).
92 Taylor, A. D. *et al.* Quantitative and simultaneous detection of four foodborne bacterial pathogens with a multi-channel SPR sensor. *Biosens Bioelectron* **22**, 752-758 (2006).
93 Balasubramanian, S., Sorokulova, I. B., Vodyanoy, V. J. & Simonian, A. L. Lytic phage as a specific and selective probe for detection of Staphylococcus aureus - A surface plasmon resonance spectroscopic study. *Biosens Bioelectron* **22**, 948-955, doi:DOI 10.1016/j.bios.2006.04.003 (2007).
94 Wan, J. H., Johnson, M. L., Guntupalli, R., Petrenko, V. A. & Chin, B. A. Detection of Bacillus anthracis spores in liquid using phage-based magnetoelastic micro-resonators. *Sensor Actuat B-Chem* **127**, 559-566, doi:DOI 10.1016/j.snb.2007.05.017 (2007).
95 Singh, A., Arutyunov, D., Szymanski, C. M. & Evoy, S. Bacteriophage based probes for pathogen detection. *Analyst* **137**, 3405-3421, doi:Doi 10.1039/C2an35371g (2012).
96 Singh, A., Arutyunov, D., McDermott, M. T., Szymanski, C. M. & Evoy, S. Specific detection of Campylobacter jejuni using the bacteriophage NCTC 12673 receptor binding protein as a probe. *Analyst* **136**, 4780-4786, doi:Doi 10.1039/C1an15547d (2011).
97 Tawil, N., Sacher, E., Mandeville, R. & Meunier, M. Surface plasmon resonance detection of E. coli and methicillin-resistant S. aureus using bacteriophages. *Biosens Bioelectron* **37**, 24-29, doi:DOI 10.1016/j.bios.2012.04.048 (2012).
98 Chibli, H., Ghali, H., Park, S., Peter, Y. A. & Nadeau, J. L. Immobilized phage proteins for specific detection of staphylococci. *Analyst* **139**, 179-186, doi:Doi 10.1039/C3an01608k (2014).
99 Ye, W. W., Shi, J. Y., Chan, C. Y., Zhang, Y. & Yang, M. A nanoporous membrane based impedance sensing platform for DNA sensing with gold nanoparticle amplification. *Sensor Actuat B-Chem* **193**, 877-882, doi:10.1016/j.snb.2013.09.115 (2014).
100 Wang, L. *et al.* A novel electrochemical biosensor based on dynamic polymerase-extending hybridization for E.coli O157:H7 DNA detection. *Talanta* **78**, 647-652, doi:10.1016/j.talanta.2008.12.001 (2009).
101 Tan, F. *et al.* A PDMS microfluidic impedance immunosensor for E. coli O157:H7 and Staphylococcus aureus detection via antibody-immobilized nanoporous membrane. *Sensor Actuat B-Chem* **159**, 328-335, doi:10.1016/j.snb.2011.06.074 (2011).

102 Rai, V., Deng, J. & Toh, C.-S. Electrochemical nanoporous alumina membrane-based label-free DNA biosensor for the detection of Legionella sp. *Talanta* **98**, 112-117, doi:10.1016/j.talanta.2012.06.055 (2012).
103 Tan, F. *Foodborne pathogens detection with nanoporous anodic aluminum oxide membrane based biosensor* M.Phil. thesis, Hong Kong Polytechnic University, (2012).
104 Rai, V. *et al.* Ultrasensitive cDNA Detection of Dengue Virus RNA Using Electrochemical Nanoporous Membrane-Based Biosensor. *Plos One* **7**, doi:10.1371/journal.pone.0042346 (2012).
105 Wigginton, K. R. & Vikesland, P. J. Gold-coated polycarbonate membrane filter for pathogen concentration and SERS-based detection. *Analyst* **135**, 1320-1326, doi:10.1039/b919270k (2010).
106 Joung, C.-K. *et al.* A nanoporous membrane-based impedimetric immunosensor for label-free detection of pathogenic bacteria in whole milk. *Biosens Bioelectron* **44**, 210-215, doi:10.1016/j.bios.2013.01.024 (2013).
107 Zhang, L. *et al.* A new system for the amplification of biological signals: RecA and complimentary single strand DNA probes on a leaky surface acoustic wave biosensor. *Biosens Bioelectron* **60**, 259-264, doi:10.1016/j.bios.2014.04.037 (2014).
108 Sang, S. & Witte, H. A novel PDMS micro membrane biosensor based on the analysis of surface stress. *Biosens Bioelectron* **25**, 2420-2424, doi:10.1016/j.bios.2010.03.035 (2010).
109 He, F. J. & Liu, S. Q. Detection of P-aeruginosa using nano-structured electrode-separated piezoelectric DNA biosensor. *Talanta* **62**, 271-277, doi:10.1016/j.talanta.2003.07.007 (2004).
110 Chua, A. L., Yean, C. Y., Ravichandran, M., Lim, B. & Lalitha, P. A rapid DNA biosensor for the molecular diagnosis of infectious disease. *Biosens Bioelectron* **26**, 3825-3831, doi:10.1016/j.bios.2011.02.040 (2011).
111 Park, S., Kim, H., Paek, S.-H., Hong, J. W. & Kim, Y.-K. Enzyme-linked immuno-strip biosensor to detect Escherichia coli O157 : H7. *Ultramicroscopy* **108**, 1348-1351, doi:10.1016/j.ultramic.2008.04.063 (2008).
112 Karthik, K., Das, P., Murugan, M. S. & Singh, P. Evaluation of bioelectronics sensor compared to other diagnostic test in diagnosis of Johne's disease in goats. *Small Ruminant Research* **109**, 56-63, doi:10.1016/j.smallrumres.2012.06.009 (2013).
113 Jeon, J.-W. *et al.* Rapid immuno-analytical system physically integrated with lens-free CMOS image sensor for food-borne pathogens. *Biosens Bioelectron* **52**, 384-390, doi:10.1016/j.bios.2013.09.004 (2014).
114 Yan, Z. *et al.* Rapid quantitative detection of Yersinia pestis by lateral-flow immunoassay and up-converting phosphor technology-based biosensor. *Sensor Actuat B-Chem* **119**, 656-663, doi:10.1016/j.snb.2006.01.029 (2006).
115 Thet, N. T. *Modified tethered bilayer lipid membranes for detection of pathogenic bacterial toxins and characterization of ion channels*]Doctor of Philosophy (PhD) thesis, University of Bath, (2010).
116 Dill, K., Stanker, L. H. & Young, C. R. Detection of salmonella in poultry using a silicon chip-based biosensor. *Journal of Biochemical and Biophysical Methods* **41**, 61-67, doi:10.1016/s0165-022x(99)00027-5 (1999).

117 Hong, H.-B. *et al.* Detection of two different influenza A viruses using a nitrocellulose membrane and a magnetic biosensor. *Journal of Immunological Methods* **365**, 95-100, doi:10.1016/j.jim.2010.12.005 (2011).
118 Karoonuthaisiri, N. *et al.* Development of antibody array for simultaneous detection of foodborne pathogens. *Biosens Bioelectron* **24**, 1641-1648, doi:10.1016/j.bios.2008.08.026 (2009).
119 Blazkova, M., Javurkova, B., Fukal, L. & Rauch, P. Immunochromatographic strip test for detection of genus Cronobacter. *Biosens Bioelectron* **26**, 2828-2834, doi:10.1016/j.bios.2010.10.001 (2011).
120 Low, S. C., Ahmad, A. L., Ideris, N. & Ng, Q. H. Interaction of isothermal phase inversion and membrane formulation for pathogens detection in water. *Bioresource Technology* **113**, 219-224, doi:10.1016/j.biortech.2011.11.048 (2012).
121 Theegala, C. S., Small, D. D. & Monroe, W. T. Oxygen electrode-based single antibody amperometric biosensor for qualitative detection of E-coli and bacteria in water. *Journal of Environmental Science and Health Part a-Toxic/Hazardous Substances & Environmental Engineering* **43**, 478-487, doi:10.1080/10934520701796325 (2008).
122 Toranzos, G. A. & Alvarez, A. J. SOLID-PHASE POLYMERASE CHAIN-REACTION - APPLICATIONS FOR DIRECT DETECTION OF ENTERIC PATHOGENS IN WATERS. *Canadian Journal of Microbiology* **38**, 365-369 (1992).
123 Luo, Y. *et al.* Surface functionalization of electrospun nanofibers for detecting E. coli O157:H7 and BVDV cells in a direct-charge transfer biosensor. *Biosens Bioelectron* **26**, 1612-1617, doi:10.1016/j.bios.2010.08.028 (2010).
124 Luo, Y. *et al.* Novel Biosensor Based on Electrospun Nanofiber and Magnetic Nanoparticles for the Detection of E. coli O157:H7. *Ieee T Nanotechnol* **11**, 676-681, doi:10.1109/tnano.2011.2174801 (2012).
125 Kumanan, V., Nugen, S. R., Baeumner, A. J. & Chang, Y.-F. A biosensor assay for the detection of Mycobacterium avium subsp paratuberculosis in fecal samples. *Journal of Veterinary Science* **10**, 35-42, doi:10.4142/jvs.2009.10.1.35 (2009).
126 Baeumner, A. J., Leonard, B., McElwee, J. & Montagna, R. A. A rapid biosensor for viable B-anthracis spores. *Analytical and bioanalytical chemistry* **380**, 15-23, doi:10.1007/s00216-004-2726-7 (2004).
127 Baeumner, A. J. *et al.* Biosensor for Dengue virus detection: Sensitive, rapid, and serotype specific. *Anal Chem* **74**, 1442-1448, doi:10.1021/ac015675e (2002).
128 Hartley, H. A. & Baeumner, A. J. Biosensor for the specific detection of a single viable B-anthracis spore. *Analytical and bioanalytical chemistry* **376**, 319-327, doi:10.1007/s00216-003-1939-5 (2003).
129 Zaytseva, N. V., Montagna, R. A., Lee, E. M. & Baeumner, A. J. Multi-analyte single-membrane biosensor for the serotype-specific detection of Dengue virus. *Analytical and bioanalytical chemistry* **380**, 46-53, doi:10.1007/s00216-004-2724-9 (2004).
130 Baeumner, A. J., Cohen, R. N., Miksic, V. & Min, J. H. RNA biosensor for the rapid detection of viable Escherichia coli in drinking water. *Biosens Bioelectron* **18**, 405-413, doi:10.1016/s0956-5663(02)00162-8 (2003).
131 Campas, M., Szydlowska, D., Trojanowicz, M. & Marty, J. L. Towards the protein phosphatase-based biosensor for microcystin detection. *Biosens Bioelectron* **20**, 1520-1530, doi:10.1016/j.bios.2004.06.002 (2005).

132 Ye, J. M., Pivarnik, P. E., Senecal, A. G. & Rand, A. G. in *Pathogen Detection and Remediation for Safe Eating* Vol. 3544 *Proceedings of the Society of Photo-Optical Instrumentation Engineers (Spie)* (ed Y. R. Chen) 2-9 (1999).
133 Serra, B. *et al.* A rapid method for detection of catalase-positive and catalase-negative bacteria based on monitoring of hydrogen peroxide evolution at a composite peroxidase biosensor. *Talanta* **75**, 1134-1139, doi:10.1016/j.talanta.2008.01.009 (2008).
134 Liu, Y. *et al.* Detection of pathogens using luminescent Cdse/ZnS dendron nanocrystals and a porous membrane immunofilter. *Anal Chem* **79**, 8796-8802, doi:10.1021/ac0709605 (2007).
135 Abdel-Hamid, I., Ivnitski, D., Atanasov, P. & Wilkins, E. Flow-through immunofiltration assay system for rapid detection of E-coli O157 : H7. *Biosens Bioelectron* **14**, 309-316 (1999).
136 Ertl, P., Wagner, M., Corton, E. & Mikkelsen, S. R. Rapid identification of viable Escherichia coli subspecies with an electrochemical screen-printed biosensor array. *Biosens Bioelectron* **18**, 907-916, doi:10.1016/s0956-5663(02)00206-3 (2003).
137 McGraw, S. K., Alocilja, E., Senecal, K. & Senecal, A. A Resistance Based Biosensor That Utilizes Conductive Microfibers for Microbial Pathogen Detection. *Open Journal of Applied Biosensor* **1**, 36-43 (2012).
138 Li, D. P., Frey, M. W. & Baeumner, A. J. Electrospun polylactic acid nanofiber membranes as substrates for biosensor assemblies. *Journal of Membrane Science* **279**, 354-363, doi:10.1016/j.memsci.2005.12.036 (2006).
139 Jain, S. *et al.* Highly sensitive detection of Salmonella typhi using surface aminated polycarbonate membrane enhanced-ELISA. *Biosens Bioelectron* **31**, 37-43, doi:10.1016/j.bios.2011.09.031 (2012).
140 Connelly, J. T. *et al.* Micro-total analysis system for virus detection: microfluidic pre-concentration coupled to liposome-based detection. *Analytical and bioanalytical chemistry* **402**, 315-323, doi:10.1007/s00216-011-5381-9 (2012).
141 Sung, Y. J. *et al.* Novel antibody/gold nanoparticle/magnetic nanoparticle nanocomposites for immunomagnetic separation and rapid colorimetric detection of Staphylococcus aureus in milk. *Biosens Bioelectron* **43**, 432-439, doi:10.1016/j.bios.2012.12.052 (2013).
142 Cai, G., Gorey, C., Zaky, A., Escobar, I. & Gruden, C. Thermally responsive membrane-based microbiological sensing component for early detection of membrane biofouling. *Desalination* **270**, 116-123, doi:10.1016/j.desal.2010.11.030 (2011).
143 Dadarwal, R., Namvar, A., Thomas, D. F., Hall, J. C. & Warriner, K. Organic conducting polymer electrode based sensors for detection of Salmonella infecting bacteriophages. *Materials Science & Engineering C-Biomimetic and Supramolecular Systems* **29**, 761-765, doi:10.1016/j.msec.2008.07.010 (2009).
144 Ertl, P. & Mikkelsen, S. R. Electrochemical biosensor array for the identification of microorganisms based on lectin-lipopolysaccharide recognition. *Anal Chem* **73**, 4241-4248, doi:10.1021/ac010324l (2001).
145 Senapati, S. *et al.* An ion-exchange nanomembrane sensor for detection of nucleic acids using a surface charge inversion Phenomenon. *Biosens Bioelectron* **60**, 92-100, doi:10.1016/j.bios.2014.04.008 (2014).
146 Gramberg, B., Kintzios, S., Schmidt, U., Mewis, I. & Ulrichs, C. A Basic Approach Towards the Development of Bioelectric Bacterial Biosensors for the Detection of Plant

Viruses. *Journal of Phytopathology* **160**, 106-111, doi:10.1111/j.1439-0434.2011.01867.x (2012).
147 Perdikaris, A., Vassilakos, N., Yiakoumettis, I., Kektsidou, O. & Kintzios, S. Development of a portable, high throughput biosensor system for rapid plant virus detection. *Journal of Virological Methods* **177**, 94-99, doi:https://doi.org/10.1016/j.jviromet.2011.06.024 (2011).
148 Moschopoulou, G. *et al.* Engineering of the membrane of fibroblast cells with virus-specific antibodies: A novel biosensor tool for virus detection. *Biosens Bioelectron* **24**, 1027-1030 (2008).
149 Michalke, A., Galla, H. J. & Steinem, C. Channel activity of a phytotoxin of Clavibacter michiganense ssp nebraskense in tethered membranes. *European Biophysics Journal with Biophysics Letters* **30**, 421-429, doi:10.1007/s002490100154 (2001).
150 Chen, H. *et al.* Construction of supported lipid membrane modified piezoelectric biosensor for sensitive assay of cholera toxin based on surface-agglutination of ganglioside-bearing liposomes. *Anal Chim Acta* **657**, 204-209, doi:10.1016/j.aca.2009.10.036 (2010).
151 Liu, N., Gao, Z., Zhou, H. & Yue, M. Detection of SEB gene by bilayer lipid membranes nucleic acid biosensor supported by modified patch-clamp pipette electrode. *Biosens Bioelectron* **22**, 2371-2376, doi:10.1016/j.bios.2006.09.037 (2007).
152 Pan, J. J. & Charych, D. *Molecular recognition and optical detection of biological pathogens at biomimetic membrane interfaces*. Vol. 3040 (1997).
153 Villalobos, P. *et al.* The application of polymerized lipid vesicles as colorimetric biosensors for real-time detection of pathogens in drinking water. *Electron. J. Biotechnol.* **15**, doi:10.2225/vol15-issue1-fulltext-5 (2012).
154 Luna, D. M. N., Oliveira, M. D. L., Nogueira, M. L. & Andrade, C. A. S. Biosensor based on lectin and lipid membranes for detection of serum glycoproteins in infected patients with dengue. *Chemistry and Physics of Lipids* **180**, 7-14, doi:10.1016/j.chemphyslip.2014.02.008 (2014).
155 Pal, S., Alocilja, E. C. & Downes, F. P. Nanowire labeled direct-charge transfer biosensor for detecting Bacillus species. *Biosensors & Bioelectronics* **22**, 2329-2336, doi:10.1016/j.bios.2007.01.013 (2007).
156 Li, Q., Gusarov, S., Evoy, S. & Kovalenko, A. Electronic structure, binding energy, and solvation structure of the streptavidin-biotin supramolecular complex: ONIOM and 3D-RISM study. *J Phys Chem B* **113**, 9958-9967, doi:10.1021/jp902668c (2009).
157 Baeumner, A. J., Leonard, B., McElwee, J. & Montagna, R. A. A rapid biosensor for viable B. anthracis spores. *Analytical and bioanalytical chemistry* **380**, 15-23, doi:10.1007/s00216-004-2726-7 (2004).
158 Hartley, H. A. & Baeumner, A. J. Biosensor for the specific detection of a single viable B. anthracis spore. *Analytical and bioanalytical chemistry* **376**, 319-327, doi:10.1007/s00216-003-1939-5 (2003).
159 Toranzos, G. A. & Alvarez, A. J. Solid-phase polymerase chain-reaction: applications for direct detection of enteric pathogens in water. *Canadian Journal of Microbiology* **38**, 365-369 (1992).
160 He, F. J. & Liu, S. Q. Detection of P. aeruginosa using nano-structured electrode-separated piezoelectric DNA biosensor. *Talanta* **62**, 271-277, doi:10.1016/j.talanta.2003.07.007 (2004).

161 Hariharan, P. in *Handbook of Optics, Volume II - Devices, Measurements, and Properties* Vol. 2 (eds Michael Bass, Eric W. Van Stryland, David R. Williams, & William L. Wolfe) Ch. 21, 28 (McGraw-Hill Inc., 1995).
162 Senapati, S., Basuray, S., Slouka, Z., Cheng, L.-J. & Chang, H.-C. A Nanomembrane-Based Nucleic Acid Sensing Platform for Portable Diagnostics. *Top Curr Chem* **304**, 153–169 (2011).
163 Takao Someya, Y. K., Tsuyoshi Sekitani, Shingo Iba, Yoshiaki Noguchi, Yousuke Murase, & Hiroshi Kawaguchi, T. S. Conformable, flexible, large-area networks of pressure and thermal sensors with organic transistor active matrixes. *Proc Natl Acad Sci U.S.A.* **102**, 12321–12325 (2005).
164 Ying, M. *et al.* Silicon nanomembranes for fingertip electronics. *Nanotechnology* **23**, 344004 (344007pp) (2012).
165 Stampfer, C. *et al.* Fabrication of Single-Walled Carbon-Nanotube-Based Pressure Sensors. *Nano Lett* **6**, 233-237 (2006).
166 Birkholz, M. *et al.* Ultrathin TiN Membranes as a Technology Platform for CMOS-Integrated MEMS and BioMEMS Devices. *Adv Funct Mater* **21**, 1652–1656 (2011).
167 Strassner, M. *et al.* Fabrication of Ultrathin and Highly Flexible InP-Based Membranes for Microoptoelectromechanical Systems at 1.55 um. *IEEE Photonic Tech L* **17**, 804-806 (2005).
168 Jaksic, Z., Vukovic, S. M., Buha, J. & Matovic, J. Nanomembrane-based plasmonics. *J Nanophotonics* **5**, 051818-051811-051820 (2011).
169 Zhu, X. *et al.* An Ultrathin Self-Humidifying Membrane for PEM Fuel Cell Application: Fabrication, Characterization, and Experimental Analysis. *J Phys Chem B* **110**, 14240-14248 (2006).
170 Striemer, C. C., Gaborski, T. R., McGrath, J. L. & Fauchet, P. M. Charge- and size-based separation of macromolecules using ultrathin silicon membranes. *Nature* **445**, 749-753 (2007).
171 Lee, J. A. *et al.* Hybrid Nanomembranes for High Power andHigh EnergyDensity Supercapacitors and Their Yarn Application. *ACS Nano* **6**, 327–334 (2012).
172 Yan, C., Xi, W., Si, W., Deng, J. & Schmidt, O. G. Highly Conductive and Strain-Released Hybrid Multilayer Ge/Ti Nanomembranes with Enhanced Lithium-Ion-Storage Capability. *Adv Mater* **25**, 539–544 (2013).
173 Savoia, A. S., Caliano, G. & Pappalardo, M. A CMUT probe for medical ultrasonography: from microfabrication to system integration. *IEEE T Ultrasoc Ferr* **59**, 1127-1138 (2012).
174 Horowitz, S. B., Sheplak, M., Cattafesta, L. N. & Nishida, T. A MEMS acoustic energy harvester *J Micromech Microeng* **16**, S174–S181 (2006).
175 Barton, R. A. *et al.* Photothermal Self-Oscillation and Laser Cooling of Graphene Optomechanical Systems. *Nano Lett* **12**, 4681−4686 (2012).
176 Matović, J. & Jakšić, Z. Simple and reliable technology for manufacturing metal-composite nanomembranes with giant aspect ratio. *Microelectronic Eng* **86**, 906-909 (2009).
177 Turchanin, A. *et al.* One Nanometer Thin Carbon Nanosheets with Tunable Conductivity and Stiffness. *Advanced Materials* **21**, 1233-1237, doi:10.1002/adma.200803078 (2009).
178 Zhang, X. *Mechanical Characterization of Carbon Nanosheets* M.Sc. thesis, Bielefeld University, (2010).

179 Nottbohm, C. T., Turchanin, A., Beyer, A., Stosch, R. & Gölzhäuser, A. Mechanically Stacked 1-nm-Thick Carbon Nanosheets: Ultrathin Layered Materials with Tunable Optical, Chemical, and Electrical Properties. *Small* **7**, 874-883, doi:10.1002/smll.201001993 (2011).
180 Nelson-Fitzpatrick, N. *et al.* Synthesis and characterization of Au–Ta nanocomposites for nanomechanical cantilever devices. *Nanotechnology* **18**, 355303 (2007).
181 Hall, E. O. The Deformation and Ageing of Mild Steel: III Discussion of Results *Proc Phys Soc B* **64**, 747–753 (1951).
182 Petch, N. J. The cleavage strength of polycrystals. *J Iron Steel Inst* **174**, 25-28 (1953).
183 Tabata, O., Kawahata, K., Sugiyama, S. & Igarishi, I. Mechanical property measurements of thin films using load-deflection of composite rectangular membranes. *Sensor Actuator* **20**, 135–141 (1989).
184 Allen, M. G., Mehregany, M., Howe, R. T. & Senturia, S. D. Microfabricated structures for the in situ measurement of residual thin films. *Appl Phys Lett* **51**, 241–243 (1987).
185 Pan, J. Y., Lin, P., Maseeh, F. & Senturia, S. D. Verification of FEM analysis of load-deflection methods for measuring mechanical property of thin films. *Technical Digest, IEEE Solid-State Sensor and Actuator Workshop* **191**, 70–73 (1990).
186 Vlassak, J. J. & Nix, W. D. A new bulge test technique for the determination of Young's modulus and Poisson's ratio of thin films. *J Mater Res Soc* **7**, 3242–3249 (1992).
187 Maier-Schneider, D., Maibach, J. & Obermeier, E. A new analytical solution for the load-deflection of square membranes. *J Microelectromech Syst* **4**, 238–241 (1995).
188 van den Hurk, R., Nelson-Fitzpatrick, N. & Evoy, S. Fabrication and characterization of aluminum-molybdenum nanocomposite membranes. *Journal of Vacuum Science & Technology B* **32**, doi:10.1116/1.4893671 (2014).
189 Olkhovets, A., Evoy, S., Carr, D. W., Parpia, J. M. & Craighead, H. G. Actuation and internal friction of torsional nanomechanical silicon resonators. *Journal of Vacuum Science & Technology B: Microelectronics and Nanometer Structures Processing, Measurement, and Phenomena* **18**, 3549-3551, doi:10.1116/1.1313571 (2000).
190 Quitoriano, N. J., Belov, M., Evoy, S. & Kamins, T. I. Single-Crystal, Si Nanotubes, and Their Mechanical Resonant Properties. *Nano Letters* **9**, 1511-1516, doi:10.1021/nl803565q (2009).
191 Mohammad, M. A., Dew, S. K., Evoy, S. & Stepanova, M. Fabrication of sub-10nm silicon carbon nitride resonators using a hydrogen silsesquioxane mask patterned by electron beam lithography. *Microelectronic Engineering* **88**, 2338-2341, doi:https://doi.org/10.1016/j.mee.2010.11.045 (2011).
192 Haynes, W. M. *CRC handbook of chemistry and physics.* (CRC Press, Boca Raton, 2010).
193 Senturia, S. D. *Microsystem Design*. 196 (Kluwer Academic Publishers, 2002).
194 Lee, H. K., Ko, S. H., Han, J. S. & Park, H. Mechanical properties measurement of silicon nitride thin films using the bulge test. *Proc. SPIE, Microelectronics: Design, Technology, and Packaging III* **6798**, 67981C-67981 - 67988 (2007).
195 Slater, J. C. & Frank, N. H. *Mechanics*. 1st edn, (McGraw-Hill, 1947).
196 French, A. P. *Vibrations and Waves*. 1st edn, (Thomas Nelson & Sons Ltd, 1971).
197 Liu, Z. W. & Ong, C. K. Microstructure and thickness dependent magnetic properties of nanogranular Co–Zn–O thin films for microwave applications. *J. Alloys Compd.* **509**, 10075– 10079 (2011).

198 Ohring, M. *Materials Science of Thin Films, 2nd Edition*. 794 (Academic Press, 2001).
199 Pramanik, C. & Saha, H. Low pressure piezoresistive sensors for medical electronics applications. *Mater. Manuf. Process.* **21**, 233-238, doi:10.1080/10426910500464446 (2006).
200 Xu, T. Z. *et al.* A high sensitive pressure sensor with the novel bossed diaphragm combined with peninsula-island structure. *Sens. Actuator A-Phys.* **244**, 66-76, doi:10.1016/j.sna.2016.04.027 (2016).
201 Sindhanaiselvi, D., Natarajan, R. A. & Shanmugananthan, T. in *Dynamics of Machines and Mechanisms, Industrial Research* Vol. 592-594 *Applied Mechanics and Materials* (eds K. R. Balasubramanian, S. P. Sivapirakasam, & R. Anand) 2193-+ (Trans Tech Publications Ltd, 2014).
202 Arjunan, N. & Thangavelu, S. Modeling and Analysis of a Multi Bossed Beam Membrane Sensor for Environmental Applications. *TRANSACTIONS ON ELECTRICAL AND ELECTRONIC MATERIALS* **18**, 25-29 (2017).
203 Maj, C. *et al.* Analytical Modelling of Bossed Membrane. *XII International Conference on Perspective Technologies and Methods in MEMS Design (MEMSTECH)* (2016).
204 Augustyniak, I. *et al.* Micromechanical high-doses radiation sensor with bossed membrane and interferometry optical detection. *Sens. Actuator A-Phys.* **232**, 353-358, doi:10.1016/j.sna.2015.05.006 (2015).
205 Nesterov, V. & Brand, U. Modelling and investigation of the mechanical and electrical characteristics of the silicon 3D-boss microprobe for force and deflection measurements. *Journal of Micromechanics and Microengineering* **16**, 1116-1127, doi:10.1088/0960-1317/16/7/003 (2006).
206 Yang, E. H., Lee, C. & Khodadadi, J. M. Development of MEMS-based piezoelectric microvalve technologies. *Sens. Mater.* **19**, 1-18 (2007).
207 Dzulkefli, N. A., Bais, B. & Majlis, B. Y. in *Nems/Mems Technology and Devices* Vol. 74 *Advanced Materials Research* (eds S. Teo, A. Q. Liu, H. Li, & B. Tarik) 287-290 (Trans Tech Publications Ltd, 2009).
208 Pozzi, M. *et al.* in *Device and Process Technologies for Microelectronics, Mems, Photonics and Nanotechnology Iv* Vol. 6800 *Proceedings of SPIE* (eds H. H. Tan *et al.*) (Spie-Int Soc Optical Engineering, 2008).
209 Jaksic, Z., Radulovic, K., Tanaskovic, D. & ieee. in *2004 24th International Conference on Microelectronics, Proceedings, Vols 1 and 2 International Conference on Microelectronics-MIEL* 231-234 (Ieee, 2004).
210 Yih, T. C., Wei, C. M. & Hammad, B. Modeling and characterization of a nanoliter drug-delivery MEMS micropump with circular bossed membrane. *Nanomed.-Nanotechnol. Biol. Med.* **1**, 164-175, doi:10.1016/j.nano.2005.01.002 (2005).
211 Meguid, S. A., Wernik, J. M. & Jahwari, F. A. Toughening mechanisms in multiphase nanocomposites. *International Journal of Mechanics and Materials in Design* **9**, 115-125 (2013).
212 Zhu, J. F., Liao, S. W. & Li, S. F. Circularly polarized 2-arm spiral antenna for 60-GHz applications. *Microw. Opt. Technol. Lett.* **59**, 3119-3123, doi:10.1002/mop.30890 (2017).
213 Yang, C. Y., Liu, S. W., Xie, X. & Livermore, C. Compact, planar, translational piezoelectric bimorph actuator with Archimedes' spiral actuating tethers. *Journal of Micromechanics and Microengineering* **26**, doi:10.1088/0960-1317/26/12/124005 (2016).

214 Yoshimatsu, K., Yamauchi, M., Tanaka, M. & Ieee. *Analyses of Motion and Acceleration Sensors using Printed Spiral Inductors by a Simulator and Actual Circuit Experiments*. (Ieee, 2009).
215 Hehn, T. & Manoli, Y. *CMOS Circuits for Piezoelectric Energy Harvesters*. Vol. 38 (2015).
216 Kim, G.-Y. *et al.* Effect of Thickness Ratio in Piezoelectric/Elastic Cantilever Structure on the Piezoelectric Energy Harvesting Performance. *Electronic Materials Letters* **15**, 61-69, doi:10.1007/s13391-018-00103-w (2019).
217 Kalafut, D., Bajaj, A. & Raman, A. Multistability of cantilever MEMS/NEMS switches induced by electrostatic and surface forces. *Int. J. Non-Linear Mech.* **95**, 209-215, doi:10.1016/j.ijnonlinmec.2017.06.009 (2017).
218 Wang, K. F. & Wang, B. L. Non-linear flexoelectricity in energy harvesting. *Int. J. Eng. Sci.* **116**, 88-103, doi:10.1016/j.ijengsci.2017.02.010 (2017).
219 Bota, S. A. *et al. Cantilever NEMS Relay-Based SRAM Devices for Enhanced Reliability*. (Ieee, 2017).
220 van den Hurk, R. & Evoy, S. *Deflection cantilever detection of interferon gamma*. Vol. 176 (2013).
221 Pinson, J. in *Aryl Diazonium Salts* 1-35 (Wiley-VCH Verlag GmbH & Co. KGaA, 2012).
222 Arkles, B. in *Kirk-Othmer Encyclopedia of Chemical Technology* (John Wiley & Sons, Inc., 2000).
223 Arkles, B., Maddox, A., Singh, M., Zazyczny, J. & Matisons, J. in *Gelest* (ed Gelest) (Gelest, Gelest, 2014).
224 Dow Corning. *Silane Coupling Agents.* (2009).
225 Singh, U. *et al.* Mycobacteriophage lysin-mediated capture of cells for the PCR detection of Mycobacterium avium subspecies paratuberculosis. *Analytical Methods* **6**, 5682-5689, doi:10.1039/C4AY01072H (2014).
226 Brambilla, C. *et al.* Mycobacteria Clumping Increase Their Capacity to Damage Macrophages. *Frontiers in microbiology* **7**, 1562-1562, doi:10.3389/fmicb.2016.01562 (2016).

Journal Papers

1. van den Hurk, R., Nelson-Fitzpatrick, N. & Evoy, S. Fabrication and characterization of aluminum-molybdenum nanocomposite membranes. Journal of Vacuum Science & Technology B 32, doi:10.1116/1.4893671 (2014).

2. van den Hurk, R. & Evoy, S. A Review of Membrane-Based Biosensors for Pathogen Detection. Sensors 15, 14045-14078, doi:10.3390/s150614045 (2015).

3. Zheng, W., Li, P., van den Hurk, R. & Evoy, S. Helium Ion Microscope-Assisted Nanomachining of Resonant Nanostrings. Sensors 16, doi:10.3390/s16071080 (2016).

4. Zheng, W. et al. Aryl Diazonium Chemistry for the Surface Functionalization of Glassy Biosensors. Biosensors 6, 8 (2016).
5. van den Hurk, R., Baghelani, M., Chen, J., Daneshmand, M., Evoy, S. Al-Mo Nanocomposite Functionalization for Membrane-based Resonance Detection of Bovine Herpesvirus-1. Submitted to Sensors and Actuators A: Physical.